River Rapids

Conference Proceedings of the Society for Experimental Mechanics Series

Nonlinear Structures & Systems, Volume 1

Ludovic Renson
Robert Kuether
Paolo Tiso
Drithi Shettya

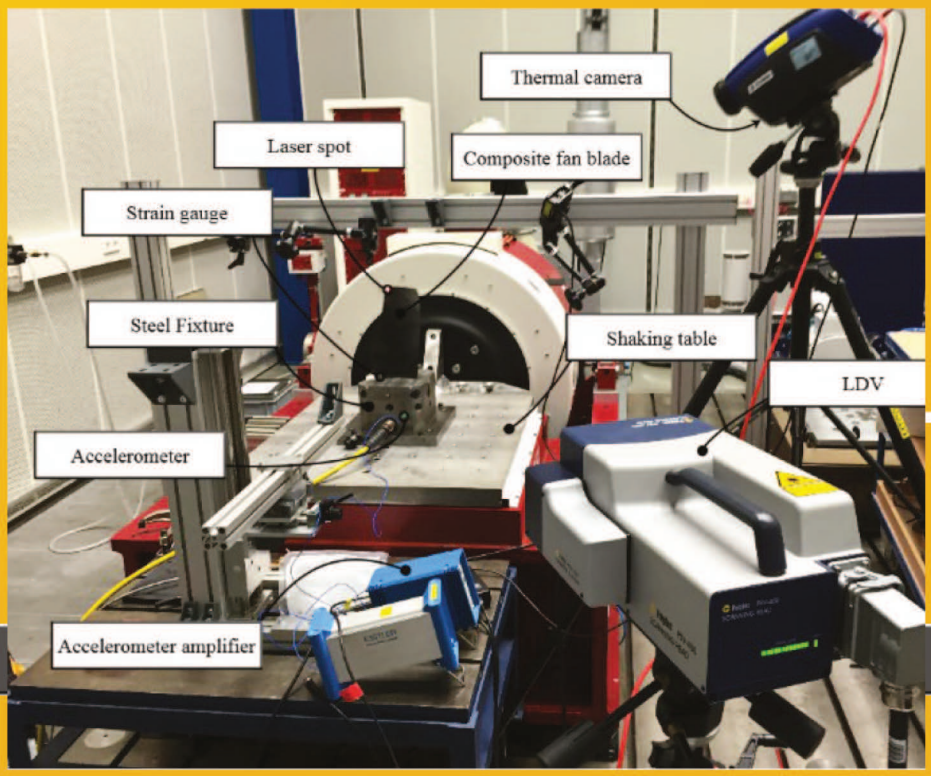

Proceedings of the 44th IMAC, A Conference and Exposition on Structural Dynamics 2026

River Publishers

Conference Proceedings of the Society for Experimental Mechanics Series

Series Editor

Kristin B. Zimmerman
Society for Experimental Mechanics, Inc.,
Bethel, USA

The Conference Proceedings of the Society for Experimental Mechanics Series presents early findings and case studies from a wide range of fundamental and applied work across the broad range of fields that comprise Experimental Mechanics. Series volumes follow the principle tracks or focus topics featured in each of the Society's two annual conferences: IMAC, A Conference and Exposition on Structural Dynamics, and the Society's Annual Conference & Exposition and will address critical areas of interest to researchers and design engineers working in all areas of Structural Dynamics, Solid Mechanics and Materials Research.

Ludovic Renson · Robert Kuether · Paolo Tiso · Drithi Shetty
Editors

Nonlinear Structures & Systems, 2026, Vol. 1

Proceedings of the 44th IMAC, A Conference and Exposition on Structural Dynamics 2026

River Publishers

Published, sold and distributed by:

River Publishers
Broagervej 10
9260 Gistrup
Denmark

www.riverpublishers.com

ISBN 97887-438-1440-5 (Hardback)

ISBN 97887-438-1412-2 (eBook)

https://doi.org/10.13052/rp-9788743814122

Conference Proceedings of the Society for Experimental Mechanics

An imprint of River Publishers

© The Society for Experimental Mechanics, Inc. 2026

This work is subject to copyright. All rights are solely and exclusively licensed by the Publisher, whether the whole or part of the material is concerned, specifically the rights of translation, reprinting, reuse of illustrations, recitation, broadcasting, or reproduction in any other physical way, and transmission or information storage and retrieval, electronic adaptation, computer software, or by similar or dissimilar methodology now known or hereafter developed.

The use of general descriptive names, registered names, trademarks, service marks, etc. in this publication does not imply, even in the absence of a specific statement, that such names are exempt from the relevant protective laws and regulations and therefore free for general use. The publisher, the authors, and the editors are safe to assume that the advice and information in this book are believed to be true and accurate at the date of publication. Neither the publisher nor the authors or the editors give a warranty, expressed or implied, with respect to the material contained herein or for any errors or omissions that may have been made. The publisher remains neutral with regard to jurisdictional claims in published maps and institutional affiliations.

Preface

Nonlinear Structures & Systems represents one of ten volumes of technical papers presented at the 44th IMAC, A Conference and Exposition on Structural Dynamics, organized by the Society for Experimental Mechanics, and held January 19–22, 2026. The full proceedings also include volumes on Dynamics of Civil Structures; Model Validation and Uncertainty Quantification; Dynamic Substructuring & Transfer Path Analysis; Special Topics & Experimental Techniques in Structural Dynamics; Computer Vision & SLDV for Structural Dynamics; Dynamic Environments & Durability Testing; Topics in Modal Analysis & Parameter Identification in Structural Dynamics; Data Science in Engineering; and Structural Health Monitoring, Metamaterials, Metastructures & Additive Manufacturing and Dynamics of Biomedical and Bioinspired Systems.

Each collection presents early findings from experimental and computational investigations on an important area within Structural Dynamics. Nonlinearity is one of these areas.

The vast majority of real engineering structures behave nonlinearly. In many cases, nonlinearities can even be exploited to achieve novel functionalities. Therefore, it is necessary to consider nonlinear effects in all of the engineering design steps, both in the experimental analysis tools (so that the nonlinear parameters can be correctly identified) and in the mathematical and numerical models of the structure (to run accurate simulations). In so doing, it is possible to create models representative of the reality that can be used for better predictions once validated.

Several papers address theoretical and numerical aspects of nonlinear dynamics (covering rigorous theoretical formulations and robust computational algorithms) as well as experimental techniques and analysis methods. There are also papers dedicated to nonlinearity in practice where real-life examples of nonlinear structures are discussed.

The organizers would like to thank the authors, presenters, session organizers, and session chairs for their participation in this track.

Editors:

Ludovic Renson – Imperial College London, London, UK;
Robert Kuether – Sandia National Laboratories, Albuquerque, NM, USA;
Paolo Tiso – ETH Zurich, Zurich, Switzerland;
Drithi Shetty – University of South Florida, Lutz, FL, USA

Contents

1 **Modelling a Multi-Degree-of-Freedom Beam using Lagrangian Neural Networks** 1
Alan Xavier and Ludovic Renson

2 **Arclength Control-based Continuation for Autonomous Systems with Fast-Slow Dynamics** 5
Alexandre Spits, Ghislain Raze, Marisa Saggio, Viktor Jirsa, and Gatan Kerschen

3 **Amplitude Resonance Tracking Using Phase-Locked Loops** 17
Franois Winand, Christophe Collette, and Gatan Kerschen

4 **Machine Learning for Experimental Bifurcation Analysis** 23
Grgoire Bourdouch, Pierre Geurts, and Gatan Kerschen

5 **Data-Driven Method for Blisk Sector Dynamics with Resonant Vibration Absorber** 29
Michael W. Reynolds, Mihai Cimpuieru, and Bogdan I. Epureanu

6 **Mapping the Nonlinear Vibration Responses of Composite Aerospace Structures during Endurance and Qualification Testing** 35
D. Di Maio, F. Oude Tanke, and J. van Tiggelen

7 **Evidential Thresholding in Sparse Bayesian Learning for Nonlinear Dynamical System Identification** 45
Jiawei Jian, Jerome Antoni, and Konstantinos Gryllias

8 **Measurement and Visualization of Nonlinear Vibration Response Using Neuromorphic Event-Based Sensing** 53
Gabriella Gallegos, DaJae Doral, Suzanna Gilbert, Deborah Fowler, Fernando Moreu, Benjamin Moldenhauer, and Tariq Khraishi

9 **Reduced-Order Modeling of Loosening of Two Bolted Joints Considering Shock Excitation** 59
William Jordan, Caleb Munger, Kaitlyn Vigil, Keegan J. Moore, Brittany Ouellette, Keith Tschohl, and Sean T. Kelly

10 **Data-Driven Nonlinear Reduced-Order Modeling for Flutter Analysis** 77
Nami Mogharabin and Amin Ghadami

11 **Polynomial Tensor-Based FEM for Parametric Reduced-Order Modelling of Nonlinear Structures via Invariant Manifolds** 83
Tiago S. Martins and Daniel J. Rixen

12 **Evaluation of NVH in Lightweight Gears: An NL-ROM Study on Contact Ratio and Web Flexibility** 93
Fabio Bruzzone, Carlo Rosso, and Daniele Fabbri

13 **Electrical Chatter and Modal Response of Pin-Receptacle Contacts in Air and Oil** 103
Marcus Behling, Phillip Misterman, Robert Justin Osborne, Robert C. Flicek, Karl Walczak, Eric Robbins, Robert J. Kuether, and Jonel Ortiz

14 **Measurement of Local Contact Stiffness Using Ultrasound** 115
R. Justin Osborne, Levi Mydlenski, and Drithi Shetty

Chapter 1
Modelling a Multi-Degree-of-Freedom Beam using Lagrangian Neural Networks

Alan Xavier and Ludovic Renson

Abstract Accurately modelling the dynamic behaviour of nonlinear structures is challenging due to the wide range of potential nonlinearities and dynamic phenomena that they can exhibit. Physics-guided machine learning (PGML) has emerged as an attractive way to combine prior knowledge with data to solve a wide range of complex, nonlinear problems in science and engineering. Lagrangian Neural Networks (LNNs) are a particular PGML approach that models nonlinear systems' Lagrangian functions using artificial neural networks (NNs). The Euler-Lagrange equation is then reconstructed through automatic differentiation (AD) to derive the equations of motion, enforcing physical consistency during training.

Previously, we used LNNs to model the nonlinear vibrations of a single-degree-of-freedom (SDOF) Duffing oscillator. We extend our earlier works to address systems with multiple-degrees-of-freedoms (MDOF) and demonstrate the method on experimental data collected on a cantilever beam featuring complex response features, such as internal resonance, isola, and Neimark-Sacker bifurcations. We analyse the physical consistency of the trained model and interpret the identified stiffness and damping nonlinearities from the partial derivatives of the potential energy and dissipation functions. The trained LNNs are then used to trace frequency response and bifurcation curves, which can be directly compared to curves measured with control-based continuation.

Keywords Physics-guided machine learning · Lagrangian neural networks · Control-based continuation

Introduction

Physics-guided machine learning (PGML) integrates physics principles with data-driven models to achieve improved accuracy and generalization compared to either approach alone. Within this framework, Cranmer et al. [1] introduced Lagrangian Neural Networks (LNNs), where the system dynamics are derived from a neural-network approximation of the Lagrangian, $\mathscr{L}_\theta(q, \dot{q})$.

For structural dynamics, however, purely conservative formulations are insufficient, since real systems experience both external excitation and dissipation. To account for these effects, we extend the standard Euler–Lagrange equations by including a dissipation function $\mathscr{D}(\dot{q})$ and an external forcing term $\mathscr{F}(t)$ [2, 3]:

$$\frac{d}{dt}\left(\frac{\partial \mathscr{L}}{\partial \dot{q}_j}\right) - \frac{\partial \mathscr{L}}{\partial q_j} + \frac{\partial \mathscr{D}}{\partial \dot{q}_j} - \mathscr{F}(t) = 0. \tag{1}$$

This yields the estimated accelerations:

$$\hat{\ddot{q}} = \left(\nabla_{\dot{q}} \nabla_{\dot{q}}^T \mathscr{L}_\theta\right)^{-1} \left[\nabla_q \mathscr{L}_\theta - \left(\nabla_q \nabla_{\dot{q}}^T \mathscr{L}_\theta\right) \dot{q} - \nabla * \dot{q} \mathscr{D}_\theta + \mathscr{F}(t)\right], \tag{2}$$

where $\mathscr{L}_\theta$ and $\mathscr{D}_\theta$ are neural networks representing the conservative and dissipative dynamics, respectively.

To ensure physically consistent rest states, we impose $\mathscr{L}(0, 0) = 0$ and $\mathscr{D}(0) = 0$. The networks are trained by mini-

Alan Xavier · Ludovic Renson
Department of Mechanical Engineering, Imperial College London, South Kensington Campus, London SW7 2AZ, UK
e-mail: aax23@ic.ac.uk; l.renson@imperial.ac.uk

© The Author(s), under exclusive license to River Publishers 2026

Emily Retzlaff et al. (eds.), *Nonlinear Structures & Systems, Vol. 1*, Conference Proceedings
of the Society for Experimental Mechanics Series, https://doi.org/10.13052/rp-9788743814122

mizing a loss function that balances data fidelity with physics-based constraints:

$$loss = \lambda_0 \cdot |\hat{\ddot{q}} - \ddot{q}| + \sum_{i=1}^{n} \lambda_i \cdot \mathscr{G}_i, \tag{3}$$

where $\ddot{q}$ are measured (or simulated) accelerations and $\mathscr{G}_i$ encodes additional constraints. This allows us to enforce any prior knowledge about the system to improve our network's performance as demonstrated in [3]. This formulation allows the LNN to learn both the conservative structure and the non-conservative dynamics of the system directly from data.

Application to a Multi-Degree-of-Freedom Beam

To evaluate the LNN approach, we consider a continuous beam, shown schematically in Figure 1 (a). This setup captures the essential features of a continuous structure under external excitation.

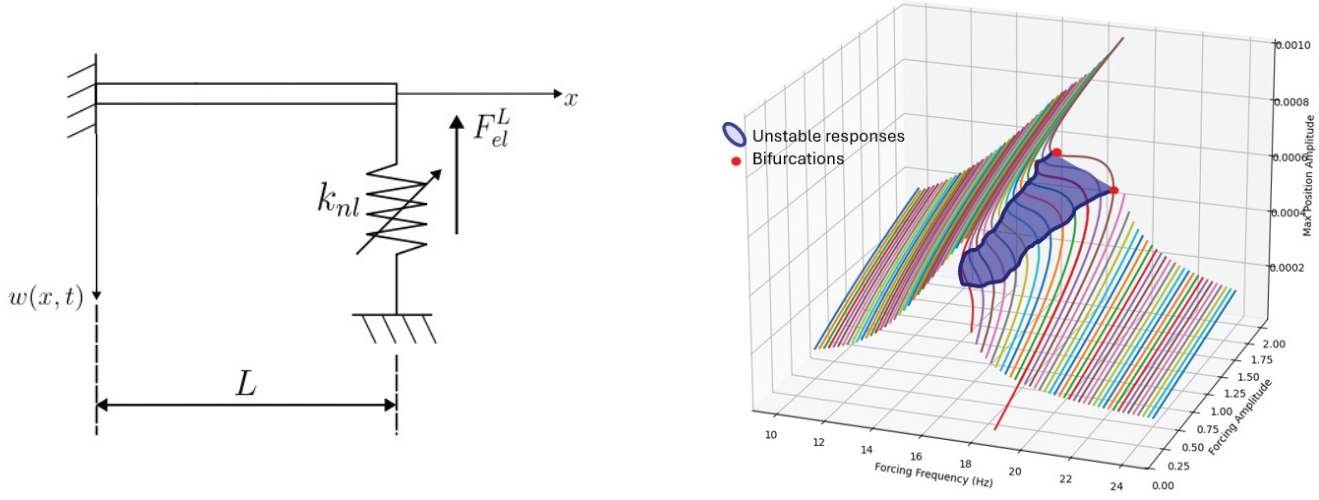

Fig. 1 (a) Picture of the beam system considered and (b) Forced response of the system showing the steady-state periodic responses computed during a series of continuations in forcing amplitude (S-curves). A portion of the dataset includes unstable responses (shaded in blue), highlighting the challenge for the LNN to accurately learn and reproduce such nonlinear dynamics

The transverse displacement of an Euler–Bernoulli beam, $w(x,t)$, is governed by the PDE (4):

$$\rho A \frac{\partial^2 w}{\partial t^2} + c\frac{\partial w}{\partial t} + EI\frac{\partial^4 w}{\partial x^4} = f(x,t) + F_{el}^L, \tag{4}$$

where ρA is the mass per unit length, EI is the flexural rigidity, c is a damping coefficient, $f(x,t)$ is the applied force, and F_{el}^L is a cubic external elastic force at the free end.

Since the beam is a continuous system with an infinite number of vibration modes, we approximate its dynamics by truncating to $N = 2$ dominant modes:

$$w(x,t) \approx \sum_{i=1}^{N} \phi_i(x) q_i(t), \tag{5}$$

where $\phi_i(x)$ are mode shapes and $q_i(t)$ are generalized coordinates. Substituting this expansion into (4) and applying the Galerkin method yields the reduced-order system:

$$M\ddot{q}(t) + C\dot{q}(t) + Kq(t) + f_{nl}(q(t), \dot{q}(t)) = F(t), \tag{6}$$

with M, C, and K being the modal mass, damping, and stiffness matrices, respectively, and f_{nl} accounting for any nonlinearities.

Thus, the beam system is described by equation (6), yielding a multi-degree-of-freedom (MDOF) model suitable for training and testing the LNN.

Simulation Data

The dataset was obtained from time-domain simulations of the beam under harmonic excitation, carried out using numerical continuation. Each simulation produced an S-curve, i.e., a set of steady-state responses measured at a fixed excitation frequency, ω as shown in Figure 1 (b). Frequencies were varied between 10.0 Hz and 24.0 Hz in increments of 0.2 Hz, resulting in 71 simulation runs and a dataset of order $\mathcal{O}(10^5)$ time samples.

The dataset was divided using an $80/20$ split applied within each S-curve rather than across the full collection of curves. This approach ensures that both training and test sets include data from the entire frequency range, while the test set still contains forcing amplitudes not seen during training. The per-S-curve split therefore provides a balanced assessment of the model's ability to generalize to unseen amplitudes within each frequency branch, rather than merely interpolating across branches. By contrast, splitting across full S-curves would exclude certain frequency branches entirely from training, creating a more stringent extrapolation task but at the cost of reduced frequency coverage during training.

As shown in Figure 1 (b), a part of the dataset includes unstable responses (highlighted in blue). This serves as both a challenging test of the LNN's learning capability and an opportunity to assess how well it reproduces such nonlinear dynamics in practice.

Network Training

The LNN architecture comprises three neural networks: $\mathscr{T}_\theta(q, \dot{q})$ for the kinetic energy, $\mathscr{V}_\theta(q, \dot{q})$ for the potential energy, and $\mathscr{D}_\theta(\dot{q})$ for the damping contribution. The kinetic and potential networks each consist of four hidden layers with 64 neurons per layer, while the damping network uses four hidden layers with 32 neurons per layer. All hidden layers employ the $\tanh$ activation function, with linear outputs at the final layer. To improve training stability, a normalization layer was applied. The networks were trained for 200 epochs using the Adam optimizer with a learning rate of 10^{-4}.

Figure 2 (a) compares predicted accelerations $\hat{\ddot{q}}$ with simulated ground truth $\ddot{q}$ across test trajectories. The LNN reproduces the overall response well, though discrepancies remain in capturing higher-order harmonics.

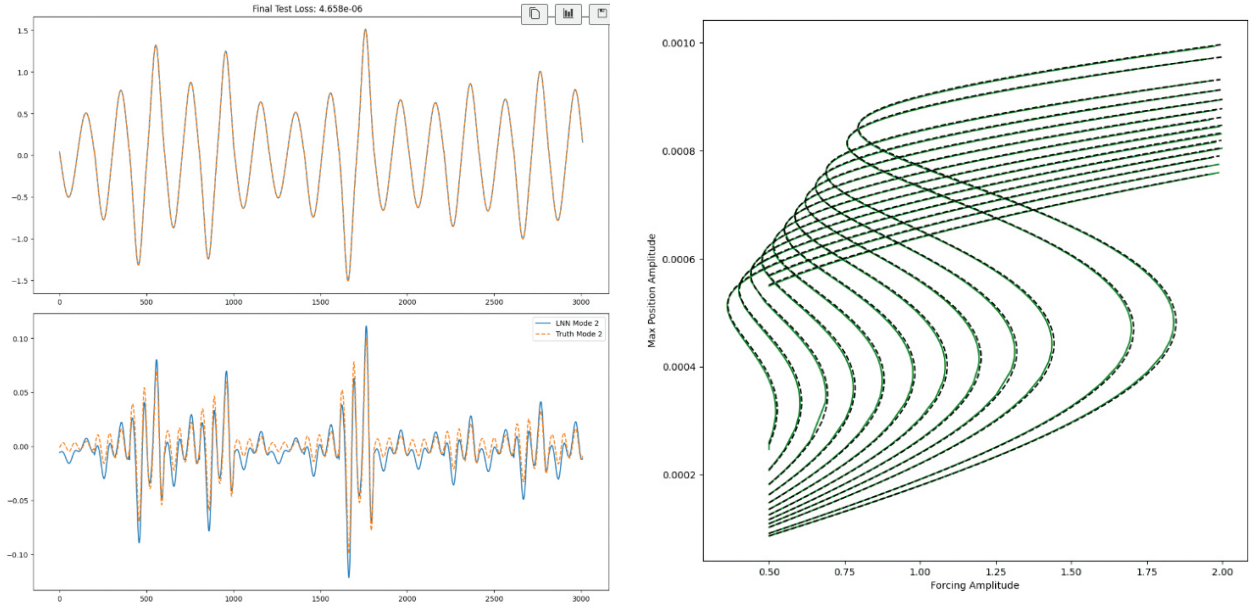

Fig. 2 Comparison of predicted accelerations, $\hat{\ddot{q}}$, from the trained LNN with ground-truth simulations, $\ddot{q}$, across sample test trajectories. (b) Backbone and forced response curves obtained via numerical continuation with the trained LNN (green), compared against the reference beam model (black). Results are shown for excitation frequencies where unstable responses and bifurcations arise (16.2 and 19.0 Hz)

Numerical Continuation

To assess the predictive capability of the trained LNN, we employed it as a surrogate within a numerical continuation scheme. Continuation was performed at fixed excitation frequencies, ω, with the forcing amplitude used as the continuation parameter. At each step, steady-state responses were obtained by integrating the learned equations of motion, and these were tracked along the continuation path.

Figure 2 (b) compares backbone and forced response curves from the LNN with those from the reference beam model, focusing on frequencies where unstable responses or bifurcations occur. These results highlight the extent to which the LNN captures key nonlinear features, including the onset of bifurcations.

References

1. Cranmer, M.D., Greydanus, S., Hoyer, S., Battaglia, P.W., Spergel, D.N., and Ho, S. "Lagrangian neural networks". *CoRR*, abs/2003.04630 (2020)
2. Meirovitch, L. *Methods of Analytical Dynamics*. Advanced engineering series. Dover Publications (2010)
3. M. J. Szydlowski, C.S. and Renson, L. "Modeling nonlinear structures using physics-guided, machine-learnt models". In *Proceedings of the 41st IMAC, A Conference and Exposition on Structural Dynamics 2023* (2023)

Chapter 2
Arclength Control-based Continuation for Autonomous Systems with Fast-Slow Dynamics

Alexandre Spits, Ghislain Raze, Marisa Saggio, Viktor Jirsa, and Gaëtan Kerschen

Abstract Bursting dynamics appear across a wide range of physical and biological systems, particularly in neuroscience, where they play a central role in modeling epilepsy. Epilepsy is characterized by abnormal, excessive or synchronous neuronal activity in the brain, marked by abrupt transitions from quiescent periods to seizures. Although EEG recordings help identify seizure patterns and affected brain regions, they often cannot predict precisely the onset, termination, or propagation of seizures. This poses a challenge for designing surgical interventions for the one-third of epilepsy patients who do not respond to medication. To deepen our understanding, phenomenological models based on nonlinear dynamics and bifurcation theory have been developed to classify seizure mechanisms by capturing fast-slow oscillations between ictal and interictal states.

Control-based continuation (CBC) techniques provide a powerful framework for experimentally exploring complex bifurcation diagrams of nonlinear systems. In this work, we present modifications to a recent extension of CBC, termed arclength control-based continuation (ACBC), for identifying fixed points and limit cycles in autonomous systems featuring fast-slow oscillations. While ACBC has been successfully applied in nonlinear vibration testing, where synchronization between the forcing and response frequencies simplifies signal analysis, autonomous systems present a unique challenge. Their self-sustained limit cycles have frequencies governed by internal dynamics which are not known a priori. To address this, we leverage angle-encoding to estimate the system's instantaneous phase and demonstrate its application within the context of seizure modeling.

Keywords Control-based continuation · Fast-slow bursters

Introduction

Nonlinear systems exhibit rich phenomena, including multistability and abrupt transitions between coexisting solutions under small parameter variations. To deal with such complex phenomena, bifurcation diagrams are used to trace the evolution of system responses and the points at which qualitative changes occur.

For decades, numerical continuation has been the standard tool for uncovering bifurcation diagrams [1–4]. It has advanced understanding across diverse engineering domains [5–8], yet its success relies on the availability of an accurate mathematical model. In many experimental settings, such models are either unavailable or too uncertain to capture the relevant dynamics. This limitation has motivated the development of experimental continuation methods [9], which combine non-invasive feedback control with continuation techniques to explore stable and unstable responses in a model-free manner.

The first experimental continuation method, known as control-based continuation (CBC) [10, 11], was conceived to extend numerical continuation principles to feedback-controlled experiments. In particular, this method leverages the Newton-Raphson algorithm and hence requires the determination of a Jacobian. Because estimating derivatives from experimental measurements is noise-sensitive and computationally expensive, derivative-free strategies were subsequently introduced.

Alexandre Spits · Ghislain Raze · Gaëtan Kerschen
Department of Aerospace & Mechanical Engineering, University of Liège, Liège, Belgium
e-mail: alexandre.spits@uliege.be; g.raze@uliege.be; g.kerschen@uliege.be

Marisa Saggio · Viktor Jirsa
Aix Marseille Univ, INSERM, INS, Inst Neurosci Syst, Marseille, France
e-mail: maria-luisa.SAGGIO@univ-amu.fr; viktor.jirsa@univ-amu.fr

© The Author(s), under exclusive license to River Publishers 2026

Kristin B. Zimmerman, PhD (eds.), *Nonlinear Structures & Systems, Vol. 1*, Conference Proceedings of the Society for Experimental Mechanics Series, https://doi.org/10.13052/rp-9788743814122

This evolution gave rise to two main approaches: simplified control-based continuation (SCBC) [12] and phase-locked loop (PLL) testing [13]. Both methods rely on parametrizing the system to unfold the nonlinear response curve and identify it by monotonically increasing the unfolding parameter. SCBC controls the fundamental harmonic of the response, whereas PLL adjusts the phase lag between the response and the excitation. When this parametrization fails to unfold the nonlinear response curve, these methods miss parts of the bifurcation diagram [9]. In contrast, state-of-the-art numerical continuation methods can traverse folds and recover the complete diagram. To bridge this gap, a new method, arclength control-based continuation (ACBC) [9, 14], was recently introduced. This approach adapts Crisfield's arclength principle [15] to SCBC, enabling navigation around fold bifurcations and uncovering the complete bifurcation diagram.

Experimental continuation techniques have been widely employed for forced nonlinear systems. SCBC has been used for frictional oscillators [16], geometrically nonlinear beams [17, 18], micro-electromechanical systems [19], and atomic force microscopy [20]. PLL testing has likewise been demonstrated on a variety of structures, including beams with geometric nonlinearities [21], beams with friction [22], and magnetic repulsion systems [23]. More recently, ACBC has been employed to experimentally explore electronic Duffing oscillators, clamped beams, and thin plates with geometric nonlinearities [9, 14]. More applications of these methods can be found in [9].

Unlike forced (non-autonomous) systems, autonomous systems have only rarely been explored with experimental continuation. In such systems, several behaviors may coexist, including stable or unstable equilibria and limit cycles, the latter being self-sustained oscillations that arise without external forcing. Whereas non-autonomous systems typically display synchronization between excitation and response frequencies, autonomous systems lack an external reference, and the frequency of a limit cycle emerges solely from the internal dynamics, which are generally unknown to the experimenter. This lack of a frequency reference introduces a phase indeterminacy, so a phase constraint must be imposed to uniquely define and track the limit cycle.

The first applications of control-based methods to obtain bifurcation diagrams for autonomous systems were demonstrated in aeroelastic systems [24, 25], cylindrical pipe flow simulations [26], synthetic biology [27], neuronal dynamics [28], and relaxation oscillations [29], using adapted versions of CBC. Distinct approaches are adopted depending on the type of bifurcation diagram to be identified: some target fixed point solutions, while others focus on limit cycles. In the former, the reference value is held constant until the controller converges, after which it is varied step by step. In the case of limit cycles, prediction and correction steps are carried out offline for each value of the bifurcation parameter. To enforce the phase constraint, these studies employed angle encoding [29]. Arclength control-based continuation has been applied to weakly nonlinear problems [30], where a PLL block is combined with ACBC to estimate the unknown phase.

The objective of this work is to investigate how arclength control-based continuation can be adapted to analyze autonomous systems with fast–slow dynamics. In this work, we place ourselves in the context of neuroscience, where such dynamics are particularly relevant. Neurons and neuronal populations naturally produce bursting, where episodes of fast oscillations alternate with quiescent phases. In epilepsy, such bursting reflects the alternation between interictal and ictal states, as observed in electroencephalography (EEG). Phenomenological models of seizure activity, such as those developed in [31, 32], describe these transitions using bifurcation theory and classify seizures according to the onset–offset bifurcations that generate them.

This work is structured as follows: we first introduce the fast–slow framework and the epileptic bursting model, then present the ACBC implementations for fixed-points and limit cycles, and finally demonstrate the method and discuss the resulting bifurcation diagrams.

Fast-slow Systems

Fast–slow systems are dynamical systems where different sets of variables evolve on widely separated timescales. They are often written in the general form

$$\frac{d\mathbf{x}}{dt} = f(\mathbf{x},\mathbf{z}), \qquad \frac{d\mathbf{z}}{dt} = c\,g(\mathbf{x},\mathbf{z}), \tag{1}$$

with $\mathbf{x} \in \mathbb{R}^m$ representing the fast variables, $\mathbf{z} \in \mathbb{R}^n$ the slow variables, and $0 < c \ll 1$ a small parameter controlling the timescale separation. Such systems can display complex dynamical features and are encountered in diverse areas.

To particularize the framework of fast–slow systems, we adopt the phenomenological model of epileptic bursting described in [31, 32]. This model is based on the unfolding of the degenerate Takens–Bogdanov singularity [33, 34] and represents seizure dynamics with two fast variables $\mathbf{x} = (x,y)$ and one slow variable $\mathbf{z} = z$. The fast subsystem is governed by

$$\begin{cases} \dot{x} = -y, \\ \dot{y} = x^3 - \mu_2(z)\,x - \mu_1(z) - y\big(\nu(z) + x + x^2\big), \end{cases} \tag{2}$$

where the linear and nonlinear terms shape the equilibria and oscillatory states of the fast subsystem. The coefficients $\mu_1(z)$, $\mu_2(z)$, and $\nu(z)$ vary with the slow variable z and shape how the bifurcations of the fast subsystem are organized.

Since z evolves on a much slower timescale than the fast variables, it can be regarded as fixed when analyzing the fast subsystem. In this fast-slow framework, the bifurcation diagram shows how the equilibria and limit cycles of the fast subsystem evolve with z. An example of such a bifurcation diagram is shown in Figure 1(a). The stable equilibria correspond to non-oscillatory states: the upper branch represents the interictal state, while the lower branch represents the active rest state considered ictal. The stable limit cycles, on the other hand, correspond to oscillatory ictal activity.

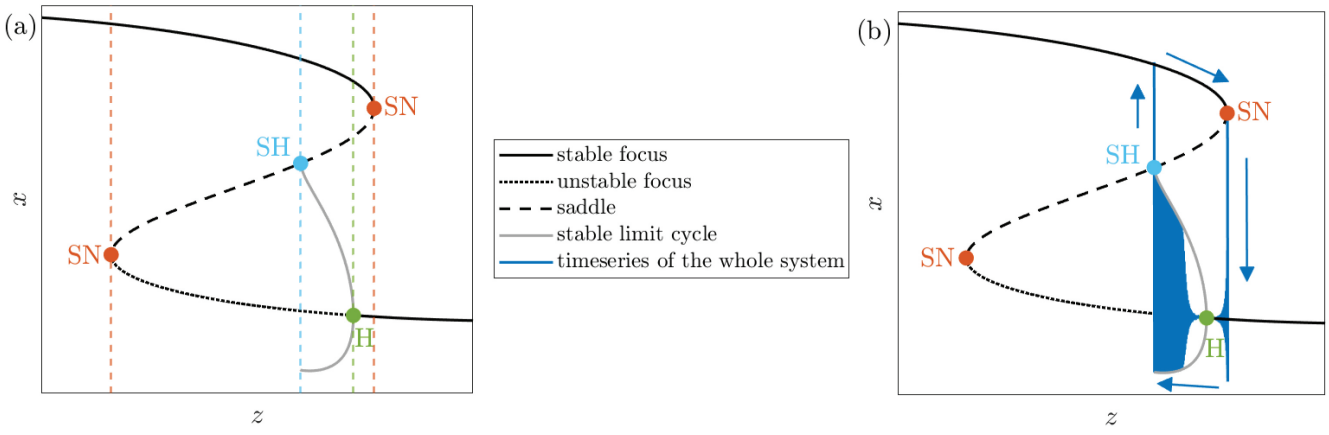

Fig. 1 Bifurcation diagram of the fast subsystem illustrating the mechanisms of seizure onset and offset. (a) Bifurcation diagram along the bursting path c10s [31], where Saddle-Node (SN), Hopf (H), and Saddle-Homoclinic (SH) bifurcations appear. (b) Example trajectory of the full system (blue) superimposed on the bifurcation diagram, showing the alternation between quiescent and oscillatory phases (interictal and ictal states) as the slow variable z drives the system through SN, H, and SH bifurcations

In the full model, the evolution of the slow variable z is given by

$$\dot{z} = -c\left(\sqrt{(x-x_s(z))^2+y^2}-d^*\right). \tag{3}$$

The dynamics of z are governed by the distance between the current state of the fast subsystem (x,y) and the silent state $(x_s(z),0)$. When the state lies within the threshold distance d^*, z changes only slowly, while during seizure-like oscillations the larger deviations of x gradually increase or decrease z. In this way, z captures a slow modulation of excitability and acts as a moving control parameter that continuously reshapes the dynamics of the fast subsystem.

As z drifts, it produces a hysteresis loop between rest and seizure, illustrated in Figure 1(b). Starting from a stable equilibrium (rest), z increases until a saddle–node bifurcation is crossed, after which the trajectory moves toward another attractor and z begins to decrease. A subsequent Hopf bifurcation gives rise to oscillations that mark seizure onset. These oscillations persist as z continues to evolve, until a saddle–homoclinic bifurcation is reached, where the limit cycle disappears and the system returns to rest, modelling seizure offset. This sequence generates bursting, alternating between quiescent and oscillatory activity.

This three-dimensional model is minimal yet sufficiently rich to capture essential features of epileptic bursting. In what follows, we apply control-based continuation methods, and in particular arclength control-based continuation (ACBC), to reconstruct the bifurcation diagram of the fast subsystem. The model is assumed unknown to the continuation procedure, which serves as a numerical validation and motivates further experimental applications.

Arclength control-based continuation for fast-slow systems

ACBC combines a feedback-controlled experiment with arclength continuation, a path-following technique. Each component serves a specific purpose, as detailed below. In autonomous systems, both equilibria and limit cycles can appear in the parameter space. An equilibrium is a time-invariant response where the system remains constant, while a limit cycle is a

time-periodic response corresponding to a self-sustained oscillation. Because of this intrinsic difference, the implementation of the method differs for the two cases, although the underlying principle remains the same.

Feedback control is required to stabilize unstable responses. In open-loop, sweeping the bifurcation parameter only reveals stable responses: near an unstable equilibrium or limit cycle, even small disturbances cause divergence and the response cannot be observed. At folds, the system undergoes sudden transitions between stable attractors, so that only a subset of stable branches is recovered. Upward and downward sweeps may reveal different stable solutions, yet others remain inaccessible.

Fixed-points identification

For fixed-point identification, the ACBC block diagram is shown in Figure 2.

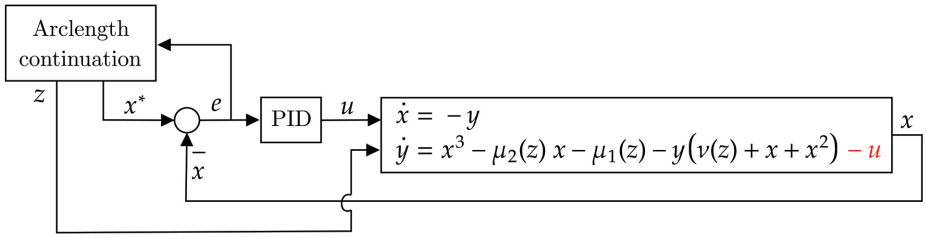

Fig. 2 ACBC block diagram for fixed-point identification in the autonomous system with fast-slow dynamics [31]. The control input u is applied to the fast dynamics

The system output $x(t)$ is compared with a reference $x^*(t)$, and the resulting error $e(t) = x^*(t) - x(t)$ drives the controller to adjust the system input $u(t)$. The controller's goal is to ensure that the response $x(t)$ converges toward the reference $x^*(t)$. With Proportional-Integral-Derivative (PID) control, the control action $u(t)$ is

$$u(t) = k_p\, e(t) + k_d \frac{d}{dt} e(t) + k_i \int_0^t e(t)\, dt, \tag{4}$$

where k_p, k_d, and k_i are the proportional, derivative, and integral gains. Both proportional and derivative control are required to stabilize the solutions, as each gain removes different bifurcations. Their combined effect unfolds the bifurcation diagram and enables access to unstable fixed points. A further analysis of how the control gains act on the system parameters $\mu_1(z)$, $\mu_2(z)$, and $\nu(z)$ can be found in the Appendix A, where local stability is examined through linearization of the controlled system with a Proportional-Derivative (PD) controller.

The control action is introduced into one of the equations governing the fast states, assuming it is experimentally feasible.

Stabilizing a response is distinct from ensuring its relevance. If the reference does not correspond to an open-loop response for a given bifurcation parameter, the closed-loop system cannot converge to the imposed reference, and the control action does not vanish. In this case, the resulting orbit does not correspond to any open-loop solution of the autonomous system, and the control is said to be invasive. Figure 3(a) shows with a colormap the regions of invasiveness in parameter space for different combinations of the reference value x^* and the bifurcation parameter z.

The continuation algorithm aims to determine the pairs (z, x^*) for which the control action vanishes, ensuring non-invasive responses. ACBC achieves this through a derivative-free adaptation of Crisfield's arclength continuation, where an integral control is introduced to perform continuation without derivatives. This integral control acts upfront of the PD controller previously described. In the (z, x^*) plane, the open-loop response is one-dimensional, as shown by the black curve in Figure 3(a). Starting from a known point (z_n, x_n^*) (white point), an ellipse (grey curve) is constructed and parametrized by an angle α:

$$(z(\alpha), x^*(\alpha)) = (z_n + \Delta z \cos\alpha,\ x_n^* + \Delta x^* \sin\alpha), \tag{5}$$

with Δz and Δx^* defining the semi-axes. The ellipse intersects the open-loop curve (black) at least twice (red and blue points), which corresponds to non-invasive solutions, while invasive ones arise along the sweep. The error associated with each point on the ellipse is shown in Figure 3(b). The integral control drives the system toward a non-invasive response by adjusting the arc angle α according to

$$\dot{\alpha}(t) = k_\alpha\, e(t), \tag{6}$$

where k_α is the integral gain. Its sign determines which of the intersections the control converges to, as illustrated in Figure 3(b). Once a new solution is reached, a new ellipse is centered at this point and the procedure is repeated to continue tracing the branch.

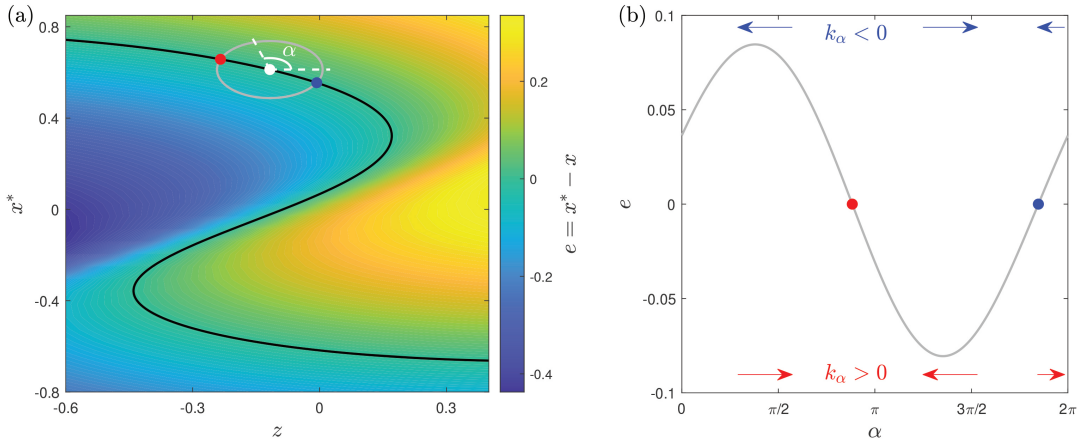

Fig. 3 (a) Colormap of the error between the imposed reference x^* and the converged response x, serving as an indicator of control invasiveness. The black curve represents the bifurcation diagram along the path c10s [31], corresponding to non-invasive control ($e = 0$). From a known point (white point), an ellipse (grey curve) is constructed to enable ACBC to identify two non-invasive solutions (red and blue points). (b) Evolution of the error $e = x^* - x$ along the ellipse parametrized by the angle α. The intersections of the ellipse with the bifurcation diagram are shown as in (a). The arrows indicate the direction of convergence of the integral control, depending on the sign of its gain k_α

The results obtained with ACBC for fixed-point identification are presented in the next section. The methodology is now extended to limit cycles.

Limit cycles identification

Limit cycles commonly originate from Hopf bifurcations and correspond to sustained oscillatory motion. They appear as closed trajectories in phase space. Figure 4(a-c) illustrates both their time evolution and their phase-plane representation in the fast–slow system previously introduced for modeling epilepsy. The frequency of a limit cycle depends on the system parameters and changes as these parameters are varied, as shown in Figure 4(e).

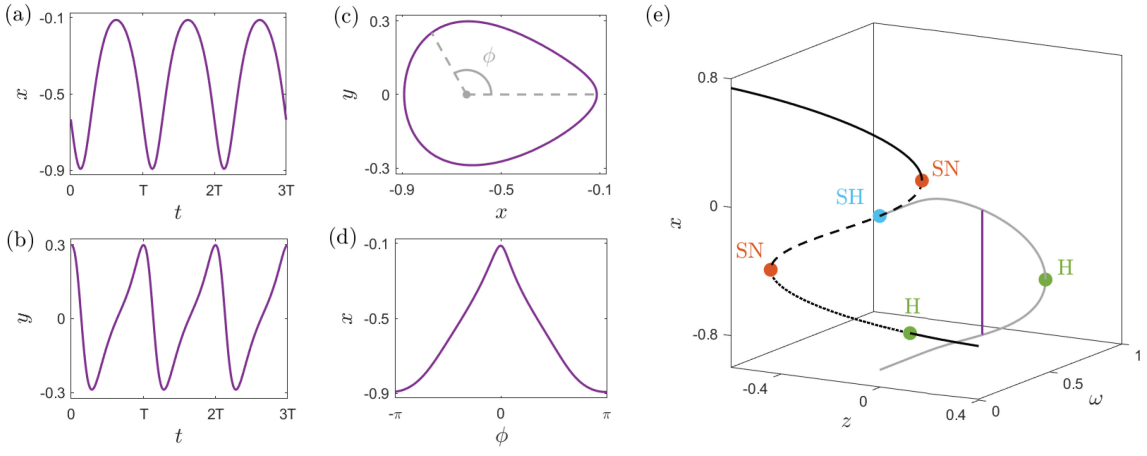

Fig. 4 (a–d) Representations of a given limit cycle: (a) time evolution of x, (b) time evolution of y, (c) phase portrait in the (x, y) plane, where the trajectory is parametrized by the angle ϕ (angle-encoding), (d) projection in the (x, ϕ) plane using this encoding. (e) Bifurcation diagram along the path c10s [31] in the space (z, ω, x). Equilibria (black) do not oscillate, while limit cycles (grey) do. The position of the limit cycle represented in (a-d) is illustrated in purple. Bifurcation points are labeled SN for Saddle-Node, H for Hopf, and SH for Saddle-Homoclinic

The absence of frequency information is a key difficulty in autonomous systems, where the frequency must be determined rather than imposed. In contrast, experimental continuation methods for non-autonomous systems, such as ACBC, prescribe the frequency as an input parameter, which typically leads to synchronization with the response. Adapting ACBC is therefore necessary in the autonomous case.

A convenient way to address this issue is to use an angle-encoding representation, where the motion along the limit cycle is described by a continuously evolving phase corresponding to a rotation along its closed trajectory. This is illustrated in Figure 4(c-d). This planar representation of the limit cycle is constructed from the measured response and another state of the system, such as $y = -\dot{x}$. The instantaneous phase ϕ is then defined as

$$\phi = \text{atan2}(y - \delta_y, x - \delta_x), \tag{7}$$

where (δ_x, δ_y) specifies the origin of the angle in the plane. For a unique angle to be assigned to every point, the chosen origin must lie inside the closed trajectory. A scaling factor may also be introduced to improve the distribution of the angle. Although another variable could be used instead of a system state, it must still provide a unique mapping between the angle and the position on the limit cycle.

This representation removes the need to impose or measure the frequency, as the phase is obtained from the system dynamics via the corresponding angle in the state space. The approach was introduced in the context of control-based continuation in [29].

Using the angle-encoding procedure, ACBC can be formulated for limit cycles. As in the case of fixed-point identification, it is structured as a combination of several blocks, as illustrated in Figure 5. Stabilization is still achieved through feedback of the response $x(t)$, which is compared with the reference $x^*(t)$ and processed by a PD controller (see Equation (4)), defining the control action applied to the autonomous system.

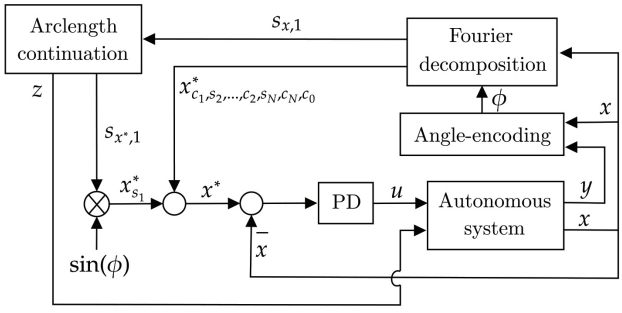

Fig. 5 ACBC Block diagram for limit cycle identification in an autonomous system with fast-slow dynamics. The control input u is applied to the fast dynamics

The difference lies in how the reference signal is constructed: oscillatory responses require additional blocks compared to the fixed-point case. The system considered in Equation (2) is nonlinear, and nonlinear systems generate harmonics in their response. All signals can therefore be decomposed into harmonic components. Using a truncated Fourier decomposition with N harmonics, any periodic signal $v(t)$ at steady state can be expressed as

$$\begin{aligned} v(t) &= \sum_{n=0}^{N} c_{v,n}\cos(n\phi) + s_{v,n}\sin(n\phi) \\ &= \sum_{n=0}^{N} v_{c_n}(t) + v_{s_n}(t) \end{aligned} \tag{8}$$

where $c_{v,n}$ and $s_{v,n}$ are the Fourier coefficients of the n-th harmonic. The goal is to construct a reference that cancels every harmonic present in the response, ensuring zero control action and thus stabilizing a non-invasive solution. To achieve this, the phase ϕ must be consistently defined between the response and the reference, a constraint enforced by angle encoding.

In practice, the Fourier decomposition is performed in real time using adaptive filters [9, 14]. These filters estimate the Fourier coefficients $c_{v,n}$ and $s_{v,n}$ by minimizing the error between the measured response and its approximation through the least mean square (LMS) algorithm. This adaptive approach avoids the need for offline procedures such as Picard iterations or B-spline fitting.

Not all Fourier coefficients are handled in the same way. Arclength continuation acts on one of the fundamental coefficients of the reference, for instance $s_{x^*,1}$, and searches in the parameter space $(z, s_{x^*,1})$ for the right couple that satisfies

the condition $s_{x^*,1} = s_{x,1}$. The remaining harmonic coefficients of the response are directly copied into the reference. This prevents additional control action from higher-order components.

The arclength continuation works in the same way as previously, except that the working plane has changed. This is illustrated in Figure 6(a). As previoulsy, an integral controller is used to drive the search along the ellipse, defined by the law,

$$\dot{\alpha} = k_\alpha (s_{x^*,1} - s_{x,1}). \tag{9}$$

Along the search, non-invasive solutions are encountered, but this controller allows to identify intersections with the uncontrolled limit cycle branch (see Figure 6(b)). The results obtained with ACBC for limit cycle identification are presented in the next section.

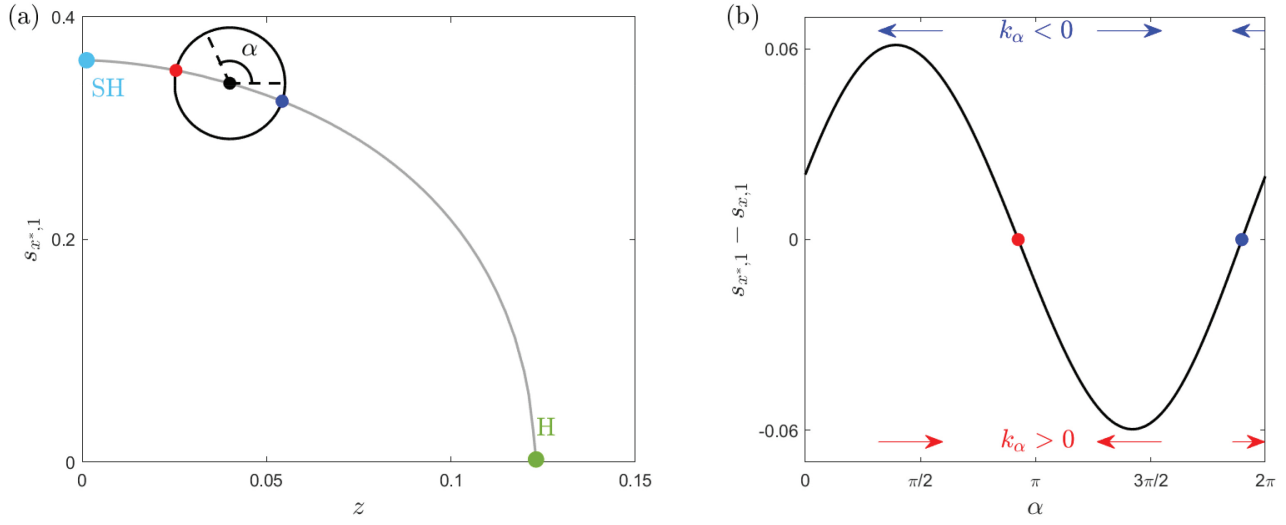

Fig. 6 (a) Working plane of the ACBC used for limit cycle identification. The grey curve represents the non-invasive solutions. From a known point (black point), an ellipse (black curve) is constructed to enable ACBC to identify two non-invasive solutions (red and blue points). (b) Evolution of the error between the sine Fourier coefficient of the first harmonic for the reference $s_{x^*,1}$ and the response $s_{x,1}$ along the ellipse parametrized by the angle α. The points where non-invasive control is achieved are shown as in (a). The arrows indicate the direction of convergence of the integral control, depending on the sign of its gain k_α

Results

Bifurcation diagrams of autonomous systems associated with bursting dynamics comprise both fixed points and limit cycles, including stable and unstable branches. To capture the complete set of solutions, two different implementations of ACBC were employed. Figure 7 illustrates two such diagrams for the bursting paths c10s and c16s [31], providing a comparison between ACBC and MatCont [4]. ACBC was also used to uncover further bifurcation diagrams corresponding to additional bursting paths from [31], which are presented in the Appendix B.

An excellent agreement is obtained between the numerical responses. ACBC successfully tracks both stable and unstable branches and smoothly continues through folds in fixed-point as well as limit-cycle solutions. In Figure 7(b), an unstable limit cycle branch emerges after the fold bifurcation and terminates at the Hopf bifurcation. Accurate tuning of the control gains is required to capture the entire branch. Stabilization near the Hopf bifurcation is particularly challenging, since the control tends to converge toward the stable fixed point branch. According to [29], the choice of the origin affects the performance of the controller. Here the objective is not to discuss performance but to demonstrate that combining distinct blocks can realize ACBC for limit cycles. For limit cycle identification with ACBC, it was essential to keep the center of the angle-encoding within the closed trajectory in the phase plane. Future work could explore adaptive adjustment of the center based on the previously identified limit cycle.

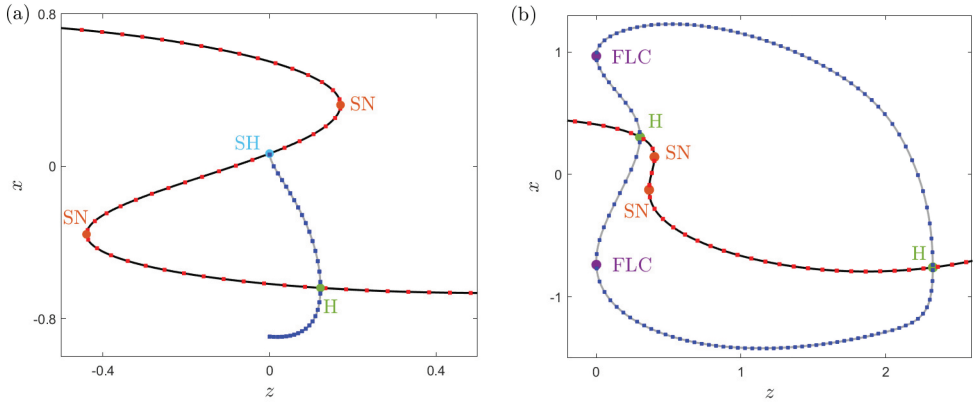

Fig. 7 Bifurcation diagrams along the bursting trajectories: (a) c10s and (b) c16b. Limit cycles from MatCont [4] (grey lines) and ACBC (blue dots) are displayed together with fixed points from MatCont (black lines) and ACBC (red dots). Stability is not indicated. Bifurcation points are marked as SN for Saddle-Node, H for Hopf, and FLC for Fold Limit Cycle

Conclusion

This work extends arclength control-based continuation (ACBC) to autonomous systems with fast–slow dynamics. By combining angle encoding with adaptive filters, the method captures both equilibria and limit cycles, including unstable branches. Numerical results on bursting paths c10s and c16s of the generalized Epileptor model confirm the ability of ACBC to reconstruct complete bifurcation diagrams. Because the approach is model-free, it can be directly applied in experiments, offering a powerful tool to probe complex dynamics such as those underlying epilepsy.

Acknowledgments Alexandre Spits and Ghislain Raze are a research fellow and a postdoctoral researcher, respectively, of the Fonds de la Recherche Scientifique - FNRS, which is gratefully acknowledged. Marisa Saggio has received funding from the European Union's Horizon Europe Programme under the Specific Grant Agreement No. 101147319 (EBRAINS 2.0 Project).

Appendix A

To better understand how control gains affect the dynamics of the system, particularly their influence on the effective unfolding parameters $\mu_1(z)$, $\mu_2(z)$, and $\nu(z)$ of the uncontrolled system, it is useful to analyze the local stability around equilibrium points (x_P, y_P). Stabilization of any response near equilibrium can be approached by linearizing the controlled system. For nonlinear systems, the local stability of a hyperbolic equilibrium is entirely determined by the linearized dynamics in its vicinity. Here, we consider the case of a proportional plus derivative (PD) controller applied to the system, resulting in the following closed-loop equations:

$$\begin{cases} \dot{x} = -y, \\ \dot{y} = x^3 - \mu_2(z)x - \mu_1(z) - y(\nu(z) + x + x^2) - k_p(x^* - x) + k_d(y^* - y). \end{cases} \tag{10}$$

To linearize the system around a given fixed point (x_P, y_P), a perturbation $(\delta x, \delta y)$ of the equilibrium can be considered, i.e.,

$$x = x_P + \delta x, \text{ and } y = y_P + \delta y. \tag{11}$$

Note that $y_P = 0$ since $\dot{x} = -y$ and we are considering fixed points ($\dot{x} = \dot{y} = 0$).

Introducing the perturbation from Eq. (11) into the closed-loop equations Eq. 10, we have:

$$\begin{cases} \dfrac{d}{dt}(x_P + \delta x) = -\delta y, \\ \dfrac{d}{dt}(\delta y) = x_P^3 + 3x_P^2\,\delta x + 3x_P\,\delta x^2 + \delta x^3 - \mu_2(z)\,x_P - \mu_2(z)\,\delta x - \mu_1(z) \\ -\delta y\,\nu(z) - \delta y\,x_P - \delta y\,\delta x - \delta y\,x_P^2 - 2\,\delta y\,\delta x\,x_P - \delta y\,\delta x^2 - k_p\,x^* + k_p\,x_P \\ +k_p\,\delta x + k_d\,y^* - k_d\,\delta y. \end{cases} \tag{12}$$

Considering only first-order terms in δx and δy and removing constant terms with respect to the perturbations, we obtain:

$$\begin{cases} \delta\dot{x} = -\delta y, \\ \delta\dot{y} = 3x_P^2\,\delta x - \mu_2(z)\,\delta x - \delta y\,\nu(z) - \delta y x_P - \delta y x_P^2 + k_p\,\delta x - k_d\,\delta y. \end{cases} \tag{13}$$

Only terms proportional to δx, δy, and their time derivatives remain. Rewriting the nonlinear dynamics in general form:

$$\begin{cases} \dot{x} &= f(x,y), \\ \dot{y} &= g(x,y). \end{cases} \tag{14}$$

the Jacobian matrix is defined by linearizing the system into its state-space form:

$$\delta\dot{\mathbf{v}} = \mathbf{J}\,\delta\mathbf{v}, \tag{15}$$

or:

$$\begin{bmatrix} \delta\dot{x} \\ \delta\dot{y} \end{bmatrix} = \begin{bmatrix} \dfrac{\partial f}{\partial x} & \dfrac{\partial f}{\partial y} \\ \dfrac{\partial g}{\partial x} & \dfrac{\partial g}{\partial y} \end{bmatrix}_{(x_P,y_P)} \begin{bmatrix} \delta x \\ \delta y \end{bmatrix} \tag{16}$$

Using Eq. 13 to identify the Jacobian terms, the Jacobian matrix writes:

$$\mathbf{J} = \begin{bmatrix} 0 & -1 \\ 3x_P^2 - \mu_2(z) + k_p & -(\nu(z) + x_P + x_P^2 + k_d) \end{bmatrix} \tag{17}$$

The trivial solution of this linear system is asymptotically stable if and only if all the roots of the characteristic polynomial $\det(\mathbf{J} - \lambda\mathbf{I}) = 0$ have negative real parts. For a second-order system, this is equivalent to requiring that all the coefficients a_i in the polynomial $a_2\lambda^2 + a_1\lambda + a_0 = 0$ are strictly positive. In our case, the characteristic equation becomes:

$$\lambda^2 + (\nu(z) + x_P + x_P^2 + k_d)\lambda + 3x_P^2 - \mu_2(z) + k_p = 0. \tag{18}$$

Hence, the stability conditions are:

$$\nu(z) + x_P + x_P^2 + k_d > 0 \quad \text{and} \quad 3x_P^2 - \mu_2(z) + k_p > 0, \tag{19}$$

which can be rewritten as:

$$k_d > -(\nu(z) + x_P + x_P^2) \quad \text{and} \quad k_p > -3x_P^2 + \mu_2(z). \tag{20}$$

These conditions are directly influenced by the value of the bifurcation parameter z. While the physical meaning of the individual coefficients may not be immediately clear, they offer important guidance on how the choice of control gains affects the stability boundaries of the system across different dynamical regimes. Note that the linearized stability condition applies only locally.

With suitable values of the control gains k_p and k_d satisfying the stability conditions obtained through linearization, the controller alters the bifurcation diagram so that unstable branches and bifurcations are no longer present.

Appendix B

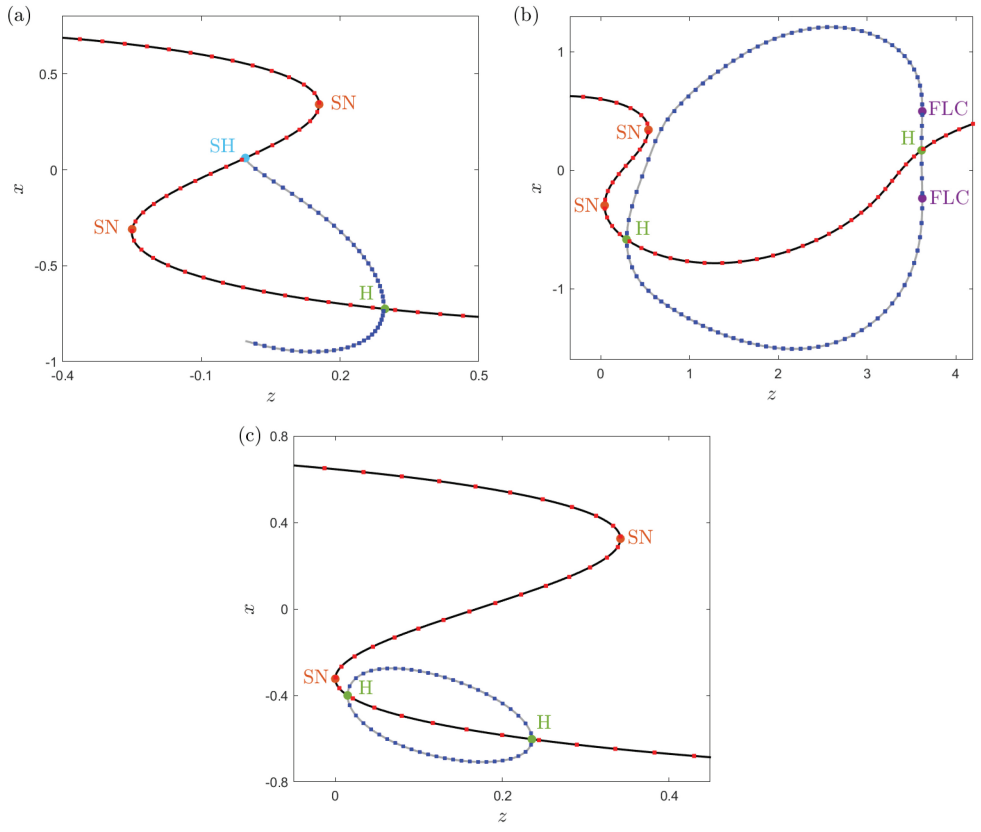

Fig. 8 Bifurcation diagrams along the bursting trajectories: (a) c2s, (b) c3s, and (c) c11s. Limit cycles from MatCont [4] (grey lines) and ACBC (blue dots) are displayed together with fixed points from MatCont (black lines) and ACBC (red dots). Stability is not indicated. Bifurcation points are marked as SN for Saddle-Node, H for Hopf, and FLC for Fold Limit Cycle

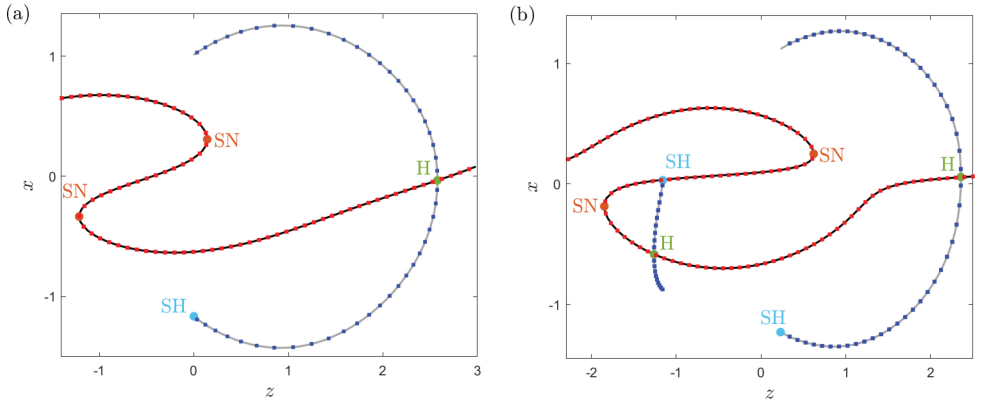

Fig. 9 Bifurcation diagrams along the bursting trajectories: (a) c2b and (b) c14b. Limit cycles from MatCont [4] (grey lines) and ACBC (blue dots) are displayed together with fixed points from MatCont (black lines) and ACBC (red dots). Stability is not indicated. Bifurcation points are marked as SN for Saddle-Node, H for Hopf, and FLC for Fold Limit Cycle

References

1. Keller, H.B. "Numerical solution of bifurcation and nonlinear eigenvalue problems". In Rabinowitz, P.H., editor, *Applications of Bifurcation Theory*, pages 359–384. Academic Press, New York (1977)
2. Allgower, E.L. and Georg, K. *Introduction to Numerical Continuation Methods*. SIAM, Philadelphia (2003)
3. Seydel, R. *Practical Bifurcation and Stability Analysis: From Equilibrium to Chaos*, volume 5 of *Interdisciplinary Applied Mathematics*. Springer-Verlag, Berlin, Heidelberg, New York, London, Paris, Tokyo, Hong Kong, 2 edition (1994)
4. Govaerts, W.J. *Numerical Methods for Bifurcations of Dynamical Equilibria*, volume 4 of *Monographs on Mathematical Modeling and Computation*. SIAM, Philadelphia (2000)
5. Knowles, J.A.C., Krauskopf, B., and Lowenberg, M.H. "Numerical continuation applied to landing gear mechanism analysis". *Journal of Aircraft*, 48(4):1254–1262 (2011)
6. Detroux, T., Renson, L., Masset, L., and Kerschen, G. "The harmonic balance method for bifurcation analysis of large-scale nonlinear mechanical systems". *Comput. Methods Appl. Mech. Eng.*, 296:18–38 (2015)
7. Dankowicz, H. and Schilder, F. "An extended continuation problem for bifurcation analysis in the presence of constraints". *Journal of Computational and Nonlinear Dynamics*, 6(3):031003 (2010)
8. Fréour, V., Guillot, L., Masuda, H., Usa, S., Tominaga, E., Tohgi, Y., Vergez, C., and Cochelin, B. "Numerical continuation of a physical model of brass instruments: Application to trumpet comparisons". *J. Acoust. Soc. Am.*, 148(2):748–758 (2020)
9. Raze, G., Abeloos, G., and Kerschen, G. "Experimental continuation in nonlinear dynamics: Recent advances and future challenges". *Nonlinear Dyn.*, 113(6):4949–4997 (2025)
10. Sieber, J., Gonzalez-Buelga, A., Neild, S.A., Wagg, D.J., and Krauskopf, B. "Experimental continuation of periodic orbits through a fold". *Phys. Rev. Lett.*, 100(24):244101 (2008)
11. Sieber, J. and Krauskopf, B. "Control based bifurcation analysis for experiments". *Nonlinear Dynamics*, 51(3):365–377 (2008)
12. Barton, D.A.W. and Sieber, J. "Systematic experimental exploration of bifurcations with noninvasive control". *Phys. Rev. E*, 87(5):052916 (2013)
13. Peter, S. and Leine, R.I. "Excitation power quantities in phase resonance testing of nonlinear systems with phase-locked-loop excitation". *Mech. Syst. Signal Process.*, 96:139–158 (2017)
14. Abeloos, G. *Control-based methods for the identification of nonlinear structures*. PhD thesis, University of Liège (2022)
15. Crisfield, M.A. "A fast incremental/iterative solution procedure that handles "snap-through"". *Comput. Struct.*, 13(1–3):55–62 (1981)
16. Kleyman, G., Paehr, M., and Tatzko, S. "Application of control-based-continuation for characterization of dynamic systems with stiffness and friction nonlinearities". *Mechanics Research Communications*, 106:103520 (2020)
17. Hayashi, S., Gutschmidt, S., Murray, R., et al. "Experimental bifurcation analysis of a clamped beam with designed mechanical nonlinearity". *Nonlinear Dynamics*, 112:15701–15717 (2024)
18. Abeloos, G., Renson, L., Collette, C., et al. "Stepped and swept control-based continuation using adaptive filtering". *Nonlinear Dynamics*, 104:3793–3808 (2021)
19. Hayashi, S., Cameron, C., Gutschmidt, S., et al. "Experimentally characterising the dynamical landscape of an active mems cantilever". *Research Square* (2025) Preprint, Version 1.
20. Böttcher, L., Wallner, H., Kruse, N., Just, W., Barke, I., Starke, J., and Speller, S. "Exposing hidden periodic orbits in scanning force microscopy". *Communications Physics*, 8(1):57 (2025)
21. Scheel, M., Peter, S., Leine, R., and Krack, M. "A phase resonance approach for modal testing of structures with nonlinear dissipation". *Journal of Sound and Vibration*, 435:56–73 (2018)
22. Scheel, M., Weigele, T., and Krack, M. "Challenging an experimental nonlinear modal analysis method with a new strongly friction-damped structure". *Journal of Sound and Vibration*, 485:115580 (2020)
23. Scheel, M., Kleyman, G., Tatar, A., Brake, M., Peter, S., Noël, J.P., Allen, M., and Krack, M. "Experimental assessment of polynomial nonlinear state-space and nonlinear-mode models for near-resonant vibrations". *Mechanical Systems and Signal Processing*, 143:106796 (2020)
24. Tartaruga, I., Barton, D.A.W., Rezgui, D., and Neild, S.A. "Experimental bifurcation analysis of a wing profile". In *Proceedings of the International Forum on Aeroelasticity and Structural Dynamics (IFASD)*, Savannah, Georgia, USA (2019)
25. Lee, K.H., Barton, D.A.W., and Renson, L. "Model identification of a fluttering aerofoil using control-based continuation and normal form analysis". In *Proceedings of ISMA2020 and USD2020*, pages 261–268, Leuven, Belgium (2020)
26. Willis, A.P., Duguet, Y., Omel'chenko, O.E., and Wolfrum, M. "Surfing the edge: finding nonlinear solutions using feedback control". *Journal of Fluid Mechanics*, 831:579–591 (2017)
27. de Cesare, I., Salzano, D., di Bernardo, M., Renson, L., and Marucci, L. "Control-based continuation: A new approach to prototype synthetic gene networks". *ACS Synthetic Biology*, 11(7):2300–2313 (2022)
28. Amakhin, D., Chizhov, A., Girier, G., Desroches, M., Sieber, J., and Rodrigues, S. "Observing hidden neuronal states in experiments". *arXiv preprint* (2025) arXiv:2308.15477 [q-bio.NC].
29. Blyth, M., Tsaneva-Atanasova, K., Marucci, L., and Renson, L. "Numerical methods for control-based continuation of relaxation oscillations". *Nonlinear Dynamics*, 111(78):7975–7992 (2023)
30. Gourc, E., Caron, R., Silva, F., Vergez, C., and Cochelin, B. "Theoretical analysis of a derivative free control based continuation algorithm with path following capability for autonomous systems". HAL preprint, hal-05042729 (2025)
31. Saggio, M.L., Spiegler, A., Bernard, C., and Jirsa, V.K. "Fast–slow bursters in the unfolding of a high codimension singularity and the ultra-slow transitions of classes". *The Journal of Mathematical Neuroscience*, 7(1):7 (2017)
32. Saggio, M.L. and Jirsa, V. "Bifurcations and bursting in the epileptor". *PLoS Computational Biology*, 20(3):e1011903 (2024)
33. Dumortier, F., Roussarie, R., and Sotomayor, J. "Generic 3-parameter families of vector fields on the plane, unfolding a singularity with nilpotent linear part. the cusp case of codimension 3". *Ergodic Theory and Dynamical Systems*, 7(3):375–413 (1987)
34. Dumortier, F., Roussarie, R., Sotomayor, J., and Żołądek, H. *Bifurcations of Planar Vector Fields: Nilpotent Singularities and Abelian Integrals*, volume 1480 of *Lecture Notes in Mathematics*. Springer, Berlin (1991)

Chapter 3
Amplitude Resonance Tracking Using Phase-Locked Loops

François Winand, Christophe Collette, and Gaëtan Kerschen

Abstract This work presents a hybrid control strategy for resonance tracking in nonlinear structural systems, combining classical phase-locked loop (PLL) control with an outer-loop extremum seeking control (ESC) scheme. Traditional PLL-based methods rely on enforcing phase quadrature between excitation and response—a condition that is not always satisfied for closely-spaced mode and high damping situations — leading to inaccurate backbone identification. To address this limitation, the proposed approach adaptively adjusts the PLL's reference phase in real time to directly maximize the response amplitude. The ESC-enhanced PLL is embedded in a continuation framework that incrementally increases the excitation level while tracking amplitude resonance at each step. The method is validated on a two-degree-of-freedom system and compared against reference solutions obtained via harmonic balance. Results show excellent agreement in both amplitude and phase, while highlighting the discrepancy between phase quadrature and true amplitude resonance. The approach enables accurate backbone extraction and shows strong potential for experimental implementation in nonlinear system identification and fatigue testing applications.

Keywords Nonlinear system identification · Experimental continuation · Phase-locked loop · Derivative-free optimization · Amplitude-based backbone curve

Introduction

In structural dynamics, identifying a system's behavior and assessing its nonlinearities are essential for validating models and ensuring reliable operation. While linear identification techniques are now well established, nonlinear systems require more advanced approaches due to effects such as amplitude-dependent resonance and mode coupling. Moreover, applications such as fatigue testing require the system to be maintained at resonance to accelerate damage accumulation, making adaptive resonance tracking critical for both identification and testing efficiency.

Over the past two decades, phase-locked loop (PLL) control has become a standard technique for tracking resonance under harmonic excitation. First applied in MEMS fatigue testing [1], PLLs were later extended to nonlinear structures, enabling real-time frequency adjustment by enforcing a fixed phase lag between excitation and response [2, 3]. This approach has been used to extract nonlinear modes and backbone curves. However, PLLs rely on the assumption that phase quadrature coincides with the amplitude maximum—an assumption that may fail in systems with damping, friction, or closely spaced modes. This limitation was evidenced in [4], where the identification of nonlinear modal parameters on an F-16 aircraft showed a mismatch between phase quadrature and actual amplitude peaks.

To overcome this limitation, we propose a hybrid strategy that combines PLL with an extremum seeking control (ESC) loop. Instead of locking to a fixed phase, the ESC adaptively adjusts the PLL reference to maximize amplitude directly, ensuring convergence to the true resonance peak. The method is model-free, robust to nonlinear effects, and particularly valuable when proper force appropriation cannot be guaranteed. Combined with a continuation strategy on the excitation level, it further enables automated construction of amplitude-based backbone curves. The effectiveness of the approach is demonstrated through numerical simulations.

François Winand · Christophe Collette · Gaëtan Kerschen
Department of Aerospace & Mechanical Engineering
University of Liège, Place du 20-Août 7, B-4000 Liège, Belgium
e-mail: francois.winand@uliege.be; Christophe.Collette@uliege.be; G.Kerschen@uliege.be

© The Author(s), under exclusive license to River Publishers 2026

Kristin B. Zimmerman, PhD (eds.), *Nonlinear Structures & Systems, Vol. 1*, Conference Proceedings
of the Society for Experimental Mechanics Series, https://doi.org/10.13052/rp-9788743814122

Background: Phase-locked loop testing with adaptive filters

Phase-locked loops are feedback control systems designed to enforce a prescribed phase lag Φ_{ref} between excitation and response. This principle exploits the unfolding of the nonlinear frequency response curve (NFRC) when parametrized in phase. A schematic implementation is shown in Figure 1.

The structure is excited by a sinusoidal force, where the excitation frequency $\omega(t)$ is dynamically adjusted through a proportional–integral (PI) control law:

$$\omega(t) = \omega_0 + K_p\big(\Phi_{\text{ref}} - \Phi(t)\big) + K_i \int_0^t \big(\Phi_{\text{ref}} - \Phi(\tau)\big)\, d\tau. \tag{1}$$

Here, ω_0 is typically initialized at the linear natural frequency, while the controller gains K_p and K_i determine stability and convergence properties. Tuning guidelines can be found in [5].

In this work, the instantaneous phase lag $\Phi(t)$ is estimated online using adaptive filtering [6]. The measured response $x(t)$ (and similarly the excitation $f(t)$) is reconstructed by a truncated Fourier series:

$$\hat{x}(t) = a_0(t) + \sum_{k=1}^{N_h} \Big[a_k(t)\sin(k\omega t) + b_k(t)\cos(k\omega t)\Big], \tag{2}$$

with the Fourier coefficients updated according to a least-mean-squares (LMS) adaptation law:

$$\begin{aligned} \dot{a}_k &= \mu\big(x(t) - \hat{x}(t)\big)\sin(k\omega t), \\ \dot{b}_k &= \mu\big(x(t) - \hat{x}(t)\big)\cos(k\omega t), \end{aligned} \tag{3}$$

where μ denotes the adaptation gain. The response phase Φ_x (and excitation phase Φ_f) is then extracted from the first harmonic as

$$\Phi_x = \text{atan2}(b_1, a_1), \qquad \Phi = \Phi_x - \Phi_f. \tag{4}$$

To trace the backbone curve of the system, the reference phase is commonly set to $\Phi_{\text{ref}} = \pi/2$, which corresponds to phase quadrature when measuring acceleration. Once the PLL has converged, the excitation amplitude U is progressively increased to continue the backbone.

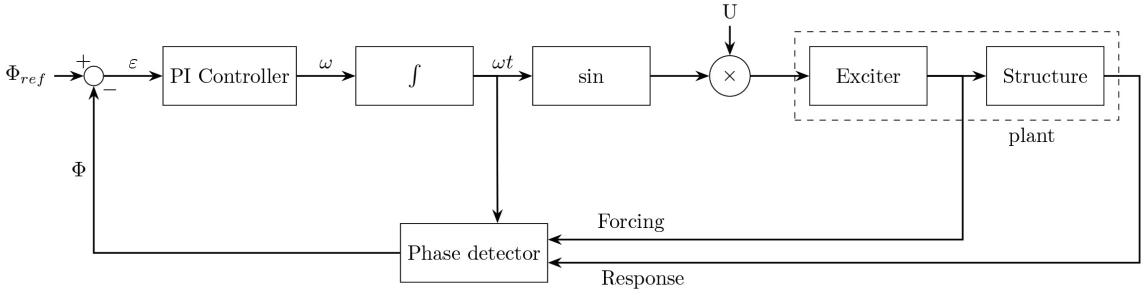

Fig. 1 Classical phase-locked loop implementation

Combining PLL with Extremum Seeking Control

Motivation for Amplitude-Based Tracking

Classical PLLs track resonance by enforcing a fixed phase lag between excitation and response, assuming that maximum amplitude occurs at phase quadrature. This assumption may fail when modes are closely spaced and the phase–amplitude relationship becomes distorted.

As an illustration, consider a two-degree-of-freedom mass–spring system with a cubic nonlinearity on the first mass:

$$\begin{aligned} \ddot{x}_1 + 0.04\,\dot{x}_1 - 0.02\,\dot{x}_2 + 2x_1 - x_2 + x_1^3 &= f\sin(\omega t), \\ \ddot{x}_2 + 0.22\,\dot{x}_2 - 0.02\,\dot{x}_1 + 2x_2 - x_1 &= 0. \end{aligned} \tag{5}$$

with linear natural frequencies at 1 and $\sqrt{3}$ rad/s. Due to modal proximity and $\sim$5% damping, the maximum amplitude no longer occurs at the nominal $-\pi/2$ phase lag.

This behavior is illustrated in Figure 2, which shows the frequency response curves of the first degree of freedom. As the excitation amplitude increases, the phase at which the maximum response occurs progressively departs from quadrature, exposing a key limitation of conventional PLL tracking. While multi-shaker force appropriation could effectively isolate the mode of interest and restore the quadrature condition allow the PLL to operate as intended, it is not always desirable in practice—for instance, industrial tests may require applying loads at fixed locations.

To address these limitations, the next section introduces an extremum seeking control (ESC) loop [7], which adaptively tunes the reference phase and drives the PLL toward the true amplitude resonance.

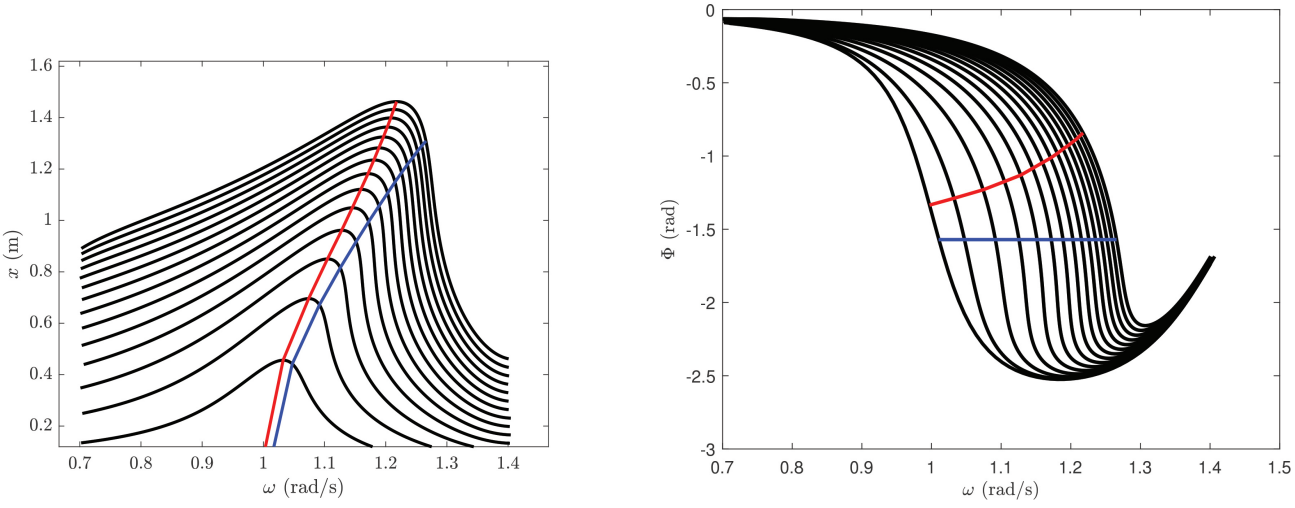

(a) Amplitude of the first harmonic

(b) Phase of the first harmonic

Fig. 2 Frequency response curves (amplitude (a) and phase (b) of first harmonic) computed via harmonic balance for excitation levels from 0.01 to 1.5 N. —— FRC, —— Amplitude resonance, —— Phase quadrature

ESC-Augmented PLL Architecture

Amplitude-based resonance tracking is achieved by augmenting the PLL with an outer-loop ESC that adaptively tunes the reference phase Φ_{ref}, as illustrated in Figure 3.

For this purpose, the reference phase is modulated by a small sinusoidal perturbation:

$$\tilde{\Phi}_{\text{ref}}(t) = \bar{\Phi}_{\text{ref}}(t) + A\sin\omega_{\text{ESA}}t, \tag{6}$$

where A and ω_{ESA} denote the perturbation amplitude and frequency respectively. The variable $\bar{\Phi}_{\text{ref}} := \Phi_{\text{ref}} + \Delta\Phi$ becomes the control parameter to be optimized. The cost function is taken as the squared response amplitude, estimated in real time using adaptive filtering.

When $\Phi_{\text{ref}} < \Phi_{\text{ref}}^{\text{opt}}$, the squared amplitude oscillates in-phase with the injected perturbation. Conversely, when $\Phi_{\text{ref}} > \Phi_{\text{ref}}^{\text{opt}}$, it becomes out-of-phase. To exploit this relationship, the squared amplitude is high-pass filtered to remove its DC component, multiplied by the perturbation (demodulated), and then low-pass filtered. The resulting signal is integrated to produce the correction $\Delta\Phi$, which updates the reference toward the optimum. The gain K controls the adaptation rate, analogous to the learning rate in gradient descent. Convergence is smooth near the optimum, with residual oscillations determined by K.

This ESC-PLL scheme is structurally similar to a classical PLL yet enables online, derivative-free optimization. However, it introduces five additional tuning parameters: the learning rate K; the perturbation frequency ω_{ESA}; the perturbation

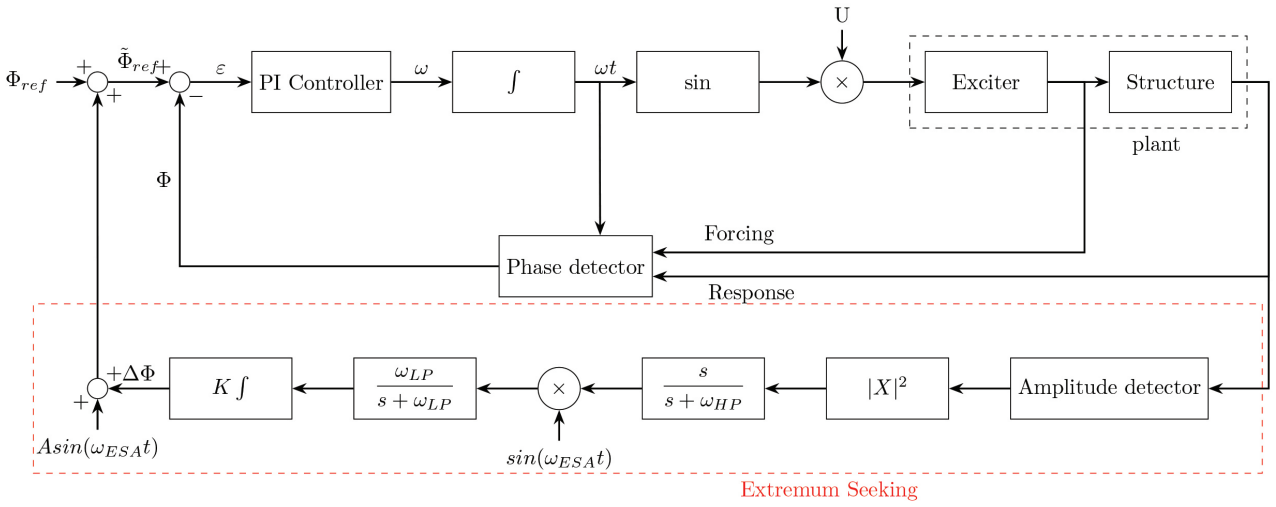

Fig. 3 ESC-augmented PLL scheme

amplitude A and the corner frequencies of the high-pass and low-pass filters, ω_{HP} and ω_{LP}, respectively. Although the tuning remains largely heuristic, some qualitative guidelines can be followed:

- ω_{ESA} should lie within the bandwidth of the PLL to preserve locking under modulation;
- ω_{HP} should be high enough to remove DC bias but low enough to retain the modulated signal;
- ω_{LP} should be low enough to suppress noise and higher harmonics;
- K is adjusted empirically, e.g. at low excitation levels where the optimal lag is well defined;
- A can be set around 0.05 rad.

In general, the ESC should evolve on a slower time scale than the PLL, and this scale separation should guide the choice of parameters.

Amplitude Backbone Identification Procedure

The proposed strategy begins by tuning a classical PLL to ensure stable frequency tracking in the linear regime. Appropriate PI gains are selected to lock the excitation frequency to the natural frequency using a fixed reference phase (typically enforcing quadrature). Once this base configuration is robust, the ESC loop is introduced and tuned at low excitation levels where the system behaves nearly linearly. This enables safe adjustment of ESC parameters (learning rate, dither frequency, and filter cutoffs) without risking instability.

After both loops are tuned, backbone identification proceeds incrementally. At each excitation level, the PLL is first allowed to lock to the current phase reference. Once convergence is achieved, the ESC loop adapts the reference phase to drive the system toward maximum amplitude. When convergence is detected—via amplitude stability or convergence of the reference phase—the ESC is paused and the optimal phase is stored.

The excitation amplitude is then incremented, and the reference phase is reinitialized using the previously optimized value. To maintain consistent optimization behavior across amplitude levels, the ESC learning rate is adjusted to account for the scaling of the cost function. Assuming linear behavior, the squared amplitude (the cost) grows quadratically with input amplitude; therefore, the learning rate is updated as

$$K \leftarrow K \left(\frac{U_{i-1}}{U_i} \right)^2 . \tag{7}$$

While this rule is exact only in the linear regime, it remains a useful heuristic in nonlinear cases. Depending on the nature of the nonlinearity, the response amplitude may grow faster or slower than quadratically, which alters the effective learning rate. As a result, the scaling is not always ideal but still provides an adjustment that limits instability and prevents overly aggressive updates.

Repeating this process over successive amplitudes yields an automated construction of the amplitude-based backbone curve, summarized in Algorithm 1.

Algorithm 1 Amplitude Backbone Identification via PLL and ESC

Initialize: $\Phi_{\text{ref}}^{(0)}$, $\omega_0^{(0)}$
Initialize (PLL): PI gains; adaptive filter gain μ and number of harmonics N_h at low amplitude U_0
Initialize (ESC): K, ω_{ESA}, ω_{HP}, ω_{LP} at U_0
for $i = 1$ to N **do**
    Set excitation amplitude U_i
    Update learning rate: $K \leftarrow K \left(\frac{U_{i-1}}{U_i}\right)^2$
    Initialize: $\Phi_{\text{ref}}^{(i)} \leftarrow \Phi_{\text{ref}}^{\text{opt},(i-1)}$, $\omega_0^{(i)} \leftarrow \omega^{\text{opt},(i-1)}$
    Run PLL until frequency convergence
    Activate ESC to adapt $\bar{\Phi}_{\text{ref}}$ until convergence
    Pause ESC
    Store $\Phi_{\text{ref}}^{\text{opt},(i)}$, $\omega^{\text{opt},(i)}$, and amplitude $|X|^{(i)}$
end for

Numerical Evaluation of the Amplitude Tracking Method

The performance of the proposed control scheme is assessed on system 5, following the continuation algorithm. Simulation parameters are listed in Table 1. Both PLL and ESC loops are first tuned at a low excitation level (0.01 N), ensuring stable frequency locking and sufficiently fast convergence of the optimization loop (Figure 4). At $t = 0$ cycles, the ESC is initialized at a reference phase of $-\pi/2$, the conventional starting point in PLL testing, and converges to the optimum value of -1.33 (corresponding to maximum amplitude) in less than 1000 oscillation cycles. To demonstrate stability, the loop is subsequently maintained at steady state for an extended period before being deactivated to collect the outputs.

The system is subsequently driven through 16 increasing excitation levels, from 0.01 N to 1.5 N. At each step, the resonance frequency is identified using the control strategy—typically within 2500 oscillation cycles, a practical limit chosen to keep simulation times reasonable. This procedure yields an amplitude-based backbone that follows the resonance peaks of the frequency response curves and deviates clearly from the quadrature backbone produced by a standard PLL (Figure 5).

All results are compared with harmonic balance reference solutions for validation. Both amplitude and phase of the first harmonic are in excellent agreement. In particular, the close match between frequency response curves measured with the PLL and those computed with HB strongly supports the applicability of the method in experimental contexts, where analytical solutions are unavailable.

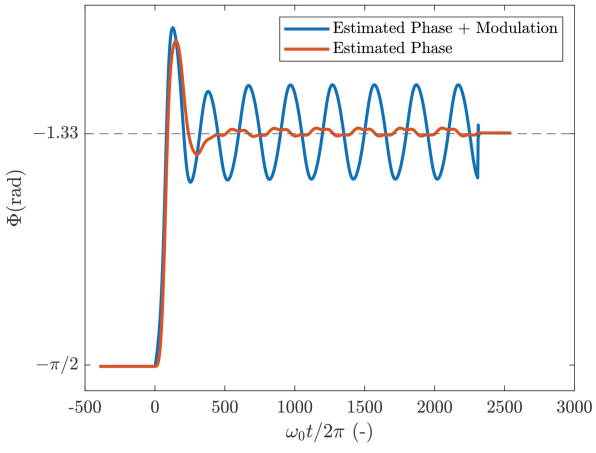

Fig. 4 Convergence of the reference phase Φ_{ref} toward the optimum at 0.01 N. Time is expressed in oscillation cycles

Parameter	Value
K_p	0.1813 s^{-1}
K_i	0.0065 s^{-2}
Adaptive filter gain μ	0.2 $(= \omega_0/5)$ s^{-1}
Harmonics N_h	10
Perturbation amplitude A	0.05 rad
Dither frequency ω_{ESA}	0.00333 $(= \mu/60)$ rad/s
Initial K	25
LPF cutoff ω_{LP}	10 rad/s
HPF cutoff ω_{HP}	0.00333 $(= \mu/120)$ rad/s

Table 1 Simulation parameters for PLL and ESC

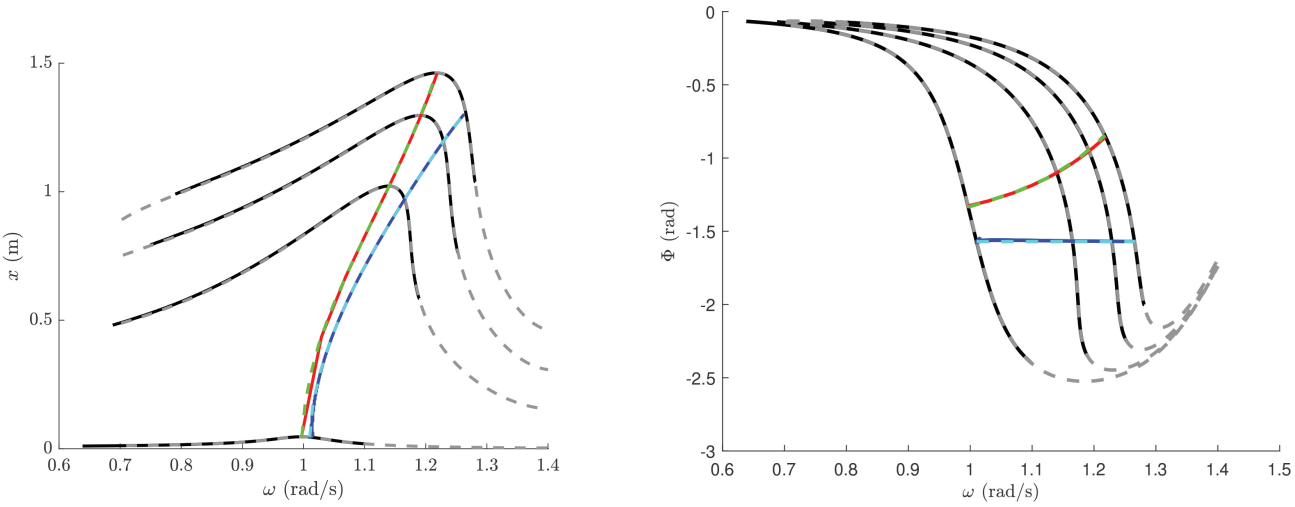

(a) Amplitude of the first harmonic

(b) Phase of the first harmonic

Fig. 5 Frequency response curves (amplitude (a) and phase (b) of first harmonic) and backbones for excitation levels from 0.01 to 1.5 N —— FRC (PLL), —— Amplitude resonance (ESC-PLL), —— Phase quadrature (PLL), - - - FRC (HB), - - - Amplitude backbone (HB), - - - Phase quadrature (HB).

Conclusion

This work presented a hybrid control strategy that enhances classical phase-locked loop resonance tracking by integrating an outer-loop extremum seeking control. The method adaptively adjusts the reference phase to locate amplitude resonance directly, avoiding reliance on the traditional quadrature assumption. A continuation scheme was further introduced to automate construction of amplitude-based backbone curves over increasing excitation levels.

The approach was validated numerically on a nonlinear two-degree-of-freedom system, showing excellent agreement with harmonic balance reference solutions. The observed divergence between amplitude and phase resonance highlights the importance of adaptive phase control. These findings support the applicability of the proposed strategy for experimental nonlinear system identification.

Future work will target improved efficiency and robustness of the ESC layer, with emphasis on faster convergence, refined continuation procedures, and systematic gain selection to facilitate experimental use.

Acknowledgments The present research is part of the Space4ReLaunch project, which is supported by the SPW Économie Emploi Recherche of the Walloon Region, under the grant agreement nr 2210181.

References

1. X. Sun, R. Horowitz, and K. Komvopoulos. Stability and Resolution Analysis of a Phase-Locked Loop Natural Frequency Tracking System for MEMS Fatigue Testing. *Journal of Dynamic Systems, Measurement, and Control*, 124(4):599–605, December 2002.
2. V. Denis, M. Jossic, C. Giraud-Audine, B. Chomette, A. Renault, and O. Thomas. Identification of nonlinear modes using phase-locked-loop experimental continuation and normal form. *Mechanical Systems and Signal Processing*, 106:430–452, June 2018.
3. S. Peter and R. Leine. Excitation power quantities in phase resonance testing of nonlinear systems with phase-locked-loop excitation. *Mechanical Systems and Signal Processing*, 96:139–158, November 2017.
4. T. Zhou, G. Raze, G. Kosova, and G. Kerschen. Experimental nonlinear modal analysis of an f-16 aircraft using phase-locked loop control. *Journal of Aircraft*, 2025.
5. P. Hippold, M. Scheel, L. Renson, and M. Krack. Robust and fast backbone tracking via phase-locked loops. *Mechanical Systems and Signal Processing*, 220:111670, November 2024.
6. S. Haykin. *Adaptive filter theory*. Always learning. Pearson, Upper Saddle River Boston Columbus San Francisco New York, fifth edition, international edition edition, 2014.
7. K. Ariyur and M. Krstić. *Real-Time Optimization by Extremum-Seeking Control*. Wiley, Hoboken, NJ, 2003.

Chapter 4
Machine Learning for Experimental Bifurcation Analysis

Grégoire Bourdouch, Pierre Geurts, and Gaëtan Kerschen

Abstract Nonlinear mechanical structures can exhibit multiple coexisting periodic solutions, including unstable responses that remain inaccessible to standard experimental testing. Conventional swept-sine measurements, rooted in linear assumptions, capture only the stable portions of the frequency response and thus overlook essential bifurcations and unstable dynamics. Beyond the fundamental resonance, nonlinear systems also resonate at integer multiples or fractions of the excitation frequency, giving rise to superharmonic and subharmonic responses, some of which may appear as isolated branches.

This work proposes a data-driven framework that leverages deep convolutional networks to complete the missing information from open-loop measurements. From open-loop experimental data alone, the method infers the full nonlinear frequency response. Experimental validation on an electronic Duffing oscillator confirms the accuracy of the predictions, while the framework can be readily extended by incorporating additional nonlinearities into the training dataset, paving the way toward a generic tool for nonlinear experimental analysis.

Keywords Nonlinear vibration testing · Secondary resonances · Isola · Machine learning · Convolutional neural networks

Introduction

Aerospace and other engineering structures may exhibit nonlinear dynamical behaviors. Geometric nonlinearities, friction, or material properties give rise to multi-stability, bifurcations, and sudden jumps between responses. Linear models and assumptions, which form the basis of conventional modal analysis, therefore fall short when applied to these systems.

Experimental data remain essential for identifying nonlinear responses, yet standard open-loop methods such as stepped-sine and swept-sine testing can only access the stable portions of the nonlinear frequency response curves (FRCs). Unstable and isolated branches, however, carry critical information about the dynamics but remain experimentally inaccessible in open-loop.

To address this limitation, several control-based approaches have been developed. Phase-locked loop (PLL) [1] testing, control-based continuation (CBC) [2], and real-time control (RTC) [3] methods use feedback control to stabilize otherwise unstable responses and thereby enable the construction of complete FRCs. While effective in principle, these methods face practical challenges such as controller instabilities, sensitivity to noise, and the need for careful gain tuning, which limit their robustness and ease of use in experimental practice.

These limitations motivate the exploration of alternative strategies. In this work, we propose a data-driven framework that uses deep learning to complete the missing information from open-loop measurements. From standard experimental data alone, the method can infer the unstable and isolated parts of the nonlinear frequency response, offering a robust and simple alternative to traditional control-based approaches.

Grégoire Bourdouch · Gaëtan Kerschen
Department of Aerospace and Mechanical Engineering,
University of Liège, 4000 Liège, Belgium
e-mail: gregbourdouch@gmail.com; G.Kerschen@uliege.be

Pierre Geurts
Department of Computer Science and Electrical Engineering, Montefiore Institute,
University of Liège, 4000 Liège, Belgium
e-mail: P.Geurts@uliege.be

© The Author(s), under exclusive license to River Publishers 2026

Kristin B. Zimmerman, PhD (eds.), *Nonlinear Structures & Systems, Vol. 1*, Conference Proceedings
of the Society for Experimental Mechanics Series, https://doi.org/10.13052/rp-9788743814122

Background and Methodology

This work employs a supervised learning framework in which the model parameters $\hat{\phi}$ are identified by minimizing a prescribed loss function, with the ultimate objective of achieving generalization, i.e., ensuring accurate predictions on previously unseen examples. A central innovation lies in reformulating FRCs as abstracted image-based representations rather than direct plots of measured amplitudes. This enables the problem to be cast as an image-to-image translation task, where experimentally accessible responses obtained from open-loop tests are mapped to the corresponding nonlinear features that remain hidden. Convolutional neural networks are particularly suited for this setting, as they efficiently exploit local spatial correlations in high-dimensional data, in contrast to fully connected networks that become computationally prohibitive. Among the available architectures, U-Net [4] has proven especially effective. It adopts a symmetric encoder–decoder structure: the encoder compresses the input into progressively more abstract features, while the decoder reconstructs spatial resolution, with skip connections preserving fine details lost during encoding. This combination allows for accurate mapping of input to output in image translation problems. A schematic representation of the deep learning framework employed in this work is shown in Fig. 1.

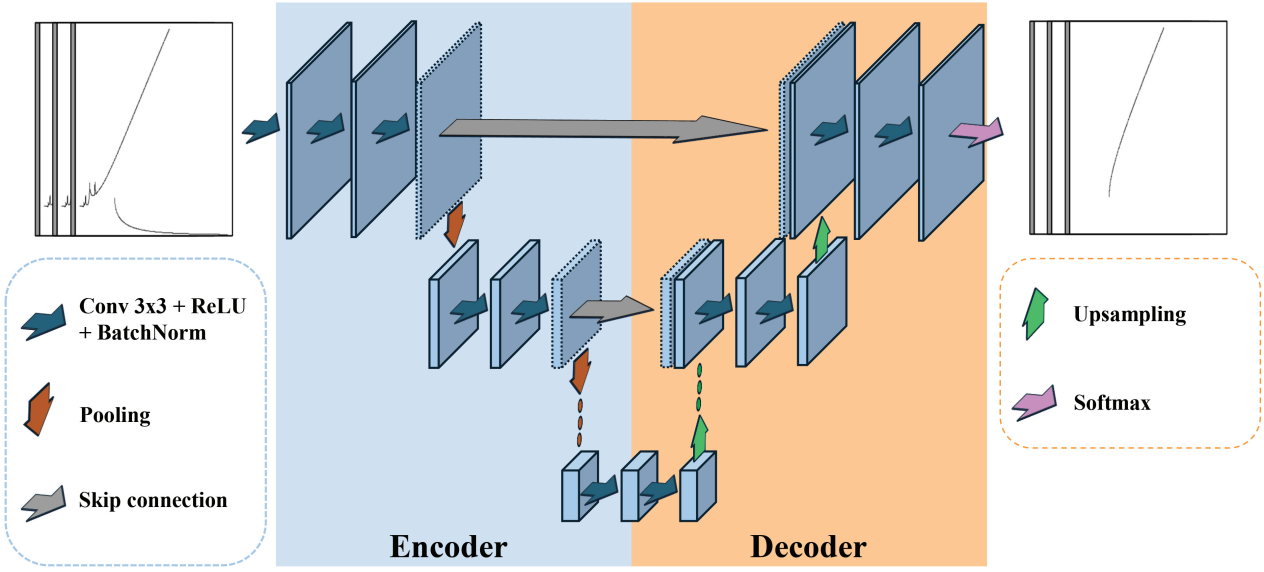

Fig. 1 Schematic of the U-Net framework for predicting the unstable branch of the fundamental resonance

The mandatory training process of a deep learning model requires a reliable dataset, yet no standard databases of FRCs exist. In this work, FRCs are generated numerically using the harmonic balance method with pseudo-arclength continuation [5], which captures both stable and unstable branches by tracking solutions through fold points. Additional disconnected solutions, such as isolated subharmonic responses, are obtained with the two-harmonic homotopy method [6]. The database is restricted to single-degree-of-freedom (SDOF) oscillators, ensuring immediate experimental applicability to SDOF setups as well as to multi-degree-of-freedom (MDOF) systems in which modal interactions remain absent. To guarantee physical relevance, the dataset incorporates canonical nonlinear oscillators: the Duffing oscillator to model cubic hardening nonlinearities in clamped–clamped beams, the Helmholtz–Duffing oscillator to introduce quadratic contributions, and piecewise linear stiffness models to represent non-smooth restoring forces such as those arising in contact problems.

Together, these numerical schemes provide a comprehensive collection of FRCs from which stable and unstable branches are extracted. The Bresenham line algorithm is then employed to discretize these curves into binary images of resolution 320×320, chosen for this study but adjustable to higher resolutions if required. Separate models are trained for the different dynamical features of interest, namely the unstable branches of the fundamental and superharmonic responses, and the isolated subharmonic responses. To support this framework, dedicated window encodings were designed [7], each relying exclusively on data obtainable from open-loop tests, thereby ensuring experimental applicability. Finally, the predictions of the individual models are combined to reconstruct the complete FRC.

Analysis

The method was experimentally validated on an analog electronic circuit replicating the Duffing oscillator behavior, which is subjected to harmonic forcing. The setup, shown in Fig. 2, was designed to exhibit minimal dissipation, pronounced nonlinearities, and relatively low resonance frequencies. This setup also offers a significant advantage, as it is not subject to shaker–structure interactions. This circuit is governed by an equation equivalent to the Duffing oscillator, written as

$$m\,\ddot{x} + c\,\dot{x} + k\,x + k_3\,x^3 \;=\; f\,\sin(\omega t) + f_0, \tag{1}$$

where the effective parameters of the equivalent oscillator are $m = 10^{-4}$ [s^2], $c = 4.9 \times 10^{-4}$ [s], $k = 1.68$ [$-$], $k_3 = 0.983$ [V^{-2}], and the forcing amplitude is $f = 2$ [V]. Here, f_0 denotes a static input voltage.

The presence of f_0 induces a static deflection, which breaks the odd symmetry of the pure Duffing nonlinearity and introduces an effective quadratic stiffness term [8]. This symmetry breaking modifies the bifurcation structure and enables even-order nonlinear phenomena, such as the 2:1 superharmonic resonance, which are absent in the symmetric Duffing case and thus not represented in the training set.

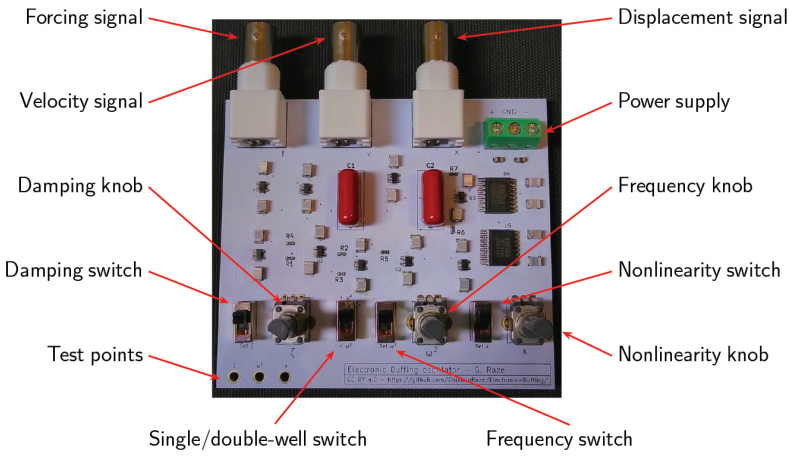

Fig. 2 Schematic of the electronic Duffing oscillator used in this study, adapted from [9]

A key advantage of the proposed method lies in its straightforward experimental implementation. Unlike control-based techniques, which often require extensive parameter tuning, the present framework relies solely on open-loop tests. In this work, swept-sine experiments were employed, a standard feature in most commercial vibration software. From these measurements, the response envelope is extracted to identify the stable branches of the frequency response, as illustrated in Fig. 3, where the swept-up and swept-down responses at an excitation amplitude of f = 2 [V] are displayed, and the stable branches are highlighted in red. The swept-up and -down sine tests capture the characteristic jump phenomena of the system, corresponding respectively to the downward and upward transitions between coexisting solutions. In addition, superharmonic resonances are observed at frequencies greater than one-third and one-half of the natural frequency, reflecting the strong nonlinear behavior of the oscillator.

Inference is performed on input images representing the stable branches, constructed from swept-sine envelopes in the same manner as for the numerically generated training samples. For validation, the predictions are compared against results obtained with the (x-)ACBC algorithm [10] on the same experimental setup. Fig. 4(a) shows the 3:1 superharmonic resonance, Fig. 4(b) the 2:1 superharmonic resonance, and Fig. 4(c) the fundamental resonance (1:1) together with the isolated 1:3 subharmonic resonance.

The results highlight the capability of the proposed framework to reconstruct nonlinear resonances with high accuracy. For the fundamental resonance, the predictions are in excellent agreement with the experimental measurements, while for the 3:1 superharmonic the correspondence is particularly strong even in the vicinity of the folds, where continuation techniques typically encounter difficulties. The 2:1 superharmonic resonance is less accurately captured, a discrepancy attributable to differences between the experimental configuration and the numerical systems employed during training. Most notably, the framework successfully predicts the complete isolated branch associated with the 1:3 subharmonic resonance. This constitutes a significant result, as subharmonic responses are notoriously difficult to capture experimentally: unlike fundamental

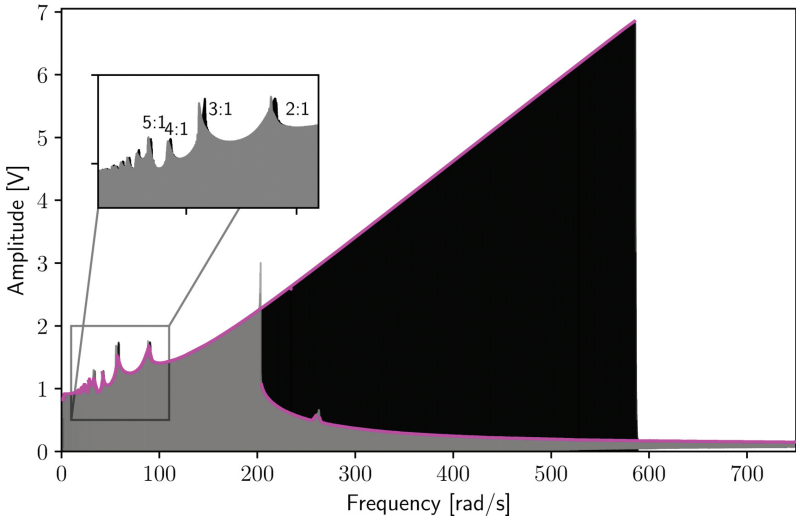

Fig. 3 Swept-up (▬), swept-down (▬) sine test responses of the electronic Duffing oscillator at $f = 2$ [V], with the stable branches highlighted (▬)

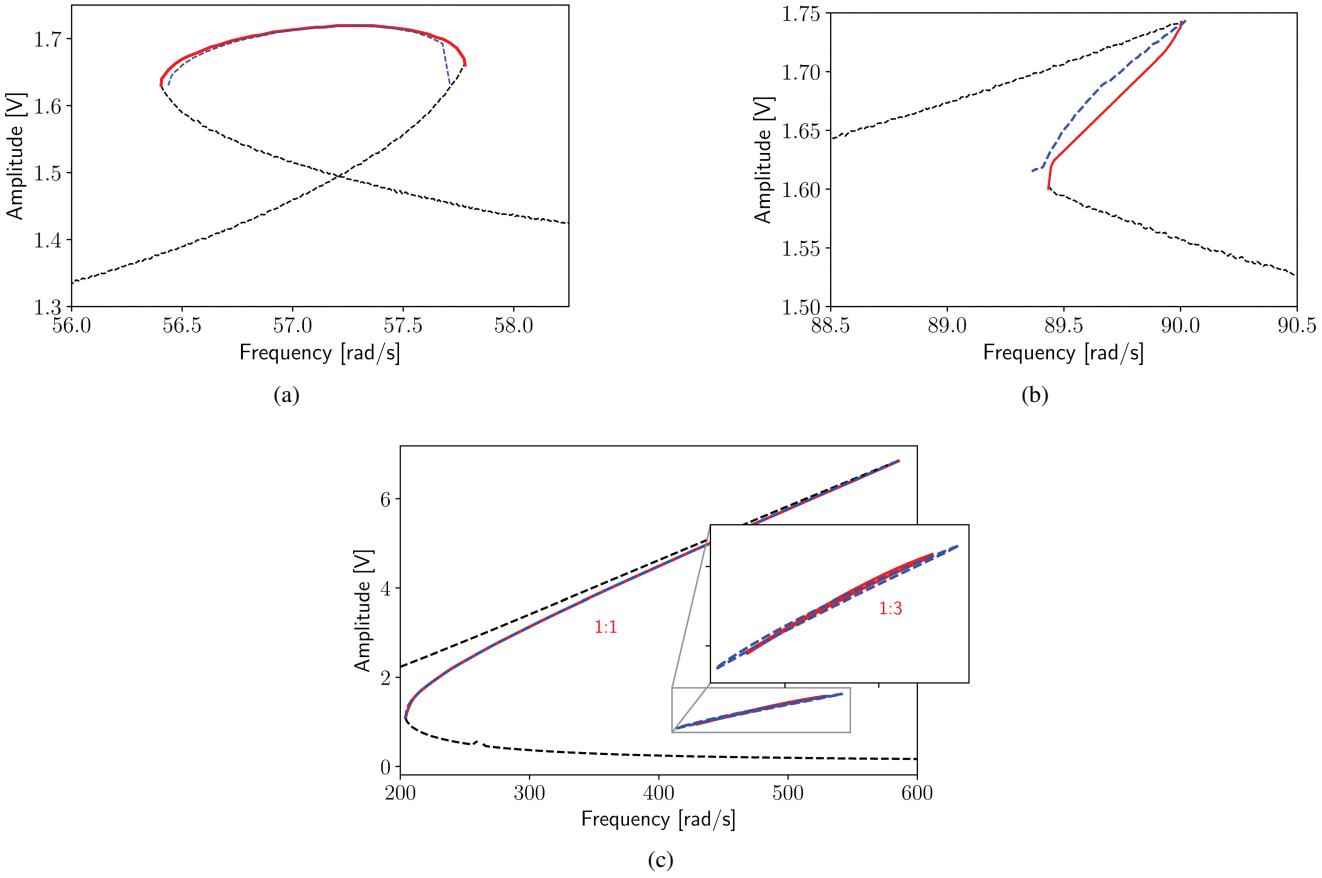

Fig. 4 FRC predictions (▬), measurements with x-ACBC (▬), and stable branches (▬ ▬) of the electronic Duffing oscillator at $f = 2$ [V]. (a) Superharmonic 3:1, (b) superharmonic 2:1, and (c) fundamental 1:1 with subharmonic 1:3

or superharmonic resonances, they do not lie on the direct continuation path of the primary frequency response and are consequently challenging to identify using continuation methods. By combining the model predictions with the experimentally measured stable branches, the complete nonlinear frequency response curve can be reconstructed, as illustrated in Fig. 5.

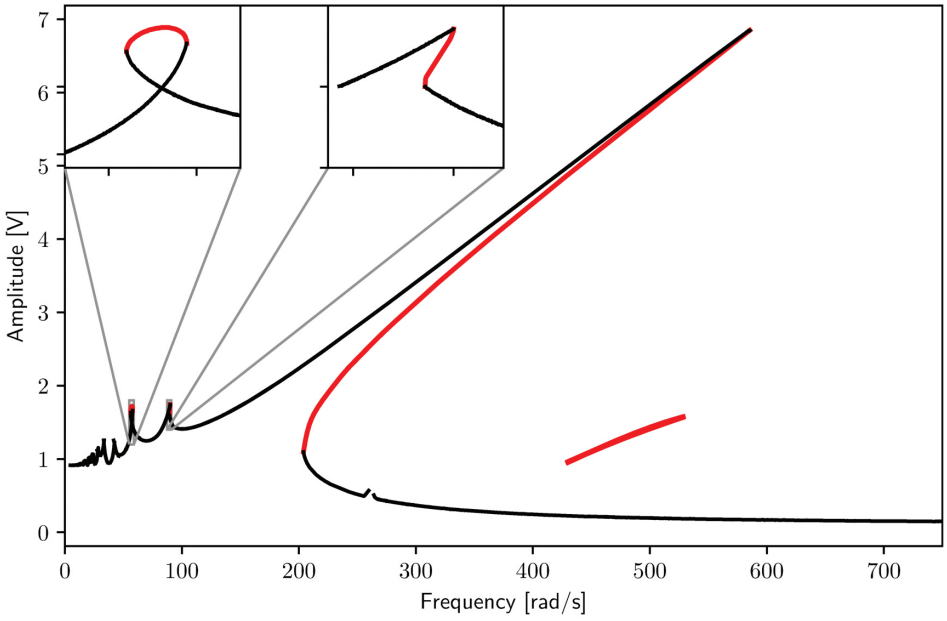

Fig. 5 Reconstructed FRC of the electronic Duffing oscillator at $f = 2$ [V]. Model predictions (—) include fundamental, subharmonic, and superharmonic components, while swept-sine envelopes are shown as black curves (—)

Conclusion

This work introduced a data-driven framework for nonlinear vibration testing that exploits open-loop measurements and deep learning to recover inaccessible responses. By reformulating frequency response curves as images, the problem was cast as an image-to-image translation task. The method was experimentally validated on an electronic Duffing oscillator, where it successfully reconstructed the complete frequency response, including unstable branches, superharmonic resonances, and the isolated 1:3 subharmonic resonance, a feature notoriously difficult to detect with continuation methods. These results demonstrate that the proposed approach bridges the gap between standard experimental modal analysis and the full characterization of nonlinear systems.

Future work will focus on extending the training database to encompass a broader range of nonlinear oscillators and MDOF systems, thereby enabling greater generalization across experimental configurations. This strategy paves the way toward a generic tool for nonlinear experimental analysis that complements control-based methods.

Acknowledgments Funded by the European Union. Views and opinions expressed are however those of the author(s) only and do not necessarily reflect those of the European Union or the European Research Council Executive Agency. This work was supported by ERC grant ENTIRE (grant agreement No. 101200365).

References

1. Peter, S. and Leine, R.I. "Excitation power quantities in phase resonance testing of nonlinear systems with phase-locked-loop excitation". *Mechanical Systems and Signal Processing*, 96:139–158 (2017).
2. Sieber, J. and Krauskopf, B. "Control based bifurcation analysis for experiments". *Nonlinear Dynamics*, 51:365–377 (2008).
3. Karaağaçlı, T. and Özgüven, H.N. "Experimental modal analysis of nonlinear systems by using response-controlled stepped-sine testing". *Mechanical Systems and Signal Processing*, 146:107023 (2021).
4. Ronneberger, O., Fischer, P., and Brox, T. "U-net: Convolutional networks for biomedical image segmentation". In *Proc. Int. Conf. Medical Image Computing and Computer-Assisted Intervention (MICCAI)*, volume 9351 of *Lecture Notes in Computer Science*, pages 234–241 (2015).
5. Detroux, T., Renson, L., Masset, L., and Kerschen, G. "The harmonic balance method for bifurcation analysis of large-scale nonlinear mechanical systems". *Computer Methods in Applied Mechanics and Engineering*, 296:18–38 (2015).
6. Raze, G. and Kerschen, G. "A two-harmonic homotopy method to experimentally uncover isolated resonances". *Mechanical Systems and Signal Processing*, 232:112670 (2025).

7. Bourdouch, G. “Machine learning for experimental bifurcation analysis”. Master’s thesis, University of Liège, Belgium (2025).
8. Kovacic, I., Brennan, M.J., and Lineton, B. “Effect of a static force on the dynamic behaviour of a harmonically excited quasi-zero stiffness system”. *Journal of Sound and Vibration*, 325(4):870–883 (2009).
9. Raze, G. “Electronic duffing oscillator”. https://github.com/GhislainRaze/Electronic-Duffing (2024). GitHub repository.
10. Spits, A., Raze, G., and Kerschen, G. “Derivative-free arclength control-based continuation for secondary resonances identification”. In *Proc. IMAC 2025*, Denmark (2025). River Publishers.

Chapter 5
Data-Driven Method for Blisk Sector Dynamics with Resonant Vibration Absorber

Michael W. Reynolds, Mihai Cimpuieru, and Bogdan I. Epureanu

Abstract Blisks are critical to the safe operation of turbomachinery. Blisks are located in the compressor or turbine stages and are exposed to extreme forces and temperatures. They are manufactured as one piece and have low damping, making them susceptible to large vibrations, which can result in high cycle fatigue. Thus, it is essential to identify and mitigate blisk vibrations. In particular, Resonant Vibration Absorbers (RVAs) are used to reduce vibrations through energy absorption. These structures can further lower vibration amplitudes by dissipating energy through friction contacts. However, while beneficial to the safe operation of blisks, insertion of RVAs changes blisk dynamics. Hence it is paramount to accurately model vibration amplitudes and resonance responses of blisks with RVAs attached. State-of-the-art includes models for blisks with RVA attached and friction contacts use the Harmonic Balance Method (HBM). While HBM can predict blisk responses, it is not designed to use experimental data for enhanced prediction accuracy, and it can be very computationally expensive for complex contact properties. Hence, to address this gap, this paper proposes to use Control-Based Continuation (CBC), a model-agnostic technique that uses a proportional-derivative controller to cancel higher-order modes and a root-finding algorithm to reach the system's resonant peak, thus tracing out the 'backbone' curve of the response. Using CBC, the response of a single blisk sector with an RVA attached is tracked experimentally, leveraging physical data for enhanced prediction accuracy. The process is repeated by isolating each blisk sector, and the coupled predictions are used to compute the full blisk response. A Lumped Mass Model (LMM) with friction contacts is used to mimic the blade level dynamics. Results show that the proposed method accurately and efficiently predicts the backbone curve of this structure. Future work involves applying this method to a large scale as-manufactured blisk sector.

Keywords Turbomachinery · Nonlinear dynamics · Vibrations · Structural dynamics

Introduction

Turbomachinery blisks are key rotary components in gas turbines. They are composed of the disk section and blade components, with all the parts manufactured as one single piece. These structures are found in the compressor and turbine stages of gas turbines, rotating at high speeds, and being exposed to large pressure waves at extreme temperatures. Hence due to their low damping and how they are manufactured, blisks experience significant stress concentrations and vibrate at large amplitudes which in time can result in failure of the system due to high cycle fatigue. This effect is exacerbated by the inherent small mistuning, described as small variations from the nominal blade properties, which break the system cyclicity and can enhance vibration amplitudes. Furthermore, due to wear formation during operation or due to significant blade damage, large mistuning can further amplify this effect and increase the risk of failure. Therefore, it is critical to mitigate blade vibrations in turbomachinery blisks to ensure the safe operation of these structures. To do so, previous research has focused on utilizing auxiliary structures that are placed in the disk portion of the blisk. These structures are designed such that at specific target vibration excitation frequencies they absorb energy from the host structure (i.e., the blisk) significantly reducing the blade vibration. These so-called Resonant Vibration Absorbers (RVAs) can further reduce blisk vibrations through energy dissipation. Therefore, some RVAs are designed to include friction or impact contact surfaces to dissipate energy and enhance vibration mitigation. Generally, RVAs are designed for specific operating conditions (e.g., frequency range, RPM, tempera-

Michael W. Reynolds · Mihai Cimpuieru · Bogdan I. Epureanu
University of Michigan, Ann Arbor, MI 48109
e-mail: mwreynol@umich.edu; mcimpi@umich.edu; epureanu@umich.edu

© The Author(s), under exclusive license to River Publishers 2026

Kristin B. Zimmerman, PhD (eds.), *Nonlinear Structures & Systems, Vol. 1*, Conference Proceedings
of the Society for Experimental Mechanics Series, https://doi.org/10.13052/rp-9788743814122

ture etc.). Hence it is critical to have the computational capability to efficiently test the system (i.e., blisk with RVA attached) under different forcing excitations to predict variations in (i.e., blisk with RVA) resonance frequencies and amplitudes ahead of designing the final RVA to be used in production.

The state of the art includes multiple methods able to predict blisk vibrations with RVA attached. In particular, some methods utilize reduced order modeling techniques such as the Craig Bampton component mode synthesis (CB-CMS) [1] approach and treat the blisk and the RVA as different components of the same system retaining a smaller subset of primary degrees of freedom and secondary modes. However, when friction contacts are enabled between the RVA and the blisk to dissipate energy, multiple methods in the literature utilize the Harmonic Balance Method (HBM)[2, 3] to compute blade responses. While this method is highly efficient and accurate, it cannot utilize experimental data to further enhance the prediction and it can be very computationally expensive for specific contact dynamics.

Thus, this paper proposes a new approach using Control-Based Continuation (CBC), a model-agnostic technique that uses a proportional-derivative controller to cancel higher-order modes and a root-finding algorithm to reach the system's resonant peak, thus tracing out the 'backbone' curve of the response. To validate this method, a simple Lumped Mass Model (LMM) is utilized. Results show that this proposed method can accurately and efficiently predict the blisk-RVA system resonance amplitudes and frequencies at different forcing levels when friction contacts are engaged.

Methodology

A lumped-mass model (LMM) was employed as a simplified representation of the sector dynamics. The system consists of a primary (large) mass coupled to a secondary (smaller) mass, which is mounted on top of the primary mass. The secondary mass is governed by a linear spring–damper system referenced to the motion of the primary mass. In addition, a slip–stick friction contact is introduced between the two masses.

During sticking, the frictional restoring force is modeled as a linear elastic force proportional to the relative displacement between the two masses with respect to an evolving equilibrium position. When sliding occurs, this equilibrium position is updated accordingly. In this configuration, the secondary mass functions as a RVA for the primary mass.

The equations of motion for the coupled system can be expressed as:

$$\begin{cases} m_1\ddot{x}_1 + c_1\dot{x}_1 - k_2\left(x_2 - x_1\right) = F sin\left(\omega t\right) - F_{nl} \\ m_2\ddot{x}_2 + c_2\left(x_2 - x_1\right) + k_2\left(x_2 - x_1\right) = F_{nl} \end{cases}, \tag{1}$$

where x_1 is the motion of the primary mass, x_2 is the motion of the secondary mass, F_{nl} is the nonlinear friction term, m_1 is primary mass, m_2 is the secondary mass, k_1 is the spring constant for the primary mass, k_2 is the spring constant for the secondary mass, c_1 is the primary damping coefficient, c_2 is the secondary damping coefficient, ω is the excitation frequency and F is the excitation force amplitude. This system is given by **Figure 1**.

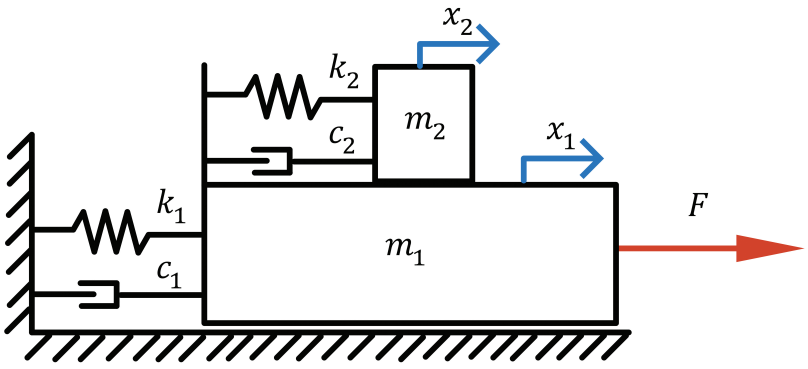

Fig. 1 LMM used for analysis. The friction force is not included but exists between at the interface between the primary mass (m_1) and the secondary mass (m_2)

Control-Based Continuation (CBC) has emerged as a powerful methodology for tracking vibrational characteristics in nonlinear systems [5, 6]. Assuming a general formulation for a linear system with nonlinear forcing, a mathematical

formulation for a proportional–derivative (PD) controller can be achieved as seen in Eq. (1).

$$M\ddot{x} + C\ddot{x} + Kx + f_{nl}\left(\dot{x}, x\right) = fsin\left(\omega t\right) + k_d\left(\dot{x}^{\star} - \dot{x}\right) + k_p\left(x^{\star} - x\right) \ \#\left(2\right)$$

For a forced system, the fixed point corresponds to a multi-harmonic trajectory, which can be formulated as a reference (or target) trajectory for the nonlinear system.

$$x^{\star}\left(t\right) = \frac{A_0^{\star}}{2} + \sum_{i=1}^{m} A_i^{\star}\cos\left(i\omega t\right) \ + B_i^{\star}\sin\left(i\omega t\right) \#\left(3\right)$$

Assuming a similar form for the solution of the oscillator, the PD controller can be described as driving the system to the trajectory described by the Fourier coefficients of the reference. The PD controller can be used to stabilize the response, provided the variation in nonlinearities around the fixed point remains sufficiently small and the reference trajectory is chosen to coincide with the fixed point [5].

When no prior knowledge of the system is available, the fixed point can be identified through iterative computation or root-finding algorithms. The procedure follows 3 steps: (1) simulate the system response using an initial estimate of the Fourier coefficients, (2) compute the Fourier coefficients of the resulting steady-state trajectory, and (3) evaluate the error between the higher-order Fourier coefficients of the simulated response and the reference coefficients. If the error lies within a user-defined tolerance, the fixed point has been numerically identified and is represented by the corresponding Fourier coefficients. If the error exceeds the tolerance, the newly calculated Fourier coefficients are adopted as the updated reference trajectory, and the process is repeated until convergence is achieved.

The definition of a *backbone curve* varies across literature. A common approach defines the backbone as the locus of points in the Frequency Response Function (FRF) where the system response is in quadrature (90° phase lag) with the excitation [6]. In the present work, the backbone is defined as the curve constructed by connecting the resonant peaks of the FRF.

To estimate each resonant peak, an initial seed frequency was selected as a starting guess. Using this seed and two additional frequencies offset by a small increment above and below, a three-point bracket of steady-state response amplitudes was established. If the bracket encompassed the peak, the midpoint amplitude exceeded the endpoint amplitudes. If the peak was not contained within the bracket, the bracket was iteratively shifted toward the side corresponding to the larger amplitude until the peak was enclosed, assuming a smooth and well-behaved resonance.

Once the peak was bracketed, a quadratic fit was applied to the three points to obtain a parabolic estimate of the peak location [4]. This procedure, analogous to a bisection method but employing parabolic interpolation, was repeated iteratively, reducing the frequency interval until the bracket endpoints converged within a user-specified tolerance. After identifying two peaks, improved initial guesses for subsequent peaks were obtained by extrapolating from the Fourier coefficients and resonance frequencies of the previously identified peaks.

Analysis

The frequency response functions (FRFs) in this work were computed using a time-marching ODE45 solver in MATLAB 2024a (MathWorks, Natick, MA). To maintain accuracy while mitigating numerical issues associated with the discontinuity at the slip–stick transition in the friction law, the friction force was linearly smoothed within a 1% region surrounding the slip-to-stick boundary. Steady-state response amplitudes were extracted from the harmonic content of the solution, with Fourier coefficients obtained using the standard FFT routine in MATLAB 2024a. The resulting FRFs are presented in Figure 2.

From these FRFs, there is a clear peak in the middle at low forcing while at high forcing there are two very prominent peaks. A linear analysis of this system shows that the first and second peak at high forcing correspond to the in-phase and out-of-phase modes of the responses. Qualitative these show that as the forcing in the system approaches zero, a dominantly.

Using the CBC algorithm and conjunction with the peak estimation algorithm, a backbone trace was conducted on both mode starting from high forcing and going towards low forcing.

It is qualitative clear to see from the FRF, that the second peak slowly evolves into the dominant peak as the first peak slowly decays away. This conclusion can be seen from the trace of the backbone as well. As forcing diminishes, the out-of-phase mode smoothly transitions into the more prominent mode of the system. In contrast, the in-phase mode shifts down in frequency and amplitude until it merges in the single-peak response at the lowest forcing. Without knowledge of the system, the combination of CBC and the quadratic interpolation peak search algorithm can be leveraged to understand the motion of the vibrational modes a vibratory system.

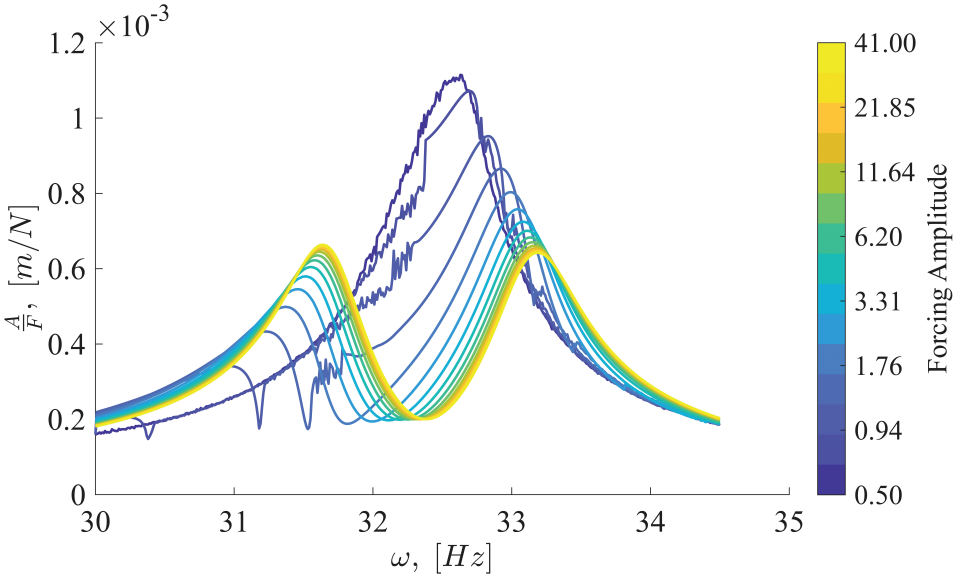

Fig. 2 Frequency response functions for the LMM. These are the amplitudes normalized by the excitation force amplitude. The color corresponds to the forcing value with yellow being 41 N and violet being 0.5 N. The forcing is logarithmically scaled from the low forcings to the high forcings

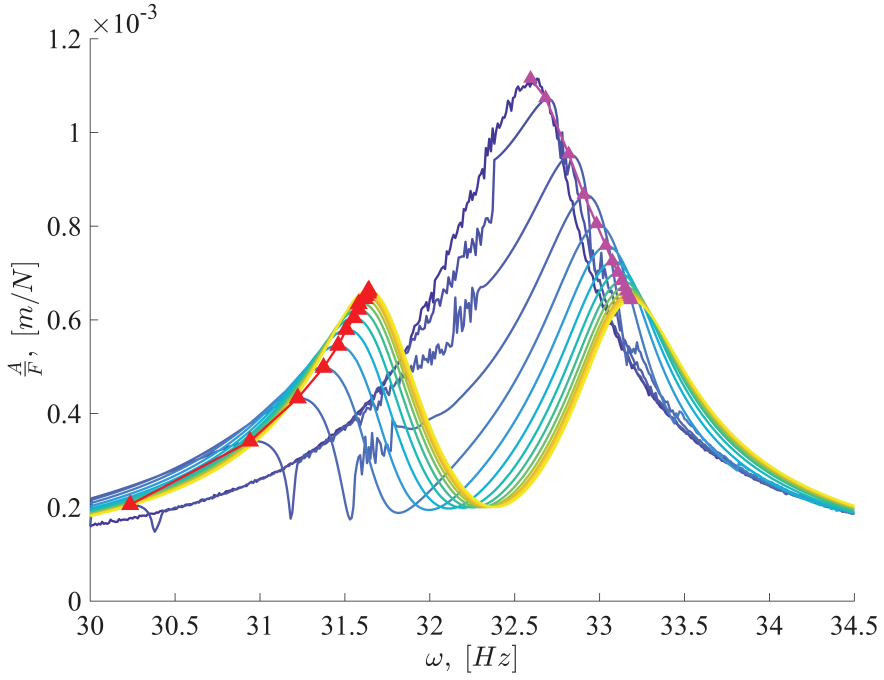

Fig. 3 Backbone trace for LMM model. Using the same FRF coloring scheme from before, yellow indicates strong forcing (41 N) and purple indicates weak forcing (0.5 N). The magenta line shows the backbone of the out-of-phase mode with triangles denoting the backbone points. Similarly, the red line and triangles show the backbone and backbone points respectively

Conclusion

To summarize, this paper proposes a novel technique to predict the backbone curve of a blisk with an RVA with friction contacts. A CBC technique is used on a LMM with 2 masses describing the blisk and the RVA motion when friction contacts are engaged. Results show highly accurate predictions, the CBC allowing efficient predictions of the system response under different coulomb friction conditions. Future work involves applying this technique to a Finite Element (FE) blisk model to further validate the approach.

References

1. Craig, R. R., and Bampton, M. C. C., 1968, "Coupling of Substructures for Dynamic Analyses.," AIAA Journal, **6**(7), pp. 1313–1319. https://doi.org/10.2514/3.4741.
2. Krack, Malte; Gross, Johann. *Harmonic Balance for Nonlinear Vibration Problems*. Springer (Cham), Mathematical Engineering series; ISBN 978-3-030-14022-9 (2019)
3. Lupini, Andrea; Epureanu, Bogdan I. *A Friction-Enhanced Tuned Ring Damper for Bladed Disks*. Journal of Engineering for Gas Turbines and Power, Vol. 143, Issue 1, 011002 (8 pages), 2021.
4. Gasior, Marek & González, José Luis. *Improving FFT Frequency Measurement Resolution by Parabolic and Gaussian Interpolation*. AIP Conference Proceedings 732 (Vol. 1), pp. 276–? (2004).
5. Barton, David A. W. *Control-based Continuation: Bifurcation and Stability Analysis for Physical Experiments*. Mechanical Systems and Signal Processing, Vol. 84 Part B, pp. 54–64 (2017).
6. Renson, L., Gonzalez-Buelga, A., Barton, D. A. W., & Neild, S. A. (2016). *Robust identification of backbone curves using control-based continuation*. Journal of Sound and Vibration, vol. 367, pp. 145-158.

Chapter 6
Mapping the Nonlinear Vibration Responses of Composite Aerospace Structures during Endurance and Qualification Testing

D. Di Maio, F. Oude Tanke, and J. van Tiggelen

Abstract While carbon fibre reinforced polymer composites are well-known for their high strength-to-weight ratio, their fatigue behaviour is difficult to predict. Fatigue of composites is generally considered one of the most challenging physical phenomena due to its multi-physics and stochastic behaviour. One of the most challenging aspects of exploring fatigue properties is the extensive time required for fatigue testing. To determine the fatigue life of a test specimen, the number of required load cycles ranges up to millions. The limitation of testing frequency is caused by the viscoelastic properties of the matrix material, which result in self-heating at high testing frequencies. The objectives of XCTE within the DSTANDART project are to increase the rate of mechanical testing by utilising the High Cycle Fatigue (HCF) testing technique and to understand how to measure, analyse, and decouple the thermo-mechanical forces under high rates of cyclic loading. Fatigue testing can be significantly accelerated when high-frequency testing methods are employed. This paper reports the technological advancement achieved through high-frequency testing on two aerospace components: a) a scaled turbine fan and b) a representative aero demonstrator. Both structures embed a typical design feature, ply termination, to change the thickness from the root to the aerofoil of the blade. Those terminations create resin pockets, which are known to be localised stress raisers leading to the onset of fatigue damage. The paper reports on high-frequency experiments conducted in two testing facilities. The first experiment was executed at the Rolls-Royce Mechanical Testing Operational Centre (MTOC) in Berlin (DE), the second experiment was conducted at the NLR testing facility in Marknesse (NL). High-frequency testing and analysis are now a key technology of the spin-off XCTE, which was born thanks to the D-STANDART European project.

Keywords Vibration fatigue · Nonlinear response · Composites

Introduction

Composite structures are known to exhibit complex fatigue behaviour due to their stacking sequence and embedded features, such as fibre discontinuity, waviness, resin pockets, and voids, among others. Therefore, any composite laminate requires mechanical testing to determine the material and fatigue properties. The latter properties can be very time-consuming when the number of excitation cycles is large, and the excitation frequency is set lower than five cycles/sec to avoid any self-heating caused by the viscoelastic properties of the resin in the composites. There are numerous research studies examining the environmental and self-heating temperature effects on fatigue life [1, 2, 3, 4, 5], which suggest a substantial reduction in residual life due to the coupling between mechanical and thermal loads during fatigue cycles. Clearly, temperature-dependent material properties are of no use for engineers who develop fatigue models, assuming a constant entropy behaviour during the development of fatigue damage. The temperature effect(s) are modelled via superposition principles by using test data generated using low excitation rates under different temperature conditions. The result is that a significant amount of time is invested in generating fatigue test data to feed fatigue damage models, even when any aerospace structure can naturally

D. Di Maio · F. Oude Tanke · J. Van Tigelen
University of Twente, Drienerlolaan 5, 7522 NB Enschede, The Netherlands
e-mail: d.dimaio@utwente.nl; f.oudetanke@utwente.nl; j.vantiggelen@utwente.nl

© The Author(s), under exclusive license to River Publishers 2026

Kristin B. Zimmerman, PhD (eds.), *Nonlinear Structures & Systems, Vol. 1*, Conference Proceedings of the Society for Experimental Mechanics Series, https://doi.org/10.13052/rp-9788743814122

be subjected to oscillatory motions higher than five cycles/sec and environmental conditions (temperature and moisture). Within the D-STANDART project, the consortium partners investigate the effects of temperature and humidity, with one partner focusing on high-frequency testing under various environmental conditions. These tests clearly indicate how the loss of stiffness correlates with the increase in self-heating temperature in the cross-laminate made of IM7-8552. The research will be published after the ICCM event, so it is advisable to monitor the upcoming literature.

The high-frequency tests were developed and proven in several research studies [1, 2, 3, 4], which are briefly summarised in this paragraph. The composite sample is held by a specific fixture consisting of two rods that support the sample during the excitation of the first bending motion, allowing the structure to rotate at the clamping region. A ply-drop, or cut-ply, features the cross-ply laminate to generate a stress away from the clamping region. That stress raiser is typically placed a few tens of millimetres away from the clamp. The test is executed at a constant excitation frequency, corresponding to the pristine resonance frequency, during the fatigue test. The frequency response phase is measured by the ratio between the input stimulus (typically a base acceleration) and the output response, as measured by a laser Doppler vibrometer (LDV). The vibration amplitude is maintained constant during the fatigue test, thus achieving a displacement control test (noting that the velocity measured by the LDV is converted into displacement). The loss of stiffness as a function of the excitation cycles is measured by the frequency response phase rather than the change of the natural frequency of the test object. The phase is calculated from the inverse tangent of the ratio between the natural frequency and the drive frequency (constant). Consequently, a minimal natural frequency change is transformed into a significant phase deviation due to the tangent function. The temperature (measured by an IR camera) and vibration measurements are synchronised, with the temperature reading sampled every N elapsed cycles to avoid overloading the PC hard drive. The experiments are typically conducted inside an environmental chamber to control the ambient temperature, which scales up or down the effect of self-heating temperatures. The fatigue test data consist of frequency response phase, peak surface temperature (in the region of the ply-drop), and base acceleration versus excitation cycles. These plots will be presented in the following sections.

The experimental technique introduced in the previous paragraph to characterise the fatigue behaviour is applied to two test structures made of composite materials. The first structure is a scaled turbine fan made of a composite material, the type of which and stacking sequence were unknown to the authors [2]. The second structure is an aero demonstrator developed in the D-STANDART consortium. The demonstrator is a quasi-isotropic stacking sequence made of IM7-8552 material. The two experiments were conducted in two different industrial testing facilities. This paper will present the experiments performed and the output generated by the fatigue tests.

Experimental set-up

This section describes the experimental set-up, which is common to both experiments, despite being executed in different years. The first experiment was conducted in Rolls-Royce MTOC in 2015, while the second experiment was conducted in NLR in 2025.

The experimental set-up is presented in Figure 1. The test structure is mounted on a slip table, which is connected to an electromagnetic shaker that exerts the excitation force. An accelerometer is attached to the slip table to measure the input base acceleration to the test structure. A strain gauge is mounted near the root of the test structure and is used for calibration between the input acceleration, output strain, and output displacement. The LDV and the IR camera are installed in front of the test structure. The XCTE sniper control panel is a custom-made software to control the sensors and exciter. The control panel can perform force or displacement control, depending on the test definition. Moreover, the frequency or phase lock loop at constant amplitude is yielded by a Proportional Integral Derivative (PID) control scheme.

The first task to accomplish is a frequency check before performing any High Cycle Fatigue with the High Frequency tests. The frequency check is a simple test where the excitation sweeps a frequency range to identify the resonances of the test structure. This step is essential to determine the first bending resonance for which a calibration step is required. In both experiments, the first mode of vibration was the target mode; however, any other fundamental mode can be tested similarly.

Once the frequency check is completed, the second task is to calibrate the base acceleration, the strain gauge, and the LDV laser output. This procedure ensures that a relationship is established between the three sensors, which typically exhibits nonlinearity due to large deformation. This calibration mustn't overload the structure; therefore, it is advisable to avoid large input forces.

At this point, the excitation frequency (resonance) and calibration are known; the final step is to set up the type of force or displacement control for the HCF test. Having decided the kind of control, the HCF can be started, and the frequency response phase is continuously tracked to monitor the loss of stiffness. At the same time, the sniper control panel measures and stores the output of the other sensors, but the strain gauge, whose wire has been cut, is not included.

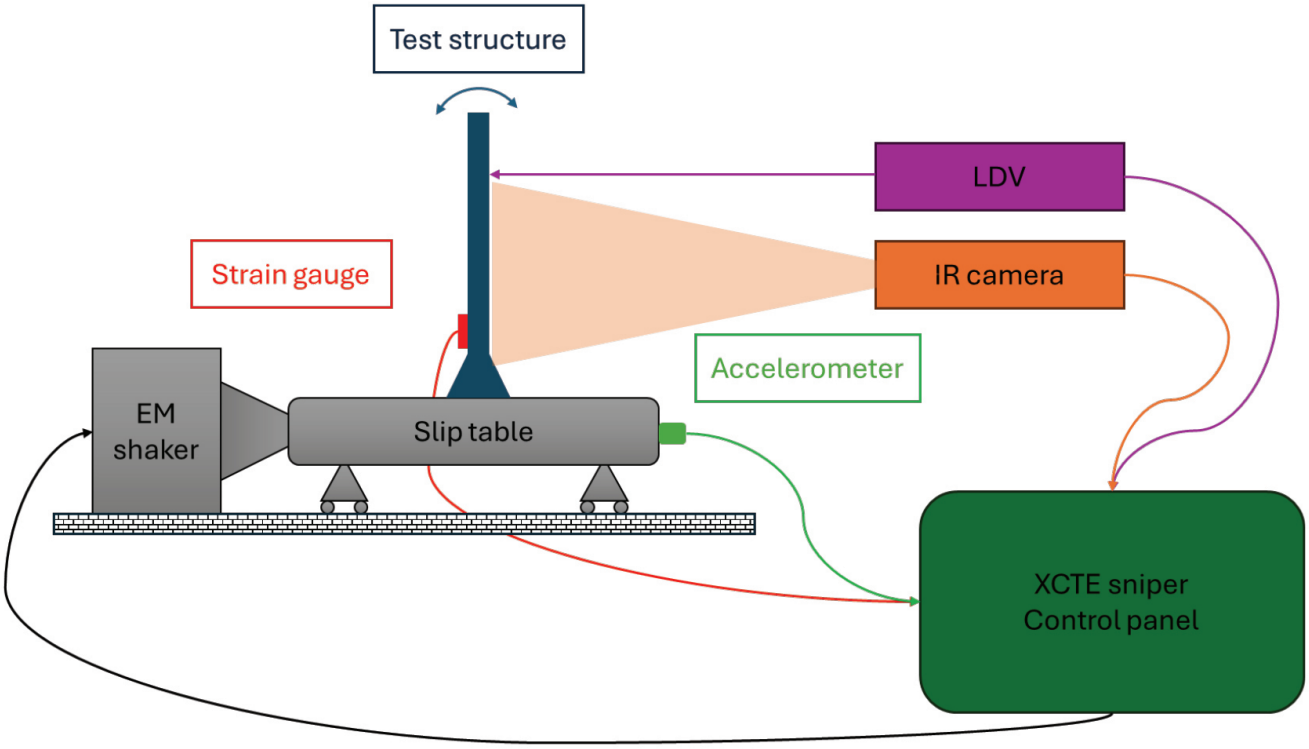

Fig. 1 Test set-up used for the two experiments

Figure 2 shows a close-up of the test set-up where the blade can be seen vibrating in its test fixture. Note that the test fixture was specifically designed to match the blade root. Figure 3 illustrates the complete measurement set-up, as schematically depicted in Figure 1.



Fig. 2 Close-up of the test set-up

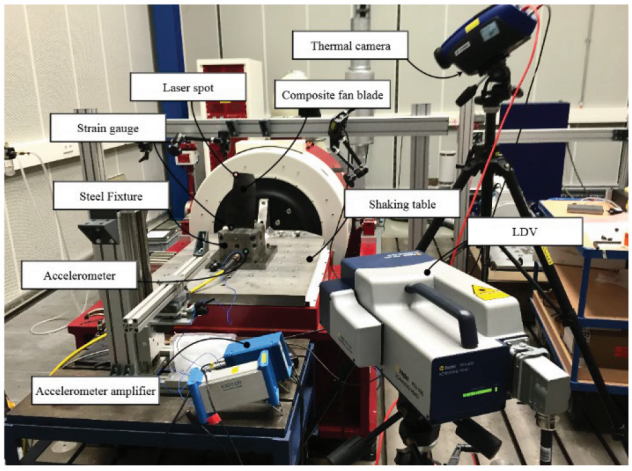

Fig. 3 Blade test set up

Although the two experiments were conducted in different years, the modus operandi remains the same. The set-up can be adapted to what the test facility can provide, as long as it can be realised as described in Figure 1. XCTE technology enables the set-up, performance, and analysis of fatigue test data in hours rather than days.

The following section presents the experimental test data and how the test data from the second experiment are used to evaluate a global master curve of fatigue onset damage growth. It is worth mentioning that the first experiment could be executed using only one fan blade; hence, it was a single shot that could not be missed. The second experiment could

be executed using three aero demonstrators, which allowed verifying the repeatability of the results across the three test structures. The comparison between the first and second experiments is not presented in this paper. Figure 4 shows a close-up of the test structure, and Figure 5 shows the full test set-up.

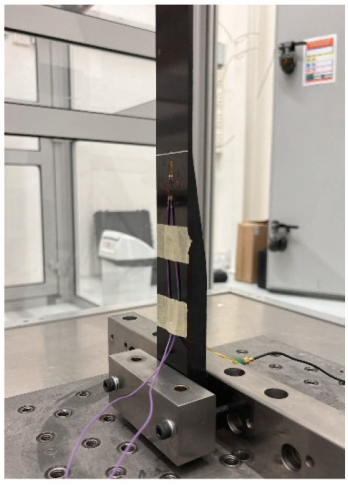

Fig. 4 Close-up of the test set-up with the strain gauge.



Fig. 5 DST aero demonstrator test set-up.

Experimental results

This section will present the experimental results obtained from the two experiments. It is worth explaining briefly hereafter why and what the objectives of the experiments were.

The first experiment of the composite blade had two objectives. The first objective was to prove that the fatigue behaviour observed from cross-ply laminate embedding ply drops [2, 3, 4] at the University of Bristol laboratory was not case-dependent. Hence, similar fatigue behaviours could be observed from scaled fan blades. The second objective was to demonstrate that such a fatigue behaviour could be reproduced and tested in an industrial testing facility.

The second experiment on the DST aero demonstrators also had two objectives. The first objective was to demonstrate that the first experiment on the fan blade was not a fortunate test case, but rather one that could be reproduced years later. The second objective was to evaluate a master curve based on the fatigue onset damage. The second goal was achieved due to the availability of three test structures and the novel testing technique used to obtain the master curve.

Calibration base acceleration, strain and displacement

Once the frequency check is executed to identify the target resonance, the calibration between the input base acceleration and the output strain and displacement responses is performed using a simple stepped sine test. The procedure consists of exciting under steady-state conditions a frequency near the resonance peak for multiple acceleration amplitude levels. The nought-to-peak of the vibration signals measured from each sensor is processed. Figure 6 shows the relationship between strain and displacement obtained from the fan blade calibration exercise. A linear relationship can be observed. However, a nonlinear behaviour might appear if the strain vs base acceleration or displacement vs base acceleration is plotted. Therefore, the calibration performed for the aero demonstrator retained the use of the three signals, rather than the two used for the fan blade.

Figure 7 shows the relationship between the input base acceleration and the output strain for the aero demonstrator. The calibration was performed up to 5 (g) to avoid overloading the test structure. However, it is visible that nonlinear behaviour, which is extrapolated up to 15 (g), where the fatigue behaviour is expected to develop. The nonlinear behaviour is expected because of the large deformation achieved under steady-state vibrations. It is essential to perform this experimental characterisation to avoid setting up incorrect vibration amplitudes during the HCF tests.

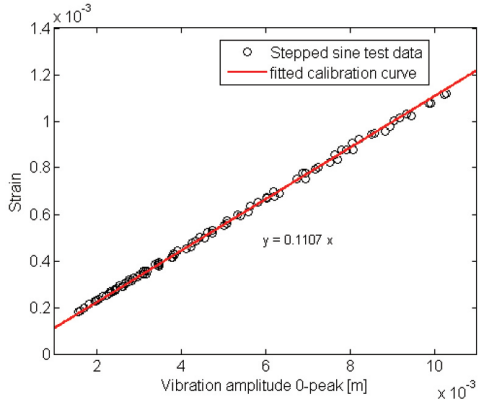

Fig. 6 Fan blade strain-displacement calibration.

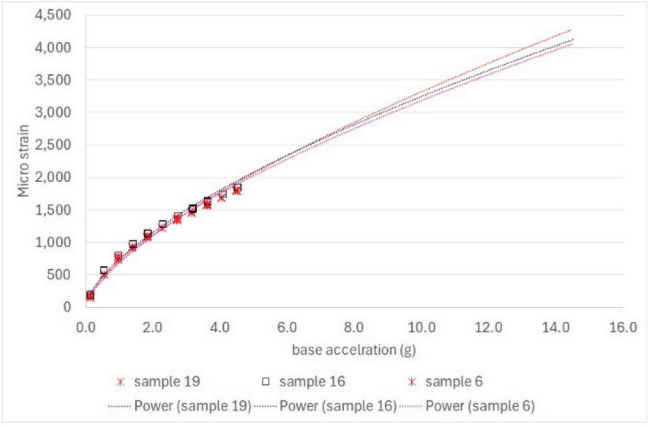

Fig. 7 Aero demonstrator strain - base acceleration calibration.

Test results

This section describes the HCF test data obtained from the fan blade and the aero demonstrator. The type of HCF test is displacement control, which involves using a single excitation frequency and vibrating the target point at a constant amplitude throughout the entire duration of the HCF trial. This procedure is also applied to the aero demonstrator, using a slightly different approach, which will be described later.

The first test results presented are from the fan blade. As previously introduced, the expectation was to observe similar fatigue behaviour already observed with small coupons tested in a university laboratory. The results of the HCF test demonstrated that the experimental procedure was valid for both small coupons and scaled fan blades, thereby meeting the objectives. Figure 8 shows a plot that reproduces three curves: the frequency response phase, the base acceleration, and the surface peak temperature. It is essential to note the correlation between phase decay and the increase in acceleration. This

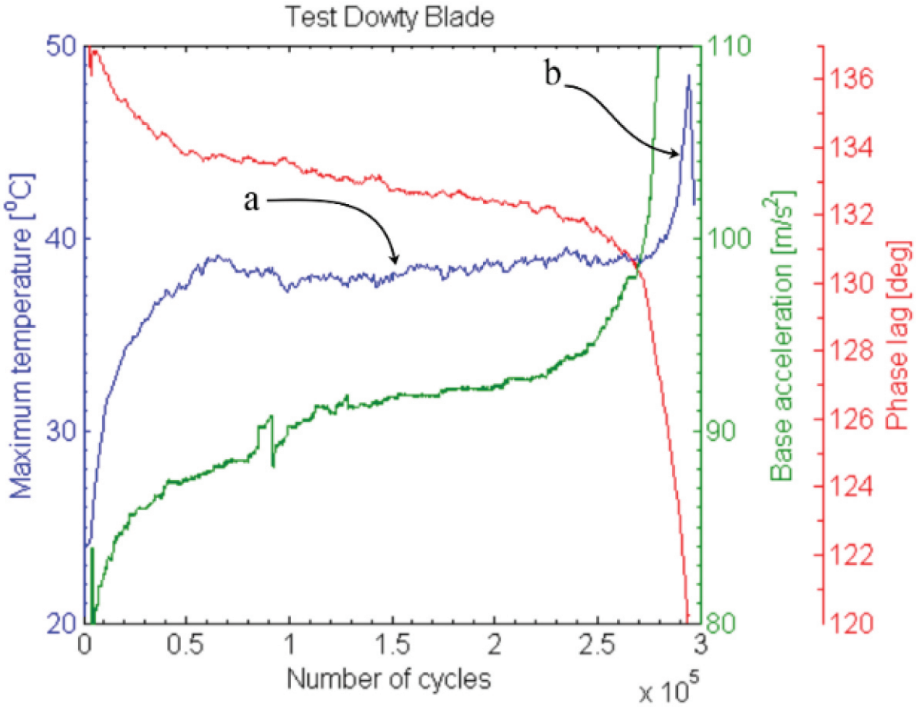

Fig. 8 Frequency response phase, base acceleration and surface temperatures of the fan blade.

behaviour occurs because the mechanical system loses stiffness due to fatigue, and thus, fatigue damage is initiated by the combined mechanical and thermal loads. Both the phase and the acceleration have a specular behaviour. At the same time, the surface peak temperature follows a trend similar to the acceleration towards the end when a temperature hot spot develops. Figure 9 shows two pictures from the IR camera at two different time instants, when the surface peak temperature reveals a stress concentration (point a) in Figure 8) and when the temperature hot spot is fully developed (point b) in Figure 8).

The main difference with the test carried out with the aero demonstrator was (i) to perform two HCF tests increasing the amplitudes every N number of cycles, instead of running a single amplitude, and (ii) to perform one HCF test at a higher amplitude than the previous two HCF tests. The latter goal was to demonstrate that one test structure was sufficient to extract a master curve capable of predicting the results of a different HCF test conducted using a new test structure.

Therefore, one aero demonstrator was tested at a very low amplitude of vibrations, which were incremented every 100,000 cycles. The test was interrupted every 100k cycles to perform nonlinear modal testing. The motivation of that modal test was to observe the change in the nonlinear dynamic response as a function of the increased fatigue behaviour. The modal test was conducted using the last HCF amplitude and was completed quickly to minimise excessive exposure to dynamic loads. At the end of each HCF test, the frequency response phase, acceleration and surface temperature were stored for analysis. These test sequences were executed for two of the three test structures; the last one was tested to HCF using a single amplitude, which was higher than the one set up for the other two demonstrators.

The HCF test data stored from the first test structure were processed into a master curve based on the onset of fatigue damage. To achieve this, the frequency response phase curves were processed using a specific data analysis toolset to extract the loss of stiffness per unit cycle, described as $d\Phi/dN$, as a function of the input base acceleration. The same procedure was applied to the single frequency response phase curves obtained from the HCF test and plotted on the graph. Figure 10 shows the power law curve extracted from the aero demonstrator tested at several amplitudes, along with a single data point from the other test structure. The single data point (in blue) in Figure 10 lies not far off the power law curve.

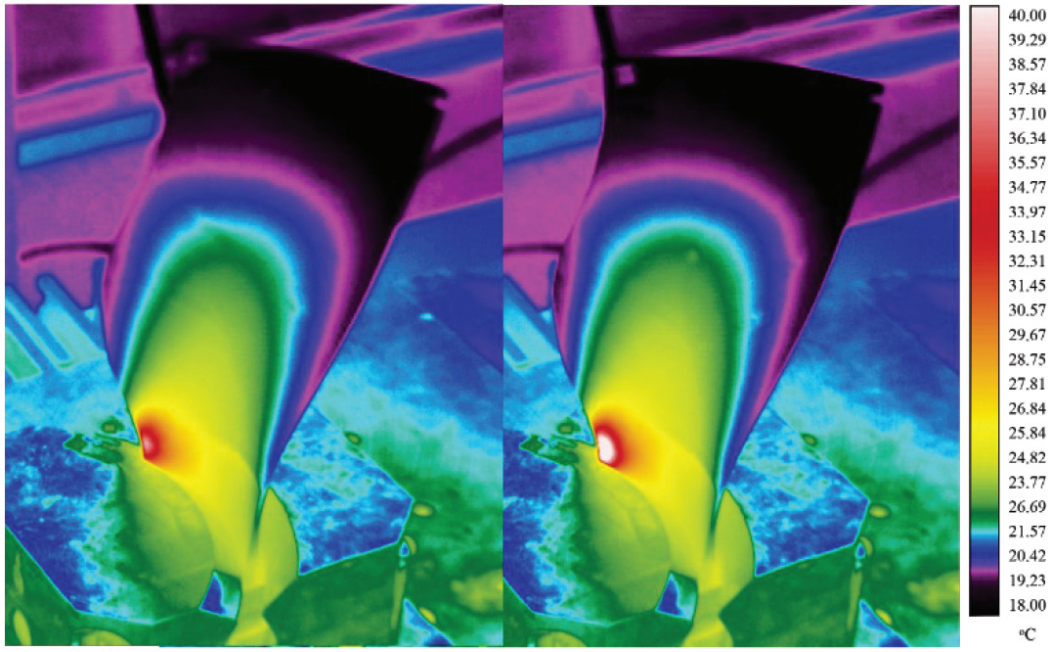

Fig. 9 Surface temperature profile in points a) and b) of Figure 8.

Finally, Figure 11 shows the infrared image of the test structure with a fully developed temperature hot spot caused by fatigue delamination.

Final remarks on the fatigue testing

There are many positive outcomes from this experimental campaign in NLR. The experimental procedure is repeatable and robust. Experiments conducted in two different environments and with two additional test structures indicate that the method for tracking loss of stiffness is valid regardless of geometry and material properties. Moreover, the experiments using the aero demonstrator show what was not possible with the fan blade. A single test structure can be used to evaluate a power law

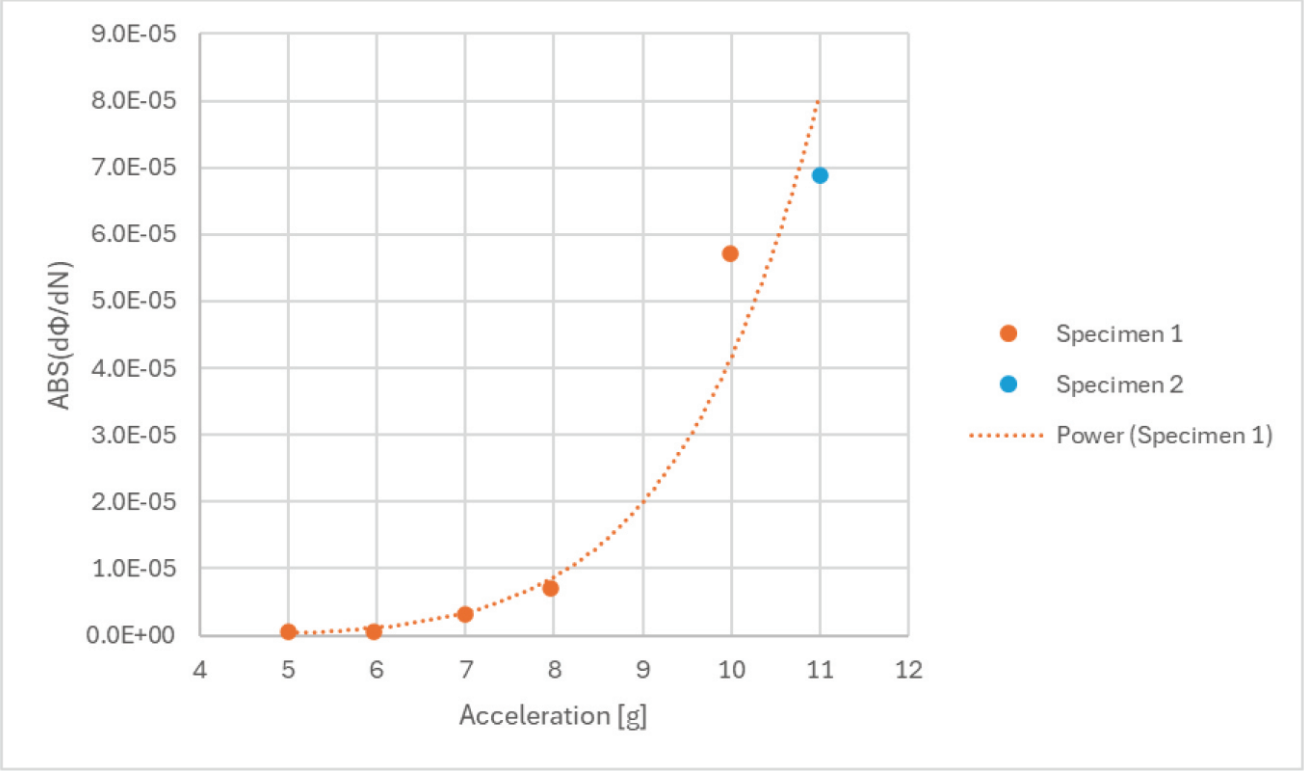

Fig. 10 Surface temperature profile in points a) and b) of Figure 8.

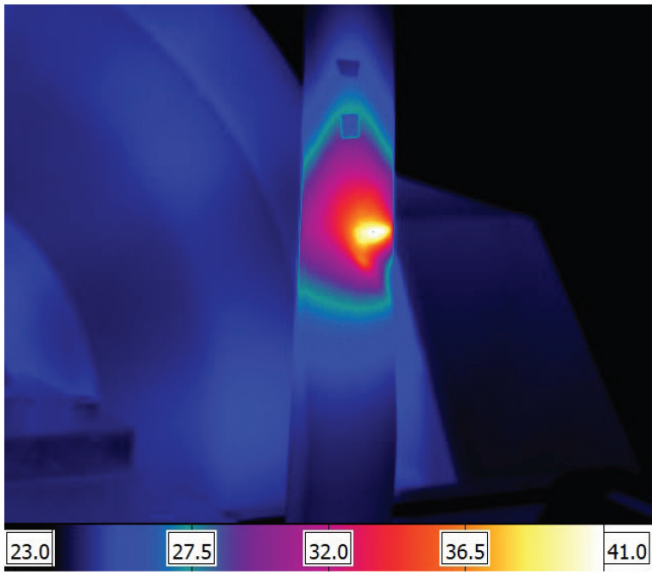

Fig. 11 Infrared picture of specimen 1 with developed temperature hot spot.

function that describes the loss of stiffness per unit excitation cycle as a function of the input load. In this example, the base acceleration was used instead of the strain load; however, the calibration curve allows the references to be interchangeable. Ultimately, the XCTE team had 60 hours to perform the HCF tests with three aero demonstrators in NLR. Despite the self-heating condition, which affected the residual life, the results showed that the fatigue behaviour of the aero demonstrator is a matter of hours rather than days. Finally, any analyst can commission such an experimental test to verify if the design choice delivers the expected durability or not.

Mapping nonlinearity during fatigue testing

One of the experimental tasks conducted during the vibration fatigue experiment was to map the nonlinear behaviour of the aero demonstrator blade. As explained earlier, the fatigue test was executed using incremental excitation steps. Hence, one modal test at the level of the fatigue test amplitude was initiated before the fatigue test began. One Frequency Response Function was measured for each excitation step. The observation of the nonlinear behaviour of the test article aimed to map the change in structural dynamic properties during fatigue damage. Figure 12 illustrates three different analysis techniques used to derive both the natural frequency and the damping loss factor at varying levels. The identification techniques used were the modified-Dobson and the AAA methods. Two of these identification methods were executed using the sweeper approach [6], while the other used the slicing approach. Each colour in the plots identifies the processed FRF at the excitation level of the fatigue test. The variation in dynamic properties is identified over the amplitude of vibration in the FRF. One observation concerns the natural frequencies, which indicate a softening behaviour as fatigue damage occurs. A sudden change is visible in the frequency plot, indicating that a major stiffness change occurred due to the onset of fatigue damage. The other observation is about the damping loss factor curves. The change in damping is continuous, and the plots do not exhibit sudden variations, unlike the natural frequencies. Hence, the damping is continuously increasing over the fatigue excitation steps. This behaviour seems to indicate that (i) the composite material is changing its loss modulus and (ii) the contact friction is increased as a function of the excitation force. Unfortunately, it is not possible to discriminate between the two damping behaviours in the presented tests.

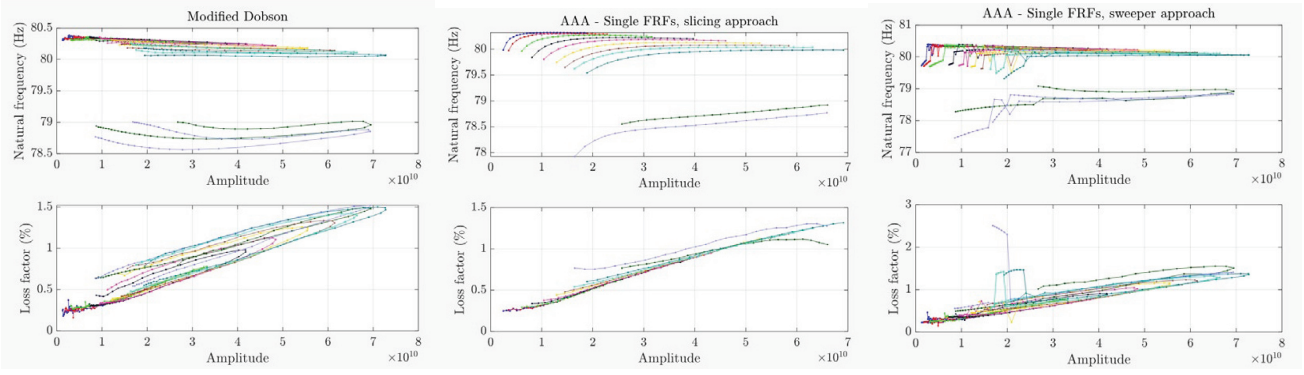

(a) Modified-Dobson (b) AAA Equal amplitude (c) Sweping method

Fig. 12 Natural frequency and damping loss factor estimations as a function of the vibration amplitude.

Conclusions

This short paper presents some new developments in the area of accelerated fatigue testing developed by XCTE, as part of the D-STANDART EU Horizon project. The testing technology proved to be robust and adaptable to different laboratory environments. Two test cases were presented in the paper; one was an experiment on a composite fan blade conducted in 2015 at a facility in Berlin, and the other was a more recent experiment on an aero demonstrator. The first experiment shows the type of testing set-up and test data generated during an HCF test. The second experiment shows how the HCF test data can be converted into a power law describing the loss of stiffness as a function of the input base acceleration. The scientific value is auspicious because one test structure is sufficient to evaluate a power law describing the fatigue behaviour. The scientific impact will enable engineers to utilise XCTE testing technology to probe structures and assess the most robust design. Moreover, the effectiveness of the proposed HCF tests is demonstrated by their time-saving and potentially cost-saving benefits. The second experiment was conducted over a 60-hour time frame, which is considerably shorter than the standard mechanical tests executed at low excitation cycle rates. Hence, engineers will be able to probe their design optimisations in a very short time. The time savings will enable optimal optimisation towards the standard route of validation and verification.

Acknowledgments Funded by the European Union under GA No. 101091409. Views and opinions expressed are however those of the author(s) only and do not necessarily reflect those of the European Union. Neither the European Union nor the granting authority can be held responsible for them.

References

1. Di Maio, D. and Magi, F., 2015. Development of testing methods for endurance trials of composites components. Journal of Composite Materials, 49(24), pp.2977-2991.
2. Magi, F., Di Maio, D. and Sever, I., 2016. Damage initiation and structural degradation through resonance vibration: Application to composite laminates in fatigue. Composites Science and Technology, 132, pp.47-56.
3. Voudouris, G., Di Maio, D. and Sever, I.A., 2020. Experimental fatigue behaviour of CFRP composites under vibration and thermal loading. International Journal of Fatigue, 140, p.105791.
4. Di Maio, D., Voudouris, G. and Sever, I.A., 2022. Investigation of fatigue damage growth and self-heating behaviour of cross-ply laminates using simulation-driven dynamic test. International Journal of Fatigue, 155, p.106617.
5. Katunin, A. and Wronkowicz, A., 2017. Characterisation of failure mechanisms of composite structures subjected to fatigue dominated by the self-heating effect. Composite Structures, 180, pp.1-8.
6. Dario Di Maio, ≪A novel analysis method for calculating nonlinear Frequency Response Functions.≫, Journal of Structural Dynamics, Issue 3, URL : https://popups.uliege.be/2684-6500/index.php?id=242

Chapter 7
Evidential Thresholding in Sparse Bayesian Learning for Nonlinear Dynamical System Identification

Jiawei Jian, Jerome Antoni, and Konstantinos Gryllias

Abstract Sparse regression provides a data-driven approach for the identification of nonlinear dynamical systems in cases where the prior knowledge of the nonlinear characteristics is unavailable. Specifically, a parsimonious governing equation can be distilled from a large dictionary of potential candidate components by imposing sparse regularization or thresholding techniques to the coefficients in a linear regression model. Owing to the capability of uncertainty quantification, sparse Bayesian learning (SBL) has been extensively studied for the identification of nonlinear dynamical systems. However, due to the interference of noise, existing SBL methods usually suffer from overfitting induced by redundant components. Traditional thresholding techniques may fail to eliminate these irrelevant components due to their inherent limitation, namely, evaluating the significance of components based solely on the magnitudes of their coefficients. As a result, redundant components with relatively large coefficients are difficult to eliminate, while the correct components with small coefficients (such as damping terms) are likely to be falsely discarded. To address this problem, this paper proposes a thresholding method, referred to as evidential thresholding, within a Bayesian framework. Instead of removing components with small coefficients, the proposed evidential thresholding approach evaluates the decoupled contribution of each candidate component to the evidence, and then eliminates those with negligible evidential contributions. Additionally, unlike traditional thresholding techniques relying on an unbounded threshold value, the threshold value in the proposed approach is naturally bounded within [0, 1], making it easier to define. From another perspective, the proposed approach can be considered as a component-wise extension of Bayesian model selection, where the components with relatively large evidential plausibility are selected. The proposed evidential thresholding method is subsequently integrated into a Gibbs sampler-based SBL (GB-SBL) framework for the identification of nonlinear dynamical systems. Numerical and experimental examples are investigated to demonstrate the effectiveness of the proposed method. The results show that it outperforms state-of-the-art approaches, namely, SINDy, relevance vector machine (RVM), and GB-SBL without evidential thresholding.

Keywords Sparse bayesian learning · System identification · Evidential thresholding · Gibbs sampler · Model selection

Introduction

Linear approximation is commonly employed to model the dynamical characteristics of engineering structures due to its simplicity and well-developed theoretical foundation. However, in practice, structures inevitably exhibit complicated nonlinear behavior, such as jumps, bifurcations, and limit cycles, which may greatly deviate the approximate linear models. Ignoring these nonlinear characteristics can lead to misinterpretations of structures. Consequently, precise modelling of nonlinear dynamics is important. To this end, nonlinear system identification has been widely studied over the past decades [1, 2].

Jiawei Jian · Konstantinos Gryllias
Department of Mechanical Engineering, KU Leuven, Celestijnenlaan 300, Leuven, 3001, Belgium
e-mail: jiawei.jian@kuleuven.be; konstantinos.gryllias@kuleuven.be

Jiawei Jian · Jerome Antoni
INSA Lyon, LVA, UR677, Villeurbanne, 69621, France
e-mail: jiawei.jian@kuleuven.be; jerome.antoni@insa-lyon.fr

Jiawei Jian · Konstantinos Gryllias
Flanders Make@KU Leuven, Belgium
e-mail: jiawei.jian@kuleuven.be; konstantinos.gryllias@kuleuven.be

© The Author(s), under exclusive license to River Publishers 2026

Kristin B. Zimmerman, PhD (eds.), *Nonlinear Structures & Systems, Vol. 1*, Conference Proceedings
of the Society for Experimental Mechanics Series, https://doi.org/10.13052/rp-9788743814122

Numerous nonlinear system identification approaches have been developed. Most of them mainly focus on parameter estimation under a given mathematical equation model. However, nonlinearity characterization, namely determination of the equation form, is also a challenging and important task in practice. To address this problem, Brunton et al. proposed the sparse identification of nonlinear dynamics (SINDy), which learns parsimonious dynamical equations from a large dictionary of candidate components [3]. Due to its explainability and computational efficiency, SINDy and its derivatives have been widely used to simultaneously characterize nonlinearity and estimate parameters. However, SINDy is fundamentally a deterministic approach, which cannot quantify the uncertainty caused by noise. Moreover, its performance heavily relies on the predefined threshold value.

In recent years, probabilistic methods have gained increasing attention for uncertainty quantification in system identification. Notably, sparse Bayesian learning (SBL), which was originally proposed by Tipping [4], has been developed for nonlinear system identification [5, 6]. SBL-based approaches inherit the concept of dictionary learning, identifying the parsimonious model from numerous candidate components by imposing sparse priors on their coefficients. However, due to the interference of noise, existing SBL methods easily result in overfitted models induced by redundant components. To alleviate this issue, some efforts attempt to incorporate thresholding technique into SBL to produce sparser results [7, 8]. Nevertheless, in this case, the correct components with small coefficients, such as damping, are likely to be eliminated by thresholding, while some irrelevant components with relatively large coefficients may still retain in the model.

To address the problems, this paper proposes a probabilistic sparsity-promoting technique, referred to as evidential thresholding. Unlike conventional thresholding techniques, which remove candidate components solely according to the magnitudes of their coefficients, evidential thresholding evaluates the contribution of each component and eliminates those with small contributions. It is demonstrated that even in cases where the correct components possess small coefficients, their corresponding evidential contributions remain relatively large. Additionally, the proposed evidential thresholding approach can be considered as a component-wise extension of Bayesian model selection. In this paper, evidential thresholding is incorporated into a Gibbs sampler-based SBL (GB-SBL) method to illustrate its performance. However, it is noteworthy that it can be flexibly combined with general SBL approaches to promote sparsity.

The remainder of this paper is organized as follows: Section 2 firstly introduces the mathematical formulation of the sparse identification model for nonlinear dynamical systems, and then proposes the evidential thresholding method incorporated with the GB-SBL. A numerical example and an experimental benchmark are investigated in Section 3 to demonstrate the effectiveness of the proposed method. Finally, conclusions are drawn in Section 4.

Methodology

Sparse identification of nonlinear dynamical systems

The mathematical formulation of the sparse regression for nonlinear dynamical system identification is briefly introduced in this section. Consider an *m*-DOF nonlinear dynamical system as follows:

$$\mathbf{M}\ddot{\mathbf{y}}\left(t\right)+\mathbf{C}\dot{\mathbf{y}}\left(t\right)+\mathbf{K}\mathbf{y}\left(t\right)+\mathbf{P_N}\left(\mathbf{y}\left(t\right),\dot{\mathbf{y}}\left(t\right)\right)=\mathbf{P}\left(t\right)\#\left(1\right) \tag{1}$$

where $\mathbf{M},\ \mathbf{C},\ \mathbf{K}\in\mathbb{R}^{m\times m}$ are the mass, damping and stiffness matrices; $\ddot{\mathbf{y}}\left(t\right),\dot{\mathbf{y}}\left(t\right),\ \mathbf{y}\left(t\right)\in\mathbb{R}^{m}$ are the acceleration, velocity and displacement vectors; and $\mathbf{P_N}\left(\mathbf{y}\left(t\right),\dot{\mathbf{y}}\left(t\right)\right)$ and $\mathbf{P}\left(t\right)$ represent the nonlinear restoring force and external load respectively. By grouping the responses and considering their discrete forms, one can obtain

$$\mathbf{Z}=\left[\begin{array}{cccc}\mathbf{y}\left(t_1\right) & \mathbf{y}\left(t_2\right) & \cdots & \mathbf{y}\left(t_N\right)\\ \dot{\mathbf{y}}\left(t_1\right) & \dot{\mathbf{y}}\left(t_2\right) & \cdots & \dot{\mathbf{y}}\left(t_N\right)\end{array}\right]^{\mathrm{T}},\ \dot{\mathbf{Z}}=\left[\begin{array}{cccc}\dot{\mathbf{y}}\left(t_1\right) & \dot{\mathbf{y}}\left(t_2\right) & \cdots & \dot{\mathbf{y}}\left(t_N\right)\\ \ddot{\mathbf{y}}\left(t_1\right) & \ddot{\mathbf{y}}\left(t_2\right) & \cdots & \ddot{\mathbf{y}}\left(t_N\right)\end{array}\right]^{\mathrm{T}}\#\left(2\right) \tag{2}$$

where $\mathbf{Z},\dot{\mathbf{Z}}\in\mathbb{R}^{N\times 2m}$ are the assembled responses.

Subsequently, a dictionary including the potential candidate components of the nonlinear system is constructed as follows:

$$\mathbf{\Phi}\left(\mathbf{Z}\right)=\left[\begin{array}{ccccccccc}\mathbf{1} & \mathbf{Z} & \mathbf{Z_2} & \mathbf{Z_3} & \cdots & \mathrm{sign}\left(\mathbf{Z}\right) & \left|\mathbf{Z}\right| & \cdots & \mathbf{P}\end{array}\right]\#\left(3\right) \tag{3}$$

where the dictionary $\mathbf{\Phi}\left(\mathbf{Z}\right)\in\mathbb{R}^{N\times n}$ encompasses constants, polynomials, sign function terms, absolute values, and inputs etc. Once the dictionary is established, the system identification can be formulated through a linear regression model:

$$\dot{\mathbf{Z}}=\mathbf{\Phi}\left(\mathbf{Z}\right)\mathbf{W}\#\left(4\right) \tag{4}$$

where $\mathbf{W}\in\mathbb{R}^{n\times 2m}$ represents the coefficients of candidate components. Ideally, Eq. (4) can be solved by linear least squares regression in the absence of noise interference. However, in practical applications, it usually suffers from overfitting

due to noisy measurements, in which irrelevant components may be assigned non-zero coefficients. This can significantly compromise the accurate understanding of the target nonlinear system.

To mitigate overfitting, sparse regularization techniques are usually used to constrain the model coefficients. In principle, L_0-norm regularization is the optimal choice, as it directly counts the component number in the identified system. However, L_0-norm regularization is a non-convex optimization problem, which is difficult to solve. As a practical alternative, L_1-norm regularization, also known as LASSO, is widely applied to provide a sub-optimal solution. Alternatively, in SBL, sparsity is promoted by imposing the automatic relevance determination (ARD) prior to the coefficients. It will be illustrated in what follows.

Gibbs sampler-based SBL

A SBL framework based on Gibbs sampling is proposed in this section to solve the aforementioned sparse regression model. The proposed approach follows the concept of the relevance vector machine (RVM) [4]. However, instead of maximum a posteriori (MAP) estimation, it utilizes a Gibbs sampler to obtain the full posterior distribution.

To start with, an error term is introduced into the regression model:

$$\mathbf{z} = \mathbf{\Phi w} + \boldsymbol{\varepsilon}_{\mathbf{z}},\ \boldsymbol{\varepsilon}_{\mathbf{z}} \sim \mathcal{N}\left(0, \sigma^2 \mathbf{I}\right) \# (5) \tag{5}$$

where $\mathbf{z} = [z_1, z_2, \ldots, z_N]^{\mathrm{T}}$ and $\mathbf{w} = [w_1, w_2, \ldots, w_n]^{\mathrm{T}}$ denote one column of matrices $\dot{\mathbf{Z}}$ and $\mathbf{W}$; $\boldsymbol{\varepsilon}_{\mathbf{z}}$ denotes the error vector, which follows an independent multivariate Gaussian distribution with zero mean and variance σ^2. Consequently, the likelihood can be obtained as

$$p\left(|\mathbf{z} \mid \mathbf{w}, \sigma^2\right) = \mathcal{N}\left(\mathbf{\Phi w}, \sigma^2 \mathbf{I}\right) \# (6) \tag{6}$$

Subsequently, the ARD prior is imposed to the coefficients $\mathbf{w}$. Additionally, owing to the conjugate property, Gamma distributions are selected as the hyperpriors to the precision parameters of coefficients and data. Specifically, the prior and hyperpriors are specified as follows:

$$\begin{aligned} p(\mathbf{w} \mid \boldsymbol{\alpha}) &= p_{\mathrm{ARD}}(\mathbf{w} \mid \boldsymbol{\varepsilon}) = \prod_{i=1} \mathcal{N}\left(w_i \mid 0, \varepsilon_i\right) \\ p(\boldsymbol{\alpha} \mid \mathbf{a}, \mathbf{b}) &= \prod_{i=1}^{n} \mathrm{Gamma}\left(\alpha_i \mid a_i, b_i\right) \\ p\left(\sigma^2 \mid c, d\right) &= \mathrm{Gamma}\left(\frac{1}{\sigma^2} \middle| c, d\right) \end{aligned} \tag{7}$$

where $\boldsymbol{\varepsilon} = [\varepsilon_1, \varepsilon_2, \ldots, \varepsilon_n]^{\mathrm{T}}$ is the coefficient variances; $\boldsymbol{\alpha} = [\alpha_1, \alpha_2, \ldots, \alpha_n]^{\mathrm{T}} = \left[\frac{1}{\varepsilon_1}, \frac{1}{\varepsilon_2}, \ldots, \frac{1}{\varepsilon_n}\right]^{\mathrm{T}}$ is the corresponding precision parameters; $\mathbf{a}$, $\mathbf{b}$, c, and d are the shape and rate parameters of Gamma distributions.

By applying Bayes theorem, a hierarchical Bayesian model is established:

$$p\left(|\mathbf{w}, \boldsymbol{\alpha}, \sigma^2 \mid \mathbf{z}, \boldsymbol{\theta}\right) = \frac{p\left(|\mathbf{z}|\mathbf{w}, \sigma^2\right) p(|\mathbf{w}|\boldsymbol{\alpha}) p\left(|\boldsymbol{\alpha}|\mathbf{a}, \mathbf{b}\right) p\left(|\sigma^2|c, d\right)}{p(|\mathbf{z}|\boldsymbol{\theta})} \tag{8}$$

where $\boldsymbol{\theta} = \{\mathbf{a}, \mathbf{b}, c, d\}$ denotes the hyperparameters, $p\left(|\mathbf{w}, \boldsymbol{\alpha}, \sigma^2 \mid \mathbf{z}, \boldsymbol{\theta}\right)$ represents the joint posterior, and $p\left(|\mathbf{z} \mid \boldsymbol{\theta}\right)$ is the evidence (or marginal likelihood). Theoretically, the target variables $\left\{\mathbf{w}, \boldsymbol{\alpha}, \sigma^2\right\}$ should be estimated simultaneously by maximizing the joint posterior. However, it is a computational nontrivial task.

To render the problem tractable, a Gibbs sampler is applied to infer the conditional posterior distributions of individual variables. Since the specified distributions follow conjugacy, the conditional posteriors of all variables have the same distribution forms as their priors. Specifically, the derived conditional posteriors for the target variables are provided as follows:

$$\begin{aligned} p\left(|\mathbf{w} \mid \mathbf{z}, \boldsymbol{\alpha}, \sigma^2\right) &\propto \mathcal{N}\ \mathbf{w} \left| \left(\mathbf{\Phi}^{\mathrm{T}} \mathbf{\Phi} + \sigma^2 \mathbf{A}\right)^{-1} \mathbf{\Phi}^{\mathrm{T}} \mathbf{z}, \left(\sigma^{-2} \mathbf{\Phi}^{\mathrm{T}} \mathbf{\Phi} + \mathbf{A}\right)^{-1} \right. \\ p\left(|\boldsymbol{\alpha} \mid \mathbf{z}, \mathbf{w}, \mathbf{a}, \mathbf{b}\right) &\propto \prod_{i=1}^{n} \mathrm{Gamma}\left(|\alpha_i \middle| a_i + \frac{1}{2}, b_i + \frac{1}{2} w_i^2\right) \\ p\left(|\sigma^2 \mid \mathbf{z}, \mathbf{w}, c, d\right) &\propto \mathrm{Gamma}\left(|\frac{1}{\sigma^2} \middle| c + \frac{N}{2}, d + \frac{1}{2} \|\mathbf{z} - \mathbf{\Phi w}\|_2^2\right) \end{aligned} \tag{9}$$

where $\mathbf{A} = \mathrm{diag}(\boldsymbol{\alpha})$ is the diagonal precision matrix. The Gibbs sampler draws samples of each variable from the conditional posterior, with other variables fixed as their latest samples. The initial samples generated by the Gibbs sampler are typically unstable and deviated from the true values. Thus, a burn-in period $N_{burn} = 500$ is predefined, while the maximum sampling number is set to 2500.

As mentioned before, SBL may fail to remove irrelevant components, resulting in overfitted models. In the next section, the evidential thresholding approach is proposed to solve this issue.

Evidential thresholding

Evidence serves as an important indicator for assessing the plausibility of candidate models in the Bayesian model selection [9]. Inspired by this principle, the decoupled evidential contributions corresponding to the candidate components in the linear regression model are derived and employed as an indicator to evaluate the plausibility of each component. Thus, it can also be interpreted as component-wise Bayesian model selection. A probabilistic thresholding method, termed evidential thresholding, is then proposed to eliminate components with relatively small evidential contributions. The method is integrated into the SBL framework to enhance sparsity.

The nonlinear system to be identified is only associated with the coefficients $\mathbf{w}$. Consequently, the corresponding evidence is calculated by marginalizing out the coefficients from the likelihood and the prior:

$$p\left(|\mathbf{z} \mid \boldsymbol{\alpha}, \sigma^2\right) = \int_{\mathbf{w}} p\left(|\mathbf{z} \mid \mathbf{w}, \sigma^2\right) p\left(|\mathbf{w} \mid \boldsymbol{\alpha}\right) d\mathbf{w}. \tag{10}$$

After applying the Sherman-Morrison formula to separate the *i*-th component from the others, one can derive the logarithmic evidence as follows:

$$\begin{aligned} \ln p\left(|\mathbf{z} \mid \boldsymbol{\alpha}, \sigma^2\right) &= \ln p\left(|\mathbf{z} \mid \boldsymbol{\alpha}_{-i}, \sigma^2\right) + \mathcal{L}\left(\alpha_i\right), \\ \mathcal{L}\left(\alpha_i\right) &= \frac{1}{2}\left[-\ln\left(1+\frac{s_i}{\alpha_i}\right) + \frac{q_i^2}{\alpha_i + s_i}\right], \end{aligned} \tag{11}$$

where $s_i = {\boldsymbol{\Phi}_i}^{\mathrm{T}}\left(\mathbf{C}_{-i}\right)^{-1}\boldsymbol{\Phi}_i$ and $q_i = {\boldsymbol{\Phi}_i}^{\mathrm{T}}\left(\mathbf{C}_{-i}\right)^{-1}\mathbf{z}$, with $\mathbf{C}_{-i} = \sigma^2\mathbf{I} + \sum_{j\neq i}\varepsilon_j\boldsymbol{\Phi}_j{\boldsymbol{\Phi}_j}^{\mathrm{T}}$. $\ln p\left(|\mathbf{z} \mid \boldsymbol{\alpha}_{-i}, \sigma^2\right)$ represents the logarithmic evidence with the *i*-th component removed, while $\mathcal{L}\left(\alpha_i\right)$ denotes the decoupled contribution of the *i*-th component to the logarithmic evidence. The evidence can then be expressed as:

$$p\left(|\mathbf{z} \mid \boldsymbol{\alpha}, \sigma^2\right) = \exp\left[\mathcal{L}\left(\alpha_i\right)\right]\ p\left(|\mathbf{z} \mid \boldsymbol{\alpha}_{-i}, \sigma^2\right). \# \tag{12}$$

Eq. (12) shows that if the evidential contribution $\mathcal{L}\left(\alpha_i\right)$ is positive, including the *i*-th component will increase the evidence; conversely, if it is negative, the *i*-th component will decrease the evidence. This provides a criterion to select the candidate components, where the components with large positive evidential contributions should be included in the identified model. Additionally, it is found that the irrelevant components due to noise interference usually have relatively small evidential contributions, even though their coefficients may be large. Therefore, to avoid overfitting, the components with relatively small evidential contributions should also be eliminated. To better evaluate the relative contributions, the evidential contribution ratios are calculated as:

$$\mathcal{R}\left(\alpha_i\right) = \frac{\mathcal{L}\left(\alpha_i\right)}{\sum_{i=1}^{n}\mathcal{L}\left(\alpha_i\right)}. \tag{13}$$

The ratio is bounded as $\mathcal{R}\left(\alpha_i\right) \in [0, 1]$ and $\sum_{i=1}^{n}\mathcal{R}\left(\alpha_i\right) = 1$.

A threshold value for the evidential contribution ratio can then be defined to remove components with ratios smaller than it. Similar to SINDy, the threshold value is a hyperparameter that can significantly affect the results. However, since it is bounded, the threshold value is much easier to be defined compared to conventional thresholding techniques. The threshold value is empirically set to 10^{-4} in this paper.

The proposed Bayesian framework for nonlinear system identification is then constructed. Firstly, the GB-SBL is conducted to obtain a preliminary estimate of the system equation. Subsequently, evidential thresholding is performed to further eliminate irrelevant components. The updated coefficients are then used as initial values for the next iteration of the GB-SBL. This process is repeated until all evidential contribution ratios exceed the predefined threshold value.

Demonstration

Numerical 3-DOF nonlinear system

Firstly, a numerical 3-DOF nonlinear dynamical system, including two cubic stiffness springs and a Coulomb friction damper, as shown in Fig. 1, is applied to demonstrate the effectiveness of the proposed method. The linear mass, damping and stiffness coefficients are defined as: $m_i = 2,\ c_i = 2,\ k_i = 200$, for $i = 1,\ 2,\ 3$, while the nonlinear parameters are set to $k_{N1} = 100,\ K_{N2} = 200,\ C_{N1} = 4$. The third mass is excited by a harmonic input $P(t) = 200\sin(1.8\pi t)$. The system responses are measured at a sampling rate of 200 Hz for 150 seconds. The data are contaminated by Gaussian white noise with 3% standard deviation.

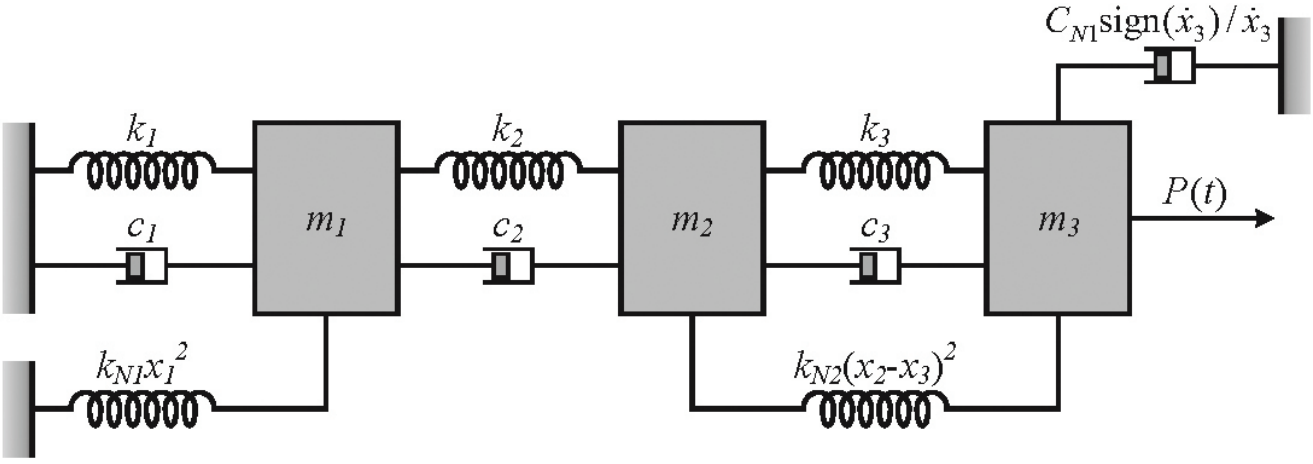

Fig. 1 Numerical 3-DOF nonlinear dynamical system

A dictionary including linear, second-order and third-order polynomials, sign function terms, absolute value terms, and inputs is constructed for the implementation of sparse regression. The time-domain responses of the identified system equation are presented in Fig. 2. It shows good agreement between the identified responses and the exact values.

The GB-SBL without evidential thresholding, RVM, and SINDy are also applied to identify the system for comparison. For brevity, only the results of the identified nonlinear terms are shown below, where the values in the brackets denote the standard deviations.

– Proposed method:

$$\mathbf{P_N}(\mathbf{t}) = \begin{bmatrix} -49.8\,(\pm 0.02)\,x_1^3 \\ -99.3\,(\pm 1.17)\,x_2^3 + 297.5\,(\pm 3.10)\,x_2^2x_3 - 296.7\,(\pm 2.75)\,x_2x_3^2 + 98.5\,(\pm 0.85)\,x_3^3 \\ 99.2\,(\pm 1.13)\,x_2^3 - 297.5\,(\pm 2.98)\,x_2^2x_3 + 297.1\,(\pm 2.53)\,x_2x_3^2 - 98.6\,(\pm 0.45)\,x_3^3 - 2.1\,(\pm 0.21)\,\text{sign}(\dot{x}_3) \end{bmatrix}$$

– GB-SBL without evidential thresholding:

$$\mathbf{P_N}(\mathbf{t}) = \begin{bmatrix} -49.8\,(\pm 0.02)\,x_1^3 + 1.2\,(\pm 0.15)\,x_2x_3 - 0.66\,(\pm 0.07)\,x_3^2 + 0.31\,(\pm 0.05)\,\text{abs}\,(x_2) + \ldots \\ -98.7\,(\pm 0.30)\,x_2^3 + 298.3\,(\pm 0.82)\,x_2^2x_3 - 297.3\,(\pm 0.78)\,x_2x_3^2 + 98.8\,(\pm 0.26)\,x_3^3 + 1.1\,(\pm 0.19)\,x_1^3 - 0.6\,(\pm 0.14)\,\text{abs}\,(x_3) + \ldots \\ 98.7\,(\pm 0.43)\,x_2^3 - 297.8\,(\pm 0.66)\,x_2^2x_3 + 296.8\,(\pm 1.42)\,x_2x_3^2 - 98.5\,(\pm 0.82)\,x_3^3 - 2.5\,(\pm 0.36)\,\text{sign}\,(\dot{x}_3) + 0.9\,(\pm 0.07)\,x_1^2 + \ldots \end{bmatrix}$$

– RVM:

$$\mathbf{P_N}(\mathbf{t}) = \begin{bmatrix} -49.8\,(\pm 0.02)\,x_1^3 + 2.7\,(\pm 0.19)\,x_2x_3 - 1.2\,(\pm 0.09)\,x_3^2 + 0.43\,(\pm 0.07)\,\text{abs}\,(x_2) + \ldots \\ -98.6\,(\pm 0.30)\,x_2^3 + 297.9\,(\pm 0.74)\,x_2^2x_3 - 298.6\,(\pm 0.70)\,x_2x_3^2 + 98.9\,(\pm 0.24)\,x_3^3 - 4.8\,(\pm 0.88)\,x_1^2 - 3.6\,(\pm 0.35)\,\text{x}_1x_2 + \ldots \\ 98.1\,(\pm 0.34)\,x_2^3 - 297.2\,(\pm 0.76)\,x_2^2x_3 + 298.1\,(\pm 0.65)\,x_2x_3^2 - 98.2\,(\pm 0.52)\,x_3^3 - 1.7\,(\pm 0.16)\,\text{sign}\,(\dot{x}_3) + 4.3\,(\pm 0.75)\,x_1^2 + \ldots \end{bmatrix}$$

– SINDy:

$$\mathbf{P_N}(\mathbf{t}) = \begin{bmatrix} -49.8x_1^3 \\ -97.4x_2^3 + 301.6x_2^2x_3 - 302.8x_2x_3^2 + 100.9x_3^3 + 22.9x_1^2x_2 + 18.5\text{x}_1x_2x_3 - 15.3x_1^2x_3 + \ldots \\ 98.2x_2^3 - 295.1x_2^2x_3 + 295.2x_2x_3^2 - 98.4x_3^3 - 2.21\text{sign}\,(\dot{x}_3) - 3.1x_1^2 + 3.8x_1x_2 - 1.8x_2x_3 + \ldots \end{bmatrix}$$

The results indicate that only the proposed approach successfully identified both the equation form and the parameters of the nonlinear dynamical system, while other methods failed due to the presence of redundant components in their identified models.

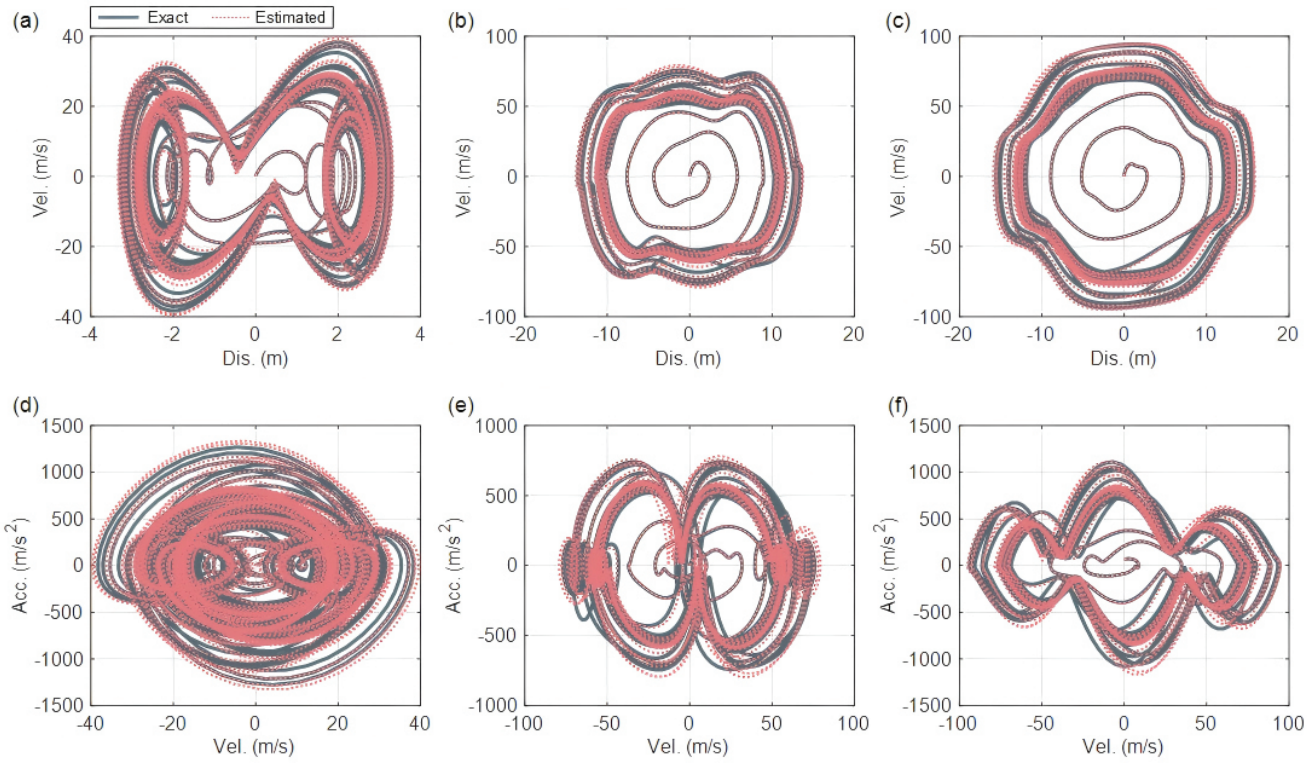

Fig. 2 The identified phase portraits of the numerical 3-DOF nonlinear dynamical system: (a) - (c) displacements and velocities of mass 1 - 3, (d) - (f) velocities and accelerations of mass 1 - 3

Experimental benchmark

An experimental benchmark of an electro-mechanical positioning system [10] is studied to further demonstrate the effectiveness of the proposed method in practical applications. The experimental setup is shown in Fig. 3, which represents a standard drive system of prismatic joints. The primary nonlinear component of the system results from friction. The detailed description of the system can be found in [10].



Fig. 3 Experimental setup of the electro-mechanical positioning system

The proposed method is applied to identify the governing equation of the system, in comparison with GB-SBL without evidential thresholding, RVM, and SINDy. The identified equations are listed in Table 1. The results indicate that the proposed method provided the most parsimonious equation of the system, while other methods identified more redundant components. However, compared to the reference model, it still includes a second-order polynomial term. It is not surprising, as the perfect Coulomb friction hardly exists in real applications [5]. The estimated accelerations are presented in Fig. 4, which correspond well to the measurements.

Table 1 The identified equation of the electro-mechanical positioning system

Reference	$\ddot{y}(t) = 0.033 - 2.140\dot{y}(t) - 0.214\text{sign}(\dot{y}(t)) + 0.370P(t)$
Proposed method	$\ddot{y}(t) = 0.014\left(\pm 2.2 \times 10^{-4}\right) - 2.146\left(\pm 3.6 \times 10^{-3}\right)\dot{y}(t) + 2.465\,(\pm 0.02)\,\dot{y}^2(t)$ $-0.213\left(\pm 3.2 \times 10^{-4}\right)\text{sign}(\dot{y}(t)) + 0.369(\pm 1.24 \times 10^{-4})P(t)$
GB-SBL	$\ddot{y}(t) = 0.020\left(\pm 3.4 \times 10^{-4}\right) - 0.077\,(\pm 0.01)\,y(t) - 2.166\left(\pm 5.5 \times 10^{-3}\right)\dot{y}(t) + 0.156\,(\pm 0.04)\,y^2(t)$ $+0.310(\pm 0.03)y(t)\dot{y}(t) + 2.454\,(\pm 0.04)\,\dot{y}^2(t) - 0.214\left(\pm 3.0 \times 10^{-4}\right)\text{sign}(\dot{y}(t))$ $+0.367(\pm 1.23 \times 10^{-4})P(t)$
RVM	$\ddot{y}(t) = 0.020\left(\pm 3.4 \times 10^{-4}\right) - 0.078\,(\pm 0.01)\,y(t) - 2.165\left(\pm 5.1 \times 10^{-3}\right)\dot{y}(t) + 0.165\,(\pm 0.04)\,y^2(t)$ $+0.299(\pm 0.03)y(t)\dot{y}(t) + 2.455\,(\pm 0.04)\,\dot{y}^2(t) - 0.214\left(\pm 3.3 \times 10^{-4}\right)\text{sign}(\dot{y}(t))$ $+0.368(\pm 1.26 \times 10^{-4})P(t)$
SINDy	$\ddot{y}(t) = 0.020 - 0.082y(t) - 2.164\dot{y}(t) + 0.180y^2(t) + 0.297y(t)\dot{y}(t) + 2.465\dot{y}^2(t) - 0.214\text{sign}(\dot{y}(t))$ $+0.368P(t)$

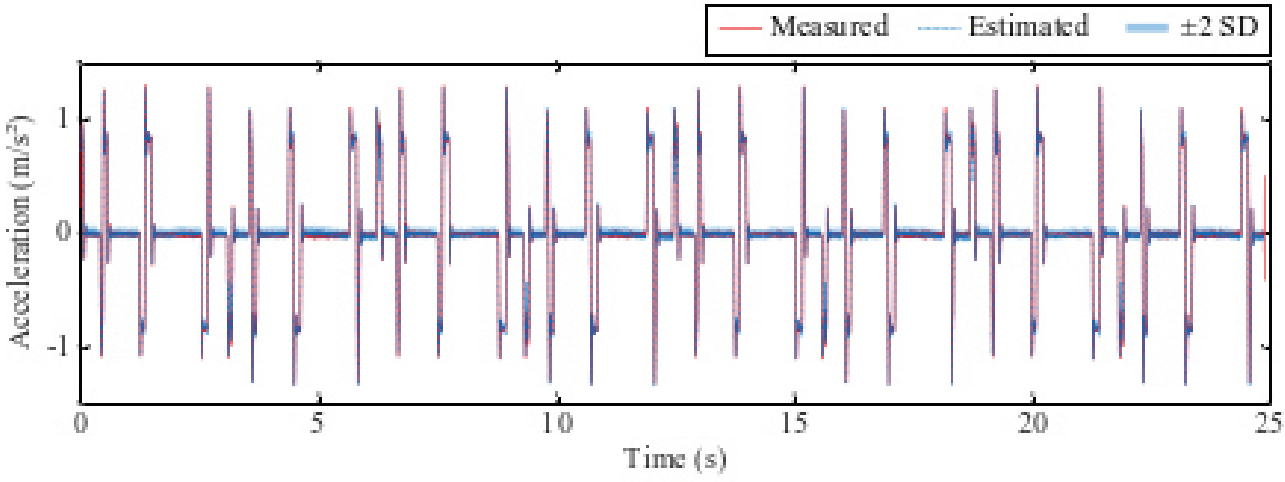

Fig. 4 The estimated accelerations with double standard deviation

Conclusion

Existing sparse identification methods for nonlinear dynamical systems commonly suffer from overfitting due to the presence of redundant components. To address this issue, this paper proposes a probabilistic thresholding technique, referred to as evidential thresholding, which is cooperated with GB-SBL to enhance the sparsity of the identified model. Firstly, the formulation of GB-SBL is briefly introduced. Subsequently, the theoretical foundation of the proposed evidential thresholding is derived. Instead of removing candidate components with small coefficients, evidential thresholding evaluates the decoupled evidential contribution of each component and eliminates those with negligible contributions. This approach can also be interpreted as a component-wise Bayesian model selection technique. It avoids circumstances where the correct components are falsely removed due to their small coefficients, while the irrelevant components with large coefficients are still retained in the model. Evidential thresholding is then integrated into GB-SBL to form the proposed Bayesian method for nonlinear dynamical system identification. A numerical example and an experimental benchmark have been studied to verify the effectiveness of the proposed method, which demonstrates its superiority over SINDy, RVM, and GB-SBL without evidential thresholding.

Acknowledgments Jiawei Jian gratefully acknowledges the support of the China Scholarship Council. The authors acknowledge the support of KU Leuven Internal Funds.

References

1. Kerschen G, Worden K, Vakakis A F, et al. Past, present and future of nonlinear system identification in structural dynamics. Mechanical systems and signal processing, 2006, 20(3): 505-592.
2. Noël J P, Kerschen G. Nonlinear system identification in structural dynamics: 10 more years of progress. Mechanical Systems and Signal Processing, 2017, 83: 2-35.
3. Brunton S L, Proctor J L, Kutz J N. Discovering governing equations from data by sparse identification of nonlinear dynamical systems. Proceedings of the national academy of sciences, 2016, 113(15): 3932-3937.
4. Tipping M E. Sparse Bayesian learning and the relevance vector machine. Journal of machine learning research, 2001, 1(Jun): 211-244.
5. Fuentes R, Nayek R, Gardner P, et al. Equation discovery for nonlinear dynamical systems: A Bayesian viewpoint. Mechanical Systems and Signal Processing, 2021, 154: 107528.
6. Chatterjee T, Shaw A D, Friswell M I, et al. Sparse Bayesian machine learning for the interpretable identification of nonlinear structural dynamics: Towards the experimental data-driven discovery of a quasi zero stiffness device. Mechanical Systems and Signal Processing, 2023, 205: 110858.
7. Hirsh S M, Barajas-Solano D A, Kutz J N. Sparsifying priors for Bayesian uncertainty quantification in model discovery. Royal Society open science, 2022, 9(2): 211823.
8. Sun L, Huang D, Sun H, et al. Bayesian spline learning for equation discovery of nonlinear dynamics with quantified uncertainty. Advances in neural information processing systems, 2022, 35: 6927-6940.
9. Beck J L, Yuen K V. Model selection using response measurements: Bayesian probabilistic approach. Journal of Engineering Mechanics, 2004, 130(2): 192-203.
10. Janot A, Gautier M, Brunot M. Data set and reference models of EMPS. Nonlinear system identification benchmarks, 2019.

Chapter 8
Measurement and Visualization of Nonlinear Vibration Response Using Neuromorphic Event-Based Sensing

Gabriella Gallegos, DaJae Doral, Suzanna Gilbert, Deborah Fowler, Fernando Moreu, Benjamin Moldenhauer, and Tariq Khraishi

Abstract Accurately capturing full-field vibration responses provides valuable insight for understanding nonlinear structural dynamic behavior, particularly in systems with large deflections, contact interactions, or bolted joints. However, when it comes to monitoring nonlinear systems, traditional sensors have limitations like limited spatial coverage and constraints on sensor channels, which can make it difficult to capture the full complexities of the system. In this research, we propose using neuromorphic event-based cameras to capture high-resolution, low-latency, and asynchronous data for structural responses of a nonlinear system in a laboratory setting. The test structure, consisting of a wing with an attached pylon, exhibits nonlinear behavior. This behavior is driven by impacts that occur between the attachment blocks of the pylon structure during the dynamic response. Using a neuromorphic event-based camera the full pylon structure was imaged. Using post-processing techniques, a region of interest within the images can be selected. These regions of interest enable the extraction of dynamic response from various areas of the structure using a single data set. This study compares vibrational responses from modal expansion results, accelerometer data, and neuromorphic event-based sensing data of the structure. The results of each method were comparable, supporting the development of advanced structural monitoring techniques using neuromorphic event-based sensing suited for low-latency applications such as vibration control and digital twin implementations.

Keywords Neuromorphic imaging · Event-based sensor · Region of interest (ROI) · Modal expansion · Nonlinear dynamics · Accelerometers · Asynchronous sensing.

Introduction

An understanding of the vibrational behavior of structures is necessary to predict their performance and failure. In industry, there is a significant focus on studying linear behavior of structures as robust tools exist for such characterization. Many structures exhibit significant nonlinear vibration responses due to large deflections, contact between parts, nonlinear material properties, or other sources of nonlinear physics. This nonlinearity can have a significant effect on the performance of these structures. Thus, this study is motivated by investigating the challenging task of characterizing nonlinear structural responses.

Gabriella Gallegos · Fernando Moreu · Tariq Khraishi
University of New Mexico, MSC01 1070, 1 University of New Mexico, Albuquerque, NM 87131
e-mail: ggallegos6@unm.edu; fmoreu@unm.edu; khraishi@unm.edu

DaJae Doral
New Mexico Institute of Mining and Technology, 801 Leroy Place, Socorro, NM, 87801
e-mail: dajae.doral@gmail.com

Suzanna Gilbert
Brigham Young University, 350 Engineering Building, Provo, UT 84602
e-mail: gsuzi26@byu.edu

Deborah Fowler · Benjamin Moldenhauer
Sandia National Laboratories, 1515 Eubank Blvd. SE, Albuquerque, NM 87123
e-mail: dfowler@sandia.gov; bmolden@sandia.gov

© The Author(s), under exclusive license to River Publishers 2026

Kristin B. Zimmerman, PhD (eds.), *Nonlinear Structures & Systems, Vol. 1*, Conference Proceedings of the Society for Experimental Mechanics Series, https://doi.org/10.13052/rp-9788743814122

Conventionally, analogue sensors like piezoelectric accelerometers have been used to measure structural responses. These sensors are limited by their invasive nature, with mass-loading effects often modifying the dynamic behavior of the structure. Additionally, they are difficult to implement on thin features and/or unsmooth surfaces and only provide a local measurement. Contactless measurement techniques such as laser doppler vibrometers (LDV), and digital image correlation (DIC) have also been used conventionally and can provide a more global measurement of structural responses. LDVs are comparable in their accuracy to accelerometers but are costly and are limited to discrete measurement points, requiring a time-intensive repetitive test procedure when a full-field response is required. DIC produces high accuracy, full-field characterization, but involves structure surface preparation, requires the use of expensive high-speed cameras for capturing dynamic events, and is computationally expensive, requiring extensive post-processing to achieve response data.

An emerging type of optical sensor, neuromorphic event-based sensors are characterized by their ability to capture high resolution, low-latency data with micro-second range temporal resolution [1]. Unlike traditional cameras, these sensors only detect changes in light intensity. When the change in light intensity across a given pixel on the sensor is over the determined threshold, data is recorded. These changes are recorded as asynchronous "events" and occur on a pixel-by-pixel basis. Light intensity shifts can occur on the surface of a structure due to displacement. This detection of displacements can be used for vibration response studies. Some studies have been conducted using neuromorphic sensors for measuring the vibrational responses of cantilever beams [2–3], objects on a shaker table, and a speaker diaphragm [4]. This work proposes the use of neuromorphic sensors to study a more complex, nonlinear structure. This study investigates the use of neuromorphic sensors to capture light intensity shifts of a nonlinear structure and resolve frequency responses which can change drastically with response amplitude in systems exhibiting nonlinear behavior. Various processing techniques were used to isolate and resolve various frequency responses of different regions of interest using a single data set. In addition to resolving frequency response, the structure was visualized using frame reconstruction techniques.

Approach

Three methods were used in this study to measure the nonlinear response of a wing-pylon structure: (1) accelerometers, (2) neuromorphic sensing, and (3) a modal expansion technique.

Experimental Set-Up for Vibration Tests

The structure under investigation in this study is comprised of a wing-shaped plate secured to a large aluminum block on one end, with a pylon attached to the opposite tip. The pylon consists of two upper blocks, a narrow strip running down the center of the blocks, and a lower block attached to the bottom of the strip as shown in Figure 1.

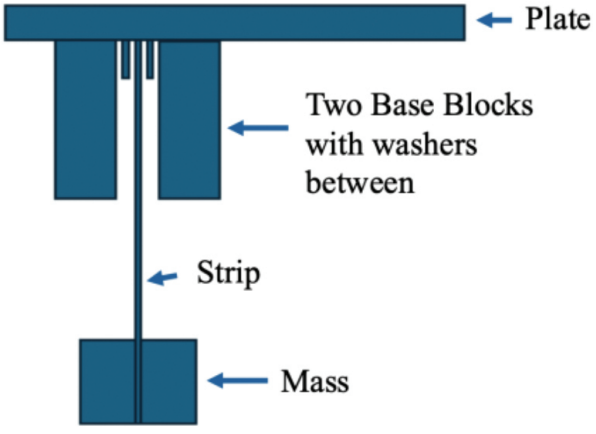

Fig. 1 Schematic of pylon structure

The entire structure was suspended using bungee cords to simulate free-free boundary conditions. A mesh of 24 uniaxial accelerometers was attached to the wing plate, block and pylon. A load cell was attached to the underside of the wing plate at the drive point, and a floor-mounted shaker was attached to the load cell. Force and acceleration responses were recorded by Siemens Testlab [5] and a Simcenter SCADAS Mobile data acquisition system. A neuromorphic camera (DVXplorer Mini by Inivation) was mounted to a tripod and pointed directly at the pylon from a distance of a few centimeters. Data from

the camera was collected using the DV software [6]. The wing-plate structure, pylon, and experimental setup are shown in Figure 2.

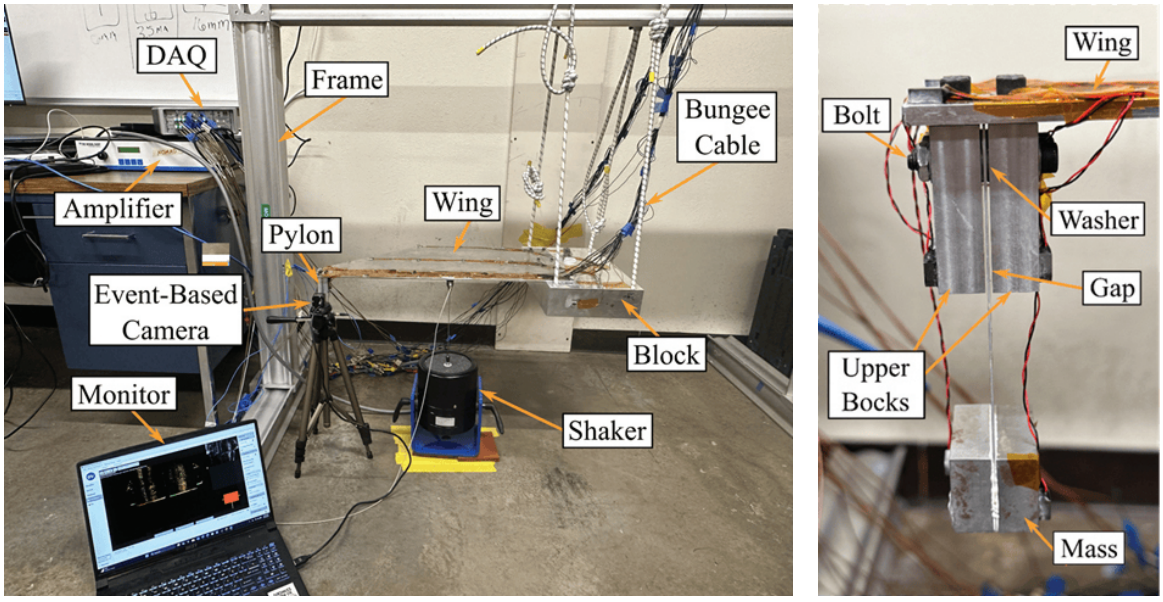

(a) (b)

Fig. 2 Experimental setup (a) and close-up of pylon structure (b)

The goal of this testing was to excite motion in the pylon at large enough amplitudes to cause contact to occur between the pylon strip and upper blocks. Then, both accelerometer and neuromorphic sensor measurements were taken to investigate if these sensors could measure the onset of contact. The structure was driven near resonance of a mode that induces large deflection of the pylon strip (∼94 Hz) via constant sine excitation for a period of 20 seconds. This was repeated at four different forcing levels: 1.9, 4.8, 5.5 and 5.7 N. The two lower force levels did not induce contact between the strip and upper blocks, and the two upper force levels did induce contact. Note, the driving frequency was not adjusted as the excitation level increased, because the mode of interest was known to not experience a significant frequency shift within the amplitude range observed. At each force level, data was recorded simultaneously with both the accelerometers and the event-based camera.

Event-Based Sensing

The camera used in this study was an event-based sensor by Inivation, the DVXplorer Mini. Event-based sensors are differentiated from conventional camera sensors by their ability to record asynchronous data in the form of "events" based on changes in light intensity rather than uniform frames of light intensities. Each event has an associated time stamp, x and y pixel coordinate, and a positive or negative polarity. An event is detected based on a light intensity change threshold. When a change in light intensity occurs over a given pixel that is greater than the defined threshold, an event at that location is generated. The event is positive or negative depending on if the light intensity increased or decreased. As the structure is vibrating, positive and negative events are generated and exported into a data stream. Using this data stream and processing techniques, the frequency behaviors of the structure can be resolved.

Results and Analysis

Camera post-processing

Due to data being collected asynchronously, event-based data packages require unique processing techniques. The neuromorphic sensor captured the entirety of the pylon structure during each experiment in this study. To characterize the frequency behavior of specific areas of the pylon structure, event-based data was parsed into smaller packages. This data parsing was done by creating regions of interest (ROIs) defined by sensor pixel dimensions. For each ROI, only events generated within

the bounds of the region are considered in the analysis. To define a ROI, event frame reconstruction is conducted. This process involves using the positive events measured over a determined time frame of recorded data. By mapping all of the positive events in their respective pixel locations in white, an image of the structure can be constructed. This image is used to hand-select a rectangular region of interest on the structure and resolve the corresponding dimensions in pixels of the area. Figure 3 features images of the pylon using a conventional camera on the left, while the frame using reconstructed events is shown on the right. For this work, four ROIs were selected to correspond to the accelerometer locations, a fifth ROI is positioned on the strip, and a sixth ROI is placed at the contact point. ROI #2 is shown with a box in Figure 3, at the location of one of the accelerometers. A key novelty of this approach is the ability to select ROIs based on engineering judgment, allowing the analysis to focus on critical structural features rather than being restricted to predefined sensor positions.

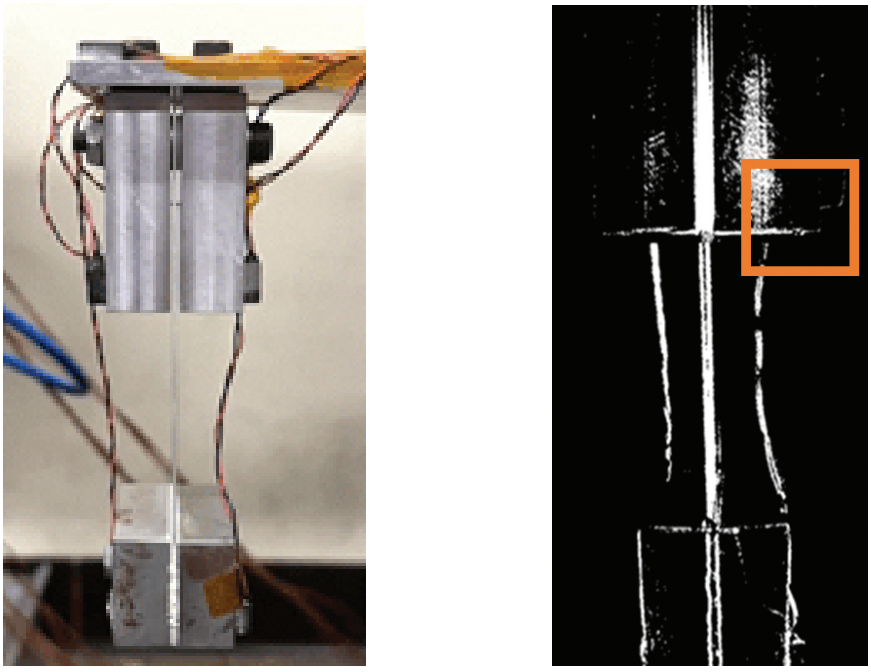

(a) (b)

Fig. 3 Image of pylon structure using a conventional camera (a) and frame reconstruction from positive event accumulation, with a box around ROI #2 (b).

With the region of interest selected, three post-processing methods were compared: time binning, event clustering, and Lomb-Scargle spectral analysis [7]. Time binning creates a time-series signal from event counts within each time bin, event clustering groups events into clusters, and Lomb-Scargle handles non-uniformly sampled data sets. Event clustering was chosen for analysis as the method resulted in clearer spectral peaks.

Comparison of Results from Accelerometers, Event-Based Sensor and Expansion

The three methods used in this study, accelerometer responses, event-clustering of neuromorphic sensor data, and modal expansion [8], are compared by overlaying the FFTs, as shown in Figure 4. These results are all from ROI #2, pictured in Figure 3, which covers one of the accelerometer locations. All three methods capture the same major frequency components: the driving frequency and a harmonic of the driving frequency. The magnitudes shown are normalized, as the camera post-processing method did not involve converting to physical units. The left graph in Figure 4 shows the results from the lowest-force test before the onset of contact (1.9 N), where contact is defined by auditory observation during the test; the right plot shows the results from the 5.5 N test, during which contact was occurring. The case where contact was not observed still shows harmonic behavior at twice the drive frequency – this indicates that there was an additional source of nonlinear behavior, possibly the bolted joint nonlinearity, large deflection of the pylon, or even the beginnings of contact that were not yet audible. When contact audibly occurs, the FFTs show richer harmonic content. Strong harmonic behavior at 0.5x, 1.5x and 2x the driving frequency can be clearly seen by all three observation methods; this indicates that the nonlinearity resulting from the contact behavior is observable using the neuromorphic sensing method. The harmonic behavior at 0.5x the driving frequency could represent either a subharmonic resonance, or a period-doubling bifurcation

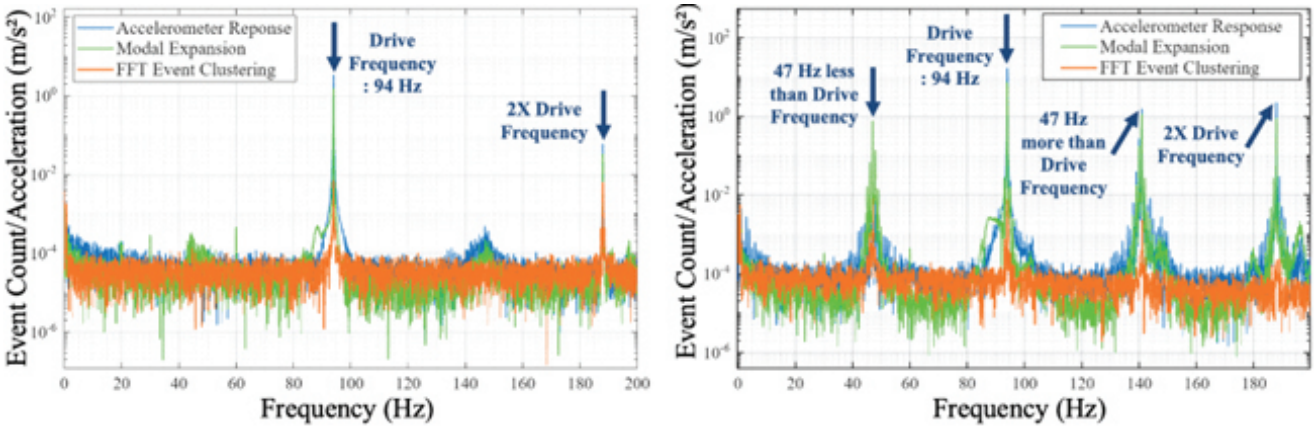

Fig. 4 FFTs of the accelerometer response, event-clustering and modal expansion results for ROI #2. The left plot is from the 1.9 N test where no contact is observed audibly, and the right plot is from the 5.5 N test where contact occurs.

In addition to quantitative data, the neuromorphic sensor is characterized by its ability to visually represent the structure. There is a noticeable increase in events observed on the structure when there is contact occurring compared to when there is no contact, as shown in Figure 5; this is likely due to the increased displacement in the case where contact occurs, resulting from the increased forcing amplitude as well as the contact behavior itself.

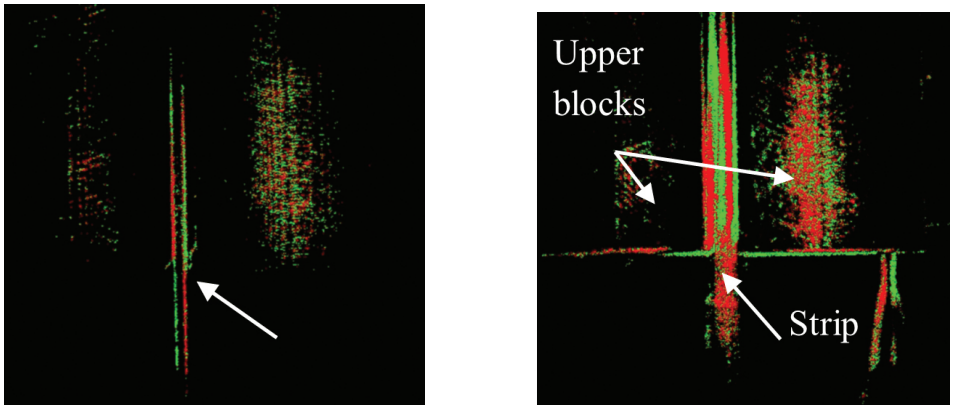

(a) (b)

Fig. 5 Positive (green) and negative (red) event accumulation frames without contact (a) and with contact (b).

Conclusion

This work demonstrates that neuromorphic event-based sensors can provide comparable frequency response results to traditional accelerometers and modal expansion techniques when measuring nonlinear vibration response data. Multiple post-processing methods for event-based data can be used to capture the frequency domain: time binning, event clustering, and Lomb-Scargle spectral analysis. Additionally, the event stream from the camera can be visually captured through event accumulation, offering an alternative way to observe response behavior. The ability to define regions of interest based on engineering judgment further strengthens the approach, allowing the analyst to focus on structural features most relevant to their application. These findings highlight the potential of neuromorphic sensing as a low-latency, non-contact sensor for structural vibration analysis and dynamic behavior characterization.

Acknowledgments This research was conducted at the 2025 Nonlinear Mechanics and Dynamics Research Institute hosted by Sandia National Laboratories and the University of New Mexico.

We would like to acknowledge the support from Bill Flynn at Siemens and Rob Warmbold at Polytec for providing experimental equipment and software to equip the laboratories at NOMAD.

* *Sandia National Laboratories is a multimission laboratory managed and operated by National Technology & Engineering Solutions of Sandia, LLC, a wholly owned subsidiary of Honeywell International Inc., for the U.S. Department of Energy's National Nuclear Security Administration under contract DE-NA0003525. SAND2025-12420C*

This paper describes objective technical results and analysis. Any subjective views or opinions that might be expressed in the paper do not necessarily represent the views of the U.S. Department of Energy or the United States Government.

This work was supported by the Laboratory Directed Research and Development program at Sandia National Laboratories, a multimission laboratory managed and operated by National Technology and Engineering Solutions of Sandia LLC, a wholly owned subsidiary of Honeywell International Inc. for the U.S. Department of Energy's National Nuclear Security Administration under contract DE-NA0003525

References

1. Lakshmi A, Chakraborty A, Thakur CS. Neuromorphic vision: From sensors to event-based algorithms. *WIREs Data Mining Knowl Discov*. 2019
2. Dorn, Charles, et al. "Efficient full-field vibration measurements and operational modal analysis using neuromorphic event-based imaging." *Journal of Engineering Mechanics*, vol. 144, no. 7, July 2018
3. Davis, Allison, et al. "Digital Twins for Photorealistic Event-Based Structural Dynamics: COM." *Taylor & Francis*, Taylor & Francis, 8 Aug. 2025
4. C. Shi et al., "Event-Based Vibration Frequency Measurement With Laser-Assisted Illumination Based on Mixture Gaussian Distribution," in IEEE Transactions on Instrumentation and Measurement, vol. 72, pp. 1-13, 2023
5. "Simcenter Testlab MIMO FRF Testing." Accessed September 17, 2025.
6. "DV — Inivation 2025-08-05 Documentation." Accessed September 17, 2025.
7. "Plomb - Lomb-Scargle Periodogram - MATLAB." Accessed September 17, 2025.
8. O'Callahan, J. (**1989**). "System Equivalent Reduction Expansion Process," Proc. 7th Int. Modal Anal. Conf., Bethel, CT.

Chapter 9
Reduced-Order Modeling of Loosening of Two Bolted Joints Considering Shock Excitation

William Jordan, Caleb Munger, Kaitlyn Vigil, Keegan J. Moore, Brittany Ouellette, Keith Tschohl, and Sean T. Kelly

Abstract Loosening of bolted joints can significantly alter the dynamics of an assembled structure when subject to operational loading environments, potentially leading to decreased efficiency or structural failure. As such, modeling this behavior is crucial to ensure long-term structural health and safe operation. While existing modeling approaches have been developed that capture the loosening of a single bolted joint, many of these approaches have relied on high-fidelity finite element models or approximate analytical techniques. In either case, these methods can struggle to generalize to structures containing many bolted joints due to underlying method assumptions and/or becoming computationally infeasible. To address these drawbacks, a novel reduced-order model (ROM) capturing the underlying dynamics of bolted-joint loosening was developed by one of the authors and experimentally validated for systems with a single bolted joint considering both axial and transverse shock excitation. This ROM has also been used to theoretically study a system with two serially connected bolted joints. In pursuit of extending this ROM's use for structures with multiple bolted joints, this work sought to expand its experimental validation and empirically study its applicability for a system with two bolted joints undergoing loosening. The system under consideration is a modified box assembly with removable component (mBARC), with both U-channels removed and the rectangular bar connected directly to the box assembly (BA). Initial experimental efforts include roving hammer modal analyses of: 1) the BA alone, and 2) the mBARC varying the preload in both bolted joints of interest. These results are used to inform linear finite element model validation and ROM parameter identification efforts. Next, experiments using high-energy shock excitation are performed to: 1) demonstrate bolt-loosening dynamics, 2) inform ROM application, and 3) compare with phenomena seen in previous studies. Lastly, conclusions regarding the applicability of this ROM to predict the system's dynamics as a function of bolt preload are provided.

Keywords Bolt loosening · Nonlinear dynamics · Reduced-order modeling · Modal testing · Finite element modeling

William Jordan
School of Civil Engineering and Environmental Science, The University of Oklahoma
e-mail: william.d.jordan-1@ou.edu

Caleb Munger
Department of Mechanical Engineering, Rose-Hulman Institute of Technology
e-mail: mungerct@rose-hulman.edu

Kaitlyn Vigil
Department of Mechanical Engineering, The University of New Mexico
e-mail: kvigil85@unm.edu

Keegan J. Moore
Daniel Guggenheim School of Aerospace Engineering, Georgia Institute of Technology
e-mail: kmoore@gatech.edu

Brittany Ouellette · Keith Tschohl · Sean T. Kelly
Los Alamos National Laboratory
e-mail: britt@lanl.gov; ktschohl@lanl.gov; stkelly@lanl.gov

*William Jordan, Caleb Munger, and Kaitlyn Vigil contributed equally to this work.

© The Author(s), under exclusive license to River Publishers 2026

Kristin B. Zimmerman, PhD (eds.), *Nonlinear Structures & Systems, Vol. 1*, Conference Proceedings of the Society for Experimental Mechanics Series, https://doi.org/10.13052/rp-9788743814122

Introduction

Bolted joints are a widely used fastening method in assembled structures due to their ease of use and versatility. However, due to a variety of factors arising from environmental loading experienced by an as-assembled structure, loosening of bolted joints may occur. This loosening can significantly change the structure's dynamics, potentially leading to joint or complete structural failure [1]. This makes accurate modeling and identification of bolted-joint loosening in as-assembled structures paramount to ensure safe operation and structural health over the structure's lifetime. As such, efforts to model and understand bolt-loosening dynamics have increased in recent decades, with applications ranging from playground equipment to aircraft carriers. In particular, developing an accurate *predictive* modeling framework is of interest to preemptively mitigate or prevent structural failures resulting from bolted-joint loosening.

Although bolt loosening can be caused by a variety of factors such as corrosion [2], relative thread sliding [3], stress relaxation [4], and axial loading [5], one primary cause of loosening is transverse excitation perpendicular to the axial bolt orientation [6, 7]. These factors, individually or together, can cause a change in bolt preload, which here is the physical phenomenon used to describe the degree of loosening that has occurred from an initial state.

Current predictive modeling frameworks for bolt loosening often use: 1) analytical approximations, and/or 2) computationally expensive finite element model (FEM) simulations [1, 8]. Analytical methods often require a large number of simplifying assumptions and are limited to (relatively) simple assembly configurations such as single-bolt connections [9]. As greater computing power has become more readily available, the use of detailed, high-fidelity FEMs to model bolt-loosening dynamics has increased [10, 11]. However, these studies require fine meshes, specifically around threads, to sufficiently capture loosening behavior. As a result, using such techniques for FEMs of assembled structures with hundreds or thousands of bolts would make the model prohibitively large, and thus infeasible to use. To address these challenges, reduced-order models (ROMs) seek to bridge the gap between analytical models and high-fidelity FEMs. In particular, often after: 1) identifying computationally, and/or 2) experimentally determining bolt-loosening parameters, ROMs seek to simulate the dynamics of bolted-joint loosening with the accuracy of FEMs but at the speed of analytical models [12]. Here, the ROM developed by Moore [13] is considered, which approximates a bolted joint as a single nonlinear time-dependent spring with stiffness that is a function of bolt torque or preload.

To empirically study bolt-loosening dynamics, many experimental setups have been developed that: 1) relate bolt preload as a function of torque, 2) explore bolt-loosening regimes under varying excitations (e.g., impact/shock or harmonic), and/or 3) study time-varying bolt stiffness based on modal testing [1, 9, 14]. This work primarily focuses on the last point to use the ROM developed by Moore in [13] for a high-energy shock excitation. Even for systems with a single bolted connection, an equivalent time-varying bolt stiffness can be difficult to predict across the lifespan of a bolt as different types of excitations and environments can additively contribute to cause bolt loosening [13]. This difficulty is further confounded for structures with multiple bolted joints as such structures can exhibit nonlinear, time-dependent responses that result from dynamic interactions between multiple joints [1].

Given the range of dynamics observed theoretically in previous work [1] and unlike previous experimental efforts applying the ROM developed by Moore [13] (which considered a single bolt), this work sought to: 1) extend this ROM's applicability to a structure with multiple bolted joints, and 2) empirically explore the effects of varying bolt preload and the degree of bolt loosening when considering two bolted connections and shock excitation. Similar to the system presented in [1], for the structure considered here which is a fixed-base modified box assembly with removable component (mBARC), a single component (i.e., the bridge or rectangular bar) serves as the primary source of coupling between the attachment locations on the box assembly (BA) (i.e., the blades). Working toward these goals, first, roving hammer modal testing with low-energy impacts was performed for the BA alone to inform initial BA-alone FEM validation efforts, in particular to characterize the fixed-base boundary condition (BC). Next, the bridge was added and a series of mBARC-specific modal tests was performed still considering low-energy impacts. From these tests, the natural frequencies of the mBARC were extracted as the preload was increased for two bolts of interest. These data were used for mBARC FEM validation efforts, with these efforts now primarily focusing on identifying parameters associated with the bolted connections between the bridge and blades. Following these modal tests, a series of high-energy impacts for shock excitation analyses was performed. For all high-energy impacts, along with measuring preload change in time, the wavelet transform (WT) of measured accelerometer response data was used to qualitatively assess the (transient) nonlinearity of the system's dynamics by demonstrating how the system's natural frequencies change as a function of time. To ensure: 1) no loosening occurred during modal testing, 2) preload loss resulting from the considered range of shock excitations was localized to bolts of interest, and 3) sufficient test repeatability, load washers were added on all bolted connections, including those associated with the fixed-base BC. Based on what were found to be necessary requirements to validate the mBARC FEM accounting for preload changes, results and discussion concerning the ROM's applicability are presented.

Methods

Initially, an FEM and ROM were created and validated for the BA alone to provide model confidence by ensuring: 1) alignment with experimental results from BA-alone modal testing, and 2) the bolted fixed-base BC was correctly modeled. The ROM at this stage consisted of developing a reduced-order representation of the BA using Craig-Chang component mode synthesis (CC-CMS). After completing model validation of the full-order and reduced-order systems of the BA alone, the bridge was added along with bushing elements to create the mBARC FEM, with the bushing elements representing the bolted connections between the blades and bridge. This FEM was then validated against experimental natural frequencies extracted from roving hammer modal testing of the mBARC for varying preload conditions with bolt preloads varied symmetrically. Nonlinearities were discovered as the bolt preloads were increased, manifesting as changes in the contact area between the blades and bridge. Thus, dedicated analyses studying the effect of contact area around bridge-to-blade bolted connections within the mBARC FEM were conducted and are discussed in the Results and Discussion section. Shock testing was then performed for a range of high-energy impact excitations in a specific location and direction of interest. Lastly, based on modeling and experimental results, the applicability of the ROM of interest (here, that developed by Moore in [13]) and effects of preload loss/variation were determined and conclusions made. Figure 1 shows a flowchart of these steps.

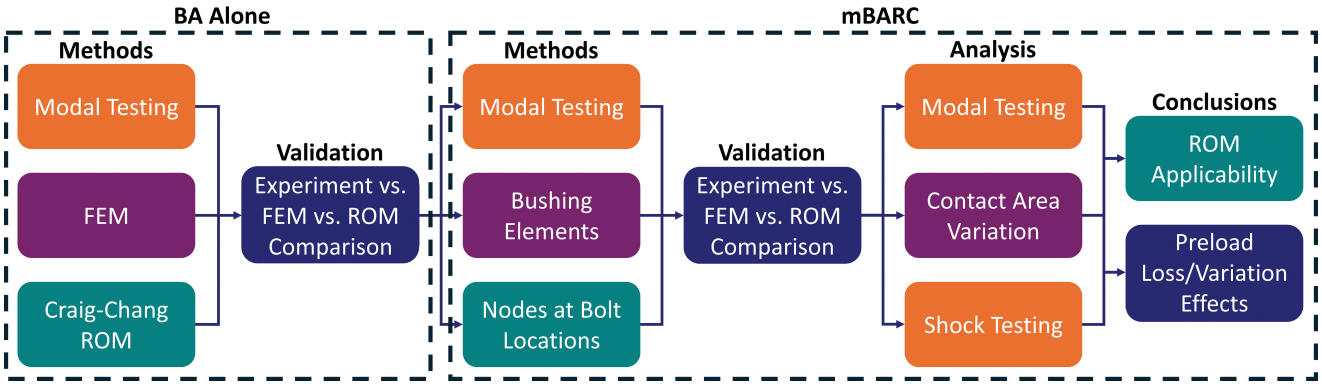

Fig. 1 Testing and analysis flowchart consisting of experimental (), FEM (), ROM (), and additional () steps

Experimental Apparatus

BA and mBARC Setup

The nominal BA of the experimental apparatus is composed of a six-inch side length by three-inch depth by quarter-inch wall thickness square hollow section of aluminum 6061 stock. There is a half-inch wide cutout removing the entire depth of the wall centered along one of the side lengths creating cantilevers on the left and right side of the structure, referred to here as the left and right blades, respectively. For this work, the BA is bolted to an optical breadboard using four 1/4-20 inch fasteners. Adding the rectangular bar (i.e., the bridge), which is also manufactured from aluminum 6061, to the BA completes the mBARC setup and introduces coupling across the (nominally) symmetric blades. Figure 2 shows the experimental setup of the BA alone, and Fig. 3 shows the assembled mBARC. Note that the bridge is bolted to the BA using 10-32 fasteners through the center holes in the group of five holes on each blade (one fastener per blade).

It was found that the BA is sensitive to even minor asymmetries in the fixed-base BC, resulting in large natural frequency differences between the two blades (e.g., experimentally, $>10\%$ difference was achievable in the first natural frequency of each blade). To mitigate the effects of any asymmetry, washers (not shown) were added between the base of the BA/mBARC and the optical breadboard to ensure a constant contact area and BC confidence. The addition of these washers significantly reduced the frequency differences between the blades, and this setup was used to validate the bolted connections at the base of the BA-alone FEM before modeling the mBARC.

Roving Hammer Modal Testing

Initial roving hammer modal testing was conducted on the BA alone to characterize the structure before the bridge was installed and to validate the fixed-base BC in the BA-alone FEM. All impact locations and directions used for this modal testing are shown in Fig. 4. This set of locations and directions remained consistent for both BA-alone and mBARC modal testing. When possible, impact excitations along the global X, Y, and Z axes at each location were considered. However,

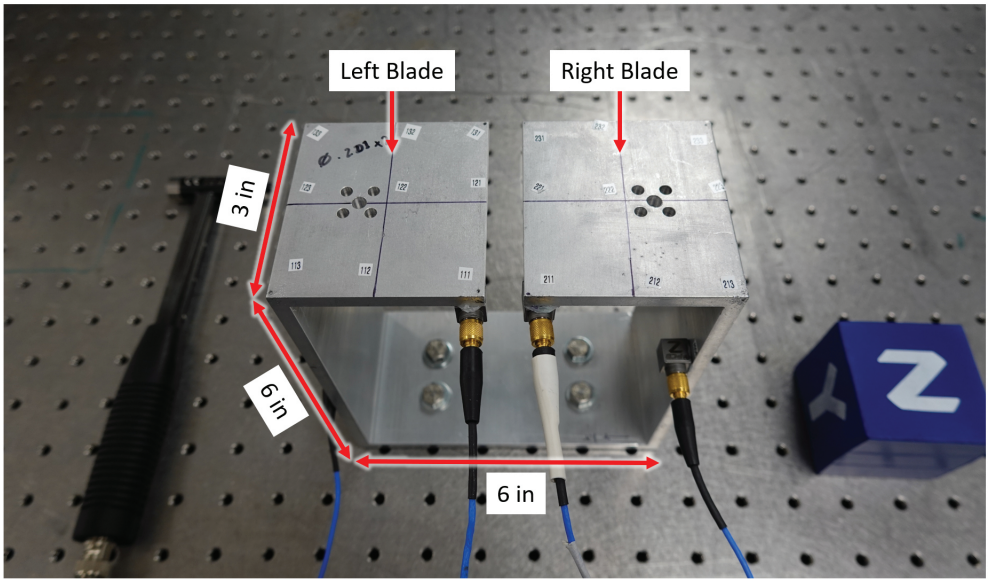

Fig. 2 Front view of the BA alone with all triaxial accelerometers applied

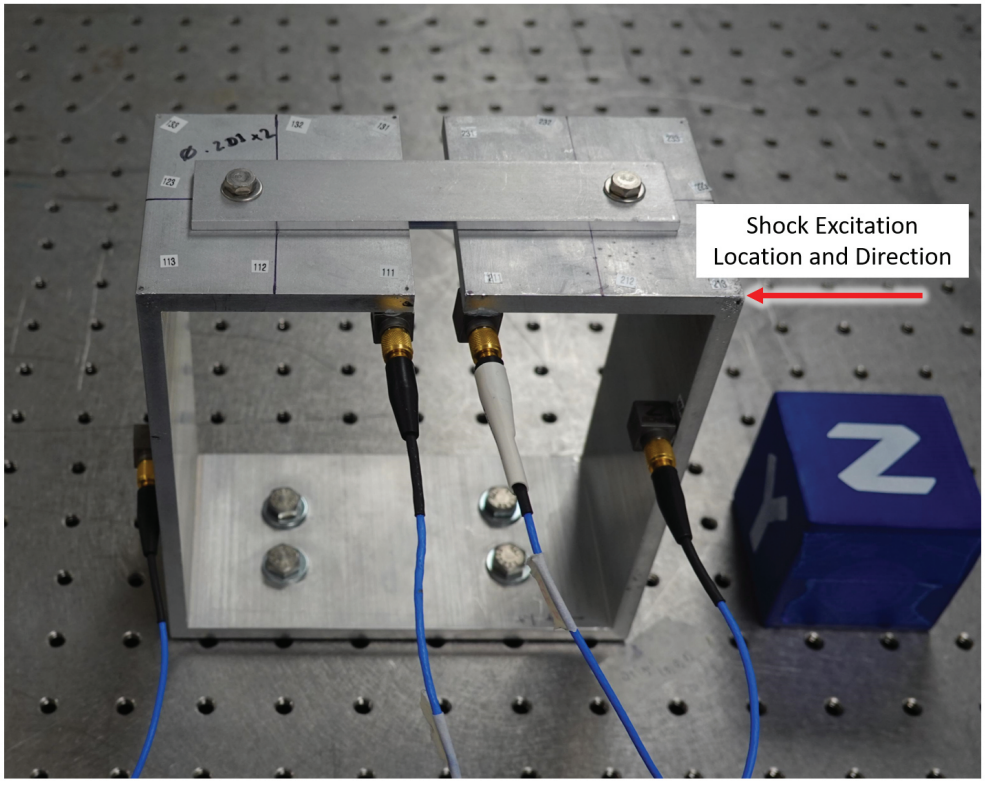

Fig. 3 Front view of the mBARC with all triaxial accelerometers applied. Shock excitation location and direction indicated

several locations could only be excited along one or two axes due to physical constraints of the hammer and/or not having access to a given excitation direction. In total, there were 12 impact locations with (collectively) 28 impact directions.

Multiple types of modal hammers and modal tips were experimented with to determine the hammer-tip combination that produced the cleanest signal. Due to the (relatively) high frequency content and response amplitudes of the BA, the blade edges would respond much quicker than was physically possible to withdraw the hammer during testing, making it challenging to avoid multiple impacts. To resolve this issue, a custom tip was created for the PCB 086C01 impact hammer

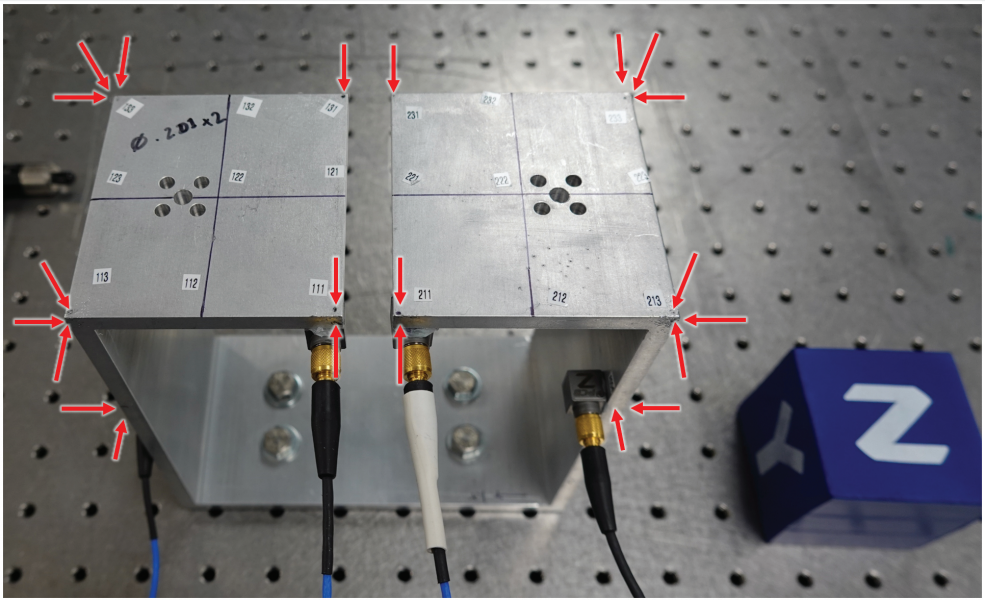

Fig. 4 BA and mBARC roving hammer modal testing impact locations and directions. Two locations and six directions are hidden in the view shown. All impact locations and directions are symmetric about the X-Z midplane

from a set screw and vinyl cap as shown in Fig. 5. This tip expedited BA-alone modal testing by reducing double impacts that often resulted from using harder tips. The PCB 086C03 impact hammer with the PCB 084B04 white, medium nylon tip (no vinyl cap) was sufficient to conduct modal testing on the mBARC and excite higher frequencies without double impacts as the bridge adds structural rigidity. The custom modal tip had a 10 dB roll-off at approximately 600 Hz, and the PCB 084B04 medium nylon tip had a 10 dB roll-off at approximately 1500 Hz. The frequency range of 0–600 Hz contains the first four symmetric modes (i.e., mode pairs) of the BA, and was deemed sufficient for initial BA-alone FEM validation. For the mBARC, the first six system modes were of interest, all of which whose natural frequencies lie below 800 Hz. Thus, the medium nylon tip was used and deemed sufficient.



Fig. 5 Custom modal hammer tip exploded and assembled view

Shock Excitation Testing

During shock excitation testing, the mBARC was impacted at the top right corner in the +Y direction as shown in Fig. 3. For all presented analyses, the bridge-to-blade bolts and their respective load washers to measure preload are labeled F1 and F2, where F2 is closest to the shock, and F1 is furthest from the shock. Figure 6 shows these bolts and their respective load washers on the mBARC. In addition, load washers were added to the four bolts connecting the mBARC to the optical breadboard. The preloads of these bolts were held constant at approximately 7000 N and monitored to ensure they did not loosen during both modal and shock testing. Throughout all testing, the four bolts at the base never loosened.

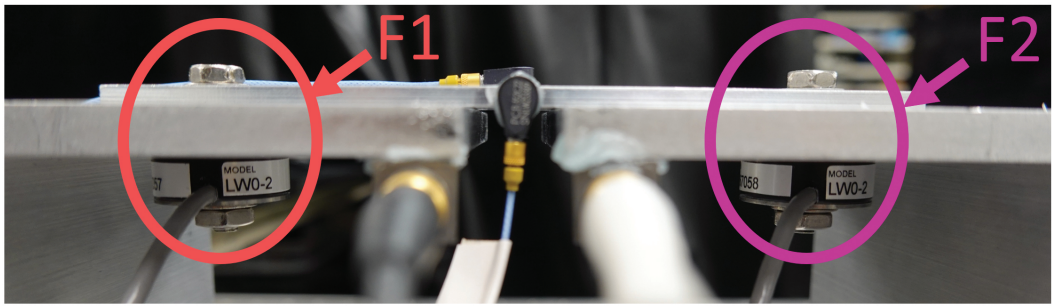

Fig. 6 Close-up view of the bridge on the mBARC with bolts F1 and F2 indicated

Modeling Methods

Finite Element Model

An FEM was iteratively developed to match the experimental apparatus and to be used with the ROM presented in [13]. Figure 7 shows the FEM of the mBARC used in this work (mesh not shown for image clarity). Abaqus/CAE 2024 software was used for all FEM development and analyses. The full mBARC FEM consisted of 33,156 quadratic hexahedral elements (type C3D20R) and 169,721 nodes.

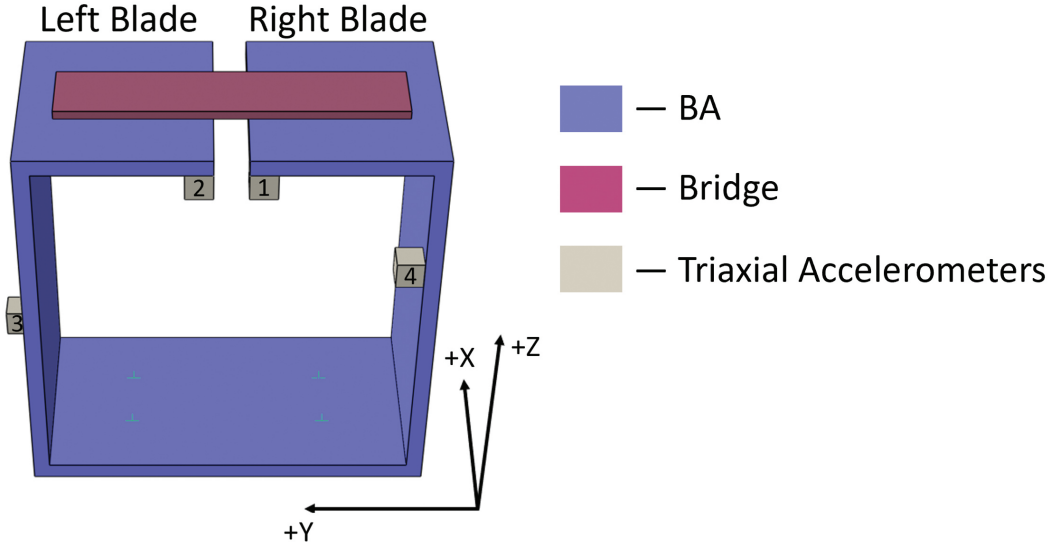

Fig. 7 Front view of the mBARC FEM assembly (mesh not shown for image clarity) with all triaxial accelerometers applied. In practice, all accelerometers were modeled as point masses

Fasteners and bushing elements were used to match experimental and FEM BCs. Specifically, fasteners were used for the fixed-base BC, where the fastener models the clamped volume approximation of the region of influence of a bolted joint [15]. The fastener constraint in Abaqus/CAE creates a specified continuum coupling region and encastres the nodes in the region to the center, which is similar to the clamped volume approximation [15]. Because the natural frequencies of the BA-alone FEM were sensitive to the size of the fastener constraints' continuum coupling regions, this size was changed until the BA-alone FEM sufficiently matched BA-alone experimental results. The experimental and final BA-alone FEM natural frequencies are shown in Table 1.

A six degree-of-freedom (DOF) bushing element was used between the bridge and each of the blades at the F1 and F2 bolt locations to model each bolt. The bushing element has an axial X, Y, and Z stiffness and rotational X, Y, and Z stiffness that can be independently varied when validating the mBARC FEM against experimental natural frequencies. However, as will be discussed, constraints that either: 1) are physically motivated, and/or 2) leverage empirical sensitivities will be added to these axial and rotational stiffness values to reduce the search space for model validation. Figure 8 shows where in the

FEM the bushing element was placed for the left blade (a similar element was added for the right blade) and how the bushing element DOFs are defined.

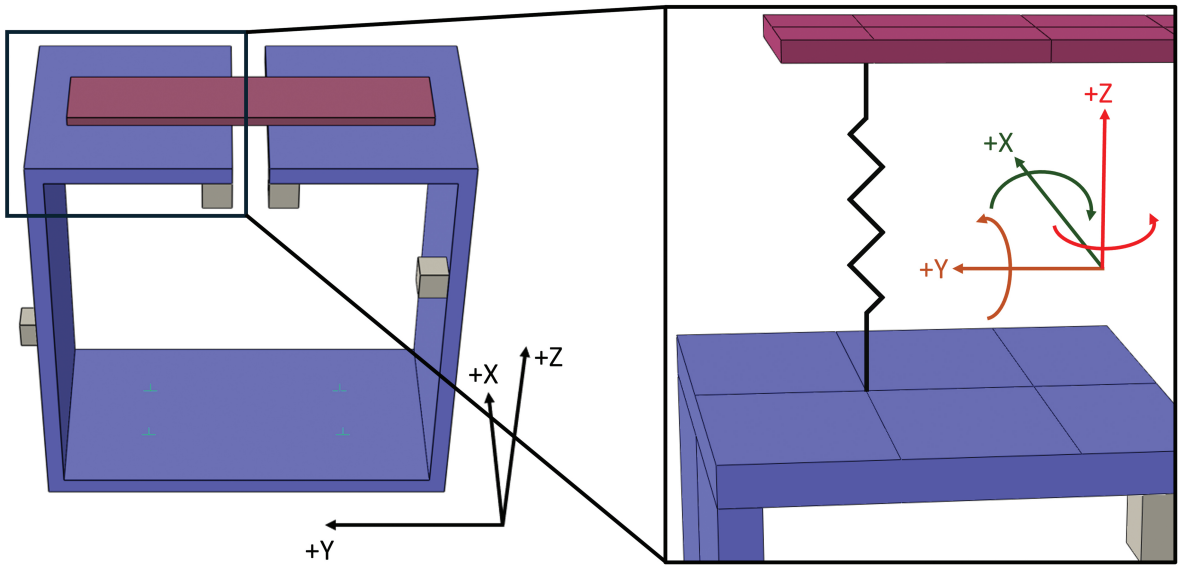

Fig. 8 Visualization of the bushing element in the mBARC FEM for the left blade, which has 3 axial DOFs and 3 rotational DOFs

In addition to changing the stiffness values of the bushing elements, the influence radius of the continuum coupling where each bushing element connects to the bridge and respective blade was changed. Changing the influence radius is an analog to changing the contact area in the experimental setup. Figure 9 shows an example of how the influence radius is specified, with all nodes within the influence radius (i.e., the participating nodes) coupled with a continuum coupling constraint.

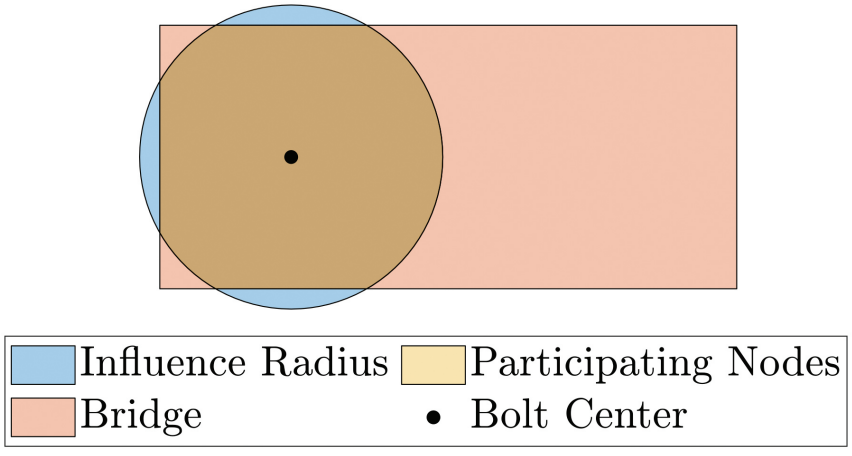

Fig. 9 Example influence radius of a bushing element. The participating nodes are coupled with a continuum coupling constraint, distributing the force over the area defined by the participating nodes

The bushing elements' stiffness values and contact areas were chosen as tunable model parameters as they can be related to physical attributes that could be changed in the experimental mBARC setup. For example, the stiffness could be changed by tightening bolts F1 and F2, and the contact area could be changed due to either bowing of the bridge or the addition of washers between the blades and bridge (discussed further in the Results and Discussion section). As shown in the ROM Applicability section, allowing the contact area and Z rotational stiffness of each bushing element to change was crucial to match experimental results.

Reduced-Order Model

The fundamental idea of the ROM introduced in [13] is that a bolted joint can be modeled as a spring with stiffness $k(T)$ that depends on the instantaneous bolt torque T (here, to be replaced with tension/preload). This model is given in Eq. 1 as:

$$k(T) = k_a \left[1 - \left(1 - \left(\frac{T}{T_m}\right)^{\alpha}\right)^{\beta}\right], \tag{1}$$

where k_a is the maximum possible stiffness, T_m is the theoretical maximum tension/preload, and α and β are dimensionless fitting parameters.

Note that torque was the metric previously used when this ROM was first developed. However, this model was transitioned in [16] to be based on tension. In addition, though the term preload is used throughout this paper, this is similar to the tension metric used in the version of this ROM in [16], and is thus used interchangeably here. Identification of the parameters $k_a = k(T_m)$, α, and β for a single bolt includes three steps. The first step involves conducting modal analyses of the structure at varying bolt preload values. Next, for a given preload, the stiffness of the bolted-joint connection is adjusted in the FEM to align with experimental natural frequencies. This process is repeated for various preloads to produce stiffness-tension (or stiffness-preload) pairs. Lastly, a curve-fitting procedure is then applied using Eq. 1 to identify α and β. k_a and T_m are estimated based on the point where increasing the torque (here, preload) no longer changes the system natural frequencies as this indicates the maximum possible stiffness achievable by the bolted connection has been reached.

This ROM was initially developed for a threaded joint of a split-Hopkinson pressure bar, where the ROM was shown to accurately model the dominant effects of bolt loosening on the dynamic response [13]. Because the impact force and threaded joint were aligned with the longitudinal axis of the bar, the stiffness $k(T)$ of the threaded joint acted only along the longitudinal axis. Therefore, torque only needed to be related to the stiffness along one direction. For the structure considered here, however, the stiffness of bolts F1 and F2 acts in multiple directions. This called for expansion of the ROM to consider multi-direction effects that influence loosening where 1:1 stiffness-torque (or stiffness-tension) pairs are not as readily applicable. In addition, it is important to note this ROM assumes all loosening behavior can be captured by varying stiffness values alone. For brevity, only a summary of this ROM is provided here; however, a comprehensive overview is provided in [13].

Model Validation

As discussed in the Roving Hammer Modal Testing section, the first model validation step was matching the fixed-base BC of the BA alone to the experimental setup. To do so, the bridge was removed from the FEM (Fig. 7, but without the bridge) to reduce model complexity and match the setup shown in Fig. 2. For the BA alone, the natural frequencies of the FEM ($f_{n,FEM}$) have good agreement with the experimental natural frequencies ($f_{n,Exp}$), with all FEM natural frequencies being within 3% for the first eight system modes (i.e., the first four mode pairs resulting from inherent system symmetry). Table 1 shows a comparison of the BA-alone FEM and experimental natural frequencies, with the highest absolute percent error being 2.85% for mode 6.

Table 1 BA-alone FEM and experimental natural frequencies, and absolute percent error in natural frequencies from FEM to experiment

Mode	$f_{n,FEM}$ [Hz]	$f_{n,Exp}$ [Hz]	Absolute % Error
1	98.983	100.23	1.24
2	99.680	100.57	0.88
3	205.13	204.45	0.33
4	206.20	205.45	0.37
5	439.88	429.17	2.50
6	**442.36**	**430.12**	**2.85**
7	478.38	483.67	1.09
8	484.55	475.20	1.97

After validating the fixed-base BC, the bridge was added to the FEM and sensitivity studies conducted using WAVES [17], a Python-based tool that interfaces with Abaqus/CAE and allows for the automation of parametric studies. The Z rotational stiffness and the X and Y axial stiffness values of the bushing elements were varied to study how those stiffness values impacted the mBARC FEM natural frequencies. It was assumed the bolts were symmetric, so the bushing elements were made symmetric (i.e., respective stiffness values in each bushing element were assumed equal). In addition, the X and

Y rotational stiffness values and Z axial stiffness value were held constant at 10^8 N-m/rad and 10^8 N/m, respectively, to prevent the bridge and blades from phasing through each other and mitigate non-physical contact phenomena. These values were chosen by estimating the aluminum 6061 material stiffness when subjected to a deformation/penetration load, though ultimately the modes of interest had little to no sensitivity with respect to these values when sufficiently high to mitigate non-physical contact. The X and Y axial stiffness values were also always assumed equal, as they represent orthogonal tangential directions on the contact surface. Figure 10 shows surface plots of the natural frequencies of modes 1 and 2 as these stiffness values are changed. As shown, the natural frequencies of modes 1 and 2 change by less than 5% over the searched region. This lack of sensitivity is important when fitting the model to experiment, since if the first two natural frequencies lie outside the ranges spanned in Fig. 10, then other model parameters not associated with the bushing element stiffness values need to modified (e.g., see the Contact Area Variability section).

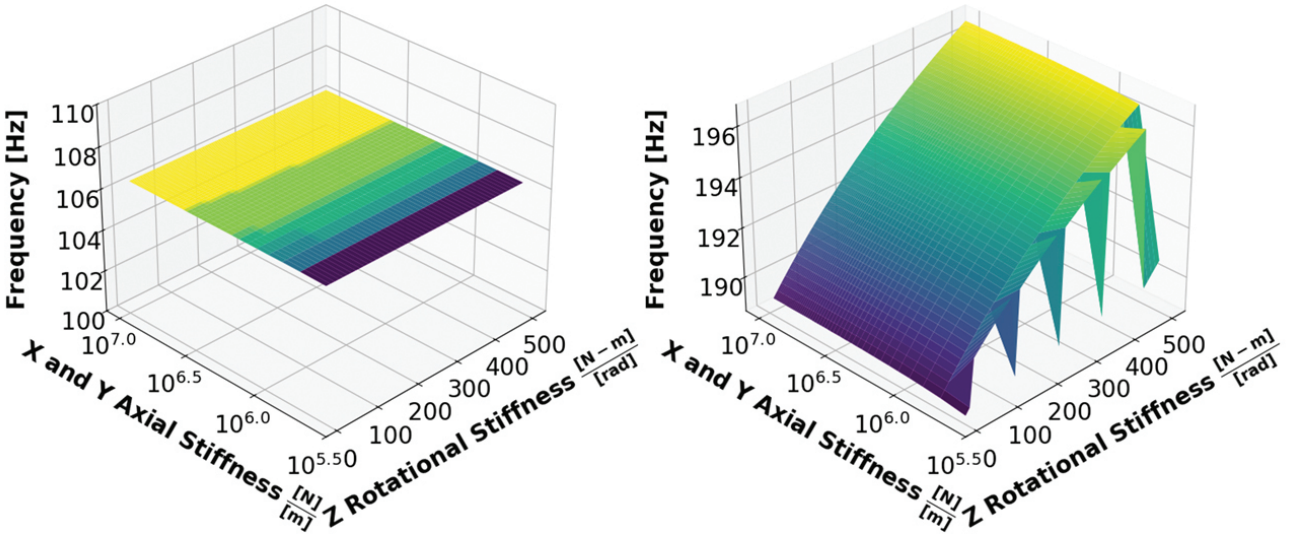

Fig. 10 Natural frequency of (left) mode 1 and (right) mode 2 as the X and Y axial and Z rotational stiffness values are varied. Both frequencies change by less than 5% over the searched region

Similarly, Fig. 11 shows the natural frequencies of modes 4 and 5 as a function of these stiffness values. As shown, the natural frequencies rapidly increase and then plateau as the X and Y axial stiffness values are increased, with minimal

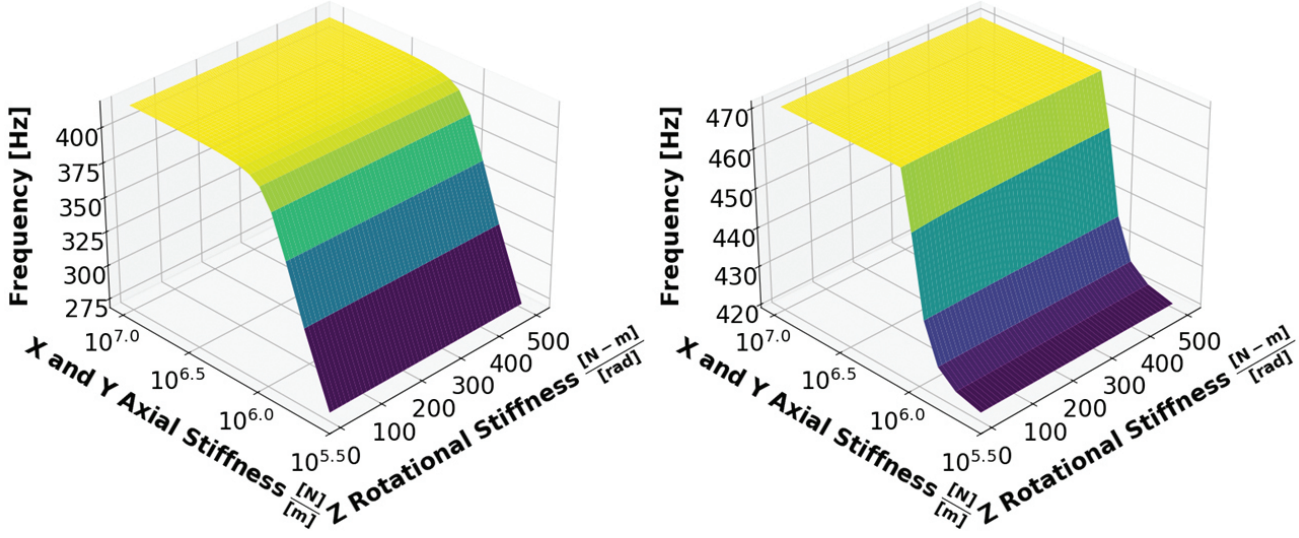

Fig. 11 Natural frequency of (left) mode 4 and (right) mode 5 as the X and Y axial and Z rotational stiffness values are varied. Both frequencies stop changing when the X and Y axial stiffness values are above $10^{6.5}$ N/m

changes resulting from variation in the Z rotational stiffness. Thus, it is clear modes 4 and 5 are almost entirely dictated by the X and Y axial stiffness values.

Figure 12 shows how the natural frequency of mode 3 changes as these stiffness values change. As shown, the natural frequency steadily increases as the Z rotational stiffness is increased, and has little sensitivity with respect to the X and Y axial stiffness values except for low values near $10^{5.5}$ N/m.

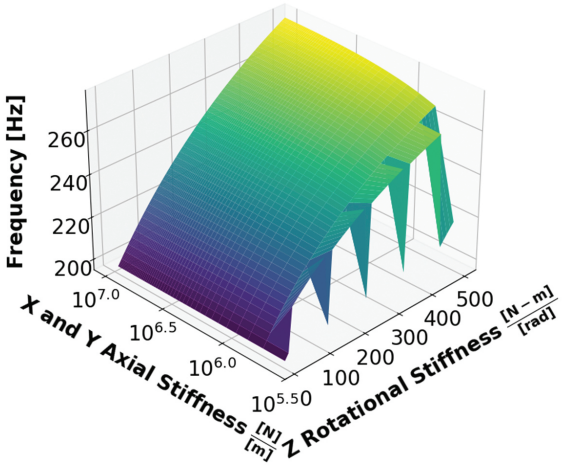

Fig. 12 Natural frequency of mode 3 as the X and Y axial and Z rotational stiffness values are varied. The frequency is primarily dictated by the Z rotational stiffness

The surface plots in Figs. 10–12 were used to tune the mBARC FEM, specifically to determine bushing element stiffness values for different preload values as required for the ROM discussed in the Reduced-Order Model section.

The last parameter in the mBARC FEM that was tuned was the bushing element influence radius. As discussed in the Finite Element Model section, the influence radius controls the simulated contact area between the bridge and each blade. Figure 13 shows how the mBARC FEM natural frequencies for modes 1–6 change as the normalized contact area is varied. A normalized value of 1 means the entire overlapping surface area of the bridge and corresponding blade is in full contact,

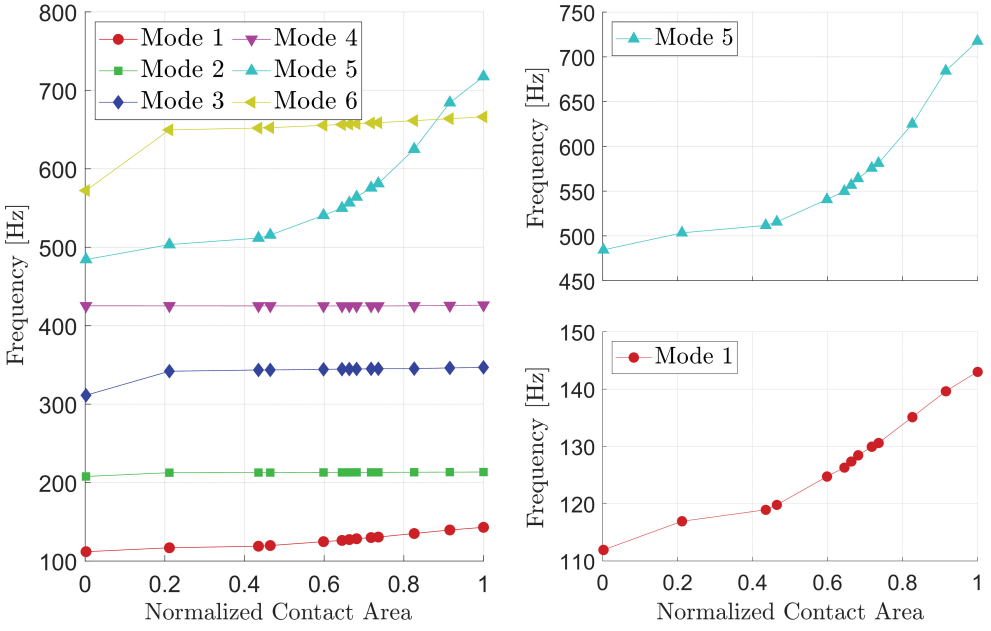

Fig. 13 (left) mBARC FEM natural frequencies for modes 1–6 as the bushing element normalized contact area is changed, with zoomed-in plots of (top right) mode 5 and (bottom right) mode 1. Modes 1 and 5 are most impacted by the changing contact area

with all nodes at the interfaces (as illustrated in Fig. 9) constrained by the bushing element. Conversely, a normalized value of 0 means the bridge and blade are not in contact at all.

As will be shown, changing the contact area was required to match the experimental natural frequencies across the range of preloads considered, as it was found that modifications to bushing element stiffness values alone were insufficient, even considering the range of values shown in Figs. 10–12. Further discussion regarding this requirement is provided in the Contact Area Variability section.

Results and Discussion

The results from this study are presented as follows. First, experimental modal analysis results for the mBARC varying the preload in bolts F1 and F2 are presented. Next, the variation of the contact area between the bridge and blades in the experimental mBARC and FEM is discussed, specifically motivating why such variability explains – and in the FEM was necessary to match – experimental trends. This is followed by results considering high-energy shock excitation to induce bolt loosening. Lastly, a discussion regarding the applicability of the proposed ROM for the mBARC system is provided.

mBARC Modal Analyses

To characterize the interface stiffness between the bridge and blades of the mBARC, separate roving hammer modal tests of the mBARC were performed as the preload in bolts F1 and F2 was simultaneously changed from 200 N to 3000 N. Figure 14 shows the experimental natural frequencies for modes 1–6 at each preload value considered in this range.

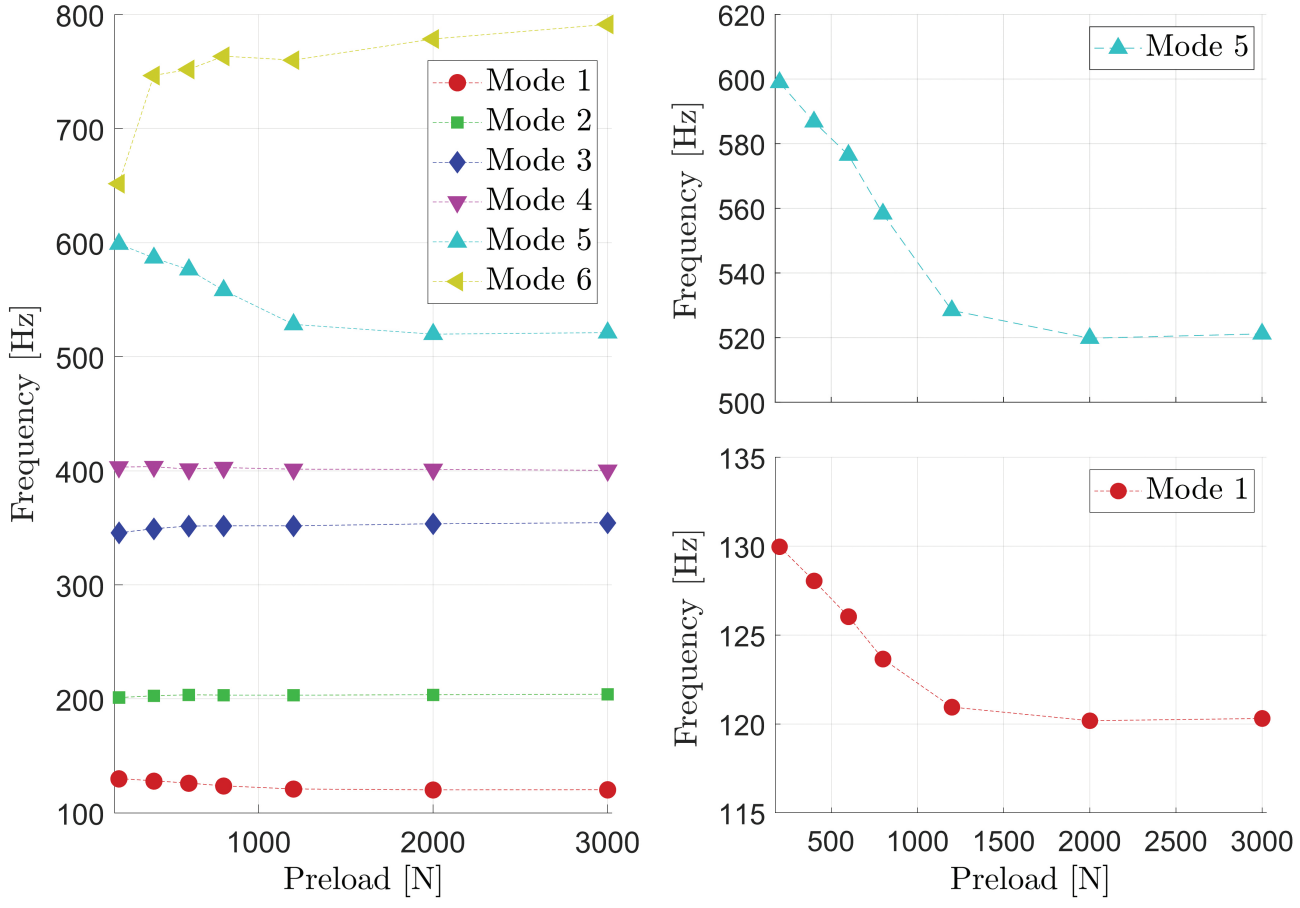

Fig. 14 (left) Experimental mBARC natural frequencies for modes 1–6 as the preload in bolts F1 and F2 was varied from 200 N to 3000 N. Zoomed-in plots of (top right) mode 5 and (bottom right) mode 1. The frequencies of modes 1 and 5 decrease as the preload increases

As shown in Fig. 14, as the preload is increased, the natural frequencies of modes 1 and 5 decrease. Though one may typically expect natural frequencies to increase if not remain constant as preload is increased, after further investigation, it was found that this discrepancy is because the contact area between the bridge and the blades was changing as the preload increased. This was due to bowing of the bridge, thereby decreasing the contact area. As shown in Fig. 13, as the contact area is increased, the natural frequencies of modes 1 and 5 increase, supporting the hypothesis that as the preload is increasing the contact area is decreasing in the experimental mBARC.

Contact Area Variability

To experimentally test the hypothesis that the contact area between the bridge and the blades was changing with preload, a washer was placed between the bridge and each blade of the mBARC for bolts F1 and F2. These added washers are shown in Fig. 15.

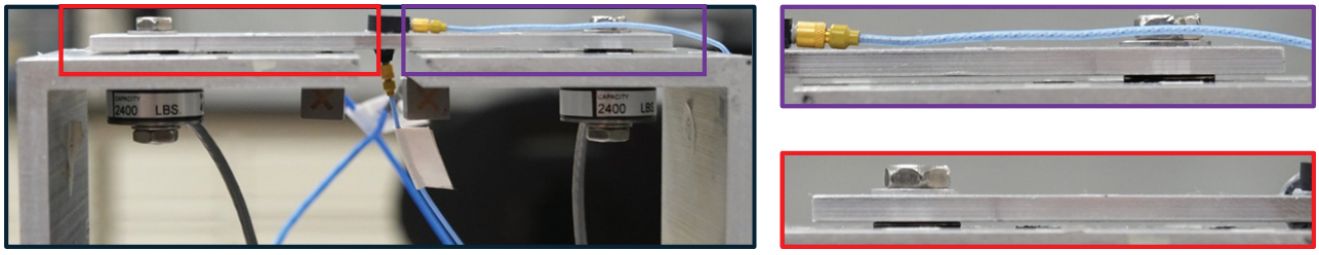

Fig. 15 (left) mBARC experimental setup with a washer added between the bridge and (top right) right and (bottom right) left blades to prevent the contact area from changing with varying preload

Adding a washer between the bridge and each blade ensures a more deterministic, constant contact area such that at all preload values the contact area remains the same. Modal analyses of the mBARC were then performed again for each considered preload to determine the new natural frequencies, which are shown in Fig. 16 overlaid with the natural frequencies from Fig. 14.

Figure 16 demonstrates the effect of adding the washers on the natural frequencies of modes 1–6, and in particular, modes 1, 5, and 6. Regarding mode 6 specifically, when analyzing the measured frequency response functions (FRFs) of the mBARC at preload values less than 1200 N, mode 6 appeared significantly more damped instead of having a sharp peak as was observed for other modes. In addition, for an 800 N preload, there were two heavily damped peaks in the 650–750 Hz frequency range with the corresponding deflection shapes at these peaks not providing sufficient distinction as to which most closely resembled mode 6 at higher bolt preloads. This is why two different natural frequencies are shown in Figs. 16 and 17 for mode 6 at an 800 N preload. Figure 17 shows the natural frequency for mode 6 specifically as the preload in bolts F1 and F2 is varied. Figure 18 shows the natural frequencies of modes 1 and 5 as the preload is varied with and without including washers between the bridge and blades.

From Fig. 18, fixing the contact area between the bridge and each blade results in the natural frequencies of modes 1 and 5 only increasing with increasing preload, as one may more typically expect. This further provides evidence that when not including washers between the bridge and blades, the bridge is bowing and the contact area is decreasing as the preload increases. This is an important conclusion because the ROM discussed in the Reduced-Order Model section neglects the effects of changes in contact area due to changes in preload, and assumes that FEM natural frequencies can sufficiently match experimental natural frequencies (for modes of interest) at each individual preload by varying spring stiffness(es) alone. If the contact area changes in such a way that this cannot be achieved, this ROM cannot be directly used to predict system dynamics during a shock event resulting in bolt loosening. Thus, this ROM was not applicable for the as-manufactured mBARC considered here (without added washers), as varying the contact area was critical and necessary to validate the mBARC FEM against experiment at each preload. This is shown explicitly in the ROM Applicability section. Note that this also rendered the CC-CMS ROM formulation for the BA-alone unusable as well (though good agreement with experiment was achieved; results not shown for brevity), as this would have been used in conjunction with the bolt-loosening ROM to more efficiently perform shock simulations.

After the completion of all experimental modal analyses of the mBARC with washers added between the bridge and the blades, these added washers were removed prior to shock testing because the mBARC as shown in Fig. 3 was ultimately of greatest interest due to using a more common bolted joint assembly configuration.

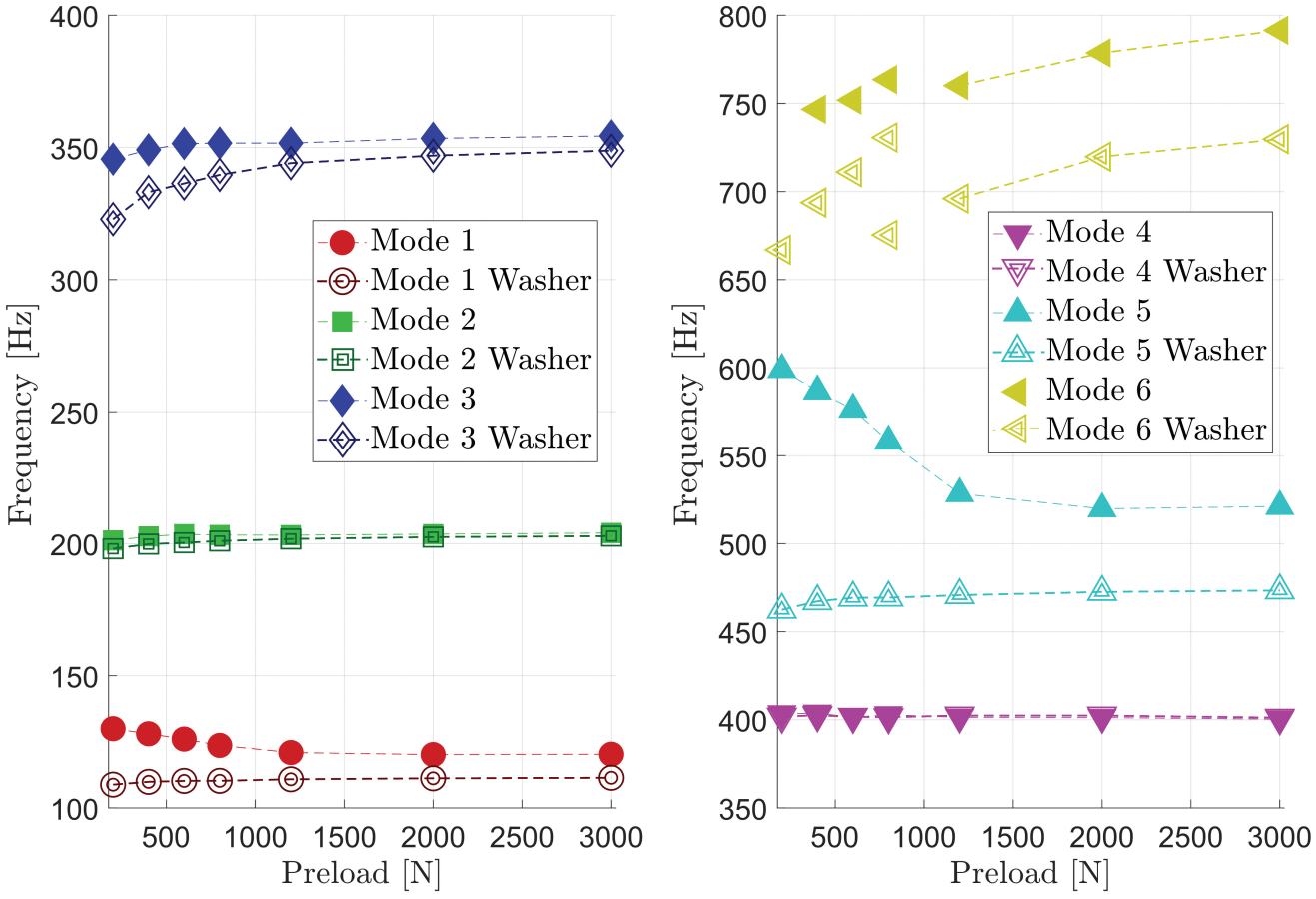

Fig. 16 Experimental mBARC natural frequencies for (left) modes 1–3 and (right) modes 4–6 vs. preload in bolts F1 and F2 with and without a washer added between the bridge and each blade

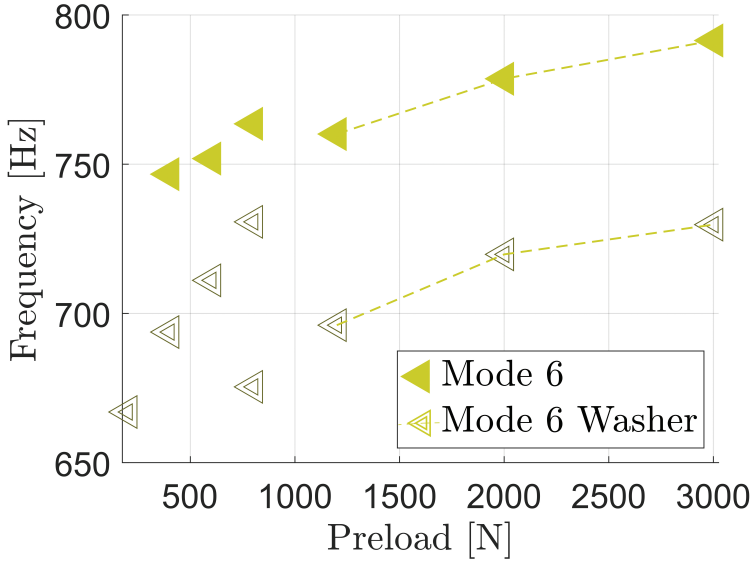

Fig. 17 Experimental mBARC mode 6 natural frequency vs. preload in bolts F1 and F2 with and without a washer added between the bridge and each blade. Below 1200 N there is low confidence in the mode 6 natural frequency due to the low amplitude of mode 6 in measured FRFs

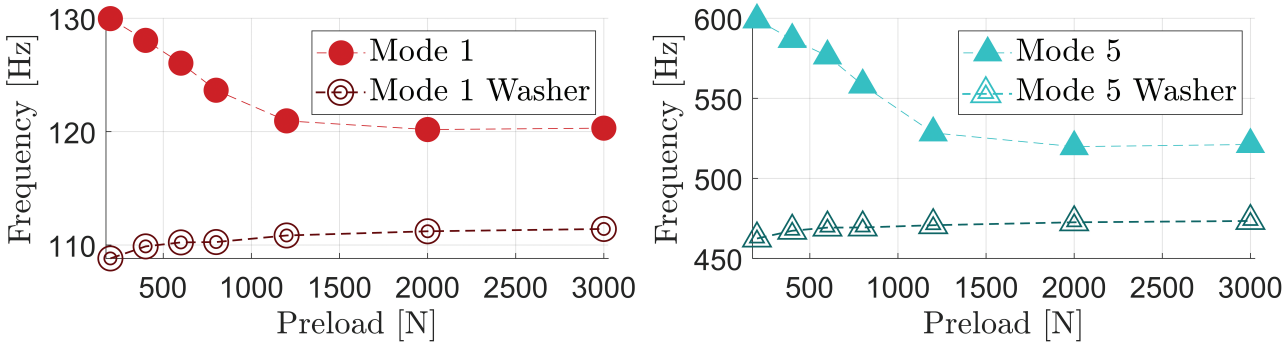

Fig. 18 Experimental mBARC natural frequencies for (left) mode 1 and (right) mode 5 vs. preload in bolts F1 and F2 with and without a washer added between the bridge and each blade. Fixing the contact area removes the decrease in natural frequency as preload increases

Shock Testing

For shock testing, high-energy impact excitation was applied to the mBARC at the location and in the direction shown in Fig. 3. An example measured shock response time series demonstrating a large decrease in the bolt F2 preload is shown is Fig. 19, though it should be noted this preload change was an outlier in the data; the average bolt F2 preload change was only -1.6 N. The filtered preload data shown in Fig. 19 was calculated by applying a zero-phase, third-order, low-pass Butterworth filter with a cutoff frequency of 20 Hz to the raw preload data (applied using the `filtfilt` function in MATLAB). For all shock excitation tests, the nominal initial preload of both the F1 and F2 bolts was 1000 N $\pm$ 20 N.

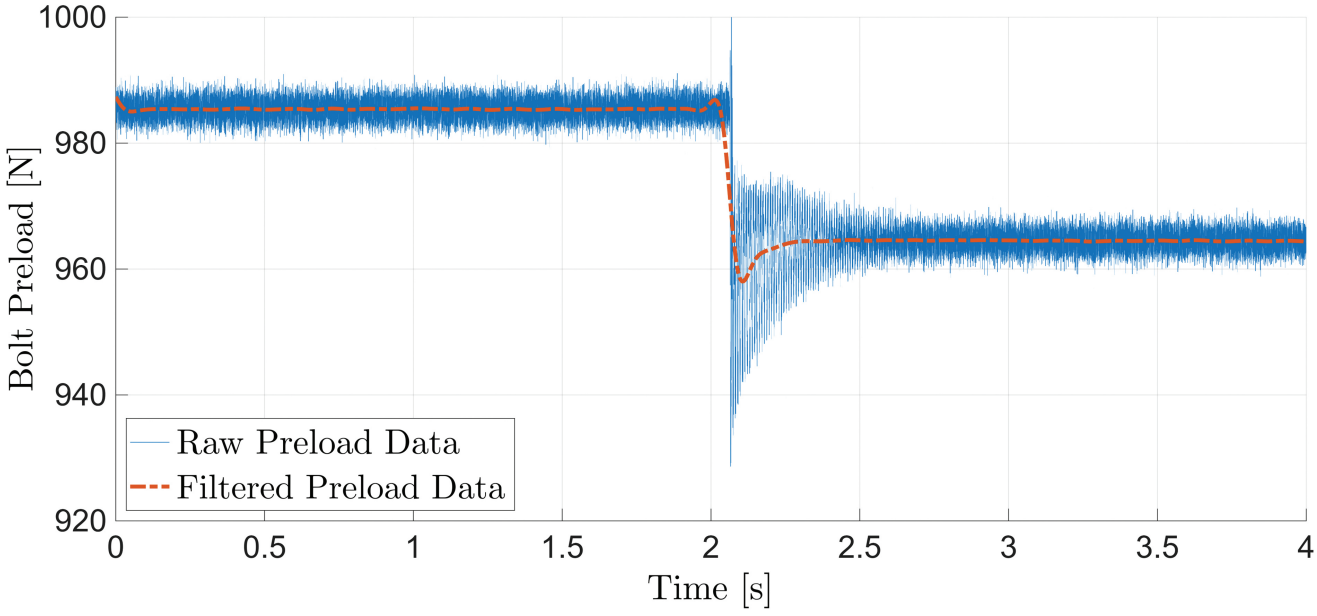

Fig. 19 Example measured shock response time series of bolt F2 preload. The shock excitation occurs just after 2 seconds, resulting in a rapid preload decrease between 2 and 2.5 seconds

As shown in Fig. 19, the preload remains stable before the shock and rapidly decreases immediately after the shock before settling at a lower preload. This preload drop shows the possibility of inducing bolt loosening for the mBARC. However, as stated previously, the extent of bolt loosening shown in Fig. 19 was an outlier. Figure 20 shows a histogram of the preload change over 36 different shocks. As shown in Fig. 20, loosening, tightening, and relatively no change among repeated bolt loosening trials was observed, with the mean and standard deviation of these trials shown in Table 2.

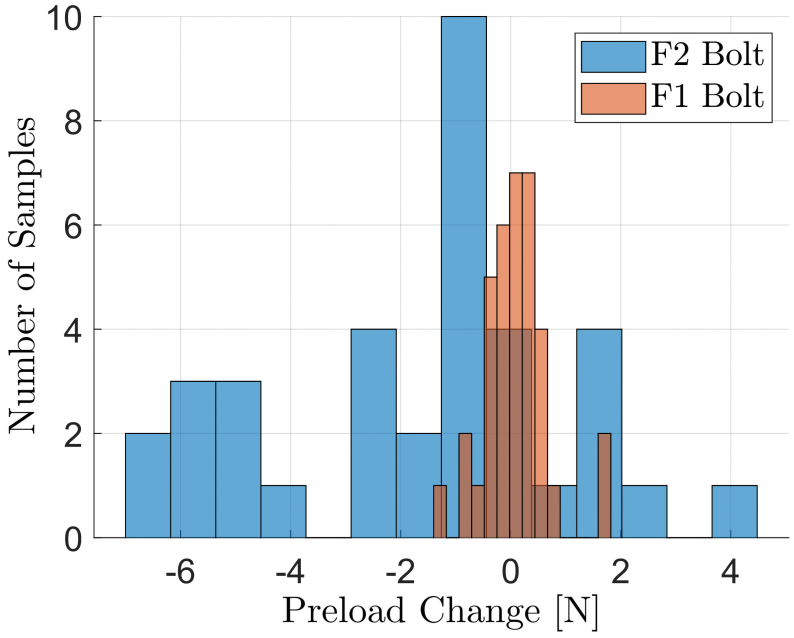

Fig. 20 Histogram of the preload change in bolts F1 and F2 resulting from 36 separate high-energy impact excitations. Bolt F2 experiences a larger range of preload change due to it being closer to the shock input location

Table 2 Mean and standard deviation of the preload change in bolts F1 and F2 for approximately 1000 N initial preload

	F1 [N]	F2 [N]
Mean Preload Change	0.098	−1.6
Standard Deviation	0.58	2.7

When applying shocks with peak magnitudes ranging from 200 N to 1100 N as was done here, no clear relationship was found between input force and change in preload. Though the results shown in Fig. 20 include a range of shock magnitudes, the preload change variation demonstrates that when the range of impact force is between 200 N and 1100 N and the initial bolt F1 and F2 preloads are both approximately 1000 N, the preload change of the as-manufactured mBARC is highly probabilistic and relatively small compared to the preload values themselves. Additionally, in [1] which considers three axially aligned rods and simulated shocks between 0 and 50 kN (i.e., regime 1 in [1]), the two joints act independently of each other. While the mBARC is a different structure than that in [1], the preload response of the mBARC has similar characteristics to regime 1 of the simulated axial rods in [1].

To track the change in mode frequencies in time during and after applying a shock excitation, the WT was used. For a linear system, mode natural frequencies do not change in time, and appear as horizontal bands in the WT whose amplitude decays depending on a given mode's damping and contribution to the measured response. For a nonstationary nonlinear system, however, the natural frequency, damping, and shape of a given mode can be time-dependent. Thus, for a structural system exhibiting nonstationary nonlinearities resulting from bolt loosening, the WT is an excellent tool for monitoring changes in natural frequencies in time, as was done in [13], for example.

Example WTs of a measured acceleration from the Z DOF of triaxial accelerometer 2 (see Fig. 7) considering a low-energy impact excitation (28.08 N peak force) from a modal test and a high-energy impact excitation (324.23 N peak force) from a shock test are shown in Fig. 21. In Fig. 21, the (largely) horizontal bands of the WT for the low-energy impact indicate a relatively linear response, with some minor nonlinearities seen primarily below 0.01 seconds. However, the more noticeable diagonal bands shown in the WT for the high-energy impact indicate a more significant nonlinear response. As demonstrated by the example WTs in Fig. 21 and from observations of WTs for other impact excitations, a key takeaway is that higher-energy impacts qualitatively appear to increase the nonlinearity in the system's shock response as expected. This result is similar to what is shown in [13], where a (relatively lower) 7 m/s impact velocity yielded a WT that only showed horizontal bands. However, for a (relatively higher) 13.5 m/s impact velocity, the WT showed non-horizontal bands for the first 0.05 seconds.

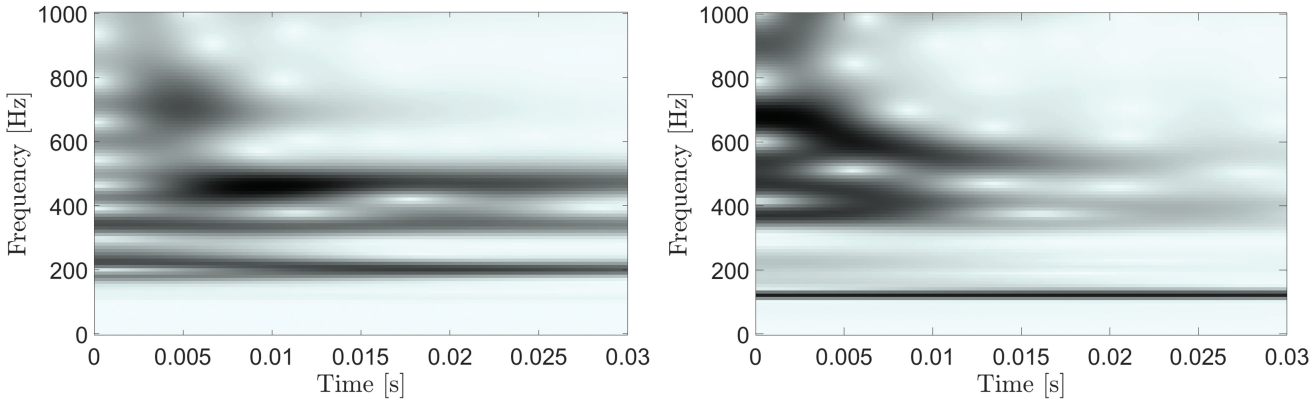

Fig. 21 Example WTs of a measured acceleration response considering (left) low-energy impact excitation and (right) high-energy impact excitation.

ROM Applicability

As discussed in the Contact Area Variability section, direct expansion and application of the ROM discussed in the Reduced-Order Model section to the as-manufactured mBARC was not achievable because of changes in the contact area between the bridge and blades resulting from varying the preloads of bolts F1 and F2. However, contact-area variation was mitigated by adding a washer between the bridge and each blade, which yielded more expected results (i.e., increasing natural frequencies with increasing preload) as shown in Fig. 16. While fixing the contact area more easily allows for the possibility of applying this ROM, expansion to include multiple nonlinear springs for bolts F1 and F2 may still be required depending on the shock excitation location and direction. In addition, modifications to a structure in this way may often not be permitted, and for the study here, significantly changed the mBARC as shown by the differences in natural frequencies with and without including these washers (see Figs. 16–18).

To further demonstrate the necessity of varying the contact area to capture mBARC bolt-loosening phenomena, additional parameter studies were conducted using the mBARC FEM to explore which parameters needed to be varied to match the modes of the FEM to experiment. Specifically, experimental modes which most significantly contributed to shock responses without washers between the blades and bridge (here, modes 1, 2, 3, and 5) were targeted, with other modes either not

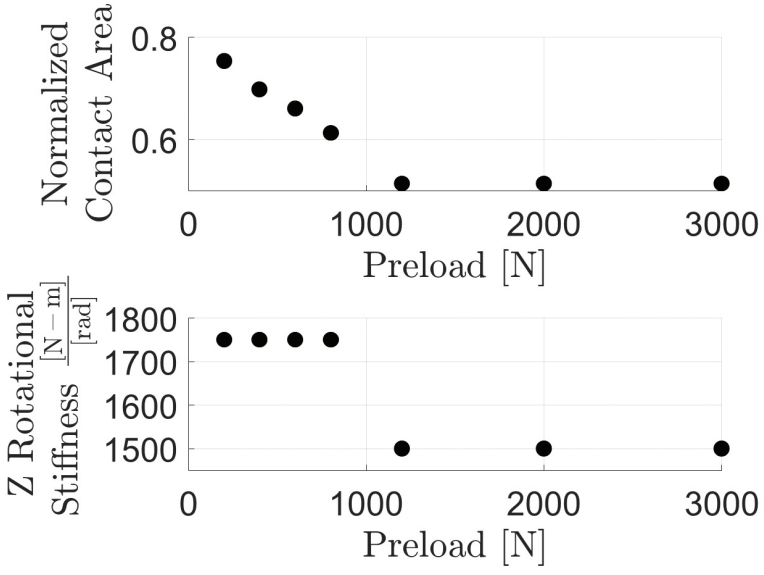

Fig. 22 (top) Normalized contact area and (bottom) Z rotational stiffness needed at each preload to match the natural frequencies of modes 1, 2, 3, and 5 of the mBARC FEM to experiment within 7% RMSE

being sensitive to the bushing element stiffness values and contact area (mode 4) or for which there was low confidence in the experimental natural frequencies (mode 6). This is similar to what is required for the ROM parameter identification, where FEM validation is needed at multiple preloads within a range of interest. Here, the normalized contact area and Z rotational stiffness were found to be the most influential parameters on the system's response. By varying these parameters alone, the natural frequencies of modes 1, 2, 3, and 5 of the mBARC FEM were able to be matched at each considered preload within 7% root mean squared error (RMSE). The final values of normalized contact area and Z rotational stiffness at each preload are shown in Fig. 22. Table 3 shows all other bushing element stiffness values when tuning the mBARC FEM, which were kept constant for all preloads. These results demonstrate that an expansion of the ROM to allow for contact area variation(s) in combination with stiffness variation(s) is needed to model mBARC bolt-loosening dynamics. More generally, this expansion is needed to apply this ROM for structures like the mBARC where the contact area of one or more bolted joints is required to be a function of preload to validate the FEM to experimental data.

Table 3 Constant bushing element stiffness values when tuning the mBARC FEM to match experimental natural frequencies at various preloads

Stiffness Direction	Value
X Axial [N/m]	10^7
Y Axial [N/m]	10^{10}
Z Axial [N/m]	10^8
X Rotational [N-m/rad]	10^8
Y Rotational [N-m/rad]	10^8

Conclusions

This research sought to extend the use and application of a previously developed ROM to capture bolt-loosening dynamics for a structure containing two bolted joints when considering a shock excitation. Here, the mBARC was considered, with the preload of the bolts connecting the blades and bridge varied to study the accelerations at points of interest to quantify bolt-loosening dynamics. After performing an initial validation of a BA-alone FEM to characterize the fixed-base BC, an mBARC FEM was developed and validated to match experimental natural frequencies within 7% RMSE for modes 1, 2, 3, and 5. Sensitivity studies were performed to study how different bushing element spring stiffness values and the contact area between the bridge and blades affected the natural frequencies of the mBARC FEM when attempting to match experimental values. Here, the contact area and Z rotational stiffness were found to be the most influential parameters. As part of mBARC FEM validation, the natural frequencies of the as-manufactured mBARC were measured with and without enforcing a constant contact area between the bridge and blades. This was done to study how changing contact area affects the natural frequencies of the first six system modes. The mBARC was also subjected to a range of high-energy shock excitations to characterize bolt loosening for this 2-bolt system. For impact excitations between 200 N and 1100 N, the bolt nearest to the shock loosened by an average of 1.6 N, though results were highly probabilistic. However, the bolt furthest from the shock excitation experienced relatively no change across all trials. The WT of measured accelerometer data was used to qualitatively demonstrate shock response dynamics for low- and high-energy impact excitations. High-energy impact excitations showed significantly more mode shifting, similar to results observed for structures studied in previous work. Lastly, with regard to applying and expanding the previously proposed ROM discussed in the Reduced-Order Model section, this ROM currently cannot model the preload change (and hence shock response dynamics) of the as-manufactured mBARC due to the contact area changing as a function of bolt preload. This was demonstrated both empirically with experimental modal testing and using a validated mBARC FEM where changing the contact area was necessary to match experimental natural frequencies at each preload.

Future Work

Based on the modeling and experimental results presented here, future research includes modifying the ROM in [13] to incorporate contact area variability as a function of preload. This would allow for the ROM to be applied to structures like the mBARC in which the contact area of one or more bolted joints is required to be a function of preload for FEM validation. In addition, efforts attempting to apply and expand this ROM to the mBARC with a fixed contact area between the bridge

and blades is of interest, as this may still yield insights into additional ROM modifications not discussed in this work. Lastly, increasing the number of bolts on the mBARC (or considering a nominal BARC structure) to study the dynamics of more complex bolted structures under shock excitation would be an interesting long-term future application of this research.

Acknowledgments This research was funded by Los Alamos National Laboratory (LANL) through the Engineering Institute's Los Alamos Dynamics Summer School (LADSS). The Engineering Institute is a research and education collaboration between LANL and the University of California San Diego's Jacobs School of Engineering. This collaboration seeks to promote multidisciplinary engineering in information research that develops and integrates advanced predictive modeling, novel sensing systems, and new developments in information technology to address LANL mission relevant problems. The authors would also like to acknowledge Alex Malliett of LANL for providing advice on sensors, data acquisition systems, and drilling additional holes into the BA to place the bridge for mBARC assembly, Fabian Vigil, Nathanael Adler, Steve Simmonds, and Roman Romero of LANL for help in wiring the load washers used for experimental efforts, Kai Newhouse of LANL and Dr. Jim Declerck of Michigan Technological University for help setting up and using Siemens Testlab, Jason Martinez, Cindy Lopez, and Amy Schiffer of LANL for administrative support of the Engineering Institute and assistance during the course of this work, and Dr. Samantha Ceballes and Dr. Shannon Danforth of LANL for leading the 2025 LADSS program.

References

1. Sandro Aldana and Keegan J Moore. Dynamic interactions between two axially aligned threaded joints undergoing loosening. *Journal of Sound and Vibration*, 520:116625, 2022. https://doi.org/10.1016/j.jsv.2021.116625
2. Guo-Ping Luo, Liang-Jun Xu, and Ji-Gao Zhang. Combination effect of fretting and corrosion on bolt-type power connectors. In *Electrical Contacts - 2000. Proceedings of the Forty-Sixth IEEE Holm Conference on Electrical Contacts (Cat. No.00CB37081)*, pages 60–66, 2000. https://doi.org/10.1109/HOLM.2000.889912
3. Long Yang, Bing Yang, Guangwu Yang, Yang Xu, Shoune Xiao, Shilin Jiang, and Jingsong Chen. Analysis of competitive failure life of bolt loosening and fatigue. *Engineering Failure Analysis*, 129:105697, 2021. https://doi.org/10.1016/j.engfailanal.2021.105697
4. Kai Jiang, Zhifeng Liu, Tao Zhang, and Feng Wang. Influence of bolt creep induced pre-tightening force relaxation on dynamic response of the bolted joint system. *Journal of Sound and Vibration*, 596:118800, 2025. https://doi.org/10.1016/j.jsv.2024.118800
5. Long Yang, Bing Yang, Guangwu Yang, Shoune Xiao, and Shilin Jiang. Research on factors affecting competitive failure between loosening and fatigue of bolt under combined excitation. *Journal of Constructional Steel Research*, 189:107110, 2022. https://doi.org/10.1016/j.jcsr.2021.107110
6. Gerhard H. Junker. New Criteria for Self-Loosening of Fasteners Under Vibration. *SAE Transactions*, 78:314–335, 1969. https://doi.org/10.4271/690055
7. N.G. PAI and D.P. HESS. Experimental study of loosening of threaded fasteners due to dynamic shear loads. *Journal of Sound and Vibration*, 253(3):585–602, 2002. https://doi.org/10.1006/jsvi.2001.4006
8. Matthew S. Allen, Daniel Rixen, Maarten van der Seijs, Paolo Tiso, Thomas Abrahamsson, and Randall L. Mayes. *Model Reduction Concepts and Substructuring Approaches for Linear Systems*, pages 25–73. Springer International Publishing, Cham, 2020. https://doi.org/10.1007/978-3-030-25532-9_3
9. Valentin Fort, Abdel-Hakim Bouzid, and Michel Gratton. Analytical Modeling of Self-Loosening of Bolted Joints Subjected to Transverse Loading. *Journal of Pressure Vessel Technology*, 141(3):031205, 03 2019. https://doi.org/10.1115/1.4042798
10. Toshimichi Fukuoka and Masataka Nomura. Proposition of Helical Thread Modeling With Accurate Geometry and Finite Element Analysis. *Journal of Pressure Vessel Technology*, 130(1):011204, 01 2008. https://doi.org/10.1115/1.2826433
11. Mingyuan Zhang, Dongfang Zeng, Liantao Lu, Yuanbin Zhang, Jing Wang, and Jingmang Xu. Finite element modelling and experimental validation of bolt loosening due to thread wear under transverse cyclic loading. *Engineering Failure Analysis*, 104:341–353, 2019. https://doi.org/10.1016/j.engfailanal.2019.05.001
12. Shriram Dravid. Study of vibration loosening of bolted joints–A review, *IAETSD Journal for Advanced Research in Applied Sciences*, 2018.
13. Keegan J Moore. A Reduced-Order Model for Loosening of Bolted Joints Subjected to Axial Shock Excitation. *Journal of Applied Mechanics*, 86(12):121007, 2019. https://doi.org/10.1115/1.4044813
14. Mingpo Zheng, Wentao Chen, Xing Yan, Zhifeng Liu, and Magd Abdel Wahab. Finite element analysis of bolted joints under torsional loads. *Tribology International*, 201:110188, 2025. https://doi.org/10.1016/j.triboint.2024.110188
15. Robert C. Juvinall and Kurt M. Marshek. *Fundamentals of Machine Component Design*, Chapter 10: Threaded Fasteners and Power Screws, page 430. John Wiley & Sons Inc., 2000.
16. Felipe Camargo de Oliveira Kobayashi, Blake Johnson, Aryan Singh, and Keegan J. Moore. A mathematical approach to representing nonlinear dynamics of bolted joint loosening, 2024.
17. Kyle Brindley, Prabhu Khalsa, Thomas Roberts, Sergio Cordova, Matthew Fister, Chris Johnson, and Scott Ouellette. waves, June 2025. https://doi.org/10.5281/zenodo.7574167

Chapter 10
Data-Driven Nonlinear Reduced-Order Modeling for Flutter Analysis

Nami Mogharabin and Amin Ghadami

Abstract Flutter instability poses a serious threat to the reliability and safety of aerospace structures. While linear analysis tools have long been employed for their simplicity, they fail to capture key nonlinear behaviors that can emerge before or after the predicted flutter point. Nonlinear bifurcation-based stability analysis methods, however, often depend on explicit governing equations, limiting their applicability when closed-form equations are unavailable, such as in experimental studies or high-fidelity simulations of aeroelastic systems. Here, we propose a data-driven bifurcation analysis framework to analyze flutter instabilities in aeroelastic systems. The proposed method constructs a low-dimensional surrogate model directly from high-dimensional time-series measurements of system dynamics. Using measured time series, the framework maps the system's high-dimensional response to a reduced-order representation, enabling interpretable and efficient nonlinear stability analysis. By integrating data-driven dimensionality reduction with concepts from nonlinear dynamics, this approach offers a practical framework for analyzing the nonlinear stability and dynamics of aeroelastic systems in situations where traditional model-based methods are not feasible.

Keywords Flutter analysis · Reduced-order modeling · Deep learning · Bifurcation analysis

Introduction

Flutter instability is a critical aeroelastic phenomenon that can lead to catastrophic structural oscillations. The risk is amplified in modern aircraft, where the use of lighter and more flexible materials increases geometric and aerodynamic nonlinearities, making flutter behavior increasingly unpredictable and difficult to control [1]. Although classical linear flutter-prediction methods remain attractive for their computational efficiency, they cannot capture nonlinear behaviors such as supercritical limit-cycle oscillations that emerge gradually beyond the flutter speed or subcritical oscillations, where large amplitudes may arise even below the linear flutter speed. Nonlinear stability analysis is therefore essential to ensure safety. Bifurcation analysis provides a more complete picture of instability around non-hyperbolic equilibria. Existing approaches typically rely either on high-fidelity simulations and experiments [2], or on mathematical models [3, 4]. The first class requires repeated runs for different parameter sets, which is often expensive, while also offering limited interpretability in large-dimensional systems. The second class depends on explicit mathematical models, which are often unavailable or difficult to derive in many practical settings.

To overcome these challenges, we propose a data-driven reduced-order modeling (ROM) method for flutter analysis in aeroelastic systems [5]. The framework integrates autoencoders with principles from dynamical systems [6, 7]—specifically center-manifold and normal form theories [8]—to capture the essential reduced-order dynamics corresponding to the system nonlinear stability and dynamics. Using limited trajectory data, the method discovers low-dimensional coordinates and reduced-order dynamics that can predict and characterize flutter instabilities. Numerical demonstrations on a representative nonlinear airfoil validate the effectiveness of the approach for nonlinear stability analysis and flutter prediction.

Nami Mogharabin · Amin Ghadami
Aerospace and Mechanical Engineering Department, University of Southern California, Los Angeles, CA, USA
e-mail: namimogh@usc.edu

Amin Ghadami
Sonny Astani Department of Civil and Environmental Engineering, University of Southern California, Los Angeles, CA, USA
e-mail: ghadami@usc.edu

© The Author(s), under exclusive license to River Publishers 2026

Kristin B. Zimmerman, PhD (eds.), *Nonlinear Structures & Systems, Vol. 1*, Conference Proceedings
of the Society for Experimental Mechanics Series, https://doi.org/10.13052/rp-9788743814122

Methods

For the system $\dot{\mathbf{x}} = \mathbf{f}(\mathbf{x}, \mu)$, where $\mathbf{x} \in \mathbb{R}^n$ represent system states and $\mu \in \mathbb{R}$ is the bifurcation parameter, flutter instabilities typically arise through a Hopf bifurcation, where at equilibrium point $(\mathbf{x_0}, \mu_\mathbf{0})$ pair of complex-conjugate eigenvalues of the linear part $D_\mathbf{x}\mathbf{f}(\mathbf{x_0}, \mu_\mathbf{0})$ crosses the imaginary axis as the flow speed varies, leading to growing oscillations. According to the center-manifold theory, the behavior of such systems near critical point can be described on an invariant manifold that passes through the bifurcation point $(\mathbf{x_0}, \mu_\mathbf{0})$. Trajectories sufficiently close to the equilibrium rapidly converge to this manifold and subsequently evolve according to the reduced dynamics. As a result, the essential stability characteristics of the original high-dimensional system can be captured by a much simpler, second-order representation defined on the manifold. The normal form theory states that there is a transformation under which the dynamics restricted on the manifold can be represented in a minimal form including only necessary terms, called resonant terms. This representation captures the critical nonlinear behavior governing stability with the fewest possible terms, thereby facilitating analysis and interpretation of nonlinear stability. In the case of Hopf bifurcation relevant to flutter, the reduced dynamics can be written in the following extended normal form:

$$\begin{aligned}
\dot{y}_1 &= a_0(\mu)y_1 - b_0(\mu)y_2 + (a_1(\mu)y_1 - b_1(\mu)y_2)(y_1^2 + y_2^2) + (a_2(\mu)y_1 - b_2(\mu)y_2)(y_1^2 + y_2^2)^2 + H.O.T \\
\dot{y}_2 &= b_0(\mu)y_1 + a_0(\mu)y_2 + (b_1(\mu)y_1 + a_1(\mu)y_2)(y_1^2 + y_2^2) + (b_2(\mu)y_1 + a_2(\mu)y_2)(y_1^2 + y_2^2)^2 + H.O.T
\end{aligned} \tag{1}$$

The coefficients of this reduced-order representation are assumed to be dependent on the bifurcation parameter μ. In flutter analysis, μ is often selected as the flow speed. Analysis of the coefficients of this normal form characterizes the nonlinear dynamics and stability profile around the flutter speed, providing interpretable and tractable description of the dynamics near the critical flutter point. The proposed method tackles two main tasks: identifying the coefficients of the normal form dynamics in Eq. (1) and learning the nonlinear transformations between the observation space and reduced coordinates directly from trajectory data. Both tasks are addressed using a deep-learning framework based on autoencoders, which extract data-driven representations while preserving dynamical structure. The architecture couples autoencoder mapping with components that estimate normal-form coefficients and enforce constraints from center-manifold and normal form theory.

The neural network architecture consists of four main components (Fig. 1a). The encoder block $\mathbf{\Phi}$ maps the high-dimensional state $\mathbf{x}$, together with the bifurcation parameter μ, to a reduced two-dimensional coordinate system $\mathbf{y} = [y_1, y_2]^T$. The decoder block $\mathbf{\Psi}$ reconstructs the original state $\mathbf{x}$ from $\mathbf{y}$ and μ, ensuring an invertible transformation between the physical and reduced spaces. The parametric block $\mathbf{B}$ determines the μ-dependent coefficients of the normal form dynamics, including $a_i(\mu)$ and $b_i(\mu)$ $(i = 0, 1, 2, \ldots)$, which characterize the nonlinear stability profile of the system. Finally, the normal-form block $\mathbf{N}$ advances the reduced coordinates $\mathbf{y}$ in time using an Euler integration scheme according to the normal form equations in Eq. (1), with the coefficients provided by $\mathbf{B}$. The training process is guided by a composite loss function that enforces both accurate reconstruction and theoretically consistent reduced-order dynamics. Each training sample consists of a state pair together with the corresponding bifurcation parameter $(x_t, x_{t+\delta t}, \mu)$. The total loss is composed of three terms. The first term, L_1, evaluates the static performance of the autoencoder by enforcing consistency between the original state and its reconstruction, i.e., $x_t \approx \Psi(\Phi(x_t, \mu), \mu)$. The second term, L_2, captures the dynamical performance of the encoder–decoder–normal form pipeline by requiring that the predicted future state matches the true state, i.e., $x_{t+\delta t} \approx \Psi(N(\Phi(x_t, \mu), B(\mu)), \mu)$. Finally, the third term, L_3, ensures that the normal-form block independently reproduces the manifold dynamics, enforcing $\Phi(x_{t+\delta t}, \mu) \approx N(\Phi(x_t, \mu), B(\mu))$. This separation prevents the decoder from masking errors in the latent dynamics and guarantees that the reduced-order model adheres to the theoretical normal form structure. Together, these three terms balance reconstruction, prediction, and latent-space consistency, enabling simultaneous identification of transformations and normal form coefficients.

Results and Discussion

The proposed framework is demonstrated on a two-degree-of-freedom (2-DOF) airfoil model (Fig. 1b), where the free-stream velocity U serves as the bifurcation parameter. The airfoil undergoes coupled pitch (α) and plunge (h) motions, with dynamics governed by nonlinear integro–differential equations that incorporate aerodynamic forces [9]. Depending on parameter selection, the system can exhibit either supercritical or subcritical flutter once U exceeds a critical threshold.

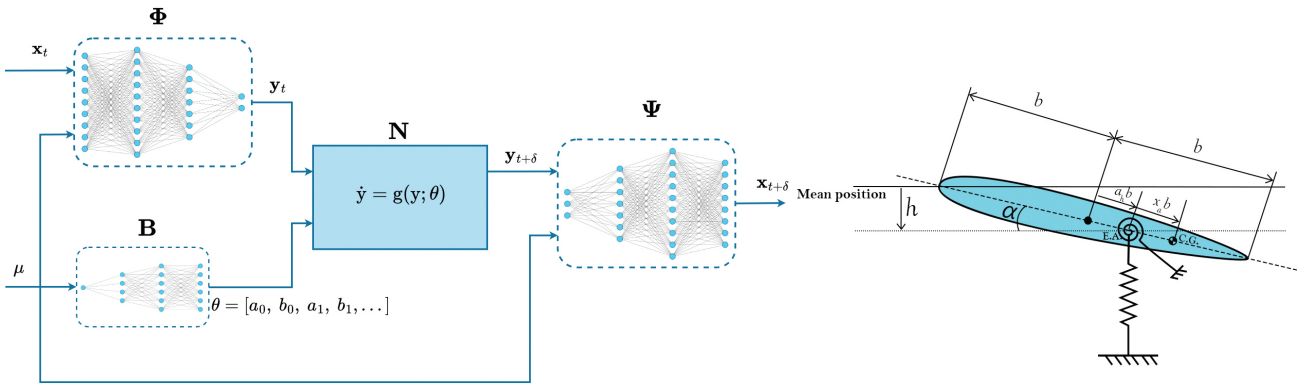

(a) Network architecture for data-driven reduced-order modeling (b) Airfoil model [5]

Fig. 1 (a) Autoencoder architecture, and (b) Airfoil model

For demonstration, the structural stiffness parameters are chosen such that the system exhibits subcritical flutter. A total of 15 trajectories are simulated for values of U in the range $U \in [6.45, 6.65]$, which corresponds to the neighborhood of the bifurcation point. To ensure that the data reflect the dynamics on the manifold of interest corresponding to flutter, the network is trained on trajectories generated from initial conditions randomly sampled along a post-bifurcation limit cycle and evolved in the pre-bifurcation regime, promoting rapid convergence to the center-manifold. Initial transients are discarded, and only the converged portions are retained for training. Figure 2 illustrates the identified coefficients of the normal form. As expected, the coefficients a_1 and a_2 exhibit positive and negative signs, respectively, which is characteristic of subcritical flutter behavior. The ability to identify these coefficients in the reduced dynamics enables the detection of unstable limit-cycle oscillations (LCOs) directly in the latent space. By passing the coordinates of these unstable LCOs through the decoder, the corresponding oscillations are reconstructed in the original state space. This capability is particularly significant, as capturing unstable LCOs in the full system is typically a challenging task using conventional approaches. Results show that the identified LCOs closely match the results obtained with the MATCONT numerical continuation toolbox.

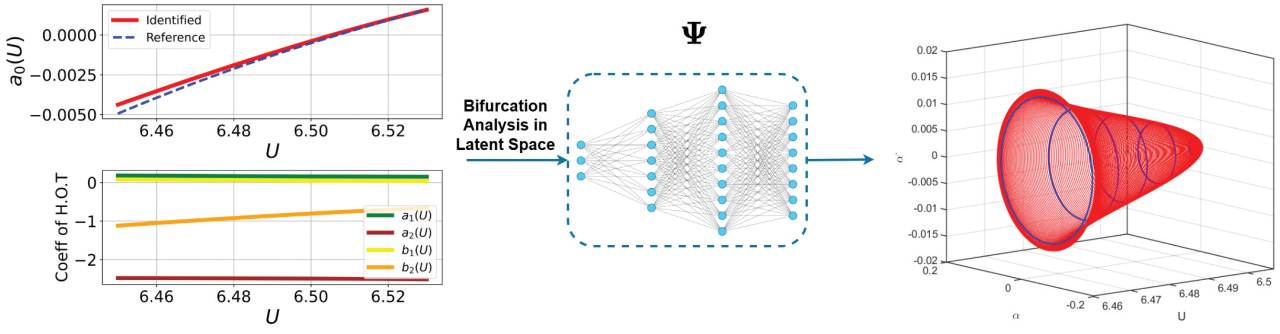

Fig. 2 Unstable limit cycles identified using reduced-order model (blue) closely match the reference limit cycles (red) calculated using MATCONT

Figure 3 presents the bifurcation diagram obtained from the analysis of the reduced-order model in the latent space. To evaluate the identification accuracy, three representative trajectories are simulated in the latent space using the initial conditions and flow speeds indicated in the figure. These trajectories are then mapped back to the original state space using the identified transformations (i.e., the trained decoder) and compared with trajectories generated directly using the full-order airfoil model. As shown in Fig. (3), the reduced-order predictions closely match the responses of the original system, highlighting the accuracy of the approach in reproducing the nonlinear dynamics and bifurcation characteristics of this aeroelastic system.

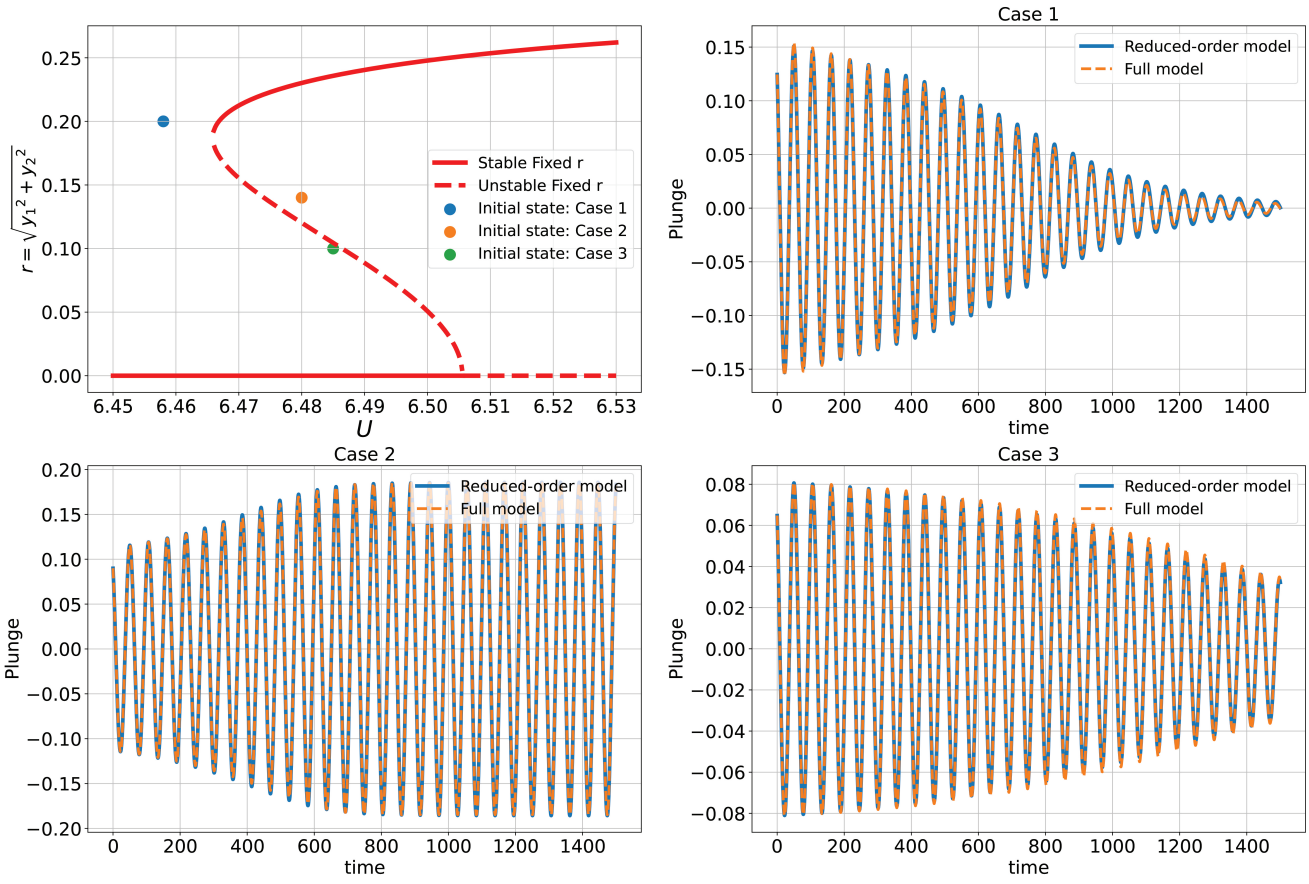

Fig. 3 Bifurcation analysis and trajectory reconstruction using the reduced-order model compared with reference trajectories

Conclusion

This work introduces a data-driven reduced-order modeling framework that integrates principles from nonlinear dynamics with deep learning for nonlinear flutter analysis. By combining autoencoder-based dimensionality reduction with center-manifold and normal form theories, the method extracts low-dimensional representations that capture bifurcation behavior and nonlinear stability using trajectory data. The proposed neural network architecture and training strategy enable identification of the key parameters governing flutter, while addressing the challenges posed by reliance on explicit mathematical models. Moreover, once trained, the reduced-order model provides an efficient and interpretable alternative to repeated high-dimensional simulations, enabling practical nonlinear stability analysis of aeroelastic systems.

Acknowledgments The authors acknowledge support from the Air Force Office of Scientific Research (AFOSR under award number FA9550-25-1-0219).

References

1. Frederico Afonso, José Vale, Éder Oliveira, Fernando Lau, and Afzal Suleman. A review on non-linear aeroelasticity of high aspect-ratio wings. *Progress in Aerospace Sciences*, 89:40–57, 2017.
2. Amin Ghadami and Bogdan I Epureanu. Bifurcation forecasting for large dimensional oscillatory systems: forecasting flutter using gust responses. *Journal of Computational and Nonlinear Dynamics*, 11(6):061009, 2016.
3. Liping Liu, YS Wong, and BHK Lee. Application of the centre manifold theory in non-linear aeroelasticity. *Journal of Sound and Vibration*, 234(4):641–659, 2000.

4. Grigorios Dimitriadis, Gareth Vio, and Jonathan Cooper. Stability and limit cycle oscillation amplitude prediction for simple nonlinear aeroelastic systems. In *45th AIAA/ASME/ASCE/AHS/ASC Structures, Structural Dynamics & Materials Conference*, page 1693, 2004.
5. Nami Mogharabin, Bogdan I Epureanu, and Amin Ghadami. Reduced-order modeling and analysis of airfoil flutter using dynamics-based autoencoders. *AIAA Journal*, pages 1–9, 2025.
6. Nami Mogharabin and Amin Ghadami. Bifurcation analysis in dynamical systems through integration of machine learning and dynamical systems theory. *Journal of Computational and Nonlinear Dynamics*, 20(2), 2025.
7. Kathleen Champion, Bethany Lusch, J Nathan Kutz, and Steven L Brunton. Data-driven discovery of coordinates and governing equations. *Proceedings of the National Academy of Sciences*, 116(45):22445–22451, 2019.
8. Stephen Wiggins. *Introduction to Applied Nonlinear Dynamical Systems and Chaos*. Springer-Verlag, 1990.
9. BHK Lee, L Gong, and YS Wong. Analysis and computation of nonlinear dynamic response of a two-degree-of-freedom system and its application in aeroelasticity. *Journal of Fluids and Structures*, 11(3):225–246, 1997.

Chapter 11
Polynomial Tensor-Based FEM for Parametric Reduced-Order Modelling of Nonlinear Structures via Invariant Manifolds

Tiago S. Martins and Daniel J. Rixen

Abstract Reduced-order modelling (ROM) of nonlinear dynamical systems using invariant manifolds has emerged as a powerful tool for capturing the essential dynamics of complex structures while drastically reducing computational cost. A critical step in this approach is the accurate and efficient computation of nonlinear forces from the full-order finite element (FE) model. This work presents a parametric nonlinear FE framework designed for the systematic assembly and extraction of polynomial nonlinear forces, essential for constructing ROMs via invariant manifolds. The framework supports parametric topology and material definitions, enabling flexible modelling of geometrically nonlinear structures. For instance, employing the Green-Lagrange strain measure, the first Piola-Kirchhoff stress, and the St. Venant-Kirchhoff constitutive relation yields quadratic and cubic nonlinear force terms, which are automatically extracted in tensor form—the tensors are also separated by parameter degree. The proposed software architecture facilitates seamless integration with model order reduction techniques, ensuring high-fidelity simulations while maintaining computational efficiency. Applications in structural dynamics, including large-deformation steady-state vibration problems, are possible uses for this approach.

Keywords NL-FEM, SSM, ROM, Polynomial Tensor Extraction

Introduction

The parametrization method for invariant manifolds, initially developed by Cabré et al. [1–3] and subsequently refined by Haro et al. [4], provides a unified framework that subsumes both classical invariant manifold and normal form approaches [5, 6] through the solution of invariance equations in either graph or normal-form styles. This methodology has been successfully extended to damped vibratory systems [7]. Further developments have incorporated generic forcing conditions, parametric excitations, non-polynomial nonlinearities, and piecewise smooth dynamics [8–10]. Computational implementations enable automated reduction for large-scale finite element models through tools such as MORFE2.0 [11] and SSMtool 2.6 [12].

Within parametric reduction frameworks, Marconi et al. [13] decomposed structural displacements into defect-induced and motion-induced components, expressing internal forces as polynomials in both fields through Neumann-expanded strain approximations. More recently, Morsy and Tiso [14] employed polynomial chaos expansions to quantify uncertainty propagation in joint dynamics, demonstrating efficient characterization of parameter-dependent damping and stiffness variations. Building upon these parametric methodologies, the present work considers a power series expansion of the inverse determinant arising in geometry morphing operations.

Regarding the formulation of the full-order model, the state of the art in tensor-based finite element methods, as implemented in the MFEM library [15], employs a partial assembly paradigm to enable high-performance, matrix-free operator evaluation—a critical capability for high-order discretisations on GPU architectures. This approach decomposes the finite element operator into a sequence of variational restrictions (such as for the subdomains and elements) acting on a point-wise operator at quadrature points (relative to the strong form of the PDE), leveraging the tensor-product structure of quadrilateral and hexahedral elements to perform basis evaluations without explicit matrix storage. Partial assembly minimises memory transfer and achieves near-optimal amount of floating point operations by storing only the operator at quadrature points, while

Tiago S. Martins · Daniel J. Rixen
Technical University of Munich, Chair of Applied Mechanics, TUM School of Engineering and Design, Department of Mechanical Engineering. Boltzmannstr. 15 85748 Garching, Germany.
e-mail: tiago.martins@tum.de; rixen@tum.de

© The Author(s), under exclusive license to River Publishers 2026

Kristin B. Zimmerman, PhD (eds.), *Nonlinear Structures & Systems, Vol. 1*, Conference Proceedings of the Society for Experimental Mechanics Series, https://doi.org/10.13052/rp-9788743814122

the parallel decomposition naturally separates communication in parallel processes, unstructured mesh topology, structured linear algebra, and point-wise physics.

Parametrisation Method for Reduced Order Modelling

The full-order system (FOM) takes the form of the autonomous first-order in time DAE: $\mathbf{B}\dot{\boldsymbol{y}} = \mathbf{A}(\boldsymbol{y})$. When external excitations are introduced, the system becomes non-autonomous (time-dependent); however, constructing an equivalent autonomous representation is achievable by appending auxiliary equations that govern the forcing terms. The FOM is of dimension N and we seek to derive a ROM of dimension $n \ll N$ with governing ODE $\dot{\boldsymbol{z}} = \mathbf{f}(\boldsymbol{z})$. The ROM must preserve the essential dynamics of the high-dimensional system near a stable equilibrium point, assumed without loss of generality to be at the origin. The ROM trajectories map to the full system's phase space via the manifold parametrisation mapping $\boldsymbol{y} = \mathbf{W}(\boldsymbol{z})$, ensuring accurate representation of the system's behavior. Substituting $\boldsymbol{y} = \mathbf{W}(\boldsymbol{z})$ and $\dot{\boldsymbol{z}} = \mathbf{f}(\boldsymbol{z})$ into $\mathbf{B}\dot{\boldsymbol{y}} = \mathbf{A}(\boldsymbol{y})$ gives rise to the invariance equation

$$\mathbf{B}\nabla\mathbf{W}(\boldsymbol{z})\,\mathbf{f}(\boldsymbol{z}) = \mathbf{A}(\mathbf{W}(\mathbf{z}))\,, \tag{1}$$

which cannot directly be solved for $\mathbf{W}$ and $\mathbf{f}$, the ROM unknowns. To overcome this issue, assume that the FOM dynamics $\mathbf{A}(\boldsymbol{y})$, the ROM dynamics $\mathbf{f}(\boldsymbol{z})$, and the manifold mapping $\mathbf{W}(\boldsymbol{z})$ can all be expressed as power series:

$$\mathbf{A}(\boldsymbol{y}) = \sum_{\boldsymbol{\alpha}\in\mathcal{I}_N} \mathbf{A}_{\boldsymbol{\alpha}}\,\boldsymbol{y}^{\boldsymbol{\alpha}}\,, \qquad \mathbf{W}(\boldsymbol{z}) = \sum_{\boldsymbol{\sigma}\in\mathcal{I}_n} \mathbf{W}_{\boldsymbol{\sigma}}\,\boldsymbol{z}^{\boldsymbol{\sigma}}\,, \qquad \mathbf{f}(\boldsymbol{z}) = \sum_{\boldsymbol{\nu}\in\mathcal{I}_n} \mathbf{f}_{\boldsymbol{\nu}}\,\boldsymbol{z}^{\boldsymbol{\nu}}\,, \tag{2}$$

where we define the set of multi-indices $\mathcal{I}_N = \mathbb{N}_0^N \setminus \{\mathbf{0}\}$ for the multi-index notation yielding $\boldsymbol{y}^{\boldsymbol{\alpha}} = y_1^{\alpha_1}\cdots y_N^{\alpha_N}$, which is monomial of order $|\boldsymbol{\alpha}| = \alpha_1 + \cdots + \alpha_N$.

Inserting the power series of equation (2) into the invariance equation (1), yields an overall equality of power series. For each multi-index $\mathbf{p} = (p_1, \ldots, p_n)$, equating the coefficients associated with the monomial $\boldsymbol{z}^{\mathbf{p}}$ generates the corresponding homological equation: $[\mathbf{B}\nabla\mathbf{W}(\boldsymbol{z})\,\mathbf{f}(\boldsymbol{z})]|_{\mathbf{p}} = \mathbf{A}(\mathbf{W}(\mathbf{z}))|_{\mathbf{p}}$ which becomes

$$\mathbf{B}\sum_{\boldsymbol{\nu}>\mathbf{0}}^{\mathbf{p}}\sum_{j=1}^{n} \mathbf{W}_{\mathbf{p}-\boldsymbol{\nu}+\mathbf{e}_j}\, f_{\boldsymbol{\nu},j}\,(p_j - \nu_j + 1) = \sum_{\substack{\boldsymbol{\alpha}\in\mathcal{I}_N \\ |\boldsymbol{\alpha}|\le|\mathbf{p}|}} \mathbf{A}_{\boldsymbol{\alpha}}\,\Xi_{\mathbf{p},\boldsymbol{\alpha}} \tag{3}$$

where the $\Xi_{\mathbf{p},\boldsymbol{\alpha}}$ are scalars described by the equation

$$\boldsymbol{\Xi}_{\mathbf{p},\boldsymbol{\alpha}} = \sum_{\substack{\boldsymbol{\sigma}_l\in\mathcal{I}_n^{|\boldsymbol{\alpha}|} \\ \sum\boldsymbol{\sigma}_l=\mathbf{p}}} \left(\prod_{m=1}^{\alpha_1} W_{\boldsymbol{\sigma}_m,1}\right)\cdots\left(\prod_{m=|\boldsymbol{\alpha}|-\alpha_N+1}^{|\boldsymbol{\alpha}|} W_{\boldsymbol{\sigma}_m,N}\right).$$

Most importantly, equation (3) relates coefficients of $\mathbf{W}$ and $\mathbf{f}$ of order $\le |\mathbf{p}|$. In other words, the coefficients $\mathbf{W}_{\mathbf{p}}$ and $\mathbf{f}_{\mathbf{p}}$ are independent from the coefficients of order larger than $|\mathbf{p}|$, which allows for an efficient construction of the ROM via recurrence with increasing order.

For first-order monomials $|\mathbf{p}| = 1$, the invariance equation reduces to the spectral problem:

$$\mathbf{B}\mathbf{W}_1\mathbf{f}_1 = \mathbf{A}_1\mathbf{W}_1, \tag{4}$$

with matrices defined as:

$$\mathbf{A}_1 = [\mathbf{A}_{\mathbf{e}_1} \mid \cdots \mid \mathbf{A}_{\mathbf{e}_N}]_{N\times N}\,, \qquad \mathbf{W}_1 = [\mathbf{W}_{\mathbf{e}_1} \mid \cdots \mid \mathbf{W}_{\mathbf{e}_n}]_{N\times n}\,, \qquad \mathbf{f}_1 = [\mathbf{f}_{\mathbf{e}_1} \mid \cdots \mid \mathbf{f}_{\mathbf{e}_n}]_{n\times n}\,.$$

This equation is solved via Jordan decomposition of the master eigenmodes. The master eigenvalues $\boldsymbol{\lambda}$ are extracted from the diagonal of $\mathbf{f}_1$, and the generalised eigenvector matrix $\boldsymbol{\Phi}$ is correspondingly redefined.

For higher order monomials $|\mathbf{p}| \ge 2$, the parametrisation method yields linear systems of the form:

$$(s_{\mathbf{p}}\mathbf{B} - \mathbf{A}_1)\mathbf{W}_{\mathbf{p}} + \mathbf{B}\boldsymbol{\Phi}\mathbf{f}_{\mathbf{p}} = \mathbf{R}_{\mathbf{p}}, \tag{5}$$

where $s_{\mathbf{p}} = \mathbf{p} \cdot \boldsymbol{\lambda}$ is the superharmonic frequency and $\mathbf{R}_{\mathbf{p}}$ contains previously computed terms (preceding monomials in graded lexicographic order). This underdetermined system ($N + n$ unknowns, N equations) is typically resolved by setting $\mathbf{f}_{\mathbf{p}} = \mathbf{0}$.

Nonlinear resonance occurs when $s_{\mathbf{p}} \approx \lambda_r$, causing ill-conditioning as $s_{\mathbf{p}}\mathbf{B} - \mathbf{A}_1$ nears singularity. Solvability requires $\mathbf{R}_{\mathbf{p}}$ to lie in the combined images of $s_{\mathbf{p}}\mathbf{B} - \mathbf{A}_1$ and $\mathbf{B}\boldsymbol{\Phi}$, leading to three cases: (i) solvable with $\mathbf{f}_{\mathbf{p}} = \mathbf{0}$ if $\mathbf{R}_{\mathbf{p}}$ is orthogonal to resonant left eigenvectors; (ii) solvable with $\mathbf{f}_{\mathbf{p},\mathcal{R}} \neq \mathbf{0}$ if resonance occurs with included modes—inner resonance; (iii) unsolvable if resonance occurs with excluded modes—outer resonance.

Here, $\mathcal{R} \subset \{1, \ldots, n\}$ marks resonant entries r that satisfy $s_{\mathbf{p}} \approx \lambda_r$.

For cases (i) and (ii), uniqueness is enforced via $\mathbf{B}$-orthogonality conditions between $\mathbf{W}_{\mathbf{p}}$ and resonant left eigenvectors. The resonant set $\mathcal{R}$ is determined using *near-resonance* criteria to account for frequency shifts at high amplitudes and for numerical robustness. Two parametrisation styles emerge: normal-form style uses finite threshold for eigenvalue proximity; and graph style treats all inner modes as resonant.

Practical matters

The computational procedure involves handling large matrices whose dimensions grow rapidly with both the reduction order and the number of degrees of freedom in the system. To mitigate these scaling challenges, it is essential to exploit matrix sparsity patterns and symmetric properties while implementing memory-efficient allocation strategies and algorithms with favourable computational complexity.

This methodology employs local polynomial expansions, which imposes inherent limitations on its applicability to nonlinear problems. The approximations remain valid primarily in neighbourhoods of equilibrium points, and extrapolation to distant regions requires careful validation of the solution fidelity. The choice of parametrisation style presents a fundamental trade-off: graph style formulations, while computationally more expensive, prove advantageous for centre manifold computations, whereas normal-form style parametrisations yield simpler reduced dynamics and provide unique characterization of manifold folding behaviour [8]. A critical requirement for avoiding outer resonance phenomena is the comprehensive inclusion of all full-order model modes that exhibit nonlinear resonance with the master modes up to the specified maximum expansion order at the initialization stage.

The case of structural dynamics

This work addresses vibration problems in structural dynamics with parametrised geometry, where a parameter θ controls the nodal coordinates in the finite element model. To parametrise the invariant manifolds, the second-order equations of motion are reformulated as a first-order differential-algebraic system:

$$\mathbf{M}(\theta)\dot{\mathbf{V}} = -\mathbf{K}(\theta)\mathbf{U} - \mathbf{C}(\theta)\mathbf{V} - \mathbf{F}^{\mathrm{nl}}(\theta, \mathbf{U}) + \mathbf{F}^{\mathrm{ext}}(\theta, \boldsymbol{r}), \qquad \dot{\mathbf{U}} = \mathbf{V}, \qquad \dot{\boldsymbol{r}} = \mathbf{E}(\boldsymbol{r}), \qquad \dot{\theta} = 0. \tag{6}$$

Here, $\mathbf{U}$ and $\mathbf{V}$ denote the generalised displacement and velocity vectors, respectively. The system matrices—mass $\mathbf{M}(\theta)$, stiffness $\mathbf{K}(\theta)$, and damping $\mathbf{C}(\theta)$—along with the polynomial nonlinear force $\mathbf{F}^{\mathrm{nl}}(\theta, \mathbf{U})$ and external force $\mathbf{F}^{\mathrm{ext}}(\theta, \boldsymbol{r})$, are functions of the geometric parameter θ. Furthermore, forcing is incorporated via an autonomous subsystem $\dot{\boldsymbol{r}} = \mathbf{E}(\boldsymbol{r})$, which describes the evolution of the forcing state $\boldsymbol{r}$.

In the reduced-order model (ROM), the forcing state $\mathbf{r}$ is embedded within the reduced coordinates as $\mathbf{z} = (\widetilde{\mathbf{z}}, \mathbf{r})$. This leads to a direct parametrization of the forcing: $\mathbf{W}^{\mathrm{r}}(\widetilde{\mathbf{z}}, \mathbf{r}) = \mathbf{r}$, and its dynamics are projected as $\dot{\mathbf{r}} = \mathbf{f}^{\mathrm{r}}(\widetilde{\mathbf{z}}, \mathbf{r}) = \mathbf{E}(\mathbf{r})$. Note that this approach requires the forcing to be representable by a finite-dimensional linear state-space model, thus excluding non-smooth periodic functions and stochastic processes.

The second-order nature of the original system imposes a compatibility condition between the displacement and velocity mappings: $\nabla \mathbf{W}^{u}(\boldsymbol{z}), \mathbf{f}(\boldsymbol{z}) = \mathbf{W}^{\mathrm{v}}(\boldsymbol{z})$. Consequently, the homological equation for displacement reduces to:

$$\sum_{\boldsymbol{\nu} > \mathbf{0}}^{\mathbf{p}} \sum_{j=1}^{n} \mathbf{W}^{u}_{\mathbf{p}-\boldsymbol{\nu}+\mathbf{e}_j} f_{\boldsymbol{\nu},j}(p_j - \nu_j + 1) = \mathbf{W}^{\mathrm{v}}_{\mathbf{p}}, . \tag{7}$$

This relation can be forward-substituted into the momentum balance invariance equation to streamline computations. The detailed derivation of the resulting equation falls beyond the scope of this work—see [8] for details.

Nonlinear Solid Mechanics

This work employs a Lagrangian description of motion, tracking material points from a fixed undeformed configuration V. While physical laws governing equilibrium and tractions are inherently defined in the deformed, current configuration, the Total Lagrangian (TL) formulation enables a consistent framework by referencing all quantities to V. This is achieved through the use of work-conjugate stress and strain measures.

The fundamental challenge is reconciling undeformed-configuration kinematics with current-configuration physics. Two primary approaches address this: 1. the Total Lagrangian (TL) formulation references all quantities to the undeformed configuration V. It employs the Green-Lagrange strain tensor, which permits polynomial expansions in terms of the displacement gradient—a key property exploited in this work; and 2. the Updated Lagrangian (UL) formulation incrementally updates the reference state to the last computed configuration. It typically uses incremental or logarithmic strain measures, where the sum of incremental strains approximates the integrated strain rate. The TL formulation is computationally efficient for hyperelasticity, large rotations, and path-independent materials, as it avoids the cost of frequent spatial frame updates. Its ability to express strain as a polynomial is essential for the parametrisation of invariant manifolds ROM technique. However, TL is unsuitable for phenomena requiring explicit tracking of the current configuration, such as large-sliding contact, fatigue damage, and finite strain plasticity; these are beyond the scope of this work and typically necessitate a UL approach.

To enforce equilibrium in the undeformed configuration, the TL formulation utilises the first Piola-Kirchhoff stress tensor, $\mathbf{P}$. This tensor is defined as the force in the *current* configuration acting per unit area in the *undeformed* configuration. Its traction relation, $\mathbf{t} = \mathbf{P}\mathbf{n}$, gives the current traction vector on a surface with original unit normal $\mathbf{n}$, thereby maintaining physical fidelity to the true force equilibrium. The linear momentum balance in the interior of the undeformed domain V, expressed in terms of the displacement field $\mathbf{u}$, yields the strong form of the equation of motion:

$$\rho\ddot{\mathbf{u}} = \nabla \cdot \mathbf{P} + \mathbf{b}, \tag{8}$$

where ρ is the density, $\ddot{\blacksquare}$ denotes the second material time derivative, ∇ is the gradient with respect to undeformed position coordinates $\mathbf{x}$, and $\mathbf{b}$ is the *present* body force per unit undeformed volume. The boundary ∂V is partitioned into a Dirichlet part S_{u}, where $\mathbf{u} = \bar{\mathbf{u}}$, and a Neumann part S_{t}, where $\mathbf{P}\mathbf{n} = \mathbf{t}$, with $S_{\mathrm{u}} \cap S_{\mathrm{t}} = \emptyset$.

The weak form is derived by multiplying the strong form by a kinematically admissible test function $\delta\mathbf{u}$ (vanishing on S_{u}) and integrating over V. Application of integration by parts and the divergence theorem, incorporating the prescribed traction boundary condition, yields the following:

$$\int_V \rho\, \delta\mathbf{u}^\top \ddot{\mathbf{u}}\, \mathrm{d}V + \int_V \nabla\delta\mathbf{u}^\top \mathbf{:}\, \mathbf{P}\, \mathrm{d}V = \int_V \delta\mathbf{u}^\top \mathbf{b}\, \mathrm{d}V + \int_{S_{\mathrm{t}}} \delta\mathbf{u}^\top \mathbf{t}\, \mathrm{d}S. \tag{9}$$

Here, the colon denotes the tensor double contraction ($\mathbf{A}^\top \mathbf{:}\, \mathbf{B} = \mathrm{tr}(\mathbf{A}\mathbf{B})$) and $\nabla\delta\mathbf{u}$ is the gradient of the virtual displacement w.r.t. to the undeformed positions $\mathbf{x}$. This weak form serves as the basis for the finite element discretization.

Applying the parametrisation method for reduced-order modelling requires the underlying dynamical system to exhibit polynomial nonlinearity. In the context of hyperelasticity, this is achieved by selecting a strain energy density function that is a polynomial in the components of the strain tensor. For incompressible materials, models such as neo-Hookean and Mooney-Rivlin naturally express strain energy as a polynomial in the invariants of the left Cauchy-Green tensor $\mathbf{F}\mathbf{F}^T$, where $\mathbf{F} = \mathbf{I} + \mathbf{u}$ is the deformation gradient. For compressible materials, however, the dependence on $J = \det(\mathbf{F})$ often introduces non-polynomial terms (e.g., $\ln J$). A common remedy is to expand the volumetric part of the strain energy as a Taylor series around $J = 1$, yielding a polynomial approximation valid for moderate volumetric deformations ($0 < J < 2$), as $J = 0$ marks singularity.

This work adopts a hyperelastic constitutive law that inherently provides polynomial nonlinearity. It posits a linear relationship between the second Piola-Kirchhoff stress $\mathbf{S}$ and the Green-Lagrange strain tensor $\mathbf{E} = \frac{1}{2}\left(\mathbf{F}^\top\mathbf{F} - \mathbf{I}\right)$:

$$\mathbf{S} = \mathcal{A} : \mathbf{E},$$

where $\mathcal{A}$ is the fourth-order elasticity tensor. The first Piola-Kirchhoff stress, $\mathbf{P}$, is then obtained via the transformation $\mathbf{P} = \mathbf{F}\mathbf{S}$. In the case of a Saint Venant-Kirchhoff material, the stress-strain relation further simplifies to $\mathbf{S} = 2\mu\mathbf{E} + \lambda\ \mathrm{tr}(\mathbf{E})\mathbf{I}$, where $\mathrm{tr}(\blacksquare)$ is the trace operator, and λ and μ are the Lamé constants.

This formulation captures geometric nonlinearity through the quadratic term in $\mathbf{E}$. For small deformation gradients, this term is neglected, recovering the linear infinitesimal strain tensor. Under finite deformations, this term must be retained, introducing higher-order elastic forces.

Substituting the linear hyperelasticity constitutive relation into the principle of virtual work, Eq. (9), reveals a polynomial structure in the displacement $\mathbf{u}$ and displacement gradient $\nabla\mathbf{u}$, which decomposes into linear, quadratic, and cubic terms:

$$
\begin{aligned}
&\int_V \rho\, \delta\mathbf{u}^\top \ddot{\mathbf{u}}\, \mathrm{d}V + \int_V (\nabla\delta\mathbf{u})_{\mathrm{sym}} : \mathcal{A} : (\nabla\mathbf{u})_{\mathrm{sym}}\, \mathrm{d}V \qquad \text{(Linear)} \\
&+ \int_V ((\nabla\mathbf{u})^\top \nabla\delta\mathbf{u})_{\mathrm{sym}} : \mathcal{A} : (\nabla\mathbf{u})_{\mathrm{sym}} + \frac{1}{2}(\nabla\delta\mathbf{u})_{\mathrm{sym}} : \mathcal{A} : ((\nabla\mathbf{u})^\top \nabla\mathbf{u})_{\mathrm{sym}} \mathrm{d}V \qquad \text{(Quadratic)} \\
&+ \int_V \frac{1}{2}(\nabla\delta\mathbf{u}\nabla\mathbf{u})_{\mathrm{sym}} : \mathcal{A} : ((\nabla\mathbf{u})^\top \nabla\mathbf{u})_{\mathrm{sym}}\, \mathrm{d}V \qquad \text{(Cubic)} \\
&= \int_V \delta\mathbf{u}^\top \mathbf{b}\, \mathrm{d}V + \int_{S_\mathrm{t}} \delta\mathbf{u}^\top \mathbf{t}\, \mathrm{d}S_\mathrm{t} \qquad \text{(External)},
\end{aligned}
\tag{10}
$$

where $(\blacksquare)_{\mathrm{sym}} = (\blacksquare + \blacksquare^\top)/2$ denotes the symmetric part of a matrix. Linear damping is incorporated by adding a velocity-proportional term to the left-hand side.

Structures with Parametric Geometry

This work addresses parametric model reduction for structures whose geometry is defined by a parameter. In the finite element method, these parameters control nodal coordinates, thereby inducing a variation in the computational domain. Consider the following three methods for parametrising geometry.

Deformation with Stress Relaxation

The body is subjected to a prescribed deformation, followed by a relaxation step that resets the internal stress state to zero. This process modifies the structural shape while conserving total mass, resulting in a redistribution of material density. The parameter governs the deformation field and the subsequent relaxation forces that eliminate the resulting pre-stress. This introduces additional explicit parametric force terms in the equation of motion.

Pre-stressed Deformation

The body is deformed while preserving the internal stress state, conserving mass via density redistribution. The parameter characterises the applied pre-stress force field that defines a new equilibrium configuration. Equivalently, the parameter may define the pre-strained deformation state directly. This introduces additional explicit parametric forces in the equation of motion.

Direct Modification of the Undeformed Configuration

The intrinsic geometry of the undeformed body is altered while preserving constitutive material properties. We require a continuously differentiable homeomorphism to that describes how the geometry changes with the parameter. Hence, the parameter directly modifies the integration domain in the weak formulation of the equations of motion. In the case of FEM, the parameter controls nodal positions in the undeformed configuration without inducing pre-stress, altering density, or introducing explicit parametric forces. This work focuses on this approach, which presents a greater mathematical and computational challenge. Mathematically, one has

$$
\mathbf{x} = \mathbf{x}(\mu, \mathbf{x}_0) \qquad \text{and} \qquad \mathbf{J} = \nabla_0 \mathbf{x}\,,
$$

where $\mathbf{x}$ is the position in the undeformed geometry that depends on the position in the reference $\mathbf{x}_0$ and depends polynomially on the geometry parameter μ. The jacobian of the undefomed positions w.r.t the reference positions is $\mathbf{J}$, its adjugate is $\mathrm{adj}\,\mathbf{J}$ and its determinant is $\det\mathbf{J}$—all polynomial on μ. The volume integral and the gradient become

$$
\int_V \blacksquare\, \mathrm{d}V = \int_{V_0} \blacksquare\, \det\mathbf{J}\, \mathrm{d}V_0 \qquad \text{and} \qquad \nabla\blacksquare = \nabla_0\blacksquare \cdot \mathbf{J}^{-1} = \nabla_0\blacksquare \cdot \mathrm{adj}\,\mathbf{J}\, (\det\mathbf{J})^{-1}\,.
$$

Three principal approaches for handling the inverse deformation gradient are identified. The first introduces an auxiliary scalar field w, constrained via $w \cdot \det\mathbf{J} = 1$, which is enforced in a weak form; this variational formulation increases the system's dimensionality by one (one new degree of freedom at every FE node) and its accuracy is contingent upon discretization choices [16]. A second approach employs a Neumann series expansion of $\mathbf{J}^{-1}$ in the parameter μ, whose accuracy is limited in practice by the truncation order of the asymptotic expansion used in model reduction [13]. We use the third technique that expresses the inverse determinant $(\det\mathbf{J})^{-1}$ itself as a power series in μ, valid within a specific range, with series coefficients given by a combinatorial sum over integer partitions.

Matrix Polynomial Expansions

In the context of parametric FEM, consider the jacobian of the position as a matrix-valued affine function on a single parameter μ, as follows $\nabla_0 \mathbf{x} = \mathbf{J} = \mathbf{J}_0 + \mu \mathbf{J}_1$, where $\mathbf{J}_0$ and $\mathbf{J}_1$ are constant matrices representing different physical contributions to the system. The computational implementation provides efficient methods for expanding the determinant, adjugate and inverse determinant of such parametric matrices as polynomials (or power series) in μ, which is particularly valuable for the ROM parametrisation method.

For the two-dimensional case with 2×2 matrices, the mathematical formulation is straightforward. The determinant expansion follows the quadratic polynomial form $\det \mathbf{J} = c_0 + c_1\mu + c_2\mu^2$, where the coefficients are computed through explicit formulas: $c_0 = \det \mathbf{J}_0$ represents the base system determinant, $c_2 = \det \mathbf{J}_1$ captures the purely parametric contribution, and $c_1 = \mathbf{J}_0^\top : \operatorname{adj} \mathbf{J}_1$ provides the coupling term between the base and parametric components. Simultaneously, the adjugate matrix exhibits a linear dependence $\operatorname{adj} \mathbf{J} = \mathbf{C}_0 + \mathbf{C}_1\mu$, with $\mathbf{C}_0 = \operatorname{adj} \mathbf{J}_0$ and $\mathbf{C}_1 = \operatorname{adj} \mathbf{J}_1$ following directly from the linearity of the adjugate operation for 2×2 matrices. Additionally, we express $(\det \mathbf{J})^{-1}$ as a power series in μ, given that $0 < \det \mathbf{J} < 2c_0$, as follows:

$$(\det \mathbf{J})^{-1} = \frac{1/c_0}{1 - [c_0 - \det \mathbf{J}]/c_0} = \frac{1}{c_0} \sum_{\kappa=0}^{\infty} \left(\frac{1}{c_0}\right)^{\kappa} (c_0 - \det \mathbf{J})^{\kappa} = \sum_{\kappa=0}^{\infty} a_\kappa \mu^\kappa \,,$$

where the polynomial coefficients are as follows

$$a_\kappa = \frac{1}{c_0} \sum_{\substack{\sigma_1,\sigma_2 \in \mathbb{N}_0 \\ \sigma_1 + 2\sigma_2 = \kappa}} \frac{(\sigma_1 + \sigma_2)!}{\sigma_1!\, \sigma_2!} \left(\frac{-c_1}{c_0}\right)^{\sigma_1} \left(\frac{-c_2}{c_0}\right)^{\sigma_2} .$$

The three-dimensional case with 3×3 matrices requires more sophisticated mathematical treatment. The determinant expands as a cubic polynomial $\det \mathbf{J} = c_0 + c_1\mu + c_2\mu^2 + c_3\mu^3$, while the adjugate matrix follows a quadratic polynomial $\operatorname{adj} \mathbf{J}(\mu) = \mathbf{C}_0 + \mathbf{C}_1\mu + \mathbf{C}_2\mu^2$. The coefficients are derived using invariant theory and properties of the characteristic polynomial. The constant terms $c_0 = \det \mathbf{J}_0$ and $\mathbf{C}_0 = \mathbf{J}_0^2 - \mathbf{J}_0 \operatorname{tr} \mathbf{J}_0 + \frac{1}{2}\mathbf{I}[(\operatorname{tr} \mathbf{J}_0)^2 - \operatorname{tr}(\mathbf{J}_0^2)]$ correspond to the base system properties. The first-order coefficient $c_1 = \operatorname{tr}(\mathbf{J}_0^2\mathbf{J}_1) - \frac{1}{2}[\operatorname{tr}(\mathbf{J}_0^2) - (\operatorname{tr} \mathbf{J}_0)^2] \operatorname{tr} \mathbf{J}_1 - \operatorname{tr} \mathbf{J}_0 \operatorname{tr}(\mathbf{J}_0\mathbf{J}_1)$ captures complex interactions between the base and parametric matrices, while the corresponding adjugate term $\mathbf{C}_1 = \mathbf{I}(\operatorname{tr} \mathbf{J}_0 \operatorname{tr} \mathbf{J}_1 - \operatorname{tr}(\mathbf{J}_0\mathbf{J}_1)) - (\mathbf{J}_0 \operatorname{tr} \mathbf{J}_1 + \mathbf{J}_1 \operatorname{tr} \mathbf{J}_0) + \mathbf{J}_0\mathbf{J}_1 + \mathbf{J}_1\mathbf{J}_0$ maintains the fundamental identity $\mathbf{J} \operatorname{adj} \mathbf{J} = \mathbf{I} \det \mathbf{J}$ throughout the expansion. The coefficients c_2, c_3 and $\mathbf{C}_2$ follow by symmetry. Finally, we express $(\det \mathbf{J})^{-1}$ as a power series in μ, given that $0 < \det \mathbf{J} < 2c_0$, as follows:

$$(\det \mathbf{J})^{-1} = \frac{1/c_0}{1 - [c_0 - \det \mathbf{J}]/c_0} = \frac{1}{c_0} \sum_{\kappa=0}^{\infty} \left(\frac{1}{c_0}\right)^{\kappa} (c_0 - \det \mathbf{J})^{\kappa} = \sum_{\kappa=0}^{\infty} a_\kappa \mu^\kappa \,,$$

where the polynomial coefficients are as follows

$$a_\kappa = \frac{1}{c_0} \sum_{\substack{\sigma_1,\sigma_2,\sigma_3 \in \mathbb{N}_0 \\ \sigma_1 + 2\sigma_2 + 3\sigma_3 = \kappa}} \frac{(\sigma_1 + \sigma_2 + \sigma_3)!}{\sigma_1!\, \sigma_2!\, \sigma_3!} \left(\frac{-c_1}{c_0}\right)^{\sigma_1} \left(\frac{-c_2}{c_0}\right)^{\sigma_2} \left(\frac{-c_3}{c_0}\right)^{\sigma_3} .$$

These mathematical formulations provide the foundation for efficient computation of system responses in parametric studies, where the polynomial expansions allow for rapid evaluation of determinant and inverse-like operations without explicit matrix inversion at each parameter value. The implementation leverages algebraic identities to minimize computational cost while maintaining numerical stability, which is crucial for large-scale finite element applications in structural dynamics where parameter studies and frequency sweeps are common analysis techniques.

Finite Element Discretisation

Closed-form solutions for elastodynamic problems are generally unavailable, necessitating numerical discretisation. The Rayleigh-Ritz method approximates the displacement field using spatially admissible functions with time-dependent coefficients:

$$\mathbf{u}(\mathbf{x}_0, t) \approx \mathbf{N}(\mathbf{x}_0)\mathbf{U}(t),$$

where $\mathbf{N}(\mathbf{x}_0)$ contains shape functions satisfying homogeneous Dirichlet conditions, and square-integrability over V. Natural boundary conditions are enforced weakly via the variational formulation.

The Finite Element Method implements this framework through domain partitioning into elements. Within each element, displacements interpolate nodal values:

$$\mathbf{u}(\mathbf{x}_0, t) \approx {}^{\mathrm{e}}\mathbf{N}(\mathbf{x}_0)\, {}^{\mathrm{e}}\mathbf{U},$$

with virtual displacements discretised similarly. Global assembly enforces kinematic compatibility through shared nodal displacements and force equilibrium through summation of element contributions, yielding global matrices $\mathbf{M}$, $\mathbf{K}$, and force vectors. For linear hyperelasticity, the internal force exhibits cubic nonlinearity:

$$\mathbf{F}^{\mathrm{int}} = \mathbf{K}\mathbf{U} + \mathbf{G}(\mathbf{U}^{\otimes 2}) + \mathbf{H}(\mathbf{U}^{\otimes 3}),$$

where $\mathbf{G}$ and $\mathbf{H}$ are symmetric tensors representing quadratic and cubic stiffness terms, and $\blacksquare^{\otimes m}$ represents the m-th Kronecker power (repeated Kronecker product with itself). The index permutation of the tensors is fully symmetric and reduces computational storage and ensures energy conservation, with force components given by:

$$\mathbf{G}(\mathbf{U}^{\otimes 2}) = \sum_{r \le s} \mathbf{G}_{\{r,s\}} U_r U_s \qquad \text{and} \qquad \mathbf{H}(\mathbf{U}^{\otimes 3}) = \sum_{r \le s \le t} \mathbf{H}_{\{r,s,t\}} U_r U_s U_t \,.$$

Now, considering the polynomial expansion of the parameter, at order μ^0, the equations of motion simplify to the standard governing equations of solid mechanics. However, at order μ^1, the linear terms, i.e. the inertia and the linear stiffness force are given by

$$\begin{aligned}\int_{V_0} \rho\, \delta\mathbf{u}^\top \ddot{\mathbf{u}}\, c_1 \,\mathrm{d}V_0 + \int_{V_0} (\nabla_0 \delta\mathbf{u}\, \mathbf{C}_1)_{\mathrm{sym}} : \mathcal{A} : (\nabla_0 \mathbf{u}\, \mathbf{C}_0)_{\mathrm{sym}}\, a_0 \\ + (\nabla_0 \delta\mathbf{u}\, \mathbf{C}_0)_{\mathrm{sym}} : \mathcal{A} : (\nabla_0 \mathbf{u}\, \mathbf{C}_1)_{\mathrm{sym}}\, a_0 + (\nabla_0 \delta\mathbf{u}\, \mathbf{C}_0)_{\mathrm{sym}} : \mathcal{A} : (\nabla_0 \mathbf{u}\, \mathbf{C}_0)_{\mathrm{sym}}\, a_1 \,\mathrm{d}V_0 \,.\end{aligned}$$

The quadratic stiffness term expands to eight terms and the cubic stiffness term to five terms, at linear order of μ. Because of the inverse of the displacement gradient, the stiffness terms expand to infinite order. However, the inertia and the external terms only expand to cubic order on μ and have only one contribution per coefficient.

Elastic Force Tensors

To derive the tensors of the elastic force, we separate the orders of the first Piola-Kirchhoff stress tensor $\mathbf{P}$. For instance, its linear part $\mathbf{P}_1$ is as follows

$$\mathbf{P}_1 = \lambda\, \mathbf{I}\, \mathrm{tr}(\nabla\mathbf{u}) + \mu\, (\nabla\mathbf{u} + \nabla\mathbf{u}^\top) = \sum_j \Big[\lambda\, \mathbf{I}\, (\nabla N_j \mathbf{U}_j) + \mu \left(\mathbf{U}_j \nabla N_j + \nabla N_j^\top \mathbf{U}_j^\top \right) \Big] \,.$$

The linear part of the elasticity term in the weak form integrand yields

$$\begin{aligned}&\nabla\delta\mathbf{u}^\top \mathbf{:}\, \mathbf{P}_1 = \mathrm{tr}\big(\nabla\delta\mathbf{u}\, \mathbf{P}_1^\top\big) = \lambda\, \mathrm{tr}(\nabla\delta\mathbf{u})\ \mathrm{tr}(\nabla\mathbf{u}) + \mu\, \mathrm{tr}(\nabla\delta\mathbf{u}\, \nabla\mathbf{u}) + \mu\, \mathrm{tr}\big(\nabla\delta\mathbf{u}\, \nabla\mathbf{u}^\top\big) = \\ &\sum_{i,j} \Big[\lambda\, \mathrm{tr}(\delta\mathbf{U}_i \nabla N_i)\ \mathrm{tr}(\mathbf{U}_j \nabla N_j) + \mu\, \mathrm{tr}(\delta\mathbf{U}_i \nabla N_i \mathbf{U}_j \nabla N_j) + \mu\, \mathrm{tr}\big(\delta\mathbf{U}_i \nabla N_i \nabla N_j^\top \mathbf{U}_j^\top\big) \Big] = \\ &\sum_{i,j} \Big[\lambda \delta\mathbf{U}_i^\top \nabla N_i^\top \nabla N_j \mathbf{U}_j + \mu \delta\mathbf{U}_i^\top \nabla N_j^\top \nabla N_i \mathbf{U}_j + \mu\, \nabla N_i \nabla N_j^\top\, \delta\mathbf{U}_i^\top \mathbf{U}_j \Big]\end{aligned}$$

Finally, integrating over the (elemental) domain yields the stiffness matrix

$$\int_V \mathrm{tr}(\nabla\delta\mathbf{u}\, \mathbf{P}_1)\,\mathrm{d}V = \sum_{i,j} \delta\mathbf{U}_i^\top \Big(\underbrace{\lambda \boldsymbol{\mathcal{B}}_{ij}^\top + \mu \boldsymbol{\mathcal{B}}_{ij} + \mu\, \mathrm{tr}(\boldsymbol{\mathcal{B}}_{ij})\mathbf{I}}_{\mathbf{K}_{ij}} \Big) \mathbf{U}_j \qquad \text{with} \qquad \boldsymbol{\mathcal{B}}_{ij} = \int_V \nabla N_j^\top \nabla N_i \,\mathrm{d}V \,,$$

where $\boldsymbol{\mathcal{B}}_{ji} = \boldsymbol{\mathcal{B}}_{ij}^\top$ and $\mathbf{K}_{ji} = \mathbf{K}_{ij}^\top$. Expressly, the stiffness matrix felt by node i due to displacements in node j is:

$$\boxed{\mathbf{K}_{ij} = \lambda \boldsymbol{\mathcal{B}}_{ij}^\top + \mu \boldsymbol{\mathcal{B}}_{ij} + \mu\, \mathrm{tr}(\boldsymbol{\mathcal{B}}_{ij})\mathbf{I}} \,.$$

For the tensor of the quadratic term we have

$$\mathbf{P}_2 = \lambda\,\nabla\mathbf{u}\,\mathrm{tr}(\nabla\mathbf{u}) + \mu\,\nabla\mathbf{u}\,(\nabla\mathbf{u}^\top + \nabla\mathbf{u}) + \lambda\,\mathbf{I}\,\mathrm{tr}\big(\nabla\mathbf{u}^\top\,\nabla\mathbf{u}\big)/2 + \mu\,\nabla\mathbf{u}^\top\,\nabla\mathbf{u} =$$
$$\sum_{j,k}\Big[\lambda\,\mathbf{U}_j\nabla N_j\,\mathrm{tr}(\mathbf{U}_k\nabla N_k) + \mu\,\mathbf{U}_j\nabla N_j\,(\nabla N_k^\top\mathbf{U}_k^\top + \mathbf{U}_k\nabla N_k) + \lambda\,\mathbf{I}\,\mathrm{tr}\big(\nabla N_j^\top\mathbf{U}_j^\top\mathbf{U}_k\nabla N_k\big)/2 + \mu\,\nabla N_j^\top\mathbf{U}_j^\top\mathbf{U}_k\nabla N_k\Big]\,.$$

And the second order term in the weak form integrand becomes

$$\mathrm{tr}(\nabla\delta\mathbf{u}\,\mathbf{P}_2) = \lambda\;\mathrm{tr}(\nabla\delta\mathbf{u}\,\nabla\mathbf{u})\,\mathrm{tr}(\nabla\mathbf{u}) + \mu\;\mathrm{tr}\big(\nabla\delta\mathbf{u}\,\nabla\mathbf{u}\,\nabla\mathbf{u}^\top\big) + \mu\;\mathrm{tr}(\nabla\delta\mathbf{u}\,\nabla\mathbf{u}\,\nabla\mathbf{u})$$
$$+\lambda\;\mathrm{tr}(\nabla\delta\mathbf{u})\,\mathrm{tr}\big(\nabla\mathbf{u}^\top\,\nabla\mathbf{u}\big)/2 + \mu\;\mathrm{tr}\big(\nabla\delta\mathbf{u}\,\nabla\mathbf{u}^\top\,\nabla\mathbf{u}\big)$$

Hence, the tensor of the quadratic term writes

$$\mathbf{G}_{ijk} = \lambda\,\boldsymbol{\mathcal{B}}_{ijk} + \mu\Big[\underset{jk}{\mathrm{tr}}\,\boldsymbol{\mathcal{B}}_{ijk}\otimes\mathbf{I}\Big]^\top + \mu\,\boldsymbol{\mathcal{B}}_{ijk}^\top + \frac{\lambda}{2}\Big[\underset{jk}{\mathrm{tr}}\,\boldsymbol{\mathcal{B}}_{ijk}\otimes\mathbf{I}\Big] + \mu\Big[\underset{ij}{\mathrm{tr}}\,\boldsymbol{\mathcal{B}}_{ijk}\otimes\mathbf{I}\Big]$$

$$\text{with}\qquad \boldsymbol{\mathcal{B}}_{ijk} = \int_V \nabla N_j\otimes\nabla N_i\otimes\nabla N_k\,\mathrm{d}V \qquad \text{such that}\qquad \int_V \mathrm{tr}(\nabla\delta\mathbf{u}\,\mathbf{P}_2)\,\mathrm{d}V = \sum_{i,j,k}\mathbf{G}_{ijk}(\delta\mathbf{U}_i\otimes\mathbf{U}_j\otimes\mathbf{U}_k)\,.$$

Here, $\underset{jk}{\mathrm{tr}}$ denotes the trace w.r.t. the second and third indices, j and k.

A similar development can be done for the cubic term, such that $\mathbf{H}_{ijkl}$—the tensor that describes the force felt in node i due to the cubic contribution of the combined displacements of nodes j, k and l—can be constructed from a linear transformation of the following tensor:

$$\boldsymbol{\mathcal{B}}_{ijkl} = \int_V \nabla N_j\otimes\nabla N_i\otimes\nabla N_k\otimes\nabla N_l\,\mathrm{d}V\,.$$

Recursive Computation of Parametric Elastic Force Tensors

We integrate the tensor product of the shape functions to build the $\boldsymbol{\mathcal{B}}$ tensors, which can be efficiently transformed into the polynomial tensors of the elastic force for assembly. For the parametric study, these integrals are reformulated in the reference domain using the identities $\mathrm{d}V = \det\mathbf{J}\;\mathrm{d}V_0$ and $\nabla\blacksquare = \nabla_0\blacksquare\cdot\mathrm{adj}\,\mathbf{J}\;(\det\mathbf{J})^{-1}$, as

$$\boldsymbol{\mathcal{B}}_{i_1\ldots i_\gamma} = \int_V \nabla N_{i_1}(\mathbf{x})\otimes\cdots\otimes\nabla N_{i_\gamma}(\mathbf{x})\mathrm{d}V = \int_{V_0}\big[\nabla_0 N_{i_1}(\mathbf{x}_0)\;\mathrm{adj}\,\mathbf{J}(\mathbf{x}_0)\big]\otimes\cdots\otimes\big[\nabla N_{i_\gamma}(\mathbf{x}_0)\;\mathrm{adj}\,\mathbf{J}(\mathbf{x}_0)\big](\det\mathbf{J}(\mathbf{x}_0))^{-\gamma}\mathrm{d}V_0$$

To optimize numerical quadrature, we separate from the integrand the tensor product of shape functions for the force term of order γ, which marks the force in node i_1 due to the combined displacements of nodes i_2, ... and $i_{\gamma+1}$:

$$\boldsymbol{\mathcal{N}}_{i_1,\ldots,i_{\gamma+1}} = \big[\nabla_0 N_{i_1}\;\mathrm{adj}\,\mathbf{J}\big]\otimes\cdots\otimes\big[\nabla N_{i_\gamma}\;\mathrm{adj}\,\mathbf{J}\big] = \boldsymbol{\mathcal{N}}_{i_1,\ldots,i_\gamma}\otimes\big[\nabla_0 N_{i_\gamma}\;\mathrm{adj}\,\mathbf{J}\big]\,.$$

In the context of FEM for structural dynamics, particularly when dealing with nonlinear problems and parametric studies, we employ a recursive algorithm for constructing higher-order force tensors. This approach systematically constructs force contributions through a hierarchical tensor product operation, enabling efficient computation of perturbation expansions or homotopy analysis solutions. The mathematical foundation of this algorithm rests on a recursive convolution structure that builds higher-order terms from lower-order components. Let $\boldsymbol{\mathcal{N}}^{(q)}_{i_1,\ldots i_{\gamma+1}}$ represent the tensor product of shape functions for the force term of order γ and polynomial degree q with respect to the geometry parameter μ. The core operation is a discrete convolution representing tensor contraction between successive force orders. The recursive relation is defined as:

$$\boldsymbol{\mathcal{N}}^{(q)}_{i_1,\ldots,i_{\gamma+1}} = \sum_{\ell=\max\{0,q-\Gamma_1\}}^{\min\{\Gamma_\gamma,q\}}\boldsymbol{\mathcal{N}}^{(\ell)}_{i_1,\ldots,i_\gamma}\otimes\big[\nabla_0 N_{i_{\gamma+1}}\;\mathrm{adj}\,\mathbf{J}|_{q-\ell}\big]$$

where $\mathrm{adj}\,\mathbf{J}|_{q-\ell}$ denotes the coefficient of degree $q-\ell$ in μ. We build these tensors for degrees $q=0,\ldots,\Gamma_\gamma$, where the maximum permissible degree at each force order is determined by $\Gamma_\gamma = \min\big\{\gamma\cdot(d-1)\cdot\deg_\mu\mathbf{J},\,\Gamma_{\max}\big\}$, where d represents the spatial dimension (e.g. 3), $\Gamma_{\max}$ is the maximum parametric expansion order in the procedure, and $\deg_\mu\mathbf{J}(\mu)$

is 1 in the examples above. This formulation creates a triangular degree structure that prevents combinatorial explosion while maintaining approximation accuracy.

The algorithm implements a depth-first traversal of the force order tree, beginning with initial conditions $\boldsymbol{\mathcal{N}}_{i_1}$ and progressively building higher-order terms. At each recursion level γ, the algorithm computes the tensor product between the previous order's result and available base operators, then proceeds to the next force order. This continues until reaching the maximum specified force order, at which point the leaf nodes are processed and the final contributions are assembled.

The number of float multiplications (time complexity) and memory required (space complexity) for computing $\boldsymbol{\mathcal{N}}^{(q)}_{i_1,\ldots,i_{\gamma+1}}$ are both $\mathcal{O}(d^{\gamma+1}\, S_{\gamma,q})$, where $S_{\gamma,q}$ is the number of terms in the summation: $q+1$ if $q < \Gamma_1$, $\Gamma_1 + 1$ if $\Gamma_1 \leq q \leq \Gamma_\gamma$, and $\Gamma_1 + \Gamma_\gamma - q + 1$ otherwise. The naive approach, that does not reuse lower order data, scales like $d^{2(\gamma+1)} \binom{q+\gamma}{\gamma}$. We compute $\boldsymbol{\mathcal{N}}^{(q)}_{i_1,\ldots,i_{\gamma+1}}$ for all multisets (unordered combinations) with $\gamma+1$ nodes, which increases the cost by a factor of $\binom{N_{\text{Nodes}}+\gamma}{\gamma+1}$.

This recursive framework is particularly valuable in structural dynamics for handling geometric nonlinearities, material nonlinearities, and parametric uncertainties. The method provides a systematic approach to computing higher-order force terms in perturbation-based solutions, asymptotic expansions, or homotopy analysis methods applied to nonlinear finite element formulations. The algorithm's structure naturally accommodates adaptive refinement strategies and can be parallelized across different force orders for improved computational performance in large-scale structural dynamics simulations.

For numerical quadrature, we loop over the elemental integration points and for each, we precompute $\boldsymbol{\mathcal{N}}_i = \nabla_0 N_i \ \mathrm{adj}\, \mathbf{J}$ for all the nodes and for all relevant parametric degrees; then for each node in the element we start the recursion. In this manner, it is possible to build the elemental tensors with minimal computation. Naturally, memory limitations prohibit assembling these tensors in domains with many elements. Nonetheless, the framework remains as a useful tool for optimization in parametric FEM and specifically for polynomial based parametrisation methods for ROM.

Conclusion

This work introduces a framework for the parametric reduced-order modelling of finite element methods, specifically addressing geometric variations controlled by a single parameter. The formulation ensures that geometric changes do not alter intrinsic material properties, stress states, or introduce spurious forces. The methodology involves a power series expansion of the inverse determinant from the weak form, with explicit derivations for the zeroth and first-order terms. A recursive computational strategy is presented for the efficient assembly of the elemental polynomial tensors representing the nonlinear elastic force. Additionally, external forcing and parametric dependence are incorporated into an enlarged autonomous system, enabling reduction through the direct parametrisation of invariant manifolds, which involves solving a sequence of homological equations.

Disclosure statement:
No potential conflict of interest is reported by the authors.

References

[1] Xavier Cabré, Ernest Fontich, and Rafael De la Llave. "The parameterization method for invariant manifolds I: manifolds associated to non-resonant subspaces". In: *Indiana University mathematics journal* (2003), pp. 283–328.

[2] Xavier Cabré, Ernest Fontich, and Rafael De la Llave. "The parameterization method for invariant manifolds II: regularity with respect to parameters". In: *Indiana University mathematics journal* (2003), pp. 329–360.

[3] Xavier Cabré, Ernest Fontich, and Rafael De La Llave. "The parameterization method for invariant manifolds III: overview and applications". In: *Journal of Differential Equations* 218.2 (2005), pp. 444–515.

[4] Alex Haro, Marta Canadell, Jordi-Lluis Figueras, Alejandro Luque, and Josep-Maria Mondelo. "The parameterization method for invariant manifolds". In: *Applied mathematical sciences* 195 (2016).

[5] John Guckenheimer and Philip Holmes. *Nonlinear oscillations, dynamical systems, and bifurcations of vector fields*. Vol. 42. Springer Science & Business Media, 2013.

[6] Cyril Touzé, Olivier Thomas, and Antoine Chaigne. "Hardening/softening behaviour in non-linear oscillations of structural systems using non-linear normal modes". In: *Journal of Sound and Vibration* 273.1-2 (2004), pp. 77–101.

[7] George Haller and Sten Ponsioen. “Nonlinear normal modes and spectral submanifolds: existence, uniqueness and use in model reduction”. In: *Nonlinear dynamics* 86 (2016), pp. 1493–1534.

[8] Andrea Opreni, Alessandra Vizzaccaro, Cyril Touzé, and Attilio Frangi. “High-order direct parametrisation of invariant manifolds for model order reduction of finite element structures: application to generic forcing terms and parametrically excited systems”. In: *Nonlinear Dynamics* 111.6 (2023), pp. 5401–5447.

[9] Aurélien Grolet, Alessandra Vizzaccaro, Marielle Debeurre, and Olivier Thomas. “High order invariant manifold model reduction for systems with non-polynomial non-linearities: geometrically exact finite element structures and validity limit”. In: (2024).

[10] Leonardo Bettini, Mattia Cenedese, and George Haller. “Model reduction to spectral submanifolds in piecewise smooth dynamical systems”. In: *International Journal of Non-Linear Mechanics* 163 (2024), p. 104753.

[11] Alessandra Vizzaccaro, Giorgio Gobat, Attilio Frangi, and Cyril Touzé. “Direct parametrisation of invariant manifolds for non-autonomous forced systems including superharmonic resonances”. In: *Nonlinear Dynamics* 112.8 (2024), pp. 6255–6290.

[12] Mingwu Li, Thomas Thurnher, Zhenwei Xu, and Shobhit Jain. “Data-free non-intrusive model reduction for nonlinear finite element models via spectral submanifolds”. In: *Computer Methods in Applied Mechanics and Engineering* 434 (2025), p. 117590.

[13] Jacopo Marconi, Paolo Tiso, Davide E Quadrelli, and Francesco Braghin. “A higher-order parametric nonlinear reduced-order model for imperfect structures using Neumann expansion”. In: *Nonlinear Dynamics* 104.4 (2021), pp. 3039–3063.

[14] Ahmed Amr Morsy and Paolo Tiso. “Predicting the variability of the dynamics of bolted joints using polynomial chaos expansion”. In: *Mechanical Systems and Signal Processing* 224 (2025), p. 112008.

[15] R. Anderson, J. Andrej, A. Barker, J. Bramwell, J.-S. Camier, J. Cerveny, V. Dobrev, Y. Dudouit, A. Fisher, Tz. Kolev, W. Pazner, M. Stowell, V. Tomov, I. Akkerman, J. Dahm, D. Medina, and S. Zampini. “MFEM: A Modular Finite Element Methods Library”. In: *Computers & Mathematics with Applications* 81 (2021), pp. 42–74.

[16] Attilio Frangi, Alessio Colombo, Alessandra Vizzaccaro, and Cyril Touzé. “Reduced Order Modelling of Fully Coupled Electro-Mechanical Systems Through Invariant Manifolds With Applications to Microstructures”. In: *International Journal for Numerical Methods in Engineering* 126.3 (2025), e7641.

Chapter 12
Evaluation of NVH in Lightweight Gears: An NL-ROM Study on Contact Ratio and Web Flexibility

Fabio Bruzzone, Carlo Rosso, and Daniele Fabbri

Abstract The drive for lightweight, power-dense, and quiet powertrains in EV and aerospace sectors demands predictive tools for complex gear dynamics. High Contact Ratio (HCR) gears (CR > 2) and thin-webbed gear bodies are critical design strategies to improve NVH performance and reduce mass. However, these features introduce significant non-linearities and potential coupling between the gear mesh and structural dynamics, which are challenging to model accurately and efficiently. This study employs a validated, computationally efficient Non-linear Reduced Order Model (NL-ROM) to investigate these phenomena. The approach integrates the full flexibility of the gear bodies from a detailed Finite Element (FE) basis without geometric simplification, while also accounting for non-linear effects such as time-varying mesh stiffness, contact loss, and vibro-impacts. We extend the model's application to systematically analyze a series of spur gear pairs featuring different contact ratios (CR > 2) and varying web thicknesses. The investigation focuses on the Dynamic Transmission Error (DTE) across a range of operating speeds and torques. A comparative analysis of the dynamic response is performed by post-processing the simulated DTE. This includes generating pseudo-experimental spectrograms to map the frequency content and amplitude of vibrations as a function of contact ratio and web flexibility. The results provide insights into the design trade-offs for modern gears, highlighting how specific geometric configurations can either mitigate or exacerbate vibrations. This work demonstrates the model's powerful capability as a high-fidelity predictive tool for the early-stage design and optimization of next-generation, lightweight gear systems.

Keywords gearbox · NVH · gears

Introduction

The automotive industry's shift towards electric powertrains, driven by environmental concerns, has introduced new challenges in Noise, Vibration, and Harshness (NVH). The absence of masking noise from internal combustion engines makes high-frequency gear whine, caused by gear meshing dynamics, a dominant and often undesirable acoustic feature. Consequently, mitigating gear noise at its source has become a critical focus for improving the perceived sound quality of electric vehicles. Similarly, the aviation industry's pursuit of higher power density and fuel efficiency has led to the adoption of lightweight gears, which can exhibit complex dynamic phenomena requiring detailed study to ensure safety and performance. The dynamic behavior of gear transmission systems has been extensively investigated through both theoretical and experimental methods [1, 2]. High-fidelity approaches, such as Finite Element (FE)/contact mechanics models, have provided deep insights. Parker and Vijayakar [3] introduced a model where dynamic mesh forces were calculated via detailed contact analysis at each time step, capturing non-linearities like contact loss but at a significant computational cost. This formulation was also applied to complex helicopter planetary gear systems [4]. Other research has focused on the influence of tooth surface modifications on Static and Dynamic Transmission Error (STE, DTE) through analytical solutions [5] and comprehensive experiments [6]. A significant body of work has explored the rich non-linear dynamics arising from gear backlash, time-dependent mesh stiffness, and bearing clearances. These studies have identified complex behaviors including periodic, quasi-periodic, and chaotic motions using both analytical and numerical methods [7, 8, 9, 10], and have investigated

Fabio Bruzzone · Carlo Rosso · Daniele Fabbri
Department of Mechanical and Aerospace Engineering
Politecnico di Torino, TO 10129, Italy
e-mail: fabio.bruzzone@polito.it; carlo.rosso@polito.it; daniele.fabbri@polito.it

© The Author(s), under exclusive license to River Publishers 2026

Kristin B. Zimmerman, PhD (eds.), *Nonlinear Structures & Systems, Vol. 1*, Conference Proceedings of the Society for Experimental Mechanics Series, https://doi.org/10.13052/rp-9788743814122

resonances in planetary systems [11]. However, many of these works either require substantial computational resources or employ simplified gear geometries, limiting their direct application in all design scenarios. To bridge the gap between accuracy and efficiency, various hybrid and reduced-order methods have been developed. For instance, hybrid FE-Analytical approaches have been used to analyze transmission error in lightweight gears [12], and multibody models have incorporated precomputed look-up tables for contact conditions [13]. Other hybrid methods combine FE static analysis with analytical vibration models to reduce computation time [14]. While effective, these methods often introduce compromises, such as assuming rigid gear bodies [13], neglecting gear blank flexibility [14], or simplifying geometry by removing teeth [15], which can limit their applicability, especially for thin-walled gears where body flexibility is crucial.

This paper presents a novel model designed to overcome these limitations. We detail a Non-linear Reduced Order Model (NL-ROM) that simulates the true rolling motion and engagement of a gear pair. To our knowledge, simulating the actual rotation and moving contact point using a ROM has not been previously reported. The model inherently captures the non-linearity of the moving contact point, amplified by a load-dependent Time-Varying Mesh Stiffness (TVMS). Contact loss is explicitly handled, and reconnection is treated as a Vibro-Impact (VI). A key advantage is that the full flexibility of axisymmetric gear bodies is retained from the underlying FE model without geometric simplification, even with a minimal set of master Degrees of Freedom (DoFs). This drastically reduces matrix sizes, enabling long time-domain simulations with minimal computational cost and high accuracy. The model's predictions are validated against a high-quality experimental campaign on a gear pair exhibiting complex non-linear phenomena, showing remarkable agreement with DTE measurements.

Methodology

This section details the iterative algorithm for obtaining the time-domain response of a gear pair. The method employs a pre-processing phase to generate a ROM that significantly reduces computational cost. The periodic nature of gear meshing is exploited by leveraging the cyclic symmetry of the gear geometry. The properties of the FE model are considered periodic over an angle $\theta = 360/Z_p$, where Z_p is the number of pinion teeth.

To simulate rotation, a set of reduced mass and stiffness matrices is pre-computed for N discrete angular positions within one mesh cycle. At each zth angular position ($z = 1, ..., N$), the full FE mass and stiffness matrices ($\boldsymbol{K_{p,z}}, \boldsymbol{M_{p,z}}, \boldsymbol{K_{g,z}}, \boldsymbol{M_{g,z}}$) for the pinion ($p$) and gear ($g$) are reduced using the Craig-Bampton Component Mode Synthesis (CB-CMS) method [16]. The reduced system matrices at position z are given by:

$$\boldsymbol{M_z^r} = \begin{bmatrix} \boldsymbol{T_{p,z}^T} & \boldsymbol{T_{g,z}^T} \end{bmatrix} \begin{bmatrix} \boldsymbol{M_{p,z}} & \boldsymbol{0} \\ \boldsymbol{0} & \boldsymbol{M_{g,z}} \end{bmatrix} \begin{bmatrix} \boldsymbol{T_{p,z}} \\ \boldsymbol{T_{g,z}} \end{bmatrix} \tag{1}$$

and similarly for the system stiffness matrix $\boldsymbol{K_z^r}$, where $\boldsymbol{T_{p,z}}$ and $\boldsymbol{T_{g,z}}$ are the CB-CMS transformation matrices. The reduction basis consists of master nodes for force exchange and auxiliary observed nodes to improve the ROM's accuracy. As shown in Figure 1, these nodes are categorized as:

- **Contact mesh stiffness nodes** ($\boldsymbol{u_{Kc,p}}, \boldsymbol{u_{Kc,g}}$): These nodes, located on the tooth flanks, are where the time-varying contact stiffness is applied, serving as the primary source of excitation and non-linearity.
- **Auxiliary observed nodes** ($\boldsymbol{u_{aux,p}}, \boldsymbol{u_{aux,g}}$): Selected using a Modal-Geometrical Selection Criterion (MoGeSeC) [17], these nodes capture the highest modal content to enhance the ROM's accuracy for the frequency range of interest.
- **Central virtual nodes** ($\boldsymbol{u_{t,p}}$, $\boldsymbol{u_{t,g}}$): These master nodes are linked to the inner radii via rigid joints. All their DoFs are constrained except for rotation about the gear axis, where torque is applied. This setup mimics the experimental test bench, isolating the gear mesh dynamics.

The DTE is calculated from the angular displacement of these central nodes as:

$$DTE(t) = \theta_p(t) r_{b,p} - \theta_g(t) r_{b,g} \tag{2}$$

where $r_{b,p}$ and $r_{b,g}$ are the respective base radii. The accuracy of the ROM was validated through extensive modal analysis, showing excellent agreement with the full FE model (e.g., maximum frequency error of -0.05% and minimum MAC value of 88.9% for the pinion's first ten flexible modes).

The coupling between the pinion and gear is modeled by a time-varying, load-dependent contact stiffness matrix $\boldsymbol{K_c}(z, L)$, which connects the corresponding contact nodes. The TVMS value $k_c(z, L)$ is derived from pre-computed Static Transmission Error curves [18, 19, 20].

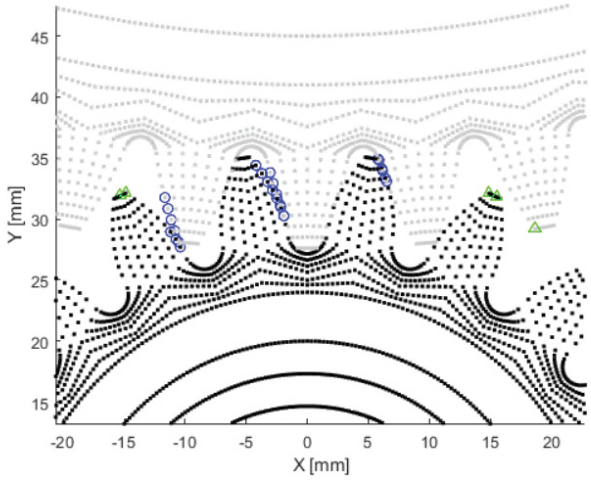

Fig. 1 Detail of the gear pair FE mesh and contact mesh stiffness nodes and auxiliary virtual nodes highlighted

The dynamic response is obtained using a Newmark direct time integration scheme [21] with parameters $\alpha_{NM} = 1/4$ and $\delta_{NM} = 1/2$ for unconditional stability without numerical damping. The system of equations to be solved at each timestep i (corresponding to angular position z) is:

$$\ddot{\boldsymbol{u}}_{\boldsymbol{i}} = \boldsymbol{S}_{\boldsymbol{i}}^{-\mathbf{1}} \boldsymbol{\delta r}_{\boldsymbol{i}} \tag{3}$$

where $\boldsymbol{S_i} = \boldsymbol{M^r_{z,i}} + \Delta t_i \boldsymbol{C^r_{z,i}} + \Delta t_i^2 \alpha_{NM} (\boldsymbol{K^r_{z,i}} + \boldsymbol{K^r_c}(z, L))$ and $\boldsymbol{\delta r_i}$ is the residual vector. The time step Δt_i varies with rotational speed to ensure that each step corresponds to a fixed angular increment $\Delta\theta_p$.

To simulate continuous rotation, the displacement, velocity, and acceleration vectors $(\boldsymbol{u_i^*}, \dot{\boldsymbol{u}}_{\boldsymbol{i}}^*, \ddot{\boldsymbol{u}}_{\boldsymbol{i}}^*)$ computed at step i are transformed using a rotation matrix $\boldsymbol{R_{\Delta\theta}}$ to serve as initial conditions for step $i + 1$, which uses the matrices for position $z + 1$.

$$\boldsymbol{u_i} = \boldsymbol{R_{\Delta\theta}} \boldsymbol{u_i^*}, \quad \dot{\boldsymbol{u}}_{\boldsymbol{i}} = \boldsymbol{R_{\Delta\theta}} \dot{\boldsymbol{u}}_{\boldsymbol{i}}^*, \quad \ddot{\boldsymbol{u}}_{\boldsymbol{i}} = \boldsymbol{R_{\Delta\theta}} \ddot{\boldsymbol{u}}_{\boldsymbol{i}}^* \tag{4}$$

At the end of a mesh cycle ($z = N$), a special procedure ensures continuity. The ROM results are expanded to the full FE model, the nodes are re-sorted to advance the gear by one tooth, and the system state is reduced back to the initial ROM basis ($z = 1$) to begin the next cycle.

Further non-linearity is introduced by modeling contact loss. At each timestep, the normal force on each contact spring is checked. If a traction force is detected, that spring's contribution is set to zero, and the timestep is re-calculated iteratively until only compressive or null forces remain. This process is outlined in Figure 2. When a disconnected contact re-engages, the event is treated as a VI [22]. A discontinuity in velocities is imposed based on a coefficient of restitution e, while displacements remain continuous:

$$\begin{aligned} \dot{\boldsymbol{u}}^+_{\boldsymbol{Kc,g,n}} &= \frac{\dot{\boldsymbol{u}}^-_{\boldsymbol{Kc,g,n}}(1 - \epsilon \cdot e) + \epsilon \dot{\boldsymbol{u}}^-_{\boldsymbol{Kc,p,n}}(e + 1)}{1 + \epsilon} \\ \dot{\boldsymbol{u}}^+_{\boldsymbol{Kc,p,n}} &= \frac{\dot{\boldsymbol{u}}^-_{\boldsymbol{Kc,g,n}}(1 + e) + \epsilon \dot{\boldsymbol{u}}^-_{\boldsymbol{Kc,p,n}}(\epsilon - e)}{1 + \epsilon} \end{aligned} \tag{5}$$

where ϵ is the ratio of the equivalent masses of the impacting bodies. This comprehensive approach allows the model to capture a wide range of non-linear dynamic phenomena with high accuracy and computational efficiency. Further details and a comprehensive validation of the model presented are available in [23].

Case Study and Results

This section presents and analyzes the dynamic response of the High Contact Ratio (HCR) spur gear pair detailed in Table 1, with the notable design modification of having dissimilar web thicknesses for the pinion (12 mm) and gear (4 mm) as

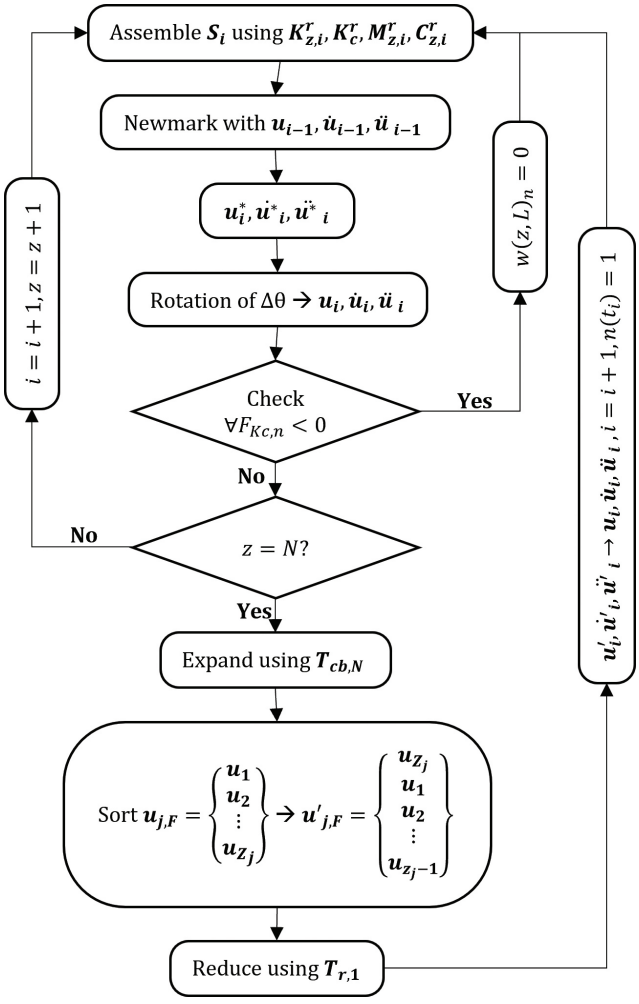

Fig. 2 Algorithm of the NL ROM

Table 1 Pinion and gear geometrical and material data

Parameter	Value	Unit
Pinion number of teeth, Z_1	21	-
Gear number of teeth, Z_2	71	-
Module, m	3	mm
Module, m	3	mm
Dedendum, h_f	1.45	-
Addendum, h_a	1.3	-
Facewidth, F	20	mm
Pinion base radius, r_b	29.6	mm
Gear base radius, r_b	100.07	mm
Total backlash, $2B$	0.125	mm
Contact ratio	2.12	-
Modulus of elasticity, E	207	GPa
Density, ρ	7600	kg/m^3
Poisson ratio, ν	0.3	-
Coefficient of restitution, e	0.56	-
Full FE number of DoFs	536004	-
Coupled ROM number of DoFs	484	-

well as having non-standard addendum and dedendum factors. The system's behavior was investigated under three distinct torque levels, namely 15 Nm, 50 Nm, and 100 Nm across a speed-up maneuver from 1000 to 5000 rpm over a 20 second duration. The results, obtained using the computationally efficient NL-ROM, are presented as pairs of plots: a spectrogram illustrating the harmonic content of the Dynamic Transmission Error (DTE) versus rotational velocity, and a corresponding plot of the mean DTE amplitude, obtained as the difference between the mean value of the STE and the mean value of the DTE in the time domain, averaged across one full revolution of the gear. The 4-hour simulation time for each extensive sweep highlights the model's capability for practical design exploration. The analysis reveals a highly non-linear system whose dynamic character changes profoundly with operating torque, demonstrating complex phenomena and load-dependent response stabilization although no contact loss event or VI has been detected in any simulation. A visualization of the FE connections of the contact nodes employed in the model is visible in Figure 5 for a single position and load. A visualization of the harmonic content of the TVMS for the current case study is visibile in Figure 3. A powerful implication of the proposed methodology is to visualize and appreciate the influence of coupled flexible modes of the system. In the current configuration a coupled mode as visible in Figure 4 is present at a meshing frequency close to 3000 rpm which will be important in the results to follow.

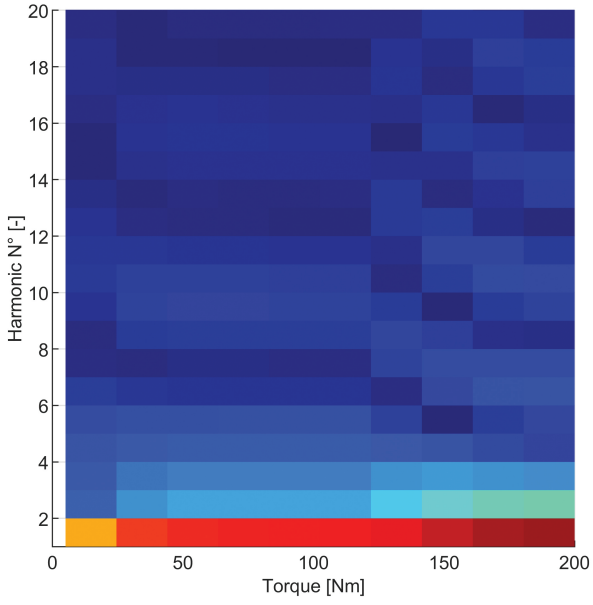

Fig. 3 Harmonic content of the TVMS for the HCR gear pair

At the lowest torque level of 15 Nm (Figure 6), the gear pair exhibits a dramatic and highly localized dynamic response. The mean DTE plot is dominated by an exceptionally sharp and high-amplitude resonance peak, reaching approximately 105 μm at a rotational velocity of about 2750 rpm. The narrowness of this peak suggests a lightly damped system mode is being strongly excited. Outside of this critical speed region, the system is relatively quiet, with only minor DTE fluctuations observed at lower speeds (e.g., around 1300 rpm). Observing the corresponding spectrogram at the 2750 rpm peak, the vibrational energy is not concentrated at the fundamental gear mesh frequency (Harmonic N° 1). Instead, the second, third, and fourth harmonics show significantly higher energy content, as indicated by the red and yellow coloring. This signifies a strong non-linear interaction, where energy from the primary mesh excitation is being channeled into higher-frequency super-harmonics. Above 3000 rpm, the system becomes remarkably stable, with negligible DTE across all harmonics. Increasing the torque to 50 Nm fundamentally alters the system's dynamic behavior as visible in Figure 7, leading to a counterintuitive reduction in overall vibration amplitude. The single, sharp resonance peak observed at 15 Nm is completely suppressed. In its place, the mean DTE plot shows a much broader and lower-amplitude response distributed across a wide speed range from approximately 1200 to 3200 rpm. The maximum DTE is now only about 36 µm, occurring near 2900 rpm, which is a nearly three-fold reduction compared to the low-torque case. Multiple smaller peaks are now evident, indicating that several system modes may be lightly excited, but none dominate the response in the same way. The spectrogram for the 50 Nm case is visibly "busier," confirming a change in the underlying dynamics. Vibrational energy is now spread across a wider array of harmonics, extending up to the 12th harmonic and beyond in the 2000-3000 rpm range. This suggests that

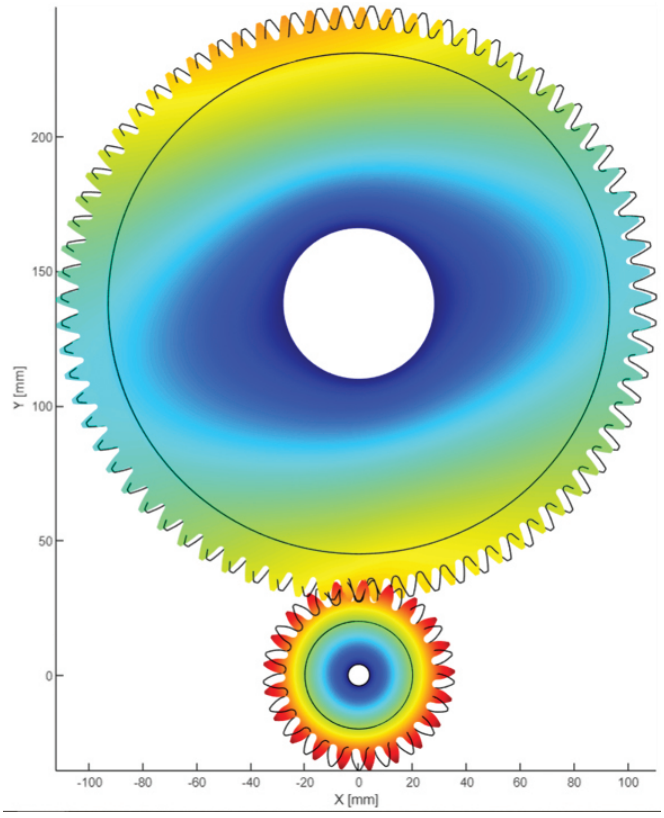

Fig. 4 Coupled modal response at 1050 Hz

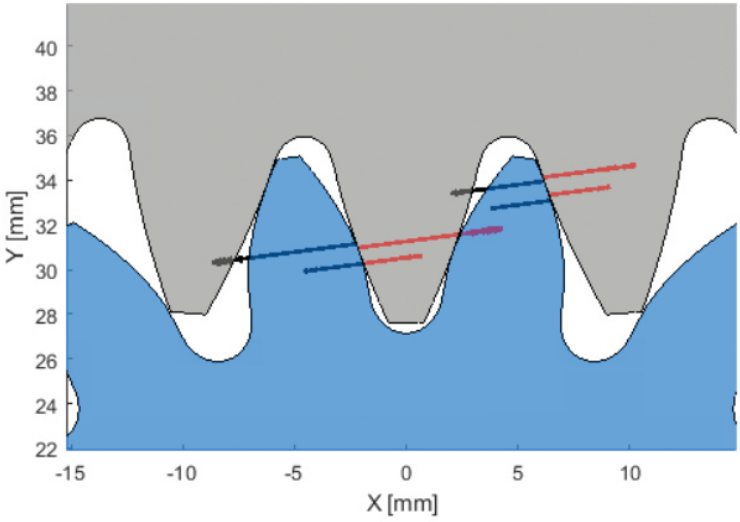

Fig. 5 Visualization of the contact nodes and stiffnesses in the FEM

while the severe, singular resonance is avoided, the system experiences more frequent, lower-intensity events, resulting in a richer, broadband harmonic spectrum. At the highest simulated torque of 100 Nm depicted in Figure 8, the system's response evolves once again, presenting a hybrid of the behaviors seen at the lower loads. The mean DTE plot shows the re-emergence of distinct resonant peaks. A dominant peak appears around 2950 rpm, reaching an amplitude of approximately 72 µm. While significant, this is still considerably lower than the 105 µm peak at 15 Nm. A secondary, but also prominent, peak is visible at a lower speed of around 1300 rpm, with an amplitude of about 40 µm. The spectrogram reveals that, similar to the 15 Nm

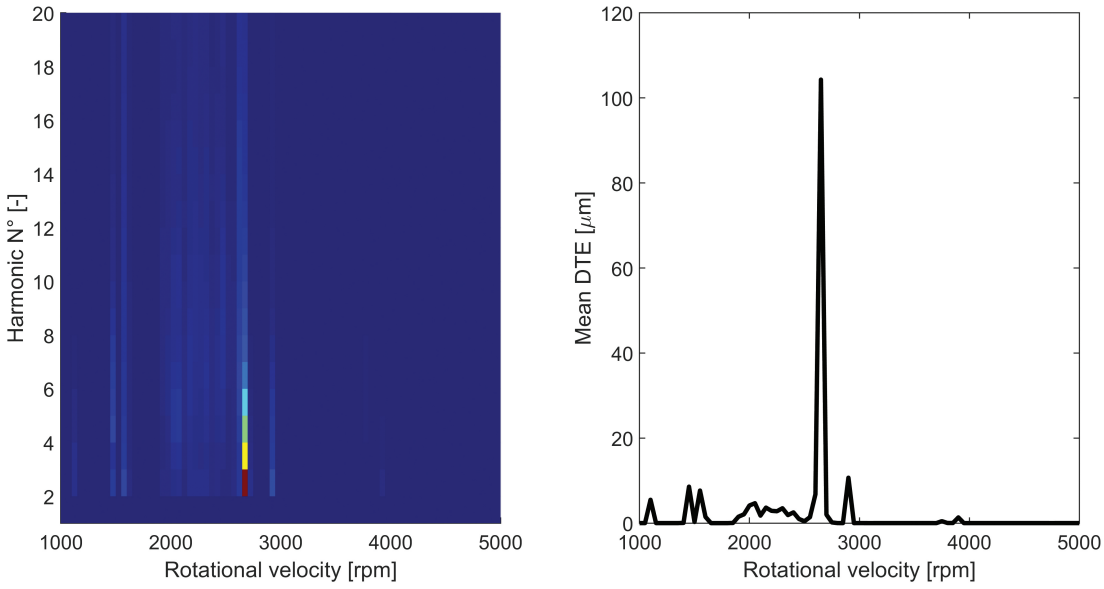

Fig. 6 Results at 15Nm

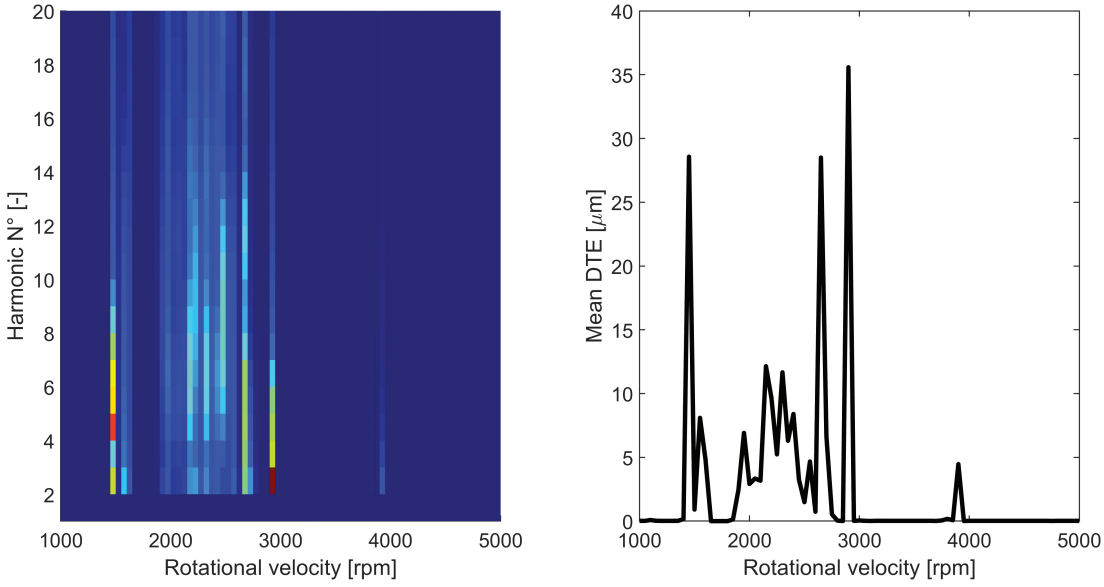

Fig. 7 Results at 50Nm

case, the energy at the main resonance near 2950 rpm is concentrated in the second and third harmonics, reaffirming the nonlinear transfer of energy to super-harmonics. However, unlike the 15 Nm case, there is also a broader distribution of energy across other harmonics and speeds, reminiscent of the 50 Nm behavior. This suggests that at 100 Nm the magnitude of the TVMS, primary excitation source, is now significantly larger due to the higher transmitted load. This stronger excitation is sufficient to re-excite system resonances, though with a different character and amplitude compared to the resonance at low torque. The significant response at 1300 rpm may correspond to the excitation of a different system mode or a sub-harmonic resonance that becomes prominent only at higher load levels.

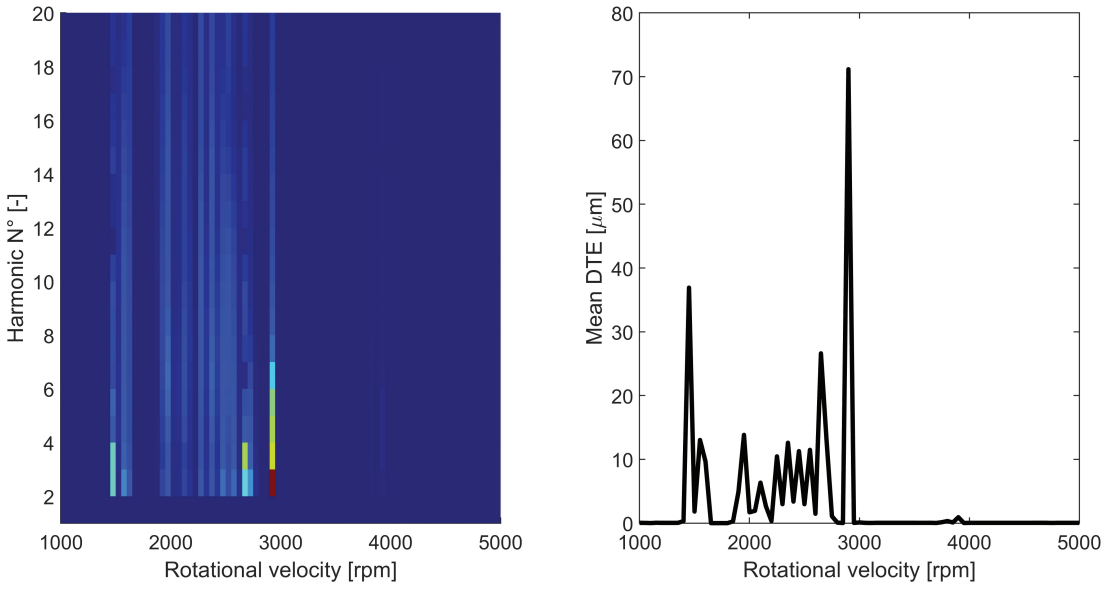

Fig. 8 Results at 100Nm

Conclusions

In this study, a computationally efficient NL-ROM was presented and employed to investigate the complex dynamic behavior of modern lightweight gear systems. The proposed methodology successfully bridges the gap between high-fidelity simulation and computational feasibility by retaining the full geometric detail of the flexible gear bodies from an underlying FE model while drastically reducing the system's degrees of freedom. A key innovation is the simulation of the gear's rolling motion by stepping through a pre-computed set of reduced matrices, which accurately captures the time-varying nature of the system. The model's predictive power is further enhanced by its ability to account for critical non-linear phenomena, including load-dependent TVMS, partial or total contact loss, and the subsequent VI upon tooth reconnection. The model was applied to analyze the dynamic response of a HCR spur gear pair with dissimilar web thicknesses under various operating conditions. The results revealed a profound and highly non-linear dependence of the DTE on the applied torque, showing that, for this scenario, at low torque the dynamic response is high, while a stabilizing effect is visible in the middle range. When the torque was increased further, resonant behavior re-emerged, though with a different character and lower peak amplitude than the low-torque case. These findings underscore the critical importance of analyzing gear dynamics across a full range of operating conditions, as system behavior at a single load point is not indicative of the overall performance. The demonstrated capability of the NL-ROM validates it as a powerful and practical tool for virtual prototyping and optimization in the early design stages of next-generation powertrains, enabling engineers to identify and mitigate potential NVH issues and explore complex design trade-offs with confidence and efficiency.

Acknowledgments This publication is part of the project PNRR-NGEU which has received funding from the MUR – DM 117/2023

References

1. Ozguven, H.N. and Houser, D.R. "Mathematical models used in gear dynamics - a review". *Journal of Sound and Vibration*, 121(3):383–411 (1988).
2. Bruzzone, F. and Rosso, C. "Sources of excitation and models for cylindrical gear dynamics: A review". *Machines*, 8(3) (2020).
3. Parker, R.G., Vijayakar, S.M., and Imajo, T. "Non-linear dynamic response of a spur gear pair: Modelling and experimental comparisons". *Journal of Sound and Vibration*, 237(3):435–455 (2000).
4. Parker, R.G., Agashe, V., and Vijayakar, S.M. "Dynamic response of a planetary gear system using a finite element/contact mechanics model". *Journal of Mechanical Design*, 122:304–310 (2000).
5. Eritnel, T. and Parker, R.G. "Nonlinear vibration of gears with tooth surface modifications". *Journal of Vibration and Acoustics*, 135:(051005)1–11 (2013).

6. Benatar, M., Handschuh, M., Kahraman, A., and Talbot, D. "Static and dynamic transmission error measurements of helical gear pairs with various tooth modifications". *Journal of Mechanical Design*, 141:103301 (2019).
7. Theodossiades, S. and Natsiavas, S. "Non-linear dynamics of gear-pair systems with periodic stiffness and backlash". *Journal of Sound and Vibration*, 229(2):287–310 (2000).
8. Natsiavas, S. and Giagopoulos, D. "25 - non-linear dynamics of gear meshing and vibro-impact phenomenon". pages 773–792 (2010).
9. Natsiavas, S. "Analytical Modeling of Discrete Mechanical Systems Involving Contact, Impact, and Friction". *Applied Mechanics Reviews*, 71(5):050802 (2019).
10. Wang, X.S., Wu, S.J., Hu, J.C., and Chen, J. "Chaos and bifurcation analysis of gear pair with wear fault". In *Material Sciences and Manufacturing Technology*, volume 629 of *Advanced Materials Research*, pages 506–510. Trans Tech Publications Ltd (2013).
11. Mohammadpour, M., Theodossiades, S., and Rahnejat, H. "Dynamics and efficiency of planetary gear sets for hybrid powertrains". *Proceedings of the Institution of Mechanical Engineers, Part C: Journal of Mechanical Engineering Science*, 230(7-8):1359–1368 (2016).
12. Shweiki, S., Rezayat, A., Tamarozzi, T., and Mundo, D. "Transmission error and strain analysis of lightweight gears by using a hybrid fe-analytical gear contact model". *Mechanical Systems and Signal Processing*, 123:573–590 (2019).
13. Palermo, A., Mundo, D., Hadjit, R., and Desmet, W. "Multibody element for spur and helical transmission error and the dynamic stress factor of spur gear pairs.". *Mechanism and Machine Theory*, 62:13–30 (2013).
14. Dai, X., Cooley, C.G., and Parker, R.G. "An efficient hybrid analytical-computational method for nonlinear vibration of spur gear pairs". *Journal of Vibration and Acoustics*, 141:(011006)1–13 (2018).
15. Guilbert, B., Velex, P., and Cutuli, P. "Quasi-static and dynamic analyses of thin-webbed high-speed gears: Centrifugal effect influence". *Proceedings of the Institution of Mechanical Engineers, Part C: Journal of Mechanical Engineering Science*, 233(21-22):7282–7291 (2019).
16. Craig, R.R. and Bampton, M.C.C. "Coupling of substructures for dynamic analyses". *AIAA Journal*, 6:1313–1319 (1968).
17. Bonisoli, E., Delprete, C., and Rosso, C. "Proposal of a modal-geometrical-based master nodes selection criterion in modal analysis". *Mechanical Systems and Signal Processing*, 23:606–620 (2009).
18. Rosso, C., Bruzzone, F., Maggi, T., and Marcellini, C. "A proposal for semi-analytical model of teeth contact with application to gear dynamics". *2019 JSAE/SAE Powertrains, Fuels and Lubricants* (2019).
19. Bruzzone, F., Maggi, T., Marcellini, C., and Rosso, C. "2d nonlinear and non-hertzian gear teeth deflection model for static transmission error calculation". *Mechanism and Machine Theory*, 166 (2021).
20. Bruzzone, F., Maggi, T., Marcellini, C., and Rosso, C. "Gear teeth deflection model for spur gears: Proposal of a 3d nonlinear and non-hertzian approach". *Machines*, 9(10) (2021).
21. Newmark, N.M. "A method of computation for structural dynamics". *Journal of the Engineering Mechanics Division*, 85:67–94 (1959).
22. Karayannis, I., Vakakis, A.F., and Georgiades, F. "Vibro-impact attachments as shock absorbers". *Proceedings of the Institution of Mechanical Engineers, Part C: Journal of Mechanical Engineering Science*, 222(10):1899–1908 (2008).
23. Bruzzone, F., Rosso, C., and Theodossiades, S. "Dynamic reduction technique for nonlinear analysis of spur gear pairs". *Nonlinear Dynamics*, 112:15797–15811 (2024).

Chapter 13
Electrical Chatter and Modal Response of Pin-Receptacle Contacts in Air and Oil

Marcus Behling, Phillip Misterman, Robert Justin Osborne, Robert C. Flicek, Karl Walczak, Eric Robbins, Robert J. Kuether, and Jonel Ortiz

Abstract Electromechanical switches are commonly used to allow electrical circuits to be mechanically connected and disconnected as needed to meet engineering design requirements. During severe shock and vibration environments, switches are sometimes observed to *chatter*, which refers to abrupt, momentary increases in the electrical resistance across the switch. Chatter is an undesirable phenomenon that is known to adversely impact signal integrity and thus degrade electrical contact performance. This work investigates the occurrence of electrical chatter in a simple pin-receptacle connection when exposed to shock-type loading. The electrical contacts are mounted in an aluminum housing referred to as the chatter fixture. The chatter fixture can be filled with viscous fluids, such as oil, to damp the vibrations and passively control the chatter behavior. In the experiments, the chatter fixture is bolted to a large metal base plate to simulate a stiff boundary condition, together making up the test assembly. This study explores the influence of oil on both the electrical chatter response as well as the modal response of the test assembly using a combination of modeling and experimentation. Experimental results provide insight into the relationship between impact force and chatter response in oil versus in air. A simplified 2D finite element model was developed and calibrated to accurately predict observed chatter responses using the range of inputs measured from the experiments. The results of this investigation demonstrate the difference in chatter performance between electrical contacts submerged in oil versus air and provide insight into the simplified model used to predict chatter in response to shock-type loading.

Keywords electrical chatter · bifurcated receptacle · impact testing · modal analysis · finite element modeling

Marcus Behling
Graduate Research Assistant, Department of Mechanical Engineering, Brigham Young University, mebehlin@byu.edu155 East 1230 North, Provo, UT 84602
e-mail: mebehlin@student.byu.edu

Phillip Misterman
Graduate Research Assistant, Department of Aerospace Engineering, Iowa State University, pgm@iastate.edu
533 Morrill Rd., Ames, IA 50011
e-mail: Phillip.misterman@gmail.com

Robert Justin Osborne
Graduate Research Assistant, Department of Mechanical and Aerospace Engineering, University of Southern Florida, rjosborn@usf.edu
4202 E Fowler Ave, Tampa, FL 33620
e-mail: rjosborn@usf.edu

Robert C. Flicek* · Karl Walczak · Eric Robbins · Robert J. Kuether · Jonel Ortiz
Sandia National Laboratories
1515 Eubank Blvd SE, Albuquerque, NM 87123
e-mail: rcflice@sandia.gov; kawalcz@sandia.gov; erobbin@sandia.gov; rjkueth@sandia.gov; jonorti@sandia.gov

* Sandia National Laboratories is a multimission laboratory managed and operated by National Technology and Engineering Solutions of Sandia, LLC., a wholly owned subsidiary of Honeywell International, Inc., for the U.S. Department of Energy's National Nuclear Security Administration under contract DE-NA-0003525. SAND2025-12294C

© The Author(s), under exclusive license to River Publishers 2026

Kristin B. Zimmerman, PhD (eds.), *Nonlinear Structures & Systems, Vol. 1*, Conference Proceedings of the Society for Experimental Mechanics Series, https://doi.org/10.13052/rp-9788743814122

Introduction

Electrical switches and relays are used extensively in engineering design to selectively allow or interrupt the flow of electrical power or data signals. Normal operating conditions often subject mechanical components to relatively severe shock and vibration environments, e.g., during aircraft takeoff and landing. These types of severe acceleration environments can cause the electrical contact resistance across a closed switch to increase abruptly, potentially corrupting or preventing the transmission of intended signals. A past study found that chatter can be caused by elastic deformation of the pin and receptacle in a switch [1]. These switches can be submerged in oil as lubricating the interface is known to improve performance, and this study seeks to characterize the chatter of the switch when submerged in oil, as the modal parameters of a structure have been observed to change when submerged in a liquid [2, 3].

As mentioned previously, physical separation between the pin and receptacle can cause chatter [4]. Initial stages of chatter research assumed that the large discrepancy between the frequency of chatter events (megahertz) and the natural frequencies of the contact pair and the test fixture (kilohertz) implied that chatter was not caused by modes of vibration. However, computational analysis by Zastrow [1] demonstrated that modes of vibration in the kilohertz range can cause very brief physical separation between the pin and the receptacle, producing chatter events on the order of megahertz. Although Zastrow's work demonstrated that the resonant modes of vibration do play a critical role in understanding chatter in electrical switches, it focused on contacts in air and did not study the effect of oil.

Johnson [5, 6] developed a novel experimental method for performing modal analysis of a pin and bifurcated receptacle submerged in oil. These experiments faced several unique challenges due to the small dimensions of these parts and the difficulty of exciting them when they are submerged in oil. However, Johnson was able to compute natural frequencies and modal damping values experimentally for the pin and receptacle in air and in oil. Johnson compared the experimental results to the natural frequencies output by a computational model, but this comparison could only be performed for tests in air, as it was not possible to include the influence of oil in the structural dynamics models available at that time.

The primary goal of this study is to understand how chatter characteristics differ for electrical switches submerged in oil versus electrical switches in air. To accomplish this, a test fixture containing the pin-receptacle is excited across a wide range of input force levels and chatter is measured in oil and air. A secondary objective is to calibrate a 2D model of the pin-receptacle to predict the chatter response. A parameter study is performed to understand the effect of each variable on predicted chatter, and experimental data is used to calibrate the model. The 2D model is then used to gain insight into the mechanisms causing chatter.

In the next section, the experimental procedure and test setup are described. In section three, a model of the fixture-pin-receptacle system is introduced, and its parameters are described. In section four, the experimentally obtained chatter results are shown and compared in oil and air. In section five, the model calibration procedure is described in detail, and the selected oil and air parameters are compared. In section six, the experimental results are compared to those predicted by the model. Finally, conclusions are given in section seven.

Experimental Setup

The experimental setup consists of a chatter fixture bolted to a steel base plate to simulate a stiff boundary condition, which is then placed on a rubber mat to isolate it from the table upon which it is placed. The fixture, shown in Figure 1, was machined out of a 6061 aluminum block to 63.5 mm x 63.5 mm x 101.6 mm and designed to hold the pin and receptacle in the inserted state of the contact pair. The cylindrical pin that has dimensions of 0.6865 mm x 6.147 mm is made of Paliney 7, and the approximately rectangular receptacle is 8.66 mm x 1.321 mm x 0.2032 mm and made of NeyoroG. The cavity is filled with Krytox GPL 101 oil that fully submerges the switch. The output of the pair is connected to a National Instruments MyRio chatter tester with a sampling rate of 40 MHz and configured to detect changes in electrical resistance greater than 120 Ohms. Because of this high resistance threshold, it is assumed that chatter occurs when there is physical separation between the receptacle and pin. An array of 500g tri-axis accelerometers is attached to the exterior of the fixture to measure the response of the experimental setup to the applied impact load. Polytec Laser Doppler Vibrometers (LDV) are used to measure the velocity of the pin and receptacle pair to measure local motions on the electrical contacts. A PCB Piezotronics 086C05 modal hammer with a range of 0-22kN is used to excite the test fixture at the red "x" location marked in the center image in Figure 1. Data from the accelerometers and LDVs is collected using a Siemens SCADAS and evaluated in the Impact Testing Module in Testlab.

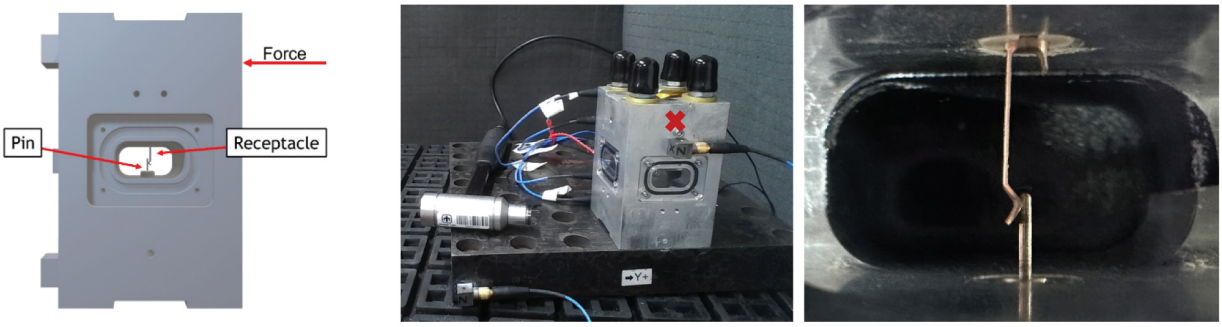

Fig. 1 Test fixture used to study chatter (left), experimental setup (center), and close-up of pin and receptacle installed in the fixture (right)

Modal Analysis and Boundary Condition

To assess the extent to which the fixture has a true fixed base in this configuration, a modal test was performed, revealing that the first elastic mode of the plate occurs at 1356 Hz. Ideally, the fixture would be attached to a larger, more rigid block to better match the desired boundary condition, but this is challenging to achieve in a laboratory setting. Despite the observed resonance of the test setup, the chosen test setup seems to reasonably approximate the boundary condition such that there was an observed first bending (cantilever) mode of the chatter fixture at 1521 Hz, as shown in Figure 2. This mode also appears in a 3D finite element model (FEM) of the test assembly, providing confidence in the understanding of the boundary conditions of the experiment. The chatter fixture was also tested in a free-free condition, in addition to the plate-mounted boundary condition, but the plate-mounted configuration was used for shock tests as chatter was more easily excited in that configuration.

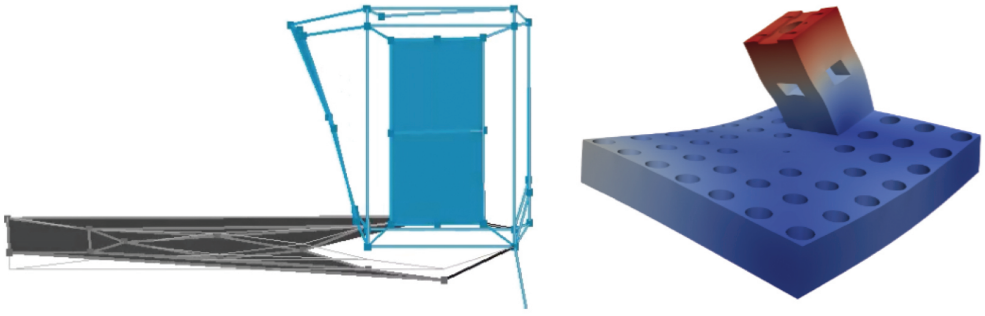

Fig. 2 First fixture bending mode at 1521 Hz (left) and 2nd elastic FEM mode at 1556 Hz

Experimental Method

Chatter events are initiated by impacting the structure with a modal hammer at the location marked by the red "x" in Fig. 1. In past studies, modal shakers were used to attempt to induce chatter, though it was discovered that the hardware limitations of the shakers failed to achieve the objective of observing chatter [7]. The impact location was chosen to readily excite chatter in the direction orthogonal to the pin and receptacle. A drive-point frequency response function (FRF) was taken at the impact location to help calibrate the simplified chatter model as described in Section 5. Hammer hits were performed at various force levels and the resulting chatter events were recorded with the MyRio tester. The number of chatter events and distribution of chatter durations were noted to change as impact amplitude increased. To accurately observe and assess

these phenomena, the force amplitudes were divided into bins of 200 N width. The force range of interest was 300-4000 N with an average impact duration of 350 μs. The lower limit was set to 300 N as no chatter events were observed below this input force, and the upper limit was set to 4000 N to prevent damage to the test fixture. A steel hammer tip was used to provide a consistent broadband frequency excitation up to 5000 Hz with less than 10 dB force power spectral density drop-off below this frequency. Thus, the modal hammer input has sufficiently broad frequency bandwidth to excite the relevant modal response of the test assembly.

Chatter measurements were first taken with the pin-receptacle submerged in oil. After sufficient data was collected, the oil was drained from the fixture, and measurements were taken with the pin-receptacle in air. The pin-receptacle was cleaned with a cloth to remove the oil, though there was likely some residual oil on the contact pair. It is likely that the test setup changed slightly in other ways during the draining process - for example, the preload in the pin-receptacle could have been altered - but efforts were made to reduce these differences.

Modeling

A simplified, two-dimensional FEM was previously developed for the purpose of predicting the chatter behavior of the pin and receptacle. A schematic of this model is shown in Figure 3. The chatter fixture is modeled as a single degree-of-freedom mass-spring-damper system, where the natural frequency of the mode is intended to represent that of the first cantilever bending mode of the fixture that is experimentally observed in the test assembly. Note that this model only captures a single mode of the chatter fixture even though there are other test assembly modes in the frequency band of interest. Though a significant simplification, this may be a reasonable assumption as higher order modes have been observed to affect chatter less significantly in [8]. The response of the system to the haversine input force was calculated using a nonlinear Newmark integration scheme which is described in [9]. The response was calculated from 0 to 0.05 seconds, and 50,000 time steps were used to minimize the temporal discretization error in numerical integration and capture small chatter durations predicted by the model.

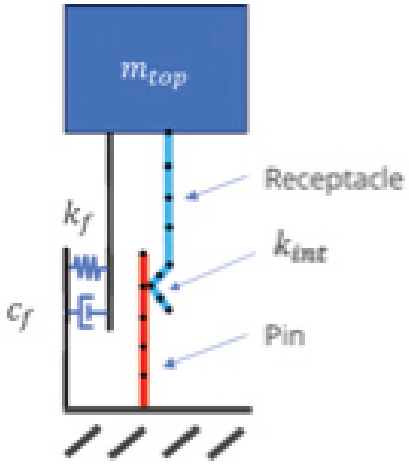

Fig. 3 2D FEM of the fixture, pin, and receptacle

The pin and receptacle represented in Figure 3 are modeled using linear beam elements according to

$$[M]\{\ddot{x}\} + [C]\{\dot{x}\} + [K]\{x\} = \{F\}, \tag{1}$$

where [M], [C], [K] are the mass, damping, and stiffness matrices, respectively, which are calculated using the method presented in [10]. In the preceding equation, {x} is the displacement vector, and {F} is a vector of applied forces, while the overdot represents the derivative with respect to time. The fixture is modeled as a single lumped mass element that is attached to the top of the receptacle and is connected to ground via a linear spring element (note that the viscous dashpot was set to zero). The base node of the pin is connected to ground.

The contact nonlinearity of this system is captured in the interface force between the pin and receptacle node pair, which is assumed to be Hertzian as derived in [11]. The following form is assumed,

$$F_{int} = e \cdot k_{int} \cdot \delta^{3/2}, \tag{2}$$

Table 1 Model input parameters

Parameter	Symbol	Units
Fixture stiffness	k_f	N/mm
Interface stiffness	k_{int}	N/mm
Target frequency	f_{target}	Hz
Fixture damping ratio	ζ	-
Impact duration	t_{impact}	S
Impact amplitude	F_{peak}	lb

where k_{int} is the interface spring constant, e is a boolean vector with appropriate entries to apply the contact force to the FEM, and δ is the relative displacement in the normal direction between the pin and receptacle contact node. Note that the beam elements are meshed in their undeformed configuration, so there is initial overlap in the model. A quasi-static preload simulation is required to first find the static equilibrium position of the system such that the static equilibrium satisfies

$$[K]\{x_{pre}\} + F_{int}(x_{pre}) = 0. \tag{3}$$

This is achieved by applying an outward force to the receptacle at the contact node and solving the quasi-static equations as the force ramps to zero using a damped Newton method. From this equilibrium position, the natural frequencies and mode shapes of the system around this linearized state were then solved according to the linearized eigenvalue problem

$$\left(K + \left.\frac{\partial F_{int}}{\partial x}\right|_{x_{pre}} - \omega^2 M\right)\phi = 0. \tag{4}$$

Rayleigh damping is used in this model, following the form

$$[C] = \alpha[M] + \beta[K], \tag{5}$$

where the α and β coefficients are calculated according to

$$\begin{bmatrix} \alpha \\ \beta \end{bmatrix} = \begin{bmatrix} \frac{1}{2\omega_1} & \frac{\omega_1}{2} \\ \frac{1}{2\omega_2} & \frac{\omega_2}{2} \end{bmatrix}^{-1} \begin{bmatrix} \zeta_1 \\ \zeta_2 \end{bmatrix}. \tag{6}$$

In the previous equation, $\omega_1$and ω_2 are the first two natural frequencies solved for in Eq. (4), and ζ_1 and ζ_2 are the corresponding viscous damping ratios. These damping values were assumed to be equal and are specified in the model as $\zeta = \zeta_1 \ = \zeta_2$.

The final nonlinear dynamic model used to simulate the time-varying contact force in the pin and receptacle due to an externally applied force is written as

$$\begin{gathered} [M]\{\ddot{x}\} + [C]\{\dot{x}\} + [K]\{x\} + F_{\text{int}}(x) = \{F\} \\ x(t=0) = x_{\text{pre}} \\ \dot{x}(t=0) = 0 \end{gathered} \tag{7}$$

Chatter duration was calculated according to the time that the pin and receptacle were out of contact and the interface force is equal to zero, i.e.,

$$t_{chatter} = \sum_{i=1}^{n} t_{i,\delta>0}, \tag{8}$$

where $t_{i,\delta>0}$ is the ith time segment where $\delta > 0$, indicating that the pin and receptacle are out of contact.

The parameters that inform the 2D model are fixture stiffness k_f, interface stiffness k_{int}, fixture damping ζ, target frequency f_{target}, impact duration t_{impact}, and impact amplitude F_{peak}; these are listed in Table 1 for ease of reference.

Experimental Results

The relationship between impact amplitude F_{peak} and chatter response was investigated first for the experiment involving the electrical contacts submerged in oil. The number of observed chatter events, along with the total duration of chatter, is

plotted against the impact force F_{peak} in Figure 4. There appears to be an exponential relationship between peak input force and the number and total duration of chatter events below ∼800 N in oil, and the relationship is fairly linear above this force. Some of the variability in the data may be attributed to changes in pulse width t_{impact} between hits.

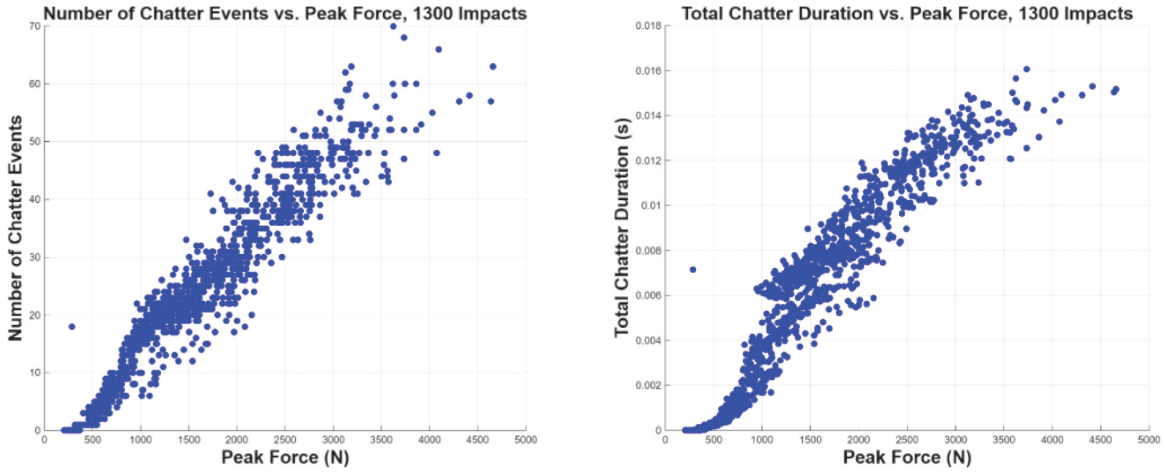

Fig. 4 Number of chatter events (left) and total chatter duration (right) versus impact amplitude in oil

The same set of chatter tests was performed with the oil drained, and these results are shown in Figure 5; as shown in this figure, more chatter events are observed in air than oil at high impact amplitudes, i.e., above 2000 N. Below this force level, there are actually more chatter events when the switch is submerged in oil, suggesting that the switch performs better in oil at high impact amplitudes but worse at lower amplitudes. In air, there is a significant increase in the number of chatter events between 1500 and 2500 N, and a similar, more understated, phenomenon is observed in oil between 500 and 1000 N.

Note that the primary intended difference between the test assemblies used for the oil and air experiments was the presence or absence of oil in the internal cavity of the chatter test fixture. However, in addition to this intended difference between the two test configurations, it is also possible that other uncontrolled factors changed between tests. These potentially uncontrolled factors are numerous, but include different bolt torque, preloaded state, or altered part alignment. Since it is not possible to isolate the effect of test-to-test variability with the present dataset, some of the observed differences between the chatter behavior in oil and air may reflect test-to-test variability.

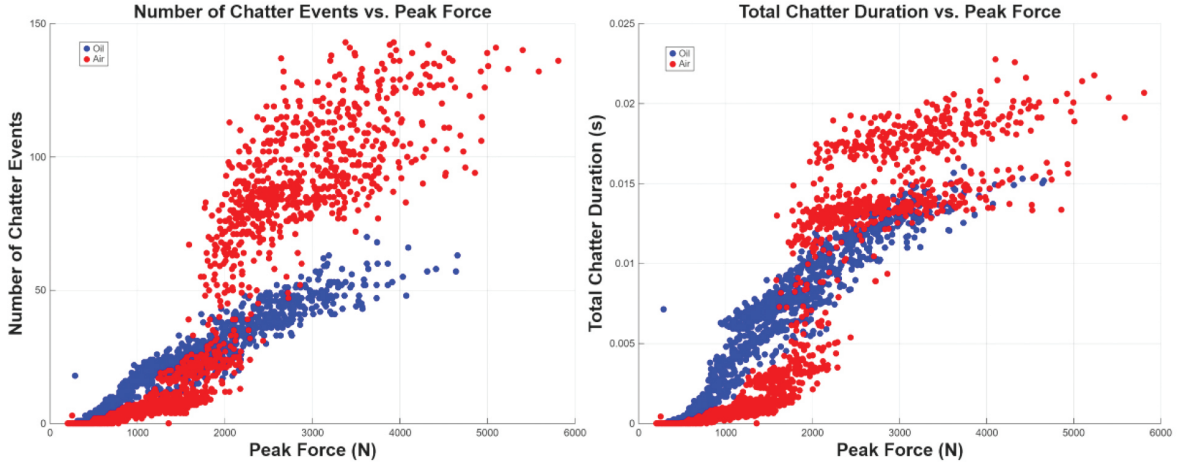

Fig. 5 Number of chatter events (left) and total chatter duration (right) vs. peak force for experiments and models in oil and air

The distributions of measured chatter durations are shown in Figure 6. They are skewed towards lower values at low force levels and are bimodal at high force levels. This suggests that there may be two distinct mechanisms causing chatter, one excited at higher force levels and the other at low force levels.

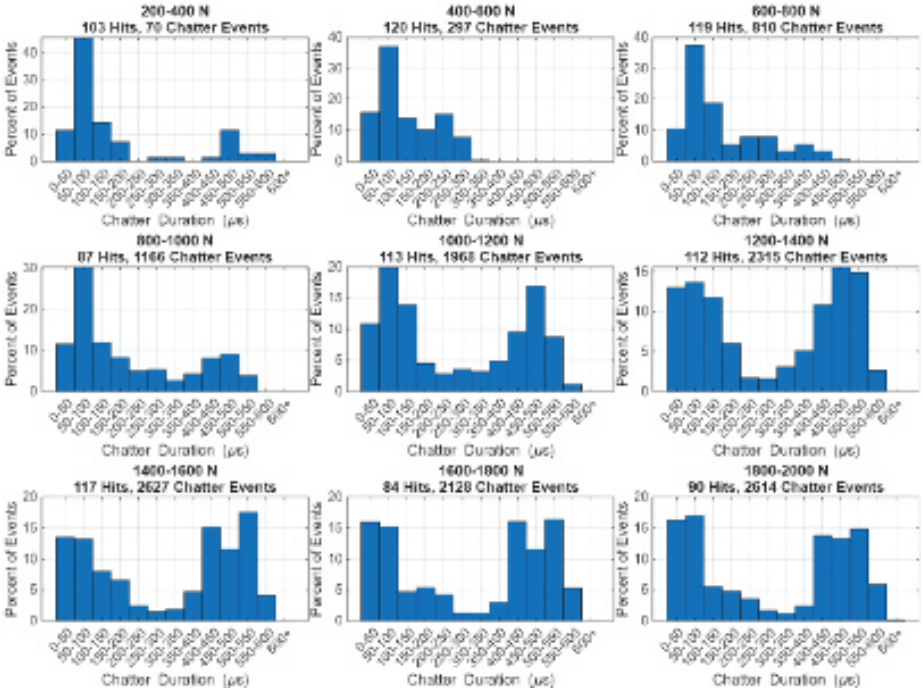

Fig. 6 Distributions of measured chatter durations in oil at varying force levels

A plot of the time history showing the chatter state measured in the experiment is shown in Figure 7 for a 500N (red) and 1928N (blue) impact. Earlier in the time response, the chatter events are longer in duration and occur in rapid succession. As the response decays, the chatter events are shorter in duration with longer time intervals between them. This supports the distributions shown in Fig. 6, as there again seem to be two different chatter regimes when the switch is excited at a high force level.

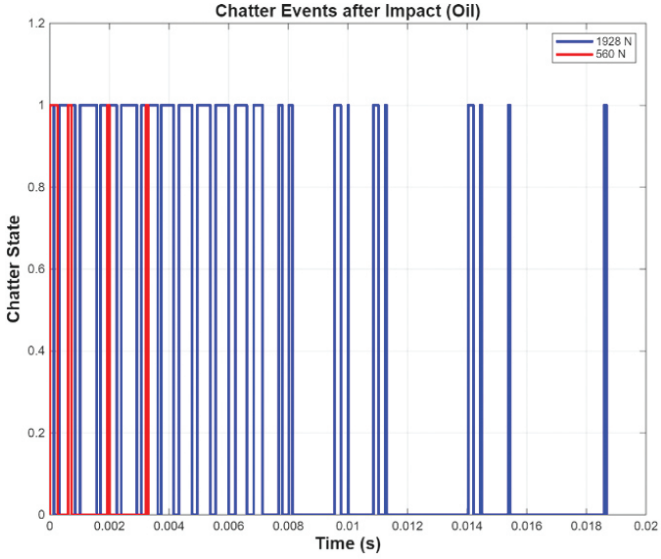

Fig. 7 Measured chatter events in oil following impacts, where “0” denotes contact and “1” denotes loss of contact

Model Calibration and Parameter Studies

Several experimental measurements were used to calibrate the simplified 2D model to match the conditions of the test. The amplitude of the impact applied to the fixture in the experiments was measured with a load cell, and the applied pulses were recorded. The impact duration was noted to vary slightly from one impact to the next but remained fairly constant, as shown in Figure 8. The impact duration was set to 350 μs to match the average value observed in the tests. The haversine force profile with this duration is overlaid on the measured forces in Figure 8. The variability in impact duration contributes to the spread of the chatter data observed in Section 4. With this determination from the tests, the input force could now be parameterized by the amplitude of the applied force.

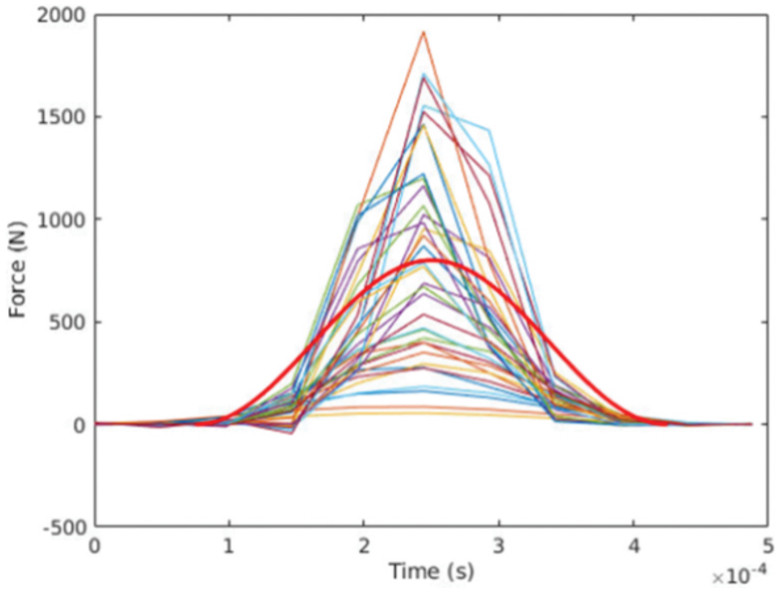

Fig. 8 Measured impact forces and haversine input used in the model (red)

It was also desired to match the natural frequency of the chatter fixture bending mode, as this mode is expected to significantly contribute to chatter, producing relative displacement between the base of the pin and that of the receptacle. The target frequency of the model f_{target} was selected to match the natural frequency of the first fixture bending mode which occurs at 1521 Hz. The fixture stiffness k_f was initially estimated using a 3D FEM but was calibrated, along with fixture damping ζ, such that the top mass drive-point FRF matched the measured drive-point FRF as shown in Figure 9. Intuitively, ζ was observed to change the width and height of the first peak. The experimentally measured damping was used as a starting point for this value but was lowered slightly to better match the chatter characteristics. As a result, the model's peak is a bit higher than that of the experimental FRF. Increasing the fixture stiffness k_f was observed to reduce the magnitude of the FRF uniformly with respect to frequency. It is noted that the FRFs do not match well past 2000 Hz as the model is only capable of capturing the first bending mode of the chatter fixture.

Parameter studies were performed by simulating the response of the 2D FEM with a selected set of parameters from 300-4000 N in increments of 50 N. The parameters were then modified, and the same process was performed to understand the effects of each parameter on the number and duration of chatter events. These effects were observed qualitatively and are shown in Table 2. In addition to the number and duration of chatter events, the table also notes the effect of the parameters on the chatter threshold, or force at which chatter starts to occur, as well as the distribution of the chatter durations. Interface stiffness and fixture damping were noted to affect the model most significantly, with interface stiffness primarily affecting the chatter threshold, and fixture damping primarily changing the slope of the curve. Using this information, this process was repeated, modifying parameters each time, until a satisfactory match was obtained between the model and experiment.

The last unknown parameter is interface stiffness of the contact penalty spring, k_{int}. Because it does not noticeably affect the shape of the drive-point FRF, it is chosen to match chatter characteristics, specifically the number and total duration of chatter events, as a function of force. The sets of parameters that best fit experimental data for the oil and air are shown in Table 2. The fixture stiffness k_f, target frequency f_{target}, and pulse width t_{impact} remain the same in oil and air, while the interface stiffness k_{int} and fixture damping ζ change significantly; the former doubles between oil and air, and the latter decreases when oil is removed.

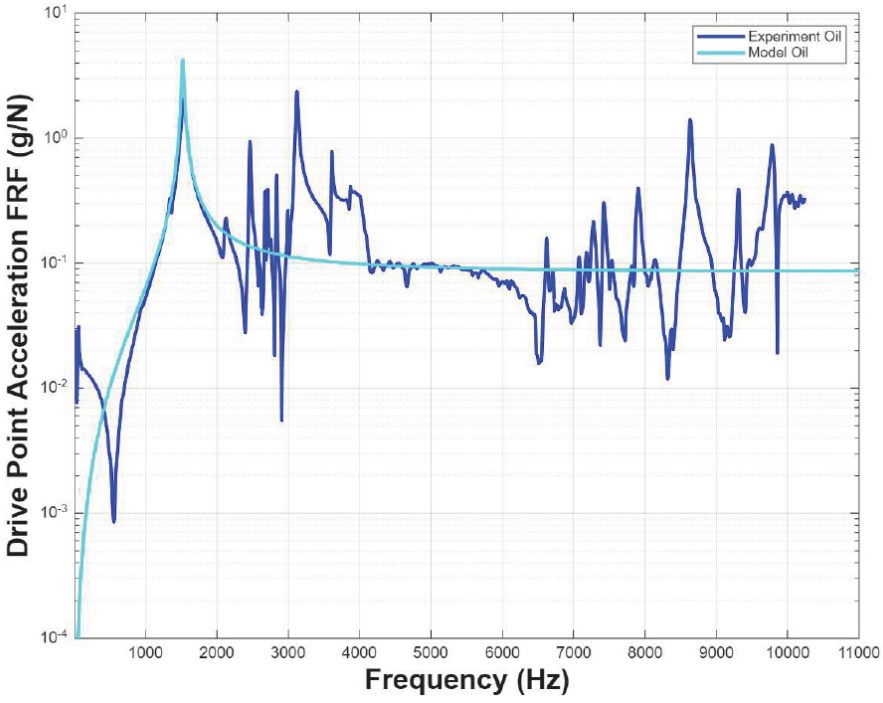

Fig. 9 Experimental (blue) and model (cyan) drive-point FRFs at top of fixture

Table 2 Observed effect of parameters on number and duration of events, chatter threshold, and chatter duration distribution

	Fixture Stiffness $\uparrow k_f$	**Interface Stiffness** $\uparrow k_{int}$	**Target Frequency** $\uparrow f_{target}$	**Fixture Damping** $\uparrow \zeta$	**Impact Amplitude** $\uparrow F_{peak}$	**Impact Duration** $\uparrow t_{impact}$
Number of Chatter Events N_{events}	↓	↓	↓	↓	↑	↑
Chatter Duration t_{dur}	↓	↓	↓	↓	↑	↑
Chatter Threshold	↑	↑	↑	↑	**N/A**	↓
Chatter Distribution	**Less bimodal**	**Less bimodal**	**Less bimodal**	**Less bimodal**	**More bimodal**	**More bimodal**

Table 3 Calibrated model parameters for oil and air

	Fixture Stiffness k_f **(N/mm)**	**Interface Stiffness** k_{int} **(N/mm)**	**Target Frequency** f_{target} **(Hz)**	**Fixture Damping Ratio** ζ	**Pulse Width** t_{impact} **(s)**
Oil	110,406	7,000	1521	0.008	3.5e-4
Air	110,406	14,500	1521	0.005	3.5e-4

The change in damping ζ from .008 in oil to .005 in air seems reasonable given that oil is more viscous than air. The difference in interface stiffness k_{int} is less intuitive, and the cause of this change is unknown, though it may reflect the changes incurred in the draining process mentioned previously.

Model-Experiment Comparison

As seen in Figure 10, the 2D models accurately predict the number of chatter events as a function of force, suggesting that the model is robust and can account for changes in the medium in which the switch operates. No mass-loading term was included to account for the fluid and the model still performed quite well. The 2D model is very computationally efficient, running in about 25 seconds per simulation.

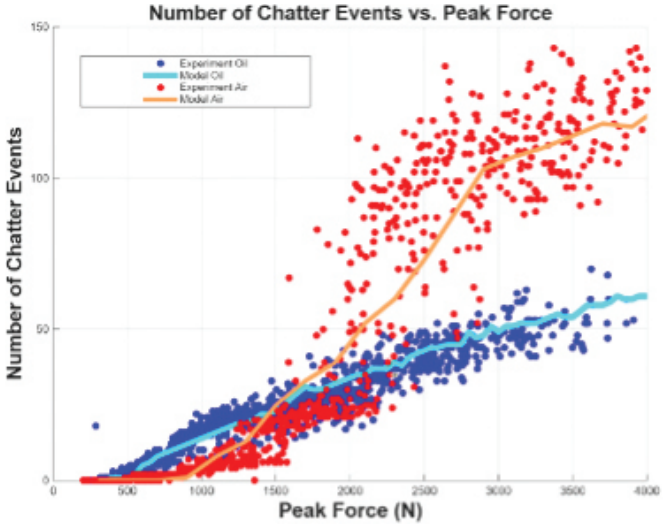

Fig. 10 Number of measured and modeled chatter events in oil and air

The distributions of chatter event duration in the calibrated oil model are shown in Figure 11. The model fails to capture the bimodal nature of the distributions of the experimental results shown in Figure 6. Though, it correctly predicts a large proportion of longer duration events, it significantly under-predicts the number of short duration events. One theory is that the long duration events are primarily caused by the bending motion that the model captures, whereas the short duration events may be caused by motion not captured in the model: sliding, lateral shearing, or torsional, for example.

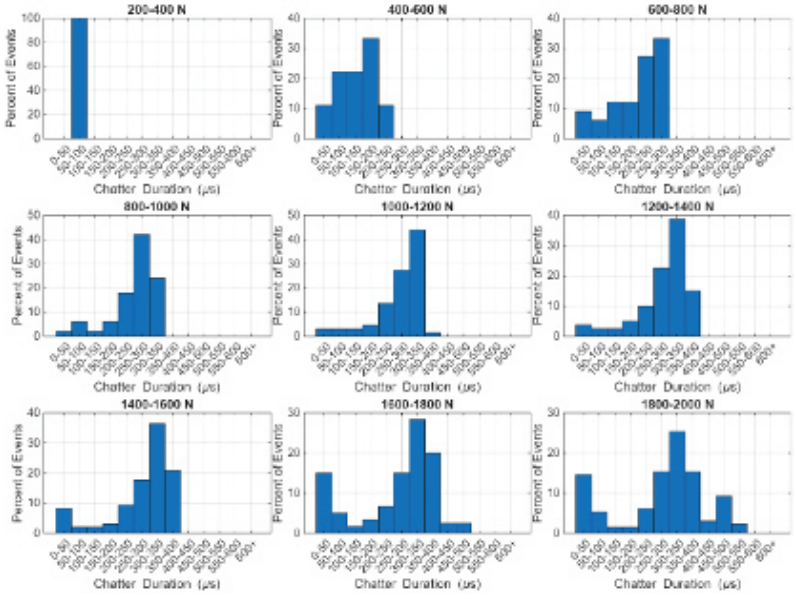

Fig. 11 Distributions of model chatter durations in oil at varying force levels

Conclusion

In this study, chatter was characterized in an electrical switch submerged in oil. This was done by impacting the chatter fixture in which the switch was installed and recording changes in resistance using a National Instruments MyRio system. Chatter events were recorded for over 1,000 hammer impacts to the system at various force levels. The data revealed that below a certain force threshold, no chatter occurred. Above this first threshold, the amount of chatter increases at a super-linear rate. As the input force increases further, another threshold is reached, above which the amount of chatter increases linearly with increasing input force.

Following the initial series of experiments in oil, the oil was removed from the fixture and the experiment was repeated with over 1,000 impacts at different force levels. The chatter data collected in air followed a similar pattern as described above, being broken into three regimes: no chatter at low forces, super-linearly increasing chatter at moderate forces, and linearly increasing chatter at high forces. However, the number of chatter events for a given input force level differed substantially for the tests in oil and in air.

A simple 2D model was used to accurately predict chatter behavior in the pin-receptacle system in the presence of air and oil. The simplicity of the model allowed us to efficiently investigate how its parameters affect chatter, and limited experimental data is required to select the model's parameters. A drive-point FRF at the impact location was used to calibrate the parameters related to the fixture's dynamics. Although many chatter measurements were obtained at various force levels during testing, the model parameters could be tuned with far fewer chatter measurements. The computational efficiency of the 2D model and limited measurements required to tune it allow chatter to be characterized quickly and efficiently, allowing for faster design iteration and ultimately, improved signal transmission.

Lastly, chatter duration was observed to follow a bimodal distribution at high force levels, suggesting two distinct chatter mechanisms. At high response levels, the model had similar distributions to those measured, suggesting that chatter is governed primarily by the fixture bending mode at higher levels. At lower response levels, the model predicted fewer chatter events than were observed, suggesting that it fails to capture a portion of the chatter events observed experimentally.

Acknowledgments This research was conducted at the 2025 Nonlinear Mechanics and Dynamics Research Institute hosted by Sandia National Laboratories and the University of New Mexico. We would like to acknowledge the support from Bill Flynn at Siemens and Rob Warmbold at Polytec for providing experimental equipment and software to equip the laboratories at NOMAD.

* Sandia National Laboratories is a multimission laboratory managed and operated by National Technology and Engineering Solutions of Sandia, LLC., a wholly owned subsidiary of Honeywell International, Inc., for the U.S. Department of Energy's National Nuclear Security Administration under contract DE-NA-0003525. SAND2025-0000.

References

1. B. G. Zastrow, R. C. Flicek, K. M. Johnson, K. A. Walczak, B. R. Pacini, B. Johnson, C. Schumann and F. Rafeedi, "Investigation of electrical chatter in bifurcated contact receptacles," in 2021 IEEE Holm Conference on Electrical Contacts, San Antonio, TX, USA, 2021.
2. G. Moraga, X. Xia, S. Roig, C. Valero, D. Valentín, M. Egusquiza, L. Zhou, E. Egusquiza, A. Presas, Experimental study on the influence of vibration amplitude on the fluid damping of a submerged disk, Journal of Sound and Vibration, Volume 569, 2024, 118099, ISSN 0022-460X, https://doi.org/10.1016/j.jsv.2023.118099.
3. D. G. Gorman, I. Trendafilova, A. J. Mulholland, J. Horáček, Analytical modelling and extraction of the modal behaviour of a cantilever beam in fluid interaction, Journal of Sound and Vibration, Volume 308, Issues 1–2, 2007, Pages 231-245, https://doi.org/10.1016/j.jsv.2007.07.032.
4. J. Brady, "Anomalous Behavior of Reed Relays Under Accelerated Life-Test Conditions," in *IEEE Transactions on Parts, Hybrids, and Packaging*, vol. 13, no. 1, pp. 51-60, March 1977, doi: 10.1109/TPHP.1977.1135170.
5. K. M. Johnson, "Characterization of a Small Electro-Mechanical Contact Using LDV Measurement Techniques (SAND2018-1206C)," Sandia National Laboratories, Albuquerque, NM, USA, 2018.
6. K. M. Johnson, "Characterization of a small electro-mechanical contact using non-conventional measurement techniques," University of New Mexico, Albuquerque, NM, USA, 2017.
7. B. Furman and L. Nester, "Final Presentation: Investigation of Electrical Contact Chatter in Pin-Receptacle Contacts," Sandia National Laboratories, Albuquerque, NM, USA, 2023.
8. C.C. Lo, A cantilever beam chattering against a stop, Journal of Sound and Vibration, Volume 69, Issue 2, 1980, Pages 245-255, https://doi.org/10.1016/0022-460X(**??**)90609-4.
9. K. Subbaraj and M. A. Dokainish, A Survey of Direct Time-Integration Methods in Computational Structural Dynamics – II. Implicit Methods, Computers & Structures, Volume 32, Issue 6, 1989, Pages 1387-1401
10. R. Craig and A. Kurdila, *Fundamentals of Structural Dynamics*, 2nd ed. Wiley, 2006.
11. K.L. Johnson, *Contact Mechanics*. Cambridge: Cambridge University Press, 1985.

Chapter 14
Measurement of Local Contact Stiffness Using Ultrasound

R. Justin Osborne, Levi Mydlenski, and Drithi Shetty*

Abstract Friction in built-up structures has a nonlinear impact on the overall dynamics and is difficult to predict due to the different phenomena occurring at various length scales. A major challenge is observing and quantifying the interfacial behavior in-situ. One solution that has long been studied is the use of ultrasound to measure the interfacial contact stiffness. However, existing research requires complete immersion of the setup in water or permanently attaching the transducer to the test article using epoxy to ensure good, consistent coupling between the transducer and metal. Immersion would change the interface conditions whereas epoxy-based coupling would mean that an array of transducers is required to measure larger contact surfaces. This paper proposes a low-cost, scalable, roving-transducer method that uses a conformable delay-line with a magnetic holder to dry-couple the transducer to the metal surface. A series of quasi-static compression tests is performed to assess the accuracy and repeatability of the proposed method.

Keywords ultrasound, interfacial contact stiffness, friction, microslip, roving transducer

Introduction

Mechanical joints are used for the assembly of components in various engineering applications from large dynamic structures such as crawler cranes to smaller components such as gas turbine blades or piston connecting rods. Partial slip contact within these joints results in the frictional dissipation of energy and changes to the structural stiffness [1]. In some cases, friction in these joints may be beneficial, but is often detrimental [2]. Improved modeling of the contact during dynamic simulation is expected to reduce the cost of prototyping and dynamic testing as well as contribute to extending the life of the component. Accurately modeling the contact interface is challenging because there are complex mechanisms occurring at various scales, from material interactions at the nanoscale to the effects of surface roughness at the microscale. Plasticity, thermal effects, the formation and breakage of chemical bonds, along with additional mechanisms, may also be involved, increasing the complexity in accurately modelling the overall response of the contact.

A significant challenge in studying the effect of these mechanisms is measuring, or even observing the change in the contact interface in-situ. However, some approaches do exist for evaluating changes in the contact interface such as Digital Image Correlation (DIC), pressure films, and optical methods but with their limitations. For example, DIC can be used to measure the relative displacement of the interface but can only be used to observe the changes on the exterior of the interface and not across the joint [3]. As an alternative, static or dynamic pressure films can be used to provide information on contact pressure at the interface. However, addition of the pressure film alters the physical properties of the contact interface [4]. Optical methods based on internal reflection [5], can also be used, but they require transparency in at least one portion of the joint, limiting their use.

An alternative method to investigate changes in the interface is the use of ultrasonic reflectometry. The contact stiffness at metal interfaces can be determined from the coefficient of reflection of an ultrasonic beam [6, 7]. L. Pesaresi et al. [8] utilized this relationship to detect stick and slip states in contact interfaces subjected to high-frequency shear vibration using epoxy coupled transducers. The use of epoxy coupling requires multiple transducers to measure across an area which can be prohibitive in both cost of the transducer array and attachment space which limits how close measurements can be

R. Justin Osborne · Levi Mydlenski · Drithi Shetty
Department of Mechanical and Aerospace Engineering, University of South Florida, Tampa, 33620, FL, USA
e-mail: rjosborn@usf.edu; lamydlenski@usf.edu; dshetty@usf.edu

*Corresponding author email: dshetty@usf.edu

© The Author(s), under exclusive license to River Publishers 2026

Kristin B. Zimmerman, PhD (eds.), *Nonlinear Structures & Systems, Vol. 1*, Conference Proceedings
of the Society for Experimental Mechanics Series, https://doi.org/10.13052/rp-9788743814122

taken. A more scalable approach is use of a roving transducer. However, one challenge with doing so is ensuring consistent coupling between the transducer and the metal surface at every measurement location. Jerome et al. [9] developed a method that used a movable water column to measure contact stiffness between aluminum plates. Shetty et al. [10] used a spring-loaded conformable delay-line to measure contact stiffness on metal specimens. Water immersion provides good consistent coupling but requires water on the test specimen which can be challenging in both dynamic measurements and across large areas. The spring method, although movable across the interface, provides too much variation in the coupling force resulting in inconsistent measurements. This work investigates the use of a dry coupled transducer with a conformable delay-line using magnetic attachment to address the drawbacks of existing techniques and enable the measurement of contact stiffness across large interfaces. The next section briefly describes the theory behind measuring contact stiffness with ultrasound and the proposed test procedure. It is followed by the preliminary results of this research.

Methodology

Proposed Approach

Ultrasound has been used as a method for measuring contact stiffness for decades. In 1996, Drinkwater demonstrated that low-frequency ultrasonic longitudinal waves can accurately measure contact stiffness between an interface consisting of two aluminum plates [7]. The interface can be modeled using a spring system, as shown in Fig. 1, where P_{nom} is the nominal contact pressure given by the load divided by the nominal contact area and u represents the average separation between the two surfaces. Contact stiffness, $K_{contact}$, is therefore defined as the pressure required to produce unit displacement, as shown in Eq. 1 [7].

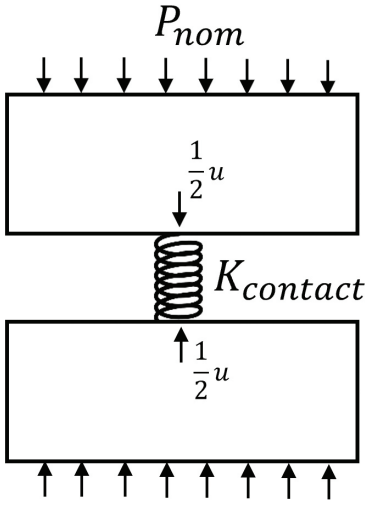

Fig. 1 Representation of the interface as a spring contact model

$$K_{\text{contact}} = -\frac{dP_{nom}}{du} \tag{1}$$

This stiffness represents a lumped parameter that accounts for the effects of the topology and surface roughness at the interface. When sound waves propagate through materials in complete contact, variations in their acoustic impedances result in a portion of the acoustic energy being reflected back to the source as shown by Eq. 2 [7], where R is the reflection coefficient, and Z is the acoustic impedance of the two materials in contact.

$$R = \frac{Z_1 - Z_2}{Z_2 + Z_1} \tag{2}$$

If the materials were of the same composition and in perfect contact there would be no reflection at the interface, as the acoustic impedance would not change, and all the energy would be transferred. Actual interfaces consist of asperities which

result in small air gaps between surfaces, causing sound waves to be reflected. By measuring the amplitude of the reflection voltage from the transducer, R can be calculated as

$$R = \frac{V_{\text{reflected}}}{V_{\text{incident}}}, \tag{3}$$

where $V_{\text{reflected}}$ and V_{incident} represent the reflected and incident ultrasonic wave respectively. Since the acoustic impedance of air is much less than that of metal, V_{incident} can be approximated using $V_{\text{reflected}}$ under no contact. Drinkwater also showed that if the wavelength of the ultrasound is significantly larger than the air gap, then the reflection coefficient can be related to the contact stiffness as shown in Eq. 4 [7], where Z is the acoustic impedance of the materials in contact, ω is the angular frequency of the transmitted wave, R is the reflection coefficient, and K is the contact stiffness at the interface.

$$K = \frac{\omega Z}{2}\sqrt{\frac{1}{R^2} - 1} \tag{4}$$

The contact stiffness across an interface at multiple points can be determined using a roving piezoelectric transducer using Eq. 4, as long as V_{incident} remains constant. Consistent coupling is required to ensure V_{incident} remains constant as the transducer moves along the interface for which we are proposing the method outlined below.

Experimental Setup

To ensure consistent coupling a conformable delay-line with magnetic attachment was chosen to couple the transducer to the test specimen. A conformable delay-line consists of a flexible polymer that adjusts to the surface and provides consistent coupling when the same force is applied, which is provided by the magnets. The conformable delay-line, depicted in Fig. 2b, was made of Aqualink^{TM} 100, a thermoset plastic from Innovation Polymers, and was attached to the bottom of the fixture using neodymium magnets embedded in a plastic holder, as shown in Fig. 2c. Additionally, the delay-line reflection can be used to determine if there is consistent coupling as this quantity represents the amount of energy reflected from the specimen and therefore relates to the amount of energy transmitted into the interface.

To validate this approach, we created a test setup to simulate the contact of a mechanical joint under quasistatic loading and is shown in Fig. 2. The test specimen (a) was comprised of a rod (D = 12.7 mm $\times$ H = 102 mm) and a corresponding cylindrical base (D = 44 mm $\times$ H =102 mm) machined to house the transducer at a depth of 12.7 mm. The test fixture was made from 410 Stainless Steel (SS) and selected for its magnetic properties and corrosion resistance. Both contact areas were flattened and polished to an average surface roughness (Ra) of less than 1 μm. The arrows in Fig. 2a show the incident and reflected waves from the transducer. An Olympus PR3072 pulser receiver was used to excite a 5 MHz, 6 mm diameter transducer in a pulse echo configuration. The size and frequency of the transducer were selected based on the acoustic properties of the material, horizontal resolution (cone width), and to account for the nearfield effect of the transducer based on its distance from the interface. A linear actuator was used to load and unload the test specimen from 0 to 4.5 kN. Data was captured using an oscilloscope and post processing was performed in MATLAB.

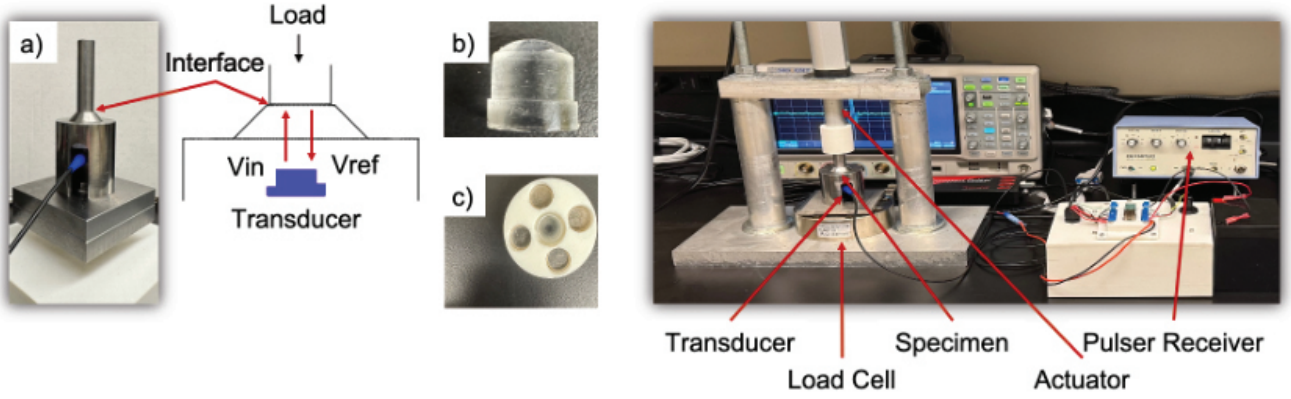

Fig. 2 Experimental Setup - (a) Test specimen (b) Conformable delay-Line (c) Magnetic holder

Preliminary Results

Prior to the quasistatic loading experiment, a metal-to-air interface consisting of a 410 stainless steel plate (145 mm × 76 mm × 12.7 mm) was used to assess consistent coupling of the magnetically attached conformable delay-line. The delay-line and transducer were held in place only by the magnetic force of the attachment device, which applies the same force regardless of where it is attached. The test involved placing the transducer at multiple locations on the test plate and measuring the delay-line and metal-to-air reflection voltages. Figure 3 shows the test plate with the magnetically attached conformable delay-line (a) and five sample delay-line reflections (b) and five metal to air reflections (c). It can be observed that delay-line and metal-to-air reflection measurements remained consistent across all test points, with reflection voltages being within ±0.1V of their average of 3.1V and 1.5V respectively. Additionally, a qualitative test was performed to investigate the effect of surface roughness on coupling performance with portions of the plate roughened to an Ra > 5 μm. The change in surface roughness had a negligible effect on the coupling performance; voltages between the roughened portion and smooth finish remained within the same ± 0.1V band. These tests demonstrate that the proposed solution of a conformable delay-line with a magnetic holder ensures consistent coupling between the metal and the transducer, regardless of the roughness of the surface the transducer is being coupled to.

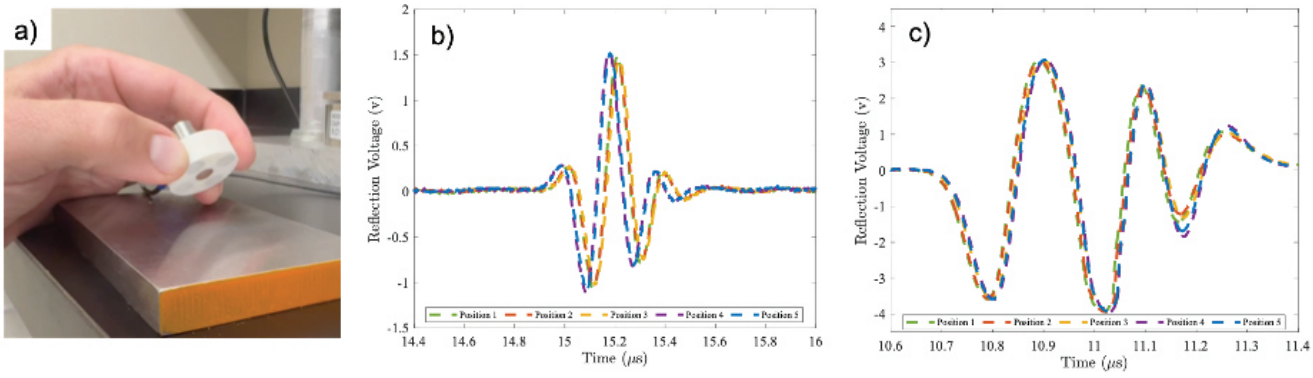

Fig. 3 Consistent Coupling – (a) Test plate (b) Reflection voltage across the plate

The quasi-static loading experiment described previously was then performed to assess the effectiveness and repeatability of contact stiffness measurements using this method. The test specimen was loaded from 0 to 4.5 kN in 200 N increments. This test was repeated several hundred times with fairly consistent results. Figure 4a shows contact stiffness measurements completed during initial testing and Fig. 4b depicts the most recent set of eighty runs. The test was repeated approximately 800 times between the measurements shown in Figs. 4a and 4b. It can be observed that the stiffness reaches an average value

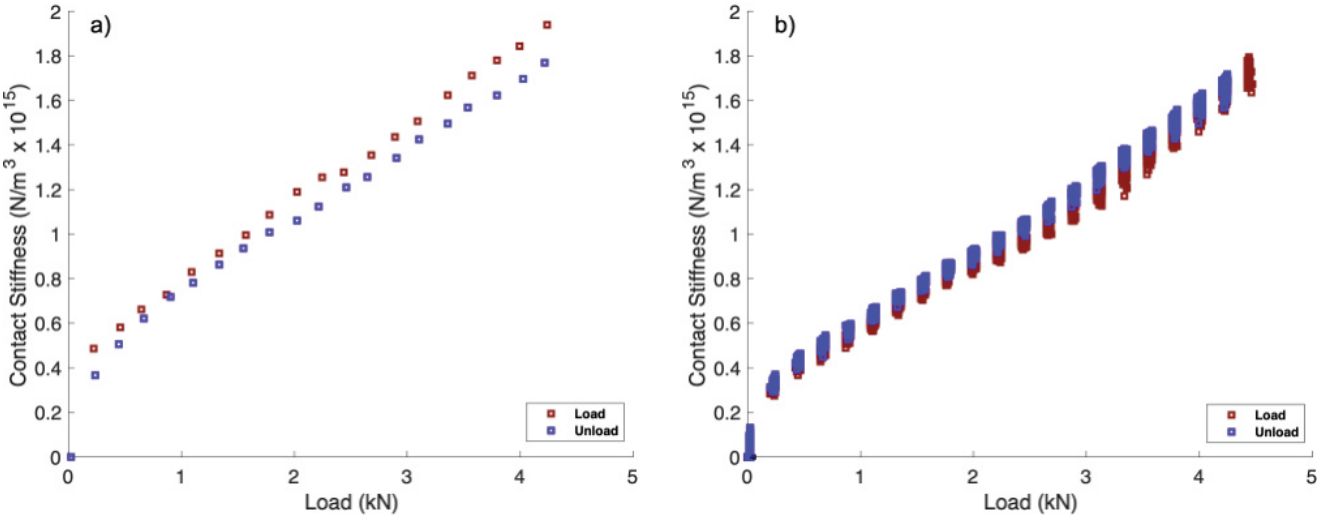

Fig. 4 Contact stiffness vs load (kN) (a) first run at the start of testing, (b) most recent set of runs

of 1.74 x 10^{15} N/m^3 for a load of 4.5 kN, with a standard deviation of 3.1 x 10^{13} N/m$^{3\cdot}$ Additionally, the slope of contact stiffness vs load from 0.5 kN to 4.5 kN is similar for all runs, with an average value of 3.2 x 10^{14} N/m^3 - kN with a standard deviation of 5.0 x 10^{13} N/m^{3}kN. This demonstrates that the proposed method that was conducted over 1,020 loading and unloading cycles is a repeatable and viable option for measuring contact stiffness across metal-to-metal interfaces.

Conclusions

This work proposes a technique for measuring contact stiffness across metal-metal interfaces utilizing an ultrasonic transducer with a dry-coupled, conformable delay-line held in place by magnetic attachment. Preliminary results indicate that this approach provides a cost effective, roving transducer solution that addresses several limitations of existing ultrasonic coupling techniques for measuring contact stiffness across larger interfaces. The study further demonstrated the repeatability of this method for measuring contact stiffness by performing measurements across 1,020 loading and unloading cycles with relatively consistent results. Future research will apply this method to study the relationship between surface roughness and contact stiffness under quasistatic loading conditions. Subsequent work will involve measurements of contact stiffness across small areas under dynamic loading with the goal of expanding these measurements to large interfaces.

References

1. E. J. Richards and D. J. Mead. *Noise and Acoustic Fatigue in Aeronautics*. Chichester, United Kingdom: John Wiley & Sons Ltd, London New York Sydney Toronto, 1st edition, 1968.
2. Li, Dongwu, Daniele Botto, Chao Xu, and Muzio Gola. “Fretting Wear of Bolted Joint Interfaces.” *Wear* 458–459, October 2020.
3. M. Brons, T. A. Kasper, G. Chauda, S. W. B. Klaassen, C. W. Schwingshackl, and M. R. W. Brake, “Experimental Investigation of Local Dynamics in a Bolted Lap Joint Using Digital Image Correlation,” *Journal of Vibration and Acoustics*, Jul. 2020.
4. T. Dreher, M. R. W. Brake, B. Seeger, and M. Krack. In situ, real-time measurements of contact pressure internal to jointed interfaces during dynamic excitation of an assembled structure. *Mechanical Systems and Signal Processing*, 160:107859, November 2021.
5. Tong Wei, Alfredo Fantetti, Frederic Cegla, and Christoph Schwingshackl. An optical method to monitor transparent contact interfaces during high frequency shear vibration cycles. *Wear*, 524-525:204840, July 2023.
6. K. Kendall and D. Tabor, An utrasonic study of the area of contact between stationary and sliding surfaces. *Proceedings of the Royal Society of London. A. Mathematical and Physical Sciences*, 323(1554):321–340, June 1971.
7. B. W. Drinkwater, R. S. Dwyer-Joyce, and P Cawley. A study of the interaction between ultrasound and a partially contacting solid—solid interface. *Proceedings of the Royal Society of London. Series A: Mathematical, Physical and Engineering Sciences*, 452(1955):2613–2628, December 1996
8. L. Pesaresi, A. Fantetti, F. Cegla, L. Salles, and C. W. Schwingshackl, “On the Use of Ultrasound Waves to Monitor the Local Dynamics of Friction Joints,” *Exp Mech*, vol. 60, no. 1, pp. 129–141, Jan. 2020.
9. Trevor W. Jerome, Micah R. Shepherd, and Stephen A. Hambric. Ultrasonic investigation of the pressure profile on the faying surface of fastened aluminum plates. *Mechanical Systems and Signal Processing*, 150:107260, March 2021.
10. D. Shetty, J. Wagner, R. Djishev, M. Brake, “In-Situ Measurement of Local Contact Stiffness using Ultrasound”, in SEM’s 42nd IMAC, February 2024.

River Rapids

Nonlinear Structures & Systems, Volume 1

Ludovic Renson ■ Robert Kuether ■ Paolo Tiso ■ Drithi Shettya

Nonlinear Structures & Systems, Volume 1: Proceedings of the 44th IMAC, A Conference and Exposition on Structural Dynamics, 2026, tthe first volume of ten from the Conference, brings together contributions to this important area of research and engineering. The collection presents early findings and case studies on fundamental and applied aspects of Nonlinear Dynamics, including papers on:

- Experimental Nonlinear Dynamics
- Jointed Structures: Identification, Mechanics, Dynamics
- Nonlinear Damping
- Nonlinear Modeling and Simulation
- Nonlinear Reduced-Order Modeling
- Nonlinearity and System Identification
- Nonlinearities & Applications
- Nonlinear Normal Modes & Interactions

ISBN 978-87-438-1440-5

9 788743 814405

River Publishers